UNIVERSITAT POLITÈCNICA DE VALÈNCIA

UNIVERSITAT POLITÈCNICA DE VALÈNCIA

DEPARTAMENTO DE COMUNICACIONES

PhD Dissertation

Development of non-conventional microwave devices based on substrate integrated technology for advanced applications

Vicente Nova Giménez

Advisor

Dr. Carmen Bachiller Martín

Thesis submitted to the Departamento de Comunicaciones,
in partial fulfillment of the requirements for:
Título de Doctor por la Universitat Politècnica de València
Valencia, October 2023

Dedicado a mi padre, ojalá pudieras estar aquí con nosotros ahora mismo.

«¿Qué pasa Sheriff?»
Vicente Nova García.

Acknowledgement

Quienes me conocen saben cuánto me cuesta abrirme y lo poco que disfruto escribiendo, lo cual se refleja en el tiempo que me ha llevado completar este documento. Sin embargo, creo conveniente dedicar unas palabras de agradecimiento a todas esas personas especiales que han contribuido a lo largo de mi etapa predoctoral.

En primer lugar, me gustaría dar las gracias a mi familia, ellos han contribuido mucho más de lo que piensan al desarrollo de esta tesis. Mis padres y mi hermano me inculcaron los principios que he intentado seguir a lo largo de todos estos años, enseñándome a perseverar y no rendirme ante las adversidades. Estoy inmensamente orgulloso de la familia que tengo.

Quiero agradecer de manera especial a mi directora, Carmen, por su inquebrantable apoyo. Siempre confió en mi capacidad y supo cómo contrarrestar mi natural pesimismo. Sinceramente, no creo que hubiera podido culminar esta tesis doctoral con otro mentor.

Agradezco a mis valiosos compañeros de trabajo por su constante apoyo. Me considero afortunado por haber tenido la oportunidad de colaborar con profesionales excepcionales en todos los lugares donde he estado. Quiero expresar un agradecimiento especial a la profesora Belén Villacampa de la Universidad de Zaragoza, de ella aprendí a cuestionar los resultados y aplicar una metodología de trabajo científica. En el equipo de Rainer Kronberger en la Universidad de Ciencias Aplicadas de Colonia, descubrí la perspectiva más aplicada de un investigador y comprendí la contribución de un ingeniero a la ciencia. Por último, mis compañeros del GAM siempre han estado dispuestos a brindarme su apoyo, y muchos de ellos me han servido como ejemplo, tanto en lo profesional como en lo personal. Les pido disculpas por no mencionarles a todos, son muchos y no quiero extenderme más de lo necesario. He conocido grandísimas personas en esta etapa de mi vida que espero que sigan acompañándome durante muchos años.

Finalmente me gustaría darle las gracias a Noelia. Tú eres la persona que más ha sufrido los pormenores de este trabajo y has estado siempre a mi lado para apoyarme y darme fuerzas. Hay decisiones que cambian vidas, y sé que acercarme a hablar con aquella desconocida en la parada de metro de Turia fue una de las decisiones más importantes de mi vida.

Resumen

El uso masivo de los sistemas de comunicaciones inalámbricas y móviles ha tenido un impacto significativo en nuestra sociedad. Estas tecnologías han experimentado una amplia adopción en el mercado, volviéndose totalmente indispensables en nuestro día a día y provocando un aumento notable en la demanda de movilidad y ancho de banda. A su vez, esto ha llevado a la rápida aparición de nuevos sistemas de comunicación y a la progresiva saturación del espectro radioeléctrico, lo que conlleva un constante aumento en los requisitos de los sistemas de radiofrecuencia. Como resultado, los dispositivos que forman parte de estos sistemas (filtros, amplificadores y antenas) se ven sometidos a especificaciones cada vez más restrictivas. Estas restricciones se han visto fuertemente incrementadas en las comunicaciones espaciales, donde los nuevos sistemas basados en satélite de alta capacidad y grandes constelaciones fuerzan la reducción de costes a la vez que requieren de altas prestaciones.

Con el fin de satisfacer las crecientes demandas de los sistemas inalámbricos, se busca el desarrollo de dispositivos de comunicación que ofrezcan altas prestaciones a bajo costo. Estos dispositivos también deben ser compactos, ligeros y fáciles de integrar con diversas tecnologías de guía de ondas, como guías de ondas convencionales, cables coaxiales y tecnologías de guía planar. En respuesta a estas necesidades, han surgido dos soluciones tecnológicas: los circuitos integrados en sustrato (*Substrate Integrated Circuit (SIC)*) y la fabricación aditiva (*Additive Manufacturing (AM)*).

La tecnología SIC permite combinar tecnologías de guiado planares y no planares en un mismo sistema, lo que resulta en unas prestaciones híbridas entre las guías de onda convencionales y las topologías planares. Además, ofrece una notable reducción de peso y una gran miniaturización y su naturaleza planar permite una integración nunca vista antes.

Por otro lado, la fabricación aditiva permite crear dispositivos con geometrías complejas y bajo peso, lo que proporciona menos limitaciones en el diseño. Esto permite el desarrollo de dispositivos con características avanzadas y la integración de los diferentes bloques que conforman la cadena de radiofrecuencia en un único dispositivo, mejorando así las especificaciones del sistema completo y reduciendo su complejidad.

Tanto la tecnología de substrato integrado (SIC) como la fabricación aditiva son de gran

interés para el sector espacial. Sin embargo, la aplicación de estas tecnologías en el agresivo entorno espacial aún no ha sido estudiada. Por ello, el objetivo principal de esta tesis es investigar la aplicación de estas tecnologías en el diseño de dispositivos de microondas para aplicaciones espaciales. A través de este estudio, se busca obtener un mayor conocimiento sobre las capacidades y limitaciones de estas tecnologías en el contexto espacial, y así explorar su potencial para mejorar y optimizar los dispositivos utilizados en este tipo de sistemas.

En primer lugar, se ha llevado a cabo una comparación de diferentes topologías de filtros implementados en tecnología SIC, los cuales han sido sometidos a pruebas ambientales que simulan las condiciones reales de operación en el espacio.

En segundo lugar, se ha estudiado la aplicación de técnicas de fabricación aditivas al desarrollo de dispositivos de microondas. Para ello, se ha desarrollado un novedoso método de metalización autocatalítico y un sistema de integración de filtros de montaje superficial. Estas tecnologías se han combinado para desarrollar una serie de filtros paso banda de montaje superficial. Finalmente, estos filtros han sido sometidos a pruebas de ambiente espacial, incluyendo: ciclado térmico, pruebas de vibración y test de efecto multipactor.

Por último, se ha estudiado el uso de cristal líquido para agregar capacidades de reconfigurabilidad a dispositivos de microondas integrados en sustrato. Se han analizado las características mecánicas y electromagnéticas de estos materiales mediante dos métodos de caracterización basados en elementos resonantes. Además, se ha desarrollado un demostrador tecnológico basado en la tecnología *Empty Substrate Integrated Coaxial Line (ESICL)*.

Los conocimientos desarrollados en esta tesis engloban tres ámbitos de gran interés para la industria: la integración en sustrato, la fabricación aditiva y la reconfiguración mediante cristal líquido. Este trabajo sienta una sólida base para futuras investigaciones que amplíen el desarrollo de estas tecnologías en aplicaciones prácticas.

Resum

L'ús massiu dels sistemes de comunicacions sense fils i mòbils ha tingut un impacte significatiu en la nostra societat. Aquestes tecnologies han experimentat una àmplia adopció en el mercat, perquè s'han tornat totalment indispensables en el nostre dia a dia i han provocat un augment notable en la demanda de mobilitat i amplada de banda. Al seu torn, això ha portat a la ràpida aparició de nous sistemes de comunicació i a la progressiva saturació de l'espectre radioelèctric, la qual cosa comporta un constant augment en els requisits dels sistemes de radiofreqüència. Com a resultat, els dispositius que formen part d'aquests sistemes (filtres, amplificadors i antenes) es veuen sotmesos a especificacions cada vegada més restrictives. Aquestes restriccions s'han vist fortament incrementades en les comunicacions espacials, on els nous sistemes basats en satèl·lits d'alta capacitat i grans constel·lacions forcen la reducció de costos alhora que requereixen altes prestacions.

Amb la finalitat de satisfer les creixents demandes dels sistemes sense fils, se cerca el desenvolupament de dispositius de comunicació que oferisquen altes prestacions a baix cost. Aquests dispositius també han de ser compactes, lleugers i fàcils d'integrar amb diverses tecnologies de guia d'ones, com ara guies d'ones convencionals, cables coaxials i tecnologies de guia planar. En resposta a aquestes necessitats, han sorgit dues soluciones tecnològiques: els circuits integrats en substrat (*Substrate Integrated Circuit (SIC)*) i la fabricació additiva (*Additive Manufacturing (AM)*).

La tecnologia SIC permet combinar tecnologies de guiatge planars i no planars en un mateix sistema, la qual cosa resulta en unes prestacions híbrides entre les guies d'ona convencionals i les topologies planars. A més, ofereix una notable reducció de pes i una gran miniaturització i la seua naturalesa planar permet una integració no vista mai abans.

D'altra banda, la fabricació additiva permet crear dispositius amb geometries complexes i baix pes, la qual cosa proporciona menys limitacions en el disseny. Això permet el desenvolupament de dispositius amb característiques avançades i la integració dels diferents blocs que conformen la cadena de radiofreqüència en un únic dispositiu, que millora així les especificacions del sistema complet i en redueix la complexitat.

Tant la tecnologia de substrat integrat (SIC) com la de fabricació additiva són de gran

interès per al sector espacial. Tanmateix, l'aplicació d'aquestes tecnologies en l'agressiu entorn espacial encara no ha sigut estudiada. Per això, l'objectiu principal d'aquesta tesi és investigar l'aplicació d'aquestes tecnologies en el disseny de dispositius de microones per a aplicacions espacials. A través d'aquest estudi, se cerca obtenir un major coneixement sobre les capacitats i limitacions d'aquestes tecnologies en el context espacial, i així explorar-ne el potencial per a millorar i optimar els dispositius utilitzats en aquest tipus de sistemes.

En primer lloc, s'ha dut a terme una comparació de diferents topologies de filtres implementats en tecnologia SIC, els quals han sigut sotmesos a proves ambientals que simulen les condicions reals d'operació a l'espai.

En segon lloc, s'ha estudiat l'aplicació de tècniques de fabricació additives al desenvolupament de dispositius de microones. Per a això, s'ha desenvolupat un nou mètode de metal·lització autocatalític i un sistema d'integració de filtres de muntatge superficial. Aquestes tecnologies s'han combinat per a desenvolupar una sèrie de filtres passabanda de muntatge superficial. Finalment, aquests filtres han sigut sotmesos a proves d'ambient espacial, incloent-hi: ciclatge tèrmic, proves de vibració i test d'efecte multipactor.

Finalment, s'ha estudiat l'ús de cristall líquid per a agregar capacitats de reconfigurabilitat a dispositius de microones integrats en substrat. S'han analitzat les característiques mecàniques i electromagnètiques d'aquests materials mitjançant dos mètodes de caracterització basats en elements ressonants. A més, s'ha desenvolupat un demostrador tecnològic basat en la tecnologia *Empty Substrate Integrated Coaxial Line (ESICL)*.

Els coneixements desenvolupats en aquesta tesi engloben tres àmbits de gran interès per a la indústria: la integració en substrat, la fabricació additiva i la reconfiguració mitjançant cristall líquid. Aquest treball senta una sòlida base per a futures investigacions que amplien el desenvolupament d'aquestes tecnologies en aplicacions pràctiques.

Abstract

The widespread use of wireless and mobile communication systems has had a significant impact on our society. These technologies have been widely adopted in the market, becoming essential in our daily lives and leading to a notable increase in the demand for mobility and bandwidth. Consequently, new communication systems are rapidly emerging, and the radio frequency spectrum is becoming increasingly crowded, resulting in continuously rising requirements for radio frequency systems. As a result, radio frequency devices, such as filters, amplifiers, and antennas, are subjected to ever more stringent specifications. These restrictions are particularly heightened in space communications, where high-capacity satellite-based systems and large constellations force mass and cost reduction while requiring high performance.

To meet the growing demands of wireless systems, there is a need to develop communication devices that offer high performance at a low cost. Additionally, these devices should be compact, lightweight, and easily integrable with various waveguide technologies, such as conventional waveguides, coaxial cables, and planar waveguide technologies. In response to these needs, two technological solutions have emerged Substrate Integrated Circuit (SIC) and Additive Manufacturing (AM).

SIC technology allows the combination of planar and non-planar guiding technologies in a single system, resulting in hybrid performance between conventional waveguides and planar topologies. It offers a significant reduction in weight and miniaturisation, and its planar nature allows for unprecedented integration.

On the other hand, additive manufacturing enables the creation of devices with complex geometries and low weight, providing fewer design limitations. This allows for the development of devices with advanced features and the integration of different blocks of the radio frequency chain into a single monolithic device, thereby enhancing the performance of the entire system and reducing its complexity.

Both SIC and AM are of great interest to the space sector. However, the application of these technologies in the harsh space environment has not been thoroughly studied. The main objective of this thesis is to investigate the application of these technologies in the design of

microwave devices for space applications. This study aims to gain a deeper understanding of the capabilities and limitations of these technologies in the space context and explore their potential for improving and optimising devices used in such systems.

The thesis first involves the design and comparison of different filter topologies implemented using SIC technology, which has been subjected to environmental tests simulating real space operation conditions.

Secondly, the application of additive manufacturing techniques to the development of microwave devices has been studied. For this purpose, a novel autocatalytic metallisation method and a system for surface-mounted filter integration have been developed. These technologies were combined to develop a series of surface-mounted bandpass filters. Finally, these filters were subjected to space environmental tests, including thermal cycling, vibration tests, and multipactor effect tests.

Lastly, the use of liquid crystal to add reconfigurability capabilities to substrate-integrated microwave devices has been investigated. The mechanical and electromagnetic characteristics of these materials have been analysed using two resonant element-based characterisation methods. Additionally, a technological demonstrator based on ESICL technology has been developed.

The knowledge developed in this thesis encompasses three areas of great interest to the industry: substrate integration, additive manufacturing, and liquid crystal reconfiguration. This work provides a solid foundation for future practical research that further develops these technologies for the space sector.

Index

Chapter 1

Introduction

1.1 Motivation and Interest of the Topic

There has been a rapid transformation in communication systems in recent years, with a particular impact on satellite communications. The high demand for data throughput, bandwidth and ubiquitous connectivity is pushing microwave technology to its limits. This change is particularly evident in the space industry, where the business focus has shifted from large Geostationary Earth Orbit (GEO) satellites to constellations of numerous satellites operating in Low Earth Orbit (LEO). The concept of large LEO constellations is reminiscent of the ambitious global phone connectivity projects of the 1990s that include Iridium, Globalstar, and Odyssey. Most of these systems were ultimately cancelled due to their high costs or technological limitations, which led the new LEO systems to focus on reducing the cost per bit.

In this evolving scenario, the feasibility of these new satellite systems heavily relies on the reduction of production, launching, and operation costs. Microwave devices used in these space communications systems must not only exhibit high performance and adaptability but also undergo a drastic reduction in weight, size, and price. These factors are crucial for the success and sustainability of the new generation of space communication systems, as highlighted by studies on large LEO constellations and industry reports [1, 2].

Different solutions can be applied to improve the performance and reduce the production cost and weight of the Radio Frequency (RF) front-ends. One notable solution is the Substrate Integrated Circuit (SIC) technology, which emerged in the late 1990s to address similar demands of the industry [3, 4]. The SIC technology involves the integration of different waveguide topologies within a substrate stack-up, combining the benefits of planar transmission lines (e.g., microstrip, coplanar, and stripline) and non-planar technologies (e.g.,

dielectric structures and metallic waveguides). This hybridisation enables the development of high-performance devices with relatively low production costs and seamless integration with planar subsystems [4, 5], effectively filling the technological gap between planar and non-planar approaches.

On the other hand, Additive Manufacturing (AM) is a versatile technology that offers unparalleled design flexibility. It has the potential to revolutionise the production of microwave devices by simplifying the manufacturing of complex geometries. At the same time, AM allows the production of multiple devices as a single monolithic part, reducing the assembling complexity and weight of the system. The design freedom provided by AM, along with the use of lightweight materials, facilitates the production of devices with exceptional performance, reduced weight, and low production costs for small and medium production runs [6, 7]. These characteristics position AM as a promising candidate for addressing the current industry needs, especially in the space sector where its lightweight nature and cost-effectiveness perfectly align with sector requirements [8].

Reconfigurability has consistently been a prominent trend in the RF and microwave sector. The increasing demand for communication systems has given rise to a dynamic and congested wireless environment. In such a context, the capability to modify the electrical response of microwave devices to align with the specific requirements of the system becomes crucial. Functional materials, particularly Liquid Crystal (LC), offer numerous advantages in this regard. However, the limited understanding of these materials at specific frequency bands challenges their widespread utilisation in practical applications.

This thesis addresses the need to develop high-performance and adaptable microwave devices for the space sector while maintaining a focus on reduced weight and cost. The core of this work is the exploration and development of a novel manufacturing and integration method that leverages additive manufacturing technology, offering an affordable alternative for SIC filters. Furthermore, the thesis presents and compares four filter technologies and three power dividers that are developed using SIC technology. Notably, this thesis makes a significant contribution to the field of the space industry by conducting the first comprehensive qualification of filters developed using the two technologies considered in this study: SIC and additive manufacturing. Finally, this thesis extends the understanding of liquid crystals as a functional material by characterising their dielectric and mechanical properties at microwave frequencies, adding these results to the existing body of knowledge in this area.

1.2 State of the Art

In this section, we will provide a comprehensive review of three key areas relevant to the research conducted in this thesis. Firstly, we will delve into satellite orbits and constellations. Next, we will explore the emerging technologies for the development of filters, with a particular emphasis on the SIC approach and the application of Additive Manufacturing (AM) techniques to the microwave sector. Lastly, we will present an overview of different tunable techniques that have garnered attention in recent years.

1.2.1 Satellites Orbits and Constellations

Communications satellites act as radio stations, receiving RF signals from Earth, amplifying or processing them, and then retransmitting the regenerated signals back to Earth. Essentially, communication satellites work as space nodes of a global network, facilitating the routing of information between remote locations on Earth [9].

The number of artificial satellites orbiting the Earth has grown steadily since the launch of the first artificial satellite, the Sputnik I, in 1.957 by the USSR. Over 12,000 satellites have been launched since then, marking a significant milestone in space exploration. Currently, there are approximately 8.840 operational satellites in orbit, with around 1.700 launched in 2021 alone [10]. These figures provide insight into the remarkable growth of the space industry in recent years. Notably, this growth is attributed to a shift of the sector towards constellations of low-earth orbits as opposed to the traditional focus on Geostationary Earth Orbit (GEO) satellites. Before delving into this emerging trend, it is essential to provide an overview of the different types of satellite orbits.

Satellite orbits can be categorised based on various factors such as inclination, height or altitude, and eccentricity. For communication satellites, altitude is a crucial parameter as it defines the orbit speed and period of the satellite, which ultimately defines the average delay of the communication and the coverage area of the system. Satellites can be classified into the following categories based on their orbit height:

- Geostationary Earth Orbit (GEO) satellites orbit the Earth at an altitude of approximately $36\,000\,\mathrm{km}$ [11]. At this altitude, satellites travel at the same rate as the Earth's rotation, making them appear stationary in the sky. This characteristic eliminates the need for complex tracking systems in the ground segment and enables near-continental coverage. A single GEO satellite can provide coverage from around 20 degrees north to 20 degrees south latitude [9]. Moreover, due to its high altitude, only three equally spaced GEO satellites are required to achieve quasi-global coverage. These characteristics make the GEO systems particularly suitable for broadcasting communications

that require global coverage and simple and cost-effective receivers. This is why these systems were the most extended during the first times of space communications.

Examples of services that benefit from GEO systems include TV broadcasting, certain web applications, and more recently, IoT data collection. However, due to the high distance between user terminals and GEO satellites, the latency can be significant (up to $300\,\mathrm{ms}$). This latency makes these systems unsuitable for real-time applications such as voice and video conferences or internet services that require low latency.

- Low Earth Orbit (LEO) is an orbit with an altitude between 160 and $1.000\,\mathrm{km}$ [11]. The average orbiting time at this altitude is less than two hours [9], so satellites in this orbit are in view from a fixed point of the Earth for a few minutes. As a result, Earth terminals must continuously commute from satellite to satellite, needing complex tracking systems and handover mechanisms. The low height reduces the coverage area, needing a large number of satellites forming a big space net (constellations) to obtain global coverage. Deploying such a big constellation may be economically prohibitive, especially if we consider that the system cannot offer services until numerous satellites are already operating in orbit. Conversely, the proximity of this orbit gives a low latency (about $10\,\mathrm{ms}$), being really suitable for interactive applications such as broadband internet access or IoT dynamic control. Additionally, the short distance between satellites and users' terminals reduces the needed communication powers, simplifying the RF front end of both users and satellites.

- Medium Earth Orbit (MEO) satellite operate at an altitude of approximately $10.000\,\mathrm{km}$. This orbit is allocated between GEO and LEO systems, offering a trade-off between these two orbits. In comparison to LEO, Medium Earth Orbit systems require a smaller constellation of satellites to achieve full Earth coverage and offer extended satellite observation time from Earth. On the other hand, when compared to GEO, Medium Earth Orbit systems can operate with lower power requirements, allowing for lighter and smaller satellites.

  While this orbit may initially appear appealing, it does not provide significantly more benefits than the aforementioned orbits, and it has primarily been reserved for global navigation systems such as Galileo (Europe), GLONASS (Russia), Beidou (China), and GPS (USA).

Communication systems have traditionally relied on Geostationary Earth Orbit satellites due to their longer service life and relatively simple user terminals compared to those operating at lower altitude orbits. Moreover, GEO satellite systems, only three satellites are needed, and the low operation cost and enhanced service life compensate for the extra launching cost.

In the past, traditional satellite systems had simpler designs, and their RF front-ends were designed with a fixed response in terms of coverage, power, and frequency that was tailored to specific services. In this context, the design and manufacturing of the satellite payload were somewhat artisanal [12].

In contrast, the emergence of new Low Earth Orbit (LEO) satellite and high-throughput GEO satellite concepts promise faster communications and higher bandwidth per user than traditional systems. This enhanced performance results from the use of reconfigurable payloads, advanced modulation schemes, and multi-beam antennas. However, the successful implementation of these new systems requires significant changes in the sector to ensure their profitability, with a particular focus on cost reduction. Satellite payloads can no longer be produced in an artisanal manner, and the development of advanced manufacturing techniques and efficient launching strategies is essential to achieve the long-desired cost reduction.

Regarding the new LEO communication systems, if the proposed satellite constellations become a reality, it is estimated that over 50.000 LEO satellites will be launched within the next decade. This represents more than a fivefold increase compared to the current number of orbiting satellites. Such a massive deployment of Low Earth Orbit satellites has the potential to lead to a paradigm shift in the space sector, with a significant emphasis on massive constellations of Low Earth Orbit satellites. Consequently, there will be a growing demand for lightweight and compact microwave devices that offer improved performance while maintaining low production costs, further highlighting the evolving needs of the sector.

1.2.2 Emerging Technologies

This section explores the emerging technologies that address the requirements of novel wireless communication systems. Specifically, three key research areas have gained significant attention in recent years: Substrate Integrated Circuit technology, Additive Manufacturing and novel tunable techniques. These areas align with the current demands of the space and mobile communications market, which include enhancing performance, reducing size and mass, improving adaptability and reconfigurability, and lowering manufacturing costs. While it is challenging to encompass the scope of these broad fields, this section aims to provide the reader with a comprehensive understanding of the significance and future prospects of each research area.

1.2.2.1 Substrate integrated technologies

The integration of planar and non-planar circuits is a critical aspect of microwave and millimetre wave front-ends. Planar transmission lines (i.e., microstrip, coplanar waveguide,

and stripline) offer seamless structural integration, topology miniaturisation, broadband designs, and mass production. However, they suffer from high losses, weak shielding, and limited power handling capabilities. On the other hand, non-planar technologies (waveguides and coaxial cables) offer improved performance with lower losses and higher power handling capabilities but come with disadvantages that include reduced operation bandwidth and bulky topologies. Moreover, non-planar technologies are unsuitable for cost-effective mass production, and integrating active circuits requires complex wire-bounding and intermediate transitions to planar lines [13].

It is evident that both technologies have complementary strengths, and their combination in a hybrid system can benefit from their individual advantages. In such hybrid systems, planar and non-planar technologies can be deployed at will following specific requirements. Planar technologies are perfect for situations where miniaturisation and seamless integration are critical, while non-planar technologies excel in areas where performance and power-handling capabilities are paramount. This flexible approach allows for the creation of advanced microwave and millimeter-wave devices that can fulfil a wide range of applications, making it a compelling solution for modern wireless communication systems.

The concept of hybridisation was first introduced in the 1980s with the development of the fin line technology [14]. The fin line structure involves a slot line embedded within a rectangular waveguide. This design aimed to integrate active devices seamlessly into waveguide systems, eliminating the need for complicated transitions and wire bonding. However, despite its potential, the fin line technology did not succeed due to its bulky topology, complex assembly and high manufacturing costs.

It was not until the early 2000s that the idea of Substrate Integrated Circuit (SIC) emerged, primarily with the development of Substrate Integrated Waveguide (SIW) [3]. The substrate-integrated waveguide implements an equivalent dielectric-filled rectangular waveguide in a Printed Circuit Board (PCB) by periodically connecting the top and bottom copper cladding of the substrate with two rows of plated-through holes or trenches, as depicted in Figure 1.1.

The fundamental idea behind SICs is to integrate planar lines and non-planar waveguides within the same stack-up of substrates. This innovative approach allows for the hybridisation of planar and non-planar technologies within a unified design and manufacturing platform, enabling an unseen integration, miniaturisation, and mass production while providing exceptional electrical performance [5].

The rapid evolution and success of substrate-integrated circuits is evident in the continuous emergence of novel topologies. Examples of these advancements include the Empty Substrate Integrated Waveguide (ESIW) and the Air-Filled Substrate Integrated Waveguide (AFSIW) that implement empty substrate-integrated rectangular waveguides, as well as the

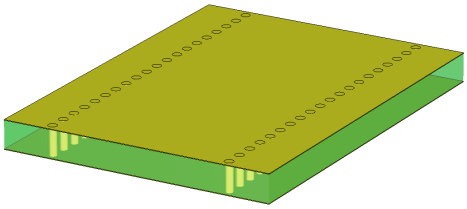

Figure 1.1: Topology of a Substrate Integrated Waveguide (SIW) consisting of a rectangular waveguide implemented in a Printed Circuit Board (PCB) by means of two parallel rows of plated through holes. Copper is depicted in yellow, and the substrate material is represented in blue.

Empty Substrate Integrated Coaxial Line (ESICL) and Ridge Empty Substrate Integrated Waveguide (RESIW) that integrate coaxial lines and ridge waveguides in planar substrates.

The significant interest in this technology has also led to the development of a wide range of devices implemented on these novel lines, including filters [15–19], power dividers [20–22], and antennas [23–26]. Regarding filters, a topic that is extensively explored in this thesis, specific topologies have garnered attention, including the alternating dielectric line section filter topology [27, 28] and the substrate-integrated coaxial filter topology [29, 30]. These topologies are further elaborated upon in Section 2.1.

In conclusion, the integration of planar and non-planar circuits in microwave and millimeter-wave front-ends presents a good solution to address the challenges of the new wireless systems. This approach enables a unified design and manufacturing platform that effectively combines the benefits of planar and non-planar technologies, opening up new design opportunities for the space sector.

1.2.2.2 New manufacturing techniques: additive manufacturing

Additive Manufacturing, 3D printing and rapid prototyping are synonymous expressions to refer to a new class of manufacturing techniques through which parts are built by selectively adding material. This approach completely differs from conventional machining techniques, where parts are fabricated by removing material through milling, machining, carving, shaping or other means. In its early days, AM was used to develop exhibition prototypes or mock-up models. However, during the last decade, significant improvements have been made in this field, enabling the use of this new manufacturing technique in the production of end-user parts, even in demanding scenarios such as the development of RF front-ends operating at microwave and millimeter-wave frequencies [6, 8]. In this field AM techniques has several advantages [7]:

- AM is capable of manufacturing geometries of great complexity that include completely enclosed cavities and curved geometries that are impossible to obtain with traditional techniques. Additionally, AM is able to produce such complex geometries in a single block, reducing the assembling complexity and its associated radiation loss. This capability is particularly beneficial for integrating cascaded devices such as filters, feeding networks, and antennas into a single component. This approach enhances the system performance and reduces the assembling and manufacturing complexity. The design flexibility and integration provided by this technology help to reduce size and mass, being particularly interesting for the space industry [6].

- The weight of parts can be drastically reduced by using lightweight polymers instead of heavy metals. Moreover, the design flexibility of AM allows for the creation of semi-hollow parts with internal lattice structures, further decreasing weight while maintaining structural integrity.

- The ability of AM to fabricate objects directly from a 3D model results in unbeatable production lead times, making it highly suitable for time-sensitive research endeavours.

- Most AM techniques eliminate the need for tooling, leading to lower maintenance costs compared to traditional machining methods. Additionally, the relatively affordable price of 3D printers enables rapid prototyping in research fields and small companies that previously relied on outsourcing manufacturing processes.

- Some AM allows using different materials simultaneously, providing unique properties. This opens many possibilities for creating composite materials or parts with variable characteristics in response to different stimuli. The emerging field of 4D printing, where objects can change shape or functionality over time, is generating significant interest in various industries.

Although AM seems to be a promising technique, several technological barriers still need to be addressed before this novel technology can be widely adopted in the industry [8]. These challenges include:

- Precision and resolution: traditional manufacturing techniques are significantly more accurate than AM. As a rule of thumb, the precision of AM is approximately an order of magnitude lower than the precision of traditional techniques ($0.1\,\mathrm{mm}$ of the AM vs $0.01\,\mathrm{mm}$ of the traditional machining).

- Material limitations: while AM offers a wide range of materials, including polymers, metals, and composites, there are still limitations in terms of material properties, such

as strength, durability, and thermal resistance. Developing new materials that meet the requirements of specific applications remains a crucial area of research.

- Scalability and production efficiency: AM processes are generally slower compared to traditional manufacturing methods when it comes to high-volume production. Improvements in printing speed, build volume, and automation of post-processing steps are needed to increase the scalability and efficiency of AM production.

- Simplification and standardisation: some AM techniques need post-processing treatments such as sinterisation, curing, hardening, shot-peening, and metallisation. This could prevent using these techniques for mass production, as these processes are usually time-consuming and expensive.

- Change of mindset: in additive manufacturing, designers and manufacturers face very different problems than those they are used to in traditional manufacturing. These problems include warping, support structure optimisation, surface roughness depending on the printing orientation, etc. A change of mindset is needed.

Despite its limitations, AM is a very attractive option for industries with a low to medium production volume. This scenario perfectly suits research groups where low cost, rapid manufacturing, and design flexibility are paramount. The space industry is another sector that can profit from this new manufacturing approach thanks to its customisation, compactness and weight reduction, which is evidenced by the large number of scientific texts written on the subject in recent years [6, 8].

There are numerous recent publications on waveguides, passive devices, and antennas over a wide range of frequencies and using different AM techniques. Based on our research, two primary approaches can be identified: metallised plastic devices and those directly printed on metal.

In the first approach, the passive components are fabricated using AM techniques that use plastic as base material. These plastic materials are then metallised to provide conductivity and obtain a fully functional device. This approach offers the advantage of lightweight and cost-effective manufacturing, as plastic materials are typically less expensive and easier to process compared to metals. However, the thermal and mechanical performance of the metallised plastic structures may not match those of fully metal-based devices. Moreover, metallisation processes are generally complex and need extensive study. Despite these problems, several studies have confirmed the viability of this approach using different AM techniques, including Stereolithography Apparatus (SLA) [31–35], Fused Deposition Modelling (FDM) [36–41], Selective Laser Sintering (SLS) [42–47], and Material Jetting (MJ) [48].

In the second approach, the passive components are directly fabricated using metal materials. This approach achieves better mechanical and thermal performance. However, it may be more challenging and expensive to print directly on metal substrates compared to plastic substrates, and printed parts tend to have a rough finish. This and the small electric conductivity of employed metals limit their practical use.

Despite these challenges, there are several notable examples of this approach successfully applied to various passive devices [42–47]. Many of these works have on the space sector, where mechanical and thermal requirements are overly demanding for plastic pieces. Swissto12 [49] is the most famous driver of this approach. This company has addressed the roughness issues by employing a patented chemical post-processing treatment, improving the surface finish of the printed metal parts. Additionally, the low electrical conductivity of the base metal is mitigated by applying silver plating, enhancing the conductivity of the printed components. The expertise and innovative solutions of this company have gained recognition, leading to collaborations with esteemed space contractors such as ESA, NASA and Hispasat.

Both approaches have advantages and limitations, and the choice between them depends on the specific requirements of the application. Metallised plastic devices are well-suited for lightweight and cost-effective applications, while directly printed metal devices offer enhanced performance at the cost of increased complexity and potential manufacturing challenges.

The continuous advancements in AM technologies and materials are expanding the possibilities for waveguides, passive devices, and antennas, enabling the development of novel designs and pushing the boundaries of performance. Further research and development in this field will undoubtedly lead to even more innovative and efficient AM-based solutions for microwave and millimeter-wave applications.

1.2.2.3 Reconfiguration techniques

Tunable techniques play a crucial role in designing and implementing microwave filters and other passive devices. These techniques enable the dynamic control of the characteristics of a device to adapt its electric response to varying requirements. This makes them highly valuable in modern wireless communication systems that require a high degree of reconfigurability and adaptation.

This section offers a brief overview of various tunable techniques used in microwave filters. We will explore three main technologies: semiconductor-based elements (e.g., PIN diodes, transistors, and varactor diodes), RF micro-electro-mechanical systems, and functional materials (e.g., ferrites and liquid crystals). Understanding the principles and capabilities of these tunable techniques will provide valuable insights into their applications and

potential benefits in wireless systems.

- Semiconductor-based tunable techniques provide versatile and efficient solutions for tuning microwave filters. These elements offer a fast response time, wide frequency range, compact size, and compatibility with planar circuits, making them attractive for many applications. However, they do have some drawbacks, including a limited tuning range, non-linear behaviour, and relatively high insertion losses. Among the semiconductor elements, the pin diode and the varactor diode stand out.

  - PIN diodes are extensively used in microwave filters due to their fast response time and low insertion loss. These diodes function as variable resistors whose value can switch between a low series resistance and a high shunt resistance (effectively an open circuit) by applying a DC bias voltage. This resistance change allows for the achievement of a reconfigurable response in the filter. In [50], PIN diodes were employed as switching elements in a combline filter implemented using SIW technology. These diodes served to connect or disconnect a series of distributed capacitors, effectively controlling the resonance frequency of the filter's resonator across a range of digital combinations.
  - Varactor diodes exploit the voltage-dependent capacitance of a p-n junction to achieve frequency tuning. The capacitance of the varactor diode can be adjusted by varying the reverse bias voltage, enabling frequency agility in microwave filters. In [51–54], varactor diodes are employed in different filter topologies to vary the effective phase of the filter's resonators. The main advantage of this technology is its capability to achieve continuous reconfigurability.

- RF micro-electro-mechanical systems offer a promising avenue for achieving reconfiguration with high precision and reliability. The micro-electro-mechanical technology enables the development of miniature mechanical devices whose properties can be modified through a mechanical movement activated by a DC signal. This technology presents an alternative to traditional semiconductor devices, offering higher linearity and lower insertion loss and power consumption than semiconductor elements. However, they are vulnerable to mechanical stress and vibrations, have a limited lifespan, necessitate high activation voltages, and are associated with higher costs. Some common examples of RF micro-electro-mechanical systems include capacitive switches and varactors.

  - Capacitive switches offer an effective solution for achieving tunable filters with reduced insertion loss and improved linearity compared to their semiconductor

counterpart. In [55–58], several micro-electro-mechanical switches are employed to increase the electrical length of filter resonators, enabling tunable responses. This can be done by connecting transmission line sections or reactive elements to the resonator, thus changing the resonance frequency. A similar approach is used in [59], where micro-electro-mechanical switches modify the coupling length in hairpin filters by connecting sections of microstrip lines. This approach allows controlling the filter bandwidth while maintaining a constant centre frequency and return loss.

  - Micro-electro-mechanical varactors or tunable capacitors provide an alternative to traditional semiconductor-based varactor diodes.

- Functional materials provide an innovative approach to achieving continuous reconfiguration in microwave devices. These materials exhibit unique properties that allow the control of their electromagnetic properties through an external stimuli (e.g., magnetic or electric field, heat, vibration, etc.). Among the functional materials investigated for microwave applications, two prominent examples are ferrites and liquid crystals.

  - Ferrite materials exhibit tunable magnetic properties that can be used for achieving continuous frequency agility in microwave devices. The magnetic permeability of the ferrite changes under the presence of a continuous magnetic field. In this way, if a small ferrite is introduced in a microwave device, the properties of the ferrite can be modified at will using a magnet or a coil, resulting in a change in the parameters of the device. In [60], a filter developed on a substrate-integrated waveguide is equipped with ferrite slabs located in the side walls of the resonators. When a magnetic field is applied, the phase of the resonators is altered, resulting in a change in the resonance frequency of the filter. The same principle was combined with pin diodes in [61] to enhance the reconfiguration range of the device, further extending its tunability capabilities.

  - Liquid crystals offer the ability to change their dielectric properties by applying electric or magnetic biasing fields. This property can be harnessed to achieve tunable devices at different frequencies. This technology has been broadly used at optical frequencies and is starting to be explored at microwave and millimetre-wave frequencies. In [62,63], liquid-crystal was used to introduce reconfigurability in different filter topologies implemented on inverted microstrips. The inverted microstrip has proved to be very convenient for liquid crystal applications due to its planar geometry, although other guiding technologies also show promise. For instance, in [61], small volumes of liquid crystal were included in the centre of

rectangular resonators implemented on a groove gap waveguide, resulting in a tunable filter design.

Functional materials provide a promising approach for implementing reconfiguration capabilities at microwave and millimeter-wave frequencies. Compared to semiconductor technologies, these materials offer continuous reconfiguration with lower power consumption and improved linearity. Moreover, these materials are more robust against vibrations and offer a longer lifespan than micro-electro-mechanical at reduced costs. Among functional materials, liquid crystals outperform ferrites due to their lightweight and compact nature. Liquid crystals enable both electric and magnetic control, providing greater design flexibility, and ferrites are limited to work at lower frequencies. For these reasons, the chosen technique for implementing reconfiguration features in this thesis is the use of liquid crystal. A comprehensive review of the properties of this material is provided in Chapter 5.

1.3 Objective of the Thesis

Substrate Integrated Circuits (SICs) have proven to be highly suitable for developing radio frequency devices operating at microwave and millimeter wave frequencies. They exhibit low losses, seamless integration with planar architectures, and facilitate mass manufacturing. However, in the context of the emerging space scenarios characterised by large constellations of high-throughput satellites, additional functionalities become desirable. These include improved performance, enhanced design flexibility, reduced weight and size, and significant cost reduction.

In this context, the focus of this thesis has been on the exploration and evaluation of innovative designs and manufacturing technologies for space applications. The aim has been to lower production costs, enhance design flexibility, and assess the feasibility of proposed technologies for the space sector. The primary objective of this thesis can be summarised as follows:

- Development and characterisation of an innovative manufacturing method based on Additive Manufacturing (AM) that provides greater design flexibility and reduces the weight and cost of communication filters. The focus will be on developing easily integrated bandpass filters as a low-cost and time-efficient alternative to substrate-integrated filters. Finally, the developed prototypes will undergo comprehensive space qualification tests to demonstrate their suitability for the demanding space sector. For this purpose, the following second objective can be defined:

  - Analysis of additive manufacturing techniques and selection of the most suitable technique for microwave applications in the space sector.
  - Developing a suitable metallisation process for the selected manufacturing technique.
  - Development, manufacturing and measurement of a classical H-plane rectangular cavity filter that serves as a technology demonstrator.
  - Analysis of integration structures between waveguide devices and planar subsystems.
  - Development of a reliable and easy-to-manufacture integration system between waveguide filters and planar subsystems implemented on microstrip.
  - Development, manufacturing and testing of easy-to-integrate filters that combine the new additive manufacturing techniques and the proposed integration system.
  - Performance analysis and space qualification of the developed devices.

- One of the challenges encountered during the course of this project was the limited availability of testing results for Substrate Integrated Circuit (SIC) structures. This limitation makes it impossible to work with these structures without the confidence of knowing whether they will survive the orbit positioning and space operation. Consequently, it is crucial to conduct a comprehensive analysis and evaluation of the performance of these structures under space conditions. The second objective of this thesis is to design, manufacture, and measure different filter technologies based on Substrate Integrated Circuit (SIC) in order to assess their suitability for the space environment. To achieve this objective, the following activities have been proposed:
  - Study of different topologies for SIC structures.
  - Design and manufacturing of the same filter response using different SIC technologies.
  - Measurement and analysis of the filters' performance to identify their strengths and weaknesses.
  - Space qualification of the most suitable filters.

- Investigation of the capacities of Liquid Crystal (LC) as functional material to the development of reconfigurable devices at microwave frequencies:
  - One of the problems regarding LC encountered during this thesis was the lack of information about the dielectric properties of commercial liquid crystals at

microwave frequencies. Thus, it is necessary to correctly characterise the liquid crystal samples before designing any tunable device. Three split-cavity resonators have been used for this purpose, using three different analysis methods to obtain an accurate permittivity and loss tangent result for the extreme polarisation states of liquid crystal samples.

- Development of an electrically tunable resonator implemented on a SIC topology. This resonator will be used to characterise the permittivity of liquid crystal mixtures at different polarisation states, the splay deformation constant (K_{11}), and the rotational viscosity (Γ_{11}).
- Design, manufacturing and testing an electrically tunable phase shifter based on the combination of liquid crystal and ESICL technology.

1.4 Structure of the Thesis

The thesis is divided into six chapters:

- **Chapter 1.** The first chapter serves as an introduction to the thesis, providing the motivation, state-of-the-art, and research objectives.
- **Chapter 2.** This chapter focuses on the extensive literature review conducted for the thesis. It begins with a short introduction to the versatile coupling matrix filter design method to further examine various filter topologies, including non-planar, planar, and hybrid or Substrate Integrated Circuit (SIC) technologies. This literature analysis concluded that integration is a crucial property for filters, making SIC the most suitable choice for the new space scenario, thanks to their compactness and lightweight characteristics.

  The chapter also discusses the space environment conditions and the required space qualification tests for microwave components, encompassing thermal, mechanical, and high-power tests. It is worth noting that while SIC technologies and additive manufacturing are seen as disruptive technologies for the space sector, there is no available information on their space qualification campaigns, being the work developed in this thesis the most completed study of this topic.
- **Chapter 3.** This chapter focuses on designing and manufacturing microwave filters using additive manufacturing techniques. Firstly, the combination of Surface-Mount Technology (SMT) and additive manufacturing is studied. Afterwards, various filter

topologies at X and C bands that combine SMT, cavity resonators, and additive manufacturing are proposed and manufactured using Stereolithography Apparatus (SLA) and novel plastic metallisation techniques. Combining these technologies provides a low-cost, high-performance alternative to SIC technology.

Finally, the developed prototypes proved their suitability for space applications by submitting them to a comprehensive space qualification campaign. This represents the most comprehensive qualification for space applications developed on additively manufactured components documented in the literature. This thorough testing emphasises the suitability of the filters and their materials for long-distance space communications systems.

- **Chapter 4.** This chapter focuses on the utilisation of Substrate Integrated Circuit (SIC) technology in the space industry. It begins with an overview of the most suitable SIC technologies. Subsequently, four filters are designed and implemented using different SIC approaches and similar stack-ups. These prototypes underwent thermal and mechanical tests for space qualification. Additionally, a theoretical study of the multipactor effect was conducted. The results of these tests highlight the suitability of such filter topologies for LEO satellite systems. Finally, the development of three power dividers operating at the C band using ESICL technology is also included in this chapter. The choice of this technology is based on its high bandwidth, compact size at low frequencies, and the absence of a requirement for good electrical continuity between layers.

- **Chapter 5.** This chapter explores the development of reconfigurable devices based on liquid crystal technology. It presents two methods for characterising the most important properties of liquid crystals. The first method involves using a split-cylinder-cavity resonator to obtain precise measurements of the dielectric properties of four different liquid crystal samples. The second method employs a substrate-integrated tunable resonator to approximate the dielectric and mechanical properties of one liquid crystal sample. Finally, a technological demonstrator of a tunable phase shifter is proposed.

- **Chapter 6.** The final chapter of the thesis establishes the main conclusions of this work. It also presents potential research and development avenues associated with the findings of the thesis.

Chapter 2

Theory

2.1 Microwave Filters

Microwave filters are employed in virtually any wireless communication, radar or measurement systems [64]. Filters are passive microwave networks that allow an efficient transmission within a specific frequency range defined by the passband while effectively attenuating outside this range (stopband) [64]. In the context of the limited electromagnetic spectrum, where multiple wireless communication and sensing systems coexist, filters play a crucial role in distinguishing desired signals from undesired ones [65]. Filters are categorized based on their ability to transmit or reject certain frequencies, leading to the classification of low-pass, high-pass, band-pass, or band-stop filter responses.

Recent developments in wireless communication systems have resulted in a significant increase in wireless system complexity. As current coding and modulation schemes are reaching the maximum limit established by the Shannon theorem [66], the need for higher data rates inevitably leads to the development of more complex and sophisticated communications systems. Therefore, filters should not only fulfil traditional requirements such as low loss, high isolation, extremely linear phase response, and low cost, but they must also comply with new requirements, including compactness, lightness, integration and frequency agility [67].

The design of microwave filters involves a series of essential steps to achieve the desired performance. In general, this process consists of selecting the filtering response, synthesising a distributed model of the filter, and synthesising the physical dimensions of the filter. Since several filters have been implemented in this doctoral thesis, it seems appropriate to introduce the basics of filter design. The following section provides an overview of these processes.

2.1.1 Filter Design

The first step of the filter design process involves determining the filtering function and order that meets the requirements of a specific application. These requirements involve various parameters of the filter response, such as Insertion Loss (IL), Return Loss (RL), Bandwidth (BW), in-band ripple, roll-off, rejection, and filtering function.

There are three widely used filtering functions: Butterworth, Chebyshev, and elliptic. The Butterworth function provides the flattest passband response but results in less steep attenuation in the rejected bands [64]. In contrast, the Chebyshev function offers a sharper cutoff response with higher rejection levels than the Butterworth, but it has a constant ripple within the passband. It is worth mentioning that the Chebyshev function is especially suitable for the most stringent applications as the ripple is limited to a certain level, and it can include transmission zeros even in non-symmetrical dispositions [68]. Lastly, the elliptic function has equal ripples in both the passband and stopband, resulting in the sharpest cutoff response without transmission zeros. However, this sharpness comes at the cost of a constant minimum rejection level within the stopband. Moreover, implementing elliptic filters in distributed structures can be more challenging, which limits their high-frequency applications [64].

In this thesis, we have selected the Chebyshev filter response for its constant ripple in the passband, being particularly advantageous for satellite communications. Additionally, the ability to introduce transmission zeros enables us to enhance rejection levels near the passband.

2.1.1.1 Synthesis of the Lumped and Distributed Models

Once the order and filter function have been defined, the next step is synthesising the equivalent circuit that implements the required response. The most extended equivalents include the coupling matrix $\boldsymbol{M}$-circuit model and the impedance or admittance inverter circuit models [69]. These prototype circuits have been extensively used from their first appearance in [70], as they simplify the filter design process.

The synthesis of the immittance inverter prototype begins with the design of the normalised low-pass prototype. This circuit has a normalised source impedance ($R_s = 1$) and cutoff frequency ($\omega_c = 1\,\mathrm{rad/s}$). Figure 2.1 shows the two possible implementations of the low-pass prototype of an N-order all-poles filter response. Both implementations are equivalent and have the same response. The values of the network elements (i.e. g_0,g_1,g_2, ... g_n) can be easily obtained from the desired transfer function using equations or tables [64, 65].

Once the elements of the low-pass prototype have been determined, impedance or admittance inverters can be used to transform it into another circuit where all elements are either

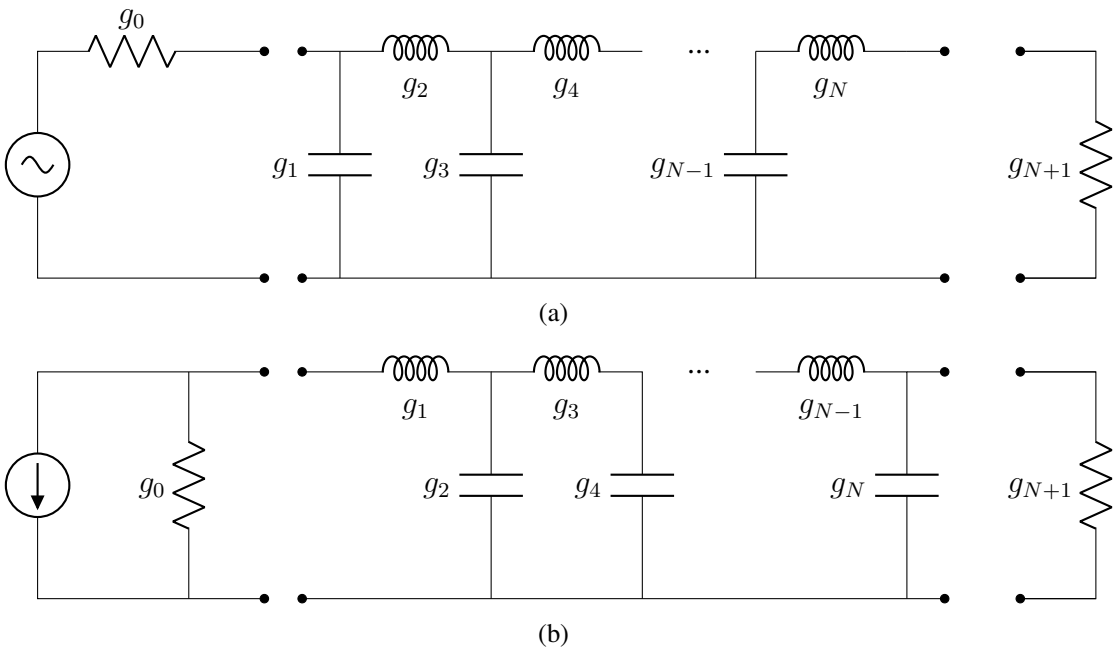

Figure 2.1: Two different implementations of the low-pass filter prototype.

series coils or parallel capacitors with arbitrary L_i/C_i values.

$$K_{0,1} = \sqrt{\frac{Z_0 L_1}{g_0 g_1}} \qquad K_{i,i+1} = \sqrt{\frac{L_i L_{i+1}}{g_i g_{i+1}}} \qquad K_{N,N+1} = \sqrt{\frac{Z_{N+1} L_N}{g_N g_{N+1}}} \tag{2.1}$$

$$J_{0,1} = \sqrt{\frac{Y_0 C_1}{g_0 g_1}} \qquad J_{i,i+1} = \sqrt{\frac{C_i C_{i+1}}{g_i g_{i+1}}} \qquad J_{N,N+1} = \sqrt{\frac{Y_{N+1} C_N}{g_N g_{N+1}}} \tag{2.2}$$

The low-pass prototype can be used to implement various filtering responses (e.g. low-pass, high-pass, band-pass, or band-stop) by applying a frequency transformation. For instance, the following frequency transformation can be used to achieve a band-pass response with a lower cutoff frequency ω_1 and an upper cutoff frequency ω_2.

$$\omega = \frac{1}{\Delta}\left(\frac{\Omega}{\omega_0} - \frac{\omega_0}{\Omega}\right) \tag{2.3}$$

where:

- $\Delta = \frac{\omega_2 - \omega_1}{\omega_0}$ denotes the fractional bandwidth

- $\omega_0 = \sqrt{\omega_1 \omega_2}$ is the centre pulsation

More accurate frequency transformations have been developed to consider the non-ideal effects of the final transmission lines [71, 72], but they will not be discussed in this thesis as they are beyond its scope.

Ideal immittance inverters are frequency invariant. Therefore, it is possible to determine the filter elements of a pass-band filter by transforming only the reactance or susceptance of the low-pass prototype, using equation 2.3. As a result, inductive/capacitive elements (L_i, C_i) are transformed into series/parallel LC resonators, while ideal inverters remain unchanged. Finally, the lumped elements of the resulting band-pass prototype should be replaced by distributed elements, such as dielectric resonators, resonant cavities, or planar resonators, to obtain a fully implementable prototype for microwave frequencies.

Alternatively, microwave filters can be modelled in matrix form through the coupling matrix ($\boldsymbol{M}$) [68, 69]. This approach is particularly useful for simplifying the synthesis and reconfiguration of the filter topology as it allows the application of matrix operations. Additionally, the physical elements of the final filtering structure (i.e., resonators and coupling elements) can be directly identified with the elements of the coupling matrix. This is especially interesting for designing and evaluating filter elements separately [68].

The circuit prototype of the coupling matrix consists of series resonators intercoupled through transformers, as shown in Figure 2.2. This circuit only supports symmetric filtering responses, but it can support an asymmetric response by including a frequency-invariant reactance within each resonator.

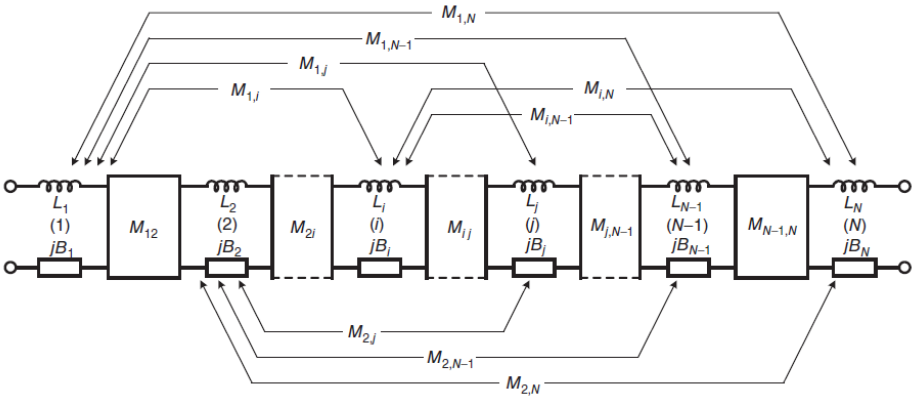

Figure 2.2: Prototype of the low-pass coupling matrix model for an equivalent bandpass filter using inverters as coupling elements [69].

The coupling matrix is represented by a $N \times N$ matrix where N is the order of the filter, and its elements represent the value of the coupling between resonators ($M_{(i,j)}$ elements) and

the self-coupling of each resonator ($M_{(i,i)}$ elements). The transformers can be replaced by immittance inverters with the same values as they approximate the characteristics of many microwave coupling elements and provide the same amount of coupling energy between resonators. Then, to represent input and output coupling, additional inverters are included at each end of the network. Therefore, the size of the matrix increases to $(N+2) \times (N+2)$.

The elements of the coupling matrix can be extracted from the desired filter response by equating the Y-matrix of a canonical coupling matrix to the Y-matrix of the rational polynomials of the desired filtering function [68]. This method requires several matrix transformations to obtain a coupling matrix whose structure reassembles the desired filter topology [68]. These transformations are complex and may not always produce the desired matrix routing, so other synthesis methods based on computer optimization are preferable [65]. In this approach, the coupling matrix of an in-line filter topology is optimised using an analytical or numerical model to achieve a more advanced response with the specific routing scheme [65].

2.1.1.2 Synthesis of the Physical Dimensions of the Filter

The design process is completed by obtaining the actual dimensions of the filter. In this stage, a numerical EM simulator is used to determine the dimensions of the distributed elements that realise the elements of the filter prototype, either the immittance inverter topology or the coupling matrix prototype. For this purpose, the CST Studio Suite (CST) was selected due to its ability to evaluate arbitrarily shaped structures, providing the necessary flexibility to evaluate the hybrid technologies developed in this thesis.

For the sake of clarity, we will describe the synthesis process for a four-poles band-pass filter with a Chebyshev response. The filter is implemented on a standard rectangular waveguide WR75 with $19.050\,\mathrm{mm}$ of width and $9.525\,\mathrm{mm}$ of height.

As depicted in Figure 2.3, the filter comprises four rectangular resonant cavities operating in single TE_{101} mode, with inductive apertures providing the resonator couplings. The synthesised filter response is a band-pass filter centered at $11\,\mathrm{GHz}$ with a bandwidth of $300\,\mathrm{MHz}$ and a $20\,\mathrm{dB}$ of in-band RL. The values of the normalised inverters $\overline{K}_{I,i+1}$ for the specified filter response are: $\overline{K}_{S,1} = \overline{K}_{4,L} = 0.2143$ and $\overline{K}_{1,2} = \overline{K}_{3,4} = 0.0390$, $\overline{K}_{2,3} = 0.0300$. The elements of the coupling matrix are $M_{(S,1)} = M_{(L,4)} = 1.035$, $M_{(1,2)} = M_{(3,4)} = 0.911$ and $M_{(2,3)} = 0.700$, while all other elements of the matrix are zero.

Dimensions of Cavities The first step consists of obtaining the initial dimensions of the resonant cavities. The initial lengths of the cavities can be calculated using the equation for the TE_{nmp} resonant modes of the rectangular waveguide. Considering that the filter is going to operate with TE_{102} the length of the cavities for a resonant frequency of $11\,\mathrm{GHz}$ is

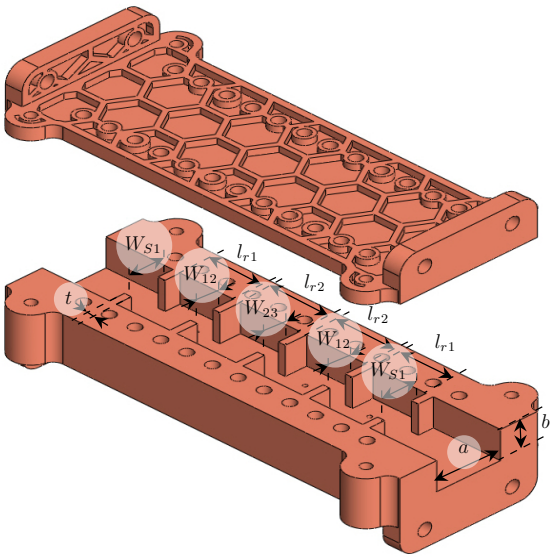

Figure 2.3: Layout of the X-band H-plane directly coupled cavity filter designed within a WR75 rectangular waveguide.

$19.500\,\mathrm{mm}$. It is essential to note that this length serves as a starting point and will require adjustments during the design process to compensate for the impact of the coupling elements.

Dimensions of the Inter-resonator Coupling In the proposed structure, the inter-resonator coupling was implemented using centred inductive apertures of thickness t and width $W_{(i,i+1)}$. Apertures are small discontinuities where evanescent higher-order modes are excited. These modes allow the coupling of a controlled fraction of energy between resonators defined by the coupling coefficient ($M_{(i,j)}$). The magnitude of the coupling is determined by the width and thickness of the aperture.

According to [69], the coupling value between two resonators can be calculated by simulating two inter-coupled resonators that are weakly coupled to the input/output ports. The coupling coefficient can be obtained from the resonant frequencies of the simulated structure as follows.

$$K_{i,i+1} = \frac{f_2^2 - f_1^2}{f_2^2 + f_1^2} \tag{2.4}$$

Where f_1 and f_2 are the two resonant frequencies extracted from the full-wave simulation.

From this result, the normalised coupling element M can be obtained as:

$$M(i, i+1) = \left(\frac{f_0}{BW}\right) \cdot K \tag{2.5}$$

Several simulations with different aperture width and thickness values were conducted to obtain the result of Figure 2.4 (a). The dimensions required to achieve the desired coupling elements can be determined using the previous graph and a fine optimisation. For an aperture thickness of $t = 2\,\text{mm}$ the corresponding widths are $W_{1,2} = W_{3,4} = 6.8\,\text{mm}$, and $W_{2,3} = 6.4\,\text{mm}$.

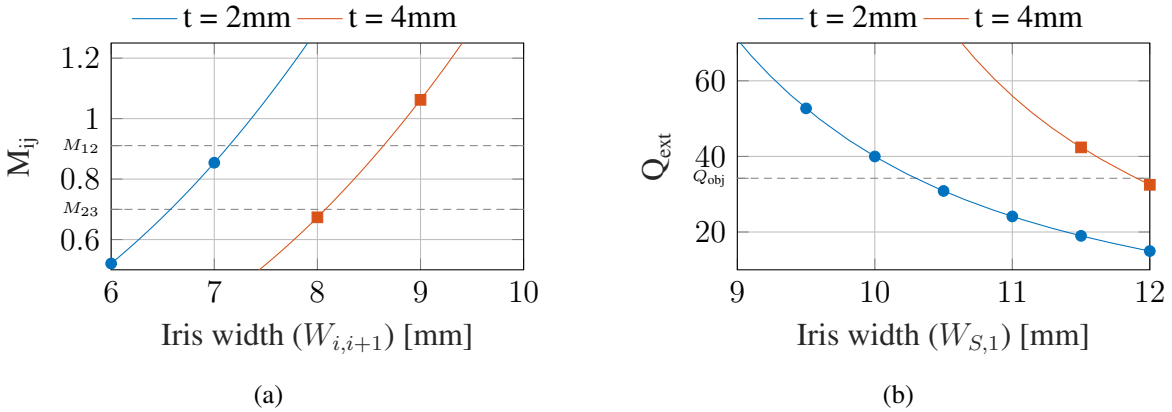

Figure 2.4: Design curves of the X-band WR75 filter: (a) Coupling as a function of aperture width W_{ij}, (b) External Quality factor as a function of aperture width W_{S1}.

Dimensions of the Input/Output Coupling The dimensions of the input and output coupling can be related to the external quality factor Q_{ext} of the first and last resonators of the filter. The relation between the Q_{ext}, the bandpass filter bandwidth (BW), and the normalised input impedance (R_s) is defined as follows [69]:

$$Q_{ext} = \frac{f_0}{BWR} \tag{2.6}$$

Thus, the required external quality factor for the proposed implementation ($R_s = M^2_{(s,1)} = 1.0715$, $f_0 = 11\,\text{GHz}$, and $BW = 300\,\text{MHz}$) is $Q_{ext} = 34.215$.

The process for determining the dimensions of the input/output coupling elements is similar to that used for determining the inter-resonator coupling. The dimensions of the coupling aperture are determined by simulating a singly loaded resonator. The external quality factor

of the simulated structure can be obtained from the group delay of the reflection coefficient ($\tau_{S_{11}}$) of the simulated structure [69].

$$Q_{ext} = \frac{2\pi f_0 \tau_{S_{11}(f_0)}}{4} \tag{2.7}$$

Figure 2.4 (b) shows the external quality factor as a function of its design parameters, i.e., the aperture width (W) and thickness (t). For this design, a thickness of $t = 2\,\mathrm{mm}$ was chosen, and the required width for this thickness is $W_{0,1} = 10.2\,\mathrm{mm}$.

Fine-tuning and Final Optimisation In this design approach, it is particularly important to consider the loading effect of the coupling elements on nearby resonators. As depicted in Figure 2.5, the coupling loading leads to a deviation in the resonant frequency of the resonator. This frequency drift must be compensated by precisely adjusting the dimensions of the resonators to ensure optimal filter performance.

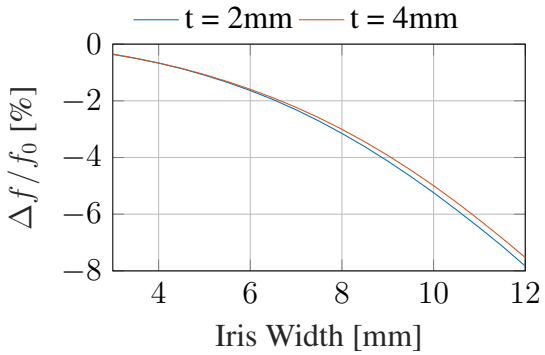

Figure 2.5: Resonant frequency of a single loaded rectangular cavity in WR75 versus the width of the input coupling aperture ($W_{S,1}$).

In order to consider the resonant shift caused by coupling loading, we can either derive an empirical formula or simply adjust the dimensions of the cavities using a full-wave simulator. The latter approach involves solving the eigenvalue of a doubly coupled resonator, which includes the cavity resonator with its two adjacent irises and two detuned adjacent cavities. We opted for this approach, using the CST eigensolver simulator to fine-tune the length of each cavity.

It is noteworthy that the frequency shift also affects the coupling values of the adjacent irises, as their coupling values are not constant across frequency. Thus, an iterative process of adjusting both the dimensions of the resonators and coupling elements is required to achieve the desired filter response. This recursive process is especially crucial for the input irises

and resonators, as they tend to exhibit the highest coupling values and, therefore, the most substantial loading effect.

The simulation result of the filter structure, after fine-tuning, is close to the desired response but may not meet the desired specifications. Thus, the proposed filter design must be optimised, obtaining the response shown in Figure 2.6.

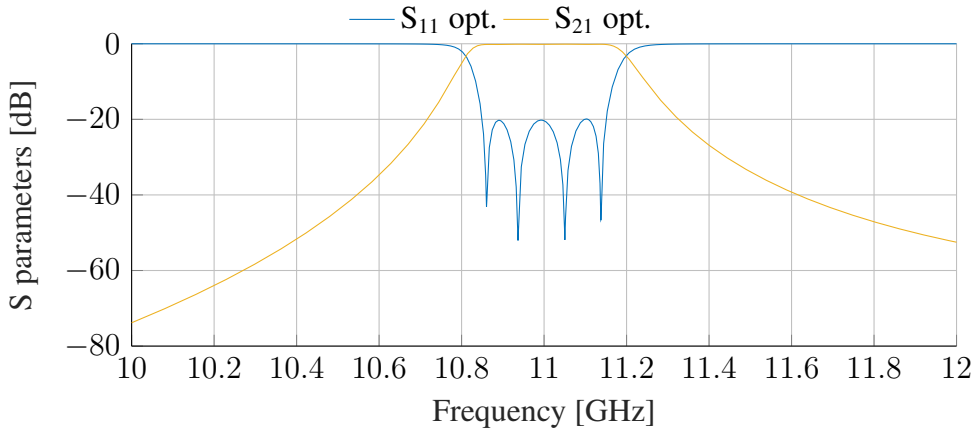

Figure 2.6: Simulated response of the 4-pole X-band filter designed within a WR75 rectangular waveguide.

2.1.2 Filter Topologies

This section presents a brief analysis of the most commonly used filter technologies to give the reader an overview of their advantages and disadvantages. The technologies have been organised according to their manufacturing technology into non-planar, planar and hybrid filters.

2.1.2.1 Non-planar technologies

Non-planar technologies are normally based on metallic waveguides and coaxial lines. Waveguides are metallic structures with a rectangular or circular cross-section that confine and guide the Electromagnetic (EM) fields. Despite the industry trend towards miniaturisation and mass production, waveguides are the most widely used technology in high-power and high-performance systems. This is because they have very low losses, perfect electromagnetic shielding (there is no radiation loss), and high power handling capabilities [73]. Moreover, waveguide resonators, key elements of microwave filters, achieve higher Q-factor than coaxial and other Transverse ElectroMagnetic (TEM) resonators.

The classic topology of waveguide filters is the directly coupled monomode resonators filter. This topology uses half-wavelength cavity resonators coupled through inductive or capacitive apertures; see Figure 2.7 (a). There are also similar topologies that use different coupling elements, such as metallic posts or bolts. In general, this type of filters have an excellent performance, although they tend to be significantly bulky and heavy. This limits their use in many scenarios, such as cellular communications and small satellites.

Numerous approaches have been proposed to minimise the mass and size of conventional waveguide filters. One of them consists of loading the resonator of the filter with dielectric materials; see Figure 2.7 (b). The idea is that the dielectric material strongly concentrates the electric field of the resonator, reducing its resonant frequency without increasing its size [74]. Another approach consists in directly using dielectric resonators, i.e. pieces of a dielectric material that resonates when they are correctly fed with an electromagnetic field. Both approaches considerably reduce the size of waveguide cavities when the dielectric parts are made of high-permittivity materials. However, they are more prone to spurious modes, have a lower power management capability and are more sensitive to manufacturing tolerances.

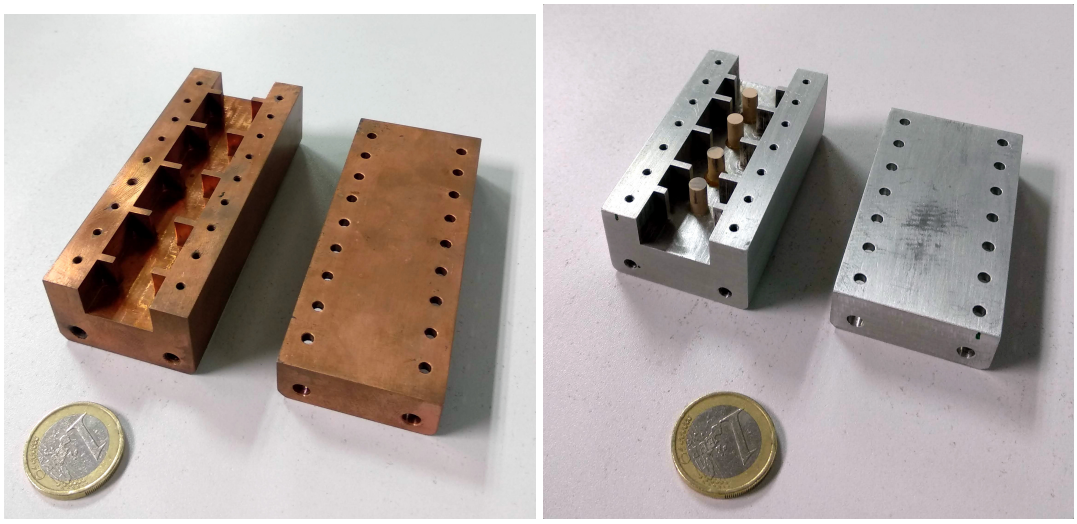

(a) (b)

Figure 2.7: Waveguide cavity filters: (a) H-plane directly coupled cavity filter, (b) H-plane directly coupled cavity filter loaded with dielectric posts. Filter prototypes are from [74].

Another topology employs multi-mode cavities to reduce the size of the filters at the cost of increased design complexity. Multi-mode filters use resonant cavities with two or more degenerate resonant modes, so each cavity implements more than one resonator; see Figure

2.8 (a). Multi-mode filters drastically reduce volume and weight and ease the introduction of cross-couplings, introducing transmission zeros at specific frequencies. However, these kinds of filters need an extensive design process, and they are susceptible to manufacturing tolerances.

At low frequencies, 5 GHz or less, waveguides are usually not used, as their size becomes impractical. In these cases, combline filters are often preferred. These filters use coaxial resonators loaded with high capacitance capacitors to reduce their length below a quarter wavelength. Although the size of these filters is much smaller than their waveguide counterpart, they are only used when very low loss and high isolation requirements are needed since there are planar alternatives with significant advantages at these frequencies.

On the other hand, waveguide structures have many problems at very high frequencies, mm-wave and above. The most critical problem is the poor electrical contact in the joints between the different parts of the waveguide structure. In order to solve this problem, the Groove Gap Waveguide (GGW) technology was developed [75]. The geometry of this waveguide comprises two parallel metallic surfaces separated by a small gap that does not require electrical contact between these two parts. One parallel surface implements a perfect magnetic conductor surface by using periodic structures, normally pins or patches [76, 77], see Figure 2.8 (b).

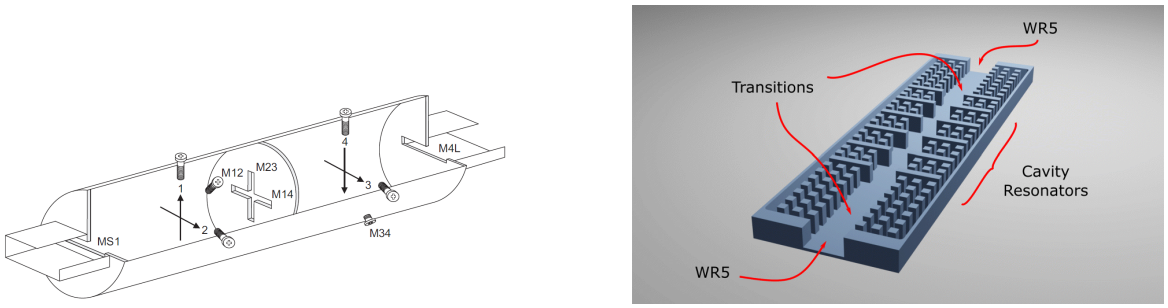

(a) (b)

Figure 2.8: (a) Structure of a dualmode filter of 4th order implemented within a circular waveguide [78]. (b) Structure of a GGW filter of 5th order [77].

All of the aforementioned technologies have excellent performance, but they are very sensitive to slight manufacturing tolerances, and the manufacturing devices tend to have slight deviations in the frequency response. If deviations are minor, they can be corrected by using tuning elements that adjust the frequency response of resonators and the coupling magnitude of the coupling elements. However, all these devices have difficulties concerning the integration of active and tunable devices, and their fabrication could be more complex, which makes

them not suitable for mass production. The need for low-cost and scalable technologies led to the development of planar technologies.

2.1.2.2 Planar technologies

Planar filters use transmission line structures implemented on a flat substrate or Printed Circuit Board (PCB). This technology has emerged as a viable alternative to waveguides as it has a compact size and is relatively easy to fabricate using standard PCB manufacturing techniques. Planar filters also have a lower profile and can be easily combined with other components, such as amplifiers and mixers, on the same substrate to create Monolithic Microwave Integrated Circuits (MMIC). This technology can implement integrated circuit devices combining active and passive components in a monolithic part.

Next, some of the several filter topologies that can be implemented in planar transmission lines will be reviewed. For the sake of simplicity, filters implemented on microstrip will be used as examples, but all the presented topologies are easily extrapolated to other topologies of planar transmission lines.

One of the simplest and most common implementations is based on the use of directly coupled resonators. The structure of this filter is based on open-ended microstrip resonators with a length of half-wavelength. The resonators are positioned in such a way that the gap between them acts as a capacitive coupling. There are two main configurations: end-coupled and parallel-coupled filters; see Figures 2.9 (a) and (b). In end-coupled filters, the resonators are arranged one behind the other, and in parallel coupled filters, they are arranged in parallel, side by side. The latter configuration is often preferred as it results in higher coupling values and, hence, a wider bandwidth and a shorter overall length of the filter [65].

The need for miniaturization drove the development of other filter topologies, such as hairpin, interdigital, and combline filters, which basic structures are depicted in Figures 2.10 (a), (b), and (c), respectively. In the hairpin filter, the resonators are folded into a "U" shape. This reduces the filter footprint but also implies some problems, e.g. the two arms of the folded resonator can act as a pair of coupled resonators themselves. In interdigital filters, resonators are open-ended at one end and short-circuited at the others, and hence, the length of the resonator is about a quarter-wavelength. This implementation not only reduces the filter size but also increases the stopband between the desired (first) and undesired (second) passband. The second passband normally appears at $2f_0$, whereas in this filter, it appears at $3f_0$. The resonators' length can be further reduced by including a capacitor in the endpoint, as in the case of combline filters. It is interesting to know that increasing the loading capacitance not only shortens the resonator but also increases the stopband between the first and second resonant modes of the filter.

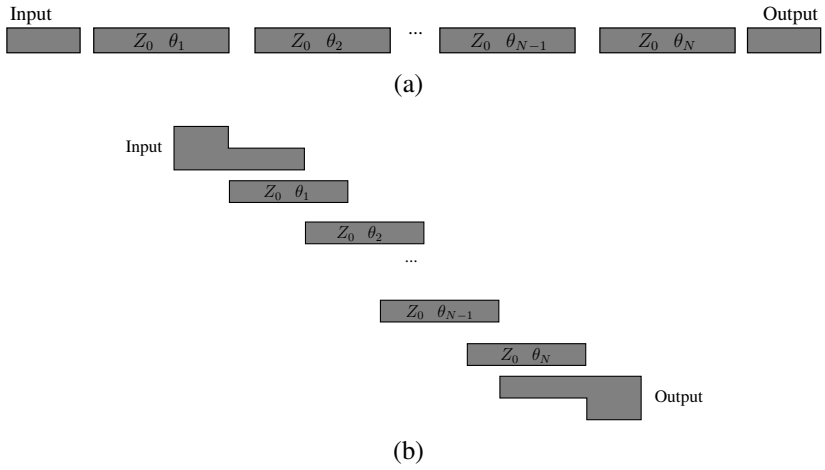

Figure 2.9: Structure of: (a) end-coupled and (b) parallel coupled microstrip filters.

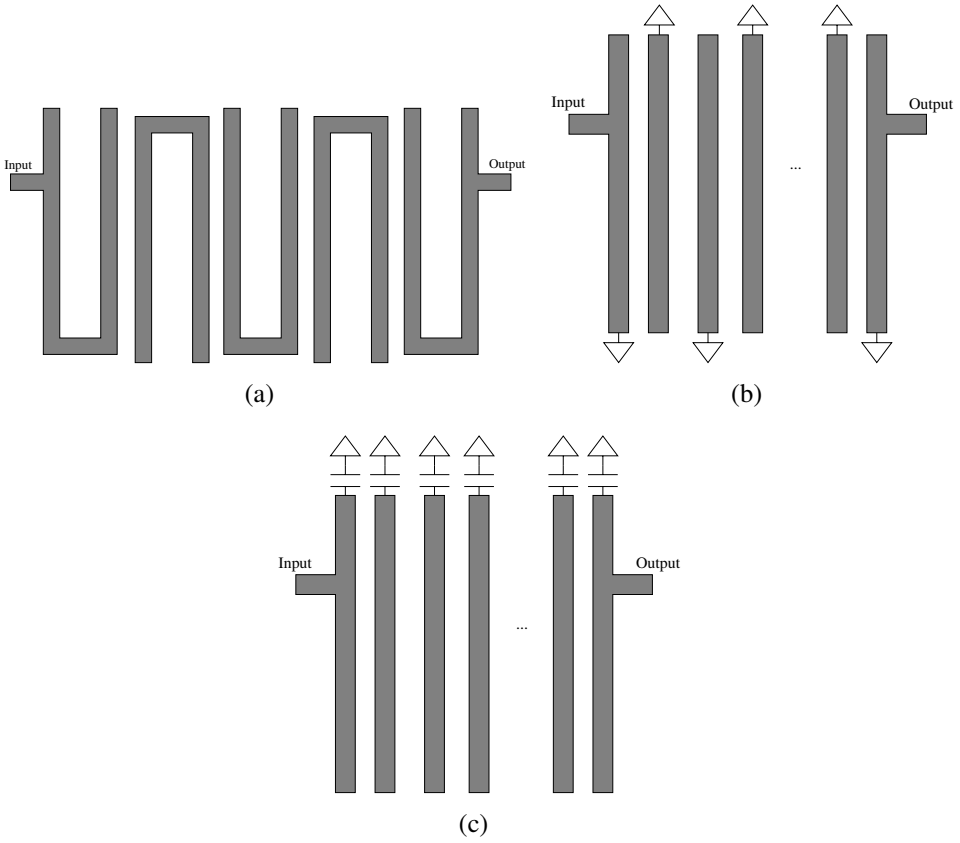

Figure 2.10: Structure of: (a) hairpin, (b) interdigital, and (c) combline microstrip filters.

While these filter technologies provide satisfactory performance, they generally do not perform as well as non-planar structures. Planar filters typically have higher losses due to the presence of dielectric and radiation losses, lower selectivity, and lower Q-factor compared to waveguides. To address the limitations of both planar and non-planar technologies, a hybrid technology called Substrate Integrated Circuit (SIC) technology was proposed.

2.1.2.3 Hybrid technologies

The idea behind SIC is to develop hybrid integration structures in which non-planar structures (waveguides and coaxial cables) are implemented in a single layer or a stack of multilayer microwave substrates [79]. This approach allows the development of hybrid circuits in which TEM and non-TEM modes can be wisely used without difficulties.

The breakthrough came in 2001 when the Substrate Integrated Waveguide (SIW) was first proposed in different implementations [3], demonstrating that the hybridisation of planar and non-planar structures was possible and indeed very useful. The Substrate Integrated Waveguide (SIW) is a rectangular waveguide implemented in a microwave substrate using standard PCB fabrication techniques. This equivalent waveguide is formed by two parallel rows of PTH connecting the top and bottom copper cladding of the PCB, see Figure 2.11 (a). If the distance between the plated holes is small enough, the radiation loss is negligible, and both rows of holes behave as solid metal surfaces. The SIW can, therefore, be modelled as a rectangular waveguide filled with dielectric.

SIW has features that are between waveguides and planar transmission lines. It has a smaller size and lower manufacturing costs than waveguide technologies and exhibits lower losses and higher Q than its planar counterpart. In addition, this technology allows the hybridisation of waveguides and planar structures on the same substrate, creating hybrid MMICs.

There are numerous examples in the literature of filters implemented in SIW. As with waveguides, the most widespread topology is the cavity-coupled filter with capacitive apertures, where the apertures are implemented with rows of Plated Through Hole (PTH) [3]. The high design flexibility of SIW allows the implementation of resonant cavities with diverse shapes (circular [80], triangular [81] and half-mode and quarter-mode cavities [82, 83]). These cavities allow the development of filters with different characteristics such as higher Q-factor, multimode response, or compactness. SIW can also implement something similar to dielectric loaded filters, which are implemented by emptying or drilling some areas of the SIW; see Figure 2.11. The holes reduce the effective permittivity and implement the coupling elements, while the undrilled areas implement the filter's resonators [27, 28].

On the other hand, there are several SIC structures that have been developed in an attempt

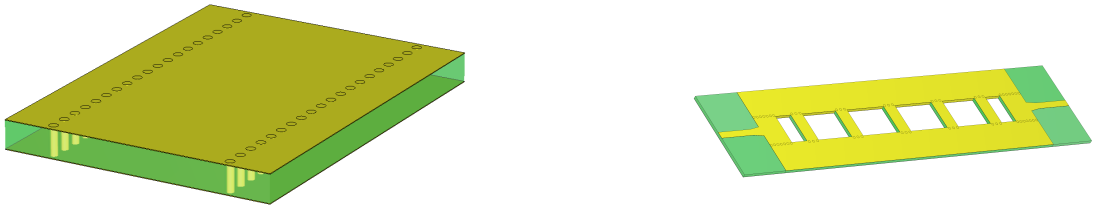

(a) (b)

Figure 2.11: (a) Basic structure of a Substrate Integrated Waveguide, (b) Inner layer of a SIW filter based on alternated dielectric line sections. Copper components are illustrated in yellow, while the substrate material is represented in green.

to reduce the size of the SIW even further. In this area are the folded and half-mode SIWs with half the width of the traditional implementation [84], and the ridge SIW, which reduces the cut-off frequency of the fundamental TE_{10} mode by introducing a central ridge [85]. Also fascinating is the development of coaxial SIW filters [29], which uses the SIW structure to develop the combline filter topology. This is done by adding a PTH in the centre of a SIW cavity and milling a circular isolation on the top copper. This structure can be modelled as a coaxial resonator (with a circular inner conductor and a rectangular outer conductor) that is short-circuited at one end and loaded with a capacitor (the circular isolation) at the other. This filter topology provides extreme size compaction at low frequencies and allows the easy integration of lumped elements that can improve the filter performance and add reconfigurability [86].

It is worth mentioning the recent development of low-loss empty SIC structures, such as the Air-Filled Substrate Integrated Waveguide (AFSIW) and Empty Substrate Integrated Waveguide (ESIW). In the former, a rectangular hole is performed in the area between the rows of PTH, see Figure 2.12 (a). Then, a top and bottom metal cover closes the structure, leaving a partially empty rectangular waveguide. As the electric field of the fundamental TE_{10} concentrates in the centre and decreases rapidly toward the sides, the effective dielectric permittivity of this waveguide is very close to the air, resulting in a virtually empty waveguide. In the case of ESIW, the walls of the rectangular hole are metallized, thus replacing the PTH row, see Figure 2.12 (b). As in the previous case, the structure needs top and bottom covers.

We can find other structures in this line, such as the Empty Substrate Integrated Coaxial Line (ESICL) or the Ridge Empty Substrate Integrated Waveguide (RESIW). The former structure realises an empty rectangular coaxial line in a stack of 5 substrates; see Figure 2.12. The resulting transmission line is non-dispersive, low loss, and has a wide mono-mode

(a) (b)

Figure 2.12: Layout of the different implementations of an Empty Substrate Integrated Waveguide: (a) Air-Filled Substrate Integrated Waveguide and (b) Empty Substrate Integrated Waveguide. Copper components are depicted in yellow, the substrate material is shown in green, and empty areas are illustrated in blue.

band [87]. The latter structure integrates an empty ridge waveguide in a stack of 4 or more substrates, somewhat reducing the ESIW footprint while increasing the single-mode bandwidth [88]. Both technologies are suitable for broadband applications, although the ESICL is more appropriate for low-frequency applications while RESIW can operate at higher frequencies.

An incredible variety of Substrate Integrated Circuit technologies and topologies has emerged in just 20 years. This is proof of the incredible versatility and design flexibility of this type of structure. However, these types of substrate-integrated structures present critical problems that need to be addressed in the coming years. SICs are generally more sensitive to manufacturing tolerances due to their reduced size. In addition, the standard PCB fabrication processes, although affordable, generally have loose dimensional tolerances, which severely affects the performance of devices developed in this technology, in which tuning techniques are not as developed as in waveguide technology. This makes it difficult to operate at high frequencies, such as the mm-wave band, where GGW are gaining ground. In addition, due to their higher losses and smaller size, substrate-integrated circuits have a reduced power handling compared to waveguides, which limits their GEO satellite and radar applications.

2.1.2.4 Comparison

As can be noticed, the above technologies are a trade-off between the key features that are required by today's communications systems. Figure 2.14 compares the performance of these three technologies in terms of size, cost and loss [4].

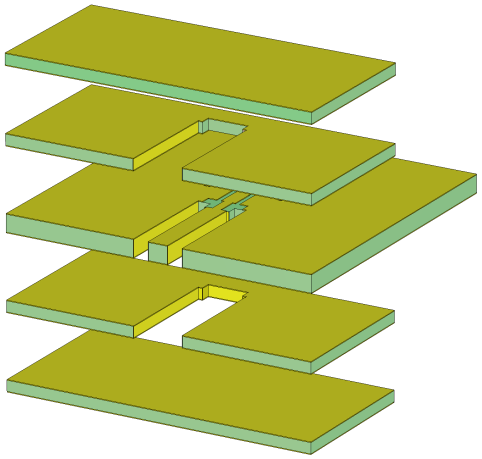

Figure 2.13: Layout of most-extended transition between the coplanar waveguide and the Empty Substrate Integrated Coaxial Line. The first and fifth layers are covers, while the second, third, and fourth layers assemble the ESICL. The coplanar line is developed in the third layer.

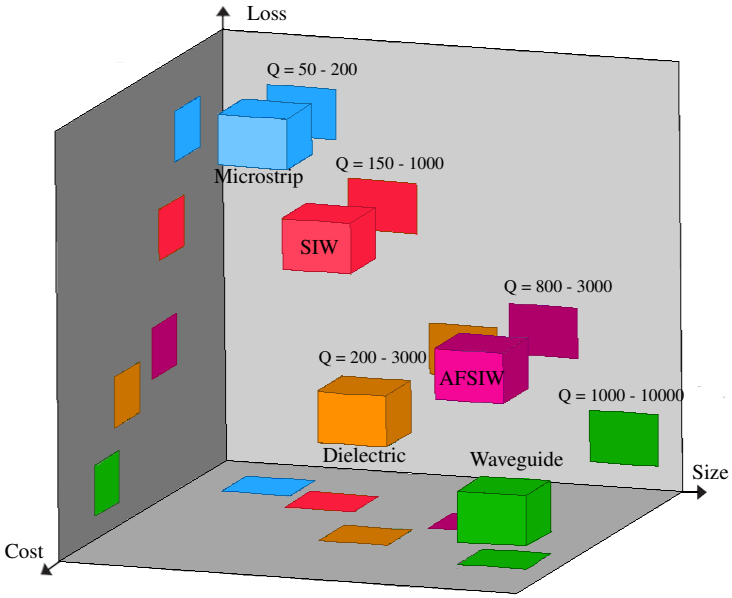

Figure 2.14: Comparison graph showcasing the performance of various microwave technologies [4].

It can be observed that planar structures achieve the most compact structures at a re-

duced cost but also exhibit a higher loss. Waveguides achieve low loss but have a large size and higher manufacturing costs, at least for high-volume production. Finally, substrate-integrated filters are a compromise between the previously mentioned technologies, allowing the development of relatively compact devices with low losses at a moderate cost.

According to the previous analysis, substrate-integrated filters are a good candidate for the new space scenario since they achieve good performance in a compact and light form. However, as the previous comparison does not consider the power handling capability, the substrate integration, or the high-frequency working capability, so it should be taken critically.

2.2 Qualification for Space Applications

Communication satellites are exposed to unique and aggressive conditions from their launching to their operation time in orbit. During orbit positioning, satellites are exposed to strong vibrations, mechanical shocks, and thermal stress. Moreover, even when satellites are allocated in a stable orbit, they face a very aggressive medium. They are working under vacuum or low-pressure conditions, are exposed to high-temperature gradients and are impacted by high-energetic particles.

Satellites cannot be repaired once they are in space, so it is imperative to ensure that their equipment is designed to operate effectively and withstand the conditions of both the launch and space environments. Additionally, since the launching process is as expensive as, or even more expensive than, the satellite itself, it is crucial to ensure that satellites have a relatively long lifespan. The average lifespan of satellites varies, ranging from 5 years for a LEO satellite (based on the expected life of SpaceX's satellites) to 15 years for the average GEO satellite, as reported by [2]. In order to do so, the space agencies, launcher companies, and satellite operators define a series of conditions and technical details of tests for "space qualification". According to the ECSS E-ST-10-03C standard [89], electronic, electrical and RF equipment of the space segment should undergo the following test:

- **Functional and performance tests**: have to be defined by the project team to ensure that the devices are operating correctly under laboratory conditions.
- **Physical properties tests**: the following physical properties should be determined by measurement or simulation: dimensions and interfaces, mass, the centre of gravity, and momentum of inertia.
- **Mechanical tests**: the following vibration tests should be performed: random vibration, sinusoidal vibration, and shock tests.

- **Thermal/temperature tests**: thermal vacuum and thermal ambient tests shall be performed for satellite equipment that will be exposed to high-temperature gradients in vacuum conditions for any period of its lifespan.
- **Electromagnetic Compatibility (EMC) tests**: the satellite equipment should pass a EMC to ensure that not undesired electromagnetic couplings are generated.
- **Corona and multipactor discharge tests**: shall be performed on dedicated models and only when necessary, i.e. when the Device Under Test (DUT) operates close to the particular conditions that can ignite these phenomena.

Among these tests, passive microwave devices, and specifically microwave filters, are suitable for testing in the following areas: functional and performance testing, physical properties inspection, mechanical tests, thermal tests and corona and multipactor discharge predictions. The following pages will discuss the characteristics of the space environment and the associated testing characteristics.

2.2.1 The Thermal Environment

Satellites are generally exposed to heat radiation without the protection of the atmosphere. This, combined with the satellite's orbit movement, can cause significant temperature variations. A satellite orbiting the Earth is generally exposed to three primary heat sources; see Figure 2.15.

- **Direct Solar**: sunlight is the most significant heating source on most communication satellites. Fortunately, this source is relatively constant and predictable.
- **Albedo**: Sunlight reflected by a planet or space body, i.e. the Earth and the Moon. This is an important heating source for LEO satellites but is much less important for GEO satellites. Moreover, it is much more variable than solar radiation and depends on the satellite's orientation, orbit, and surface properties of the Earth. Clouds, water, sand, cities, and forests have different reflection factors.
- **Earth IR**: The Earth absolves part of the incident sunlight that eventually is re-emitted to the space as infrared radiation. However, this source of heat is negligible in the case of satellites orbiting the Earth [90].
- **Satellite subsystems**: internal parts of the satellite (high-power amplifiers, attenuators, antennas, etc.) generate heat that has to be considered in thermal analyses. The satellite's thermal control systems should manage and radiate this residual heat.

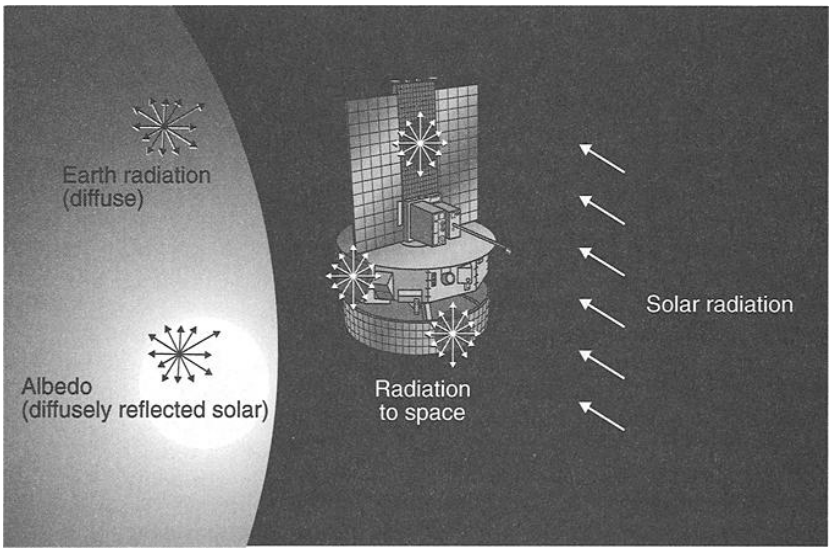

Figure 2.15: Scheme of a satellite's most usual heat exchange mechanisms. Image is from [90].

Satellites and Earth are not static in the space, presenting periods of light and shadow (eclipses caused by the Earth or the Moon). When the satellite is in a light period, it is directly exposed to the direct solar and Albedo heat sources, causing an increase in temperature. Meanwhile, the satellite has to face the cold space in an eclipse zone, causing its temperature to decrease. This cycle produces a huge variation in the satellite temperature that depends on various factors, such as the satellite size, its materials and the performance of its temperature control system. This makes it difficult to define standard temperature gradients for orbits in general, and each mission needs a specific temperature analysis.

However, the temperature control subsystem of most communication satellites can mitigate the temperature variation of some parts of the satellite. In this respect, there has been a general agreement on typical operation temperatures for the different pieces of satellites equipment. The typical operational temperature ranges, as outlined in [90, 91], are typically as follows

- Electronics: -20 to 40 °C
- TTC and special electronics: 0 to 40 °C
- Solar panels: -100 to 100 °C
- Antenna dish: -80 to 60 °C
- Inactive structures: -100 to 100 °C

As can be noticed, although the thermal control systems mitigate the temperature variation in critical parts of the satellite, the expected variation for electronics or antennas is high enough to influence the performance of very sensitive equipment such as transponders and the RF subsystem. This is especially important in microwave filters since their electric response is strongly influenced by temperature changes, even if it is small.

2.2.2 Effect of Temperature Gradient on Passive Microwave Components

Temperature fluctuations have a detrimental impact on the different subsystems of the satellites. Abrupt temperature changes can lead to material fractures or cracks in different materials, causing mission failure. Additionally, continuous exposure to temperature variations can accelerate material ageing, ultimately reducing the satellite's lifespan. Leaving these effects aside, it's important to note that temperature gradients significantly influence the functioning of passive microwave components such as directional couplers, phase shifters, and filters. The electrical response of these devices depends on their dimensions/geometry and the electromagnetic properties of their materials, both of which are temperature-dependent factors.

On the one hand, temperature changes can cause alterations in the shape, volume, and density of matter. When a material is heated, its molecules vibrate and move faster, leading to an increase in the distance between them and resulting in changes in the geometry of the device. This variation in size can negatively impact the electric response of devices, potentially leading to critical failure in satellite subsystems. Fortunately, the size change can be easily characterized by the Coefficient of Thermal Expansion (CTE) and the deviation in the devices' performance can also be predicted through simulations.

On the other hand, the EM properties of matter (conductivity, dielectric permittivity and magnetic permeability) also change with temperature. The drift of the metal conductivity with temperature is not a critical parameter in most passive devices as it only impacts the transmission loss and can be easily compensated. However, the drift of dielectric permittivity and magnetic permeability significantly impacts the electric response of resonant devices such as microwave filters. In fact, this property has been extensively used as a compensation mechanism to reduce the drift caused by thermal expansion deformation [92, 93].

2.2.3 Temperature Tests

Temperature tests shall be performed on the different subsystems of the satellite to ensure their correct performance under the expected thermal environment. The purpose of these

tests is to demonstrate that the different satellite parts would survive the thermal stress of space, demonstrating the proper performance of the satellite over a wide temperature range, and obtain information on the heat propagation through the heat control system.

Concerning passive microwave devices and bandpass filters in particular, these tests evaluate the variation of their frequency response (IL, RL, BW, stopband rejection, and group delay (τ)) within the expected temperature range. Last but not least, these tests also evaluate that the thermal stress does not induce any permanent change or critical failure in the DUT.

These tests consist in setting the Device Under Test at the different temperatures under a specific atmosphere while a functional test is conducted. Governmental space agencies establish the general requirement to perform a coherent and realistic test. In particular, the European Space Agency through the European Cooperation for Space Standardization secretariat states in the ECSS-E-ST-10-03C standard [89] the general requirements for spacecraft thermal testing [94]. The most important requirements of the tests defined in this standard are summarised below.

1. The test temperatures of the satellite equipment shall be defined for the minimum and maximum qualification and acceptance levels.
2. The rate of temperature change shall be limited at $20\,\mathrm{K/min}$.
3. Functional test shall be performed as a minimum at hot and cold operating temperatures after a proper dwell time.
4. DUT shall be submitted to functional test before and after the thermal tests.
5. The test method and setup shall be defined according to the thermal environment characteristics.

Accordingly, to the last requirement of the previous list, the European Cooperation for Space Standardization secretariat defines two types of temperature test:

- **Thermal ambient test**, also known as **thermal cycling**: is a temperature test carried out in the presence of a particular atmosphere. The atmospheric pressure shall be adapted to the expected level during the operation of the space mission. Although the ECSS-E-ST-10-03C standard establishes that this test is only mandatory for satellites operating in a non-vacuum environment during its entire lifetime, the NASA standard includes it as mandatory for every mission [90].
- **Thermal vacuum test:** shall be performed for satellite equipment operating in a space vacuum environment at any time of its lifespan. DUT shall be tested at a maximum

pressure of $1 \times 10^{-5}\,\mathrm{hPa}$, and the test condition should avoid contamination of the equipment. As we stated in [95], there are no significant differences in temperature testing results for passive microwave devices in the presence or absence of an atmosphere. The primary purpose of this test is to verify the heat management system's effectiveness without the presence of convection rather than verify the proper operating condition of isolated devices.

2.2.4 Vibration Environment

The positioning of a satellite into a stable orbit is typically facilitated by a rocket. This process exposes the spacecraft and its payload to extreme accelerations and vibrations that can be caused by several transportation-related factors, such as rocket stage detachment, aerodynamic effects, and the activity of the propulsion system [96]. Although orbital positioning is staggered by using the Hohmann transfer orbits [91], see Figure 2.16 (a), the spacecraft experiences huge accelerations and shocks. This is evident in the spectral density of vibrations observed during a typical Soyuz launcher flight to GEO, illustrated in Figure 2.16 (b).

The mechanical stress of the launching can result in irreversible deformations that can damage the satellite equipment, including the communication devices. Therefore, these devices must be designed to withstand this hostile environment, and their survival should be proven through several vibration and shock tests.

Regarding communication and RF equipment, mechanical tests should include random vibration, sinusoidal sweep and shock test. These tests generally consist in submitting the DUT to the high power vibrations and shocks. In order to do so, the DUT is fastened to a mechanical, and similar vibrations to those expected during the orbit positioning are stimulated over the DUT. Some accelerometers are placed on specific positions of the DUT and the test bench to monitor the applied vibration.

During the sinusoidal sweep test, narrow-band vibration waves are excited in the DUTs. During this test, the device is subjected to a sine vibration, whose frequency increases with time. This test tries to assess the behaviour of the devices under the stress waves that manifest during the atmospheric flight of the launching process. The different launcher companies specify the typical values of the spectral density of vibration of their space launchers, and the governmental space associations define a Minimum Workmanship (MW) in the case of the NASA [98], and safety margins in the case of ESA. The MW defined by the NASA consists of a sweep from 4 to $140\,\mathrm{Hz}$ with an amplitude of $1.25\,\mathrm{g}$ and a sweep speed of 2 octaves per minute. Figure 2.17 shows this minimum workmanship of the most widely used space launchers after applying the safety margin defined by the ESA.

On the other hand, the random vibration test assesses the feasibility of the DUTs under

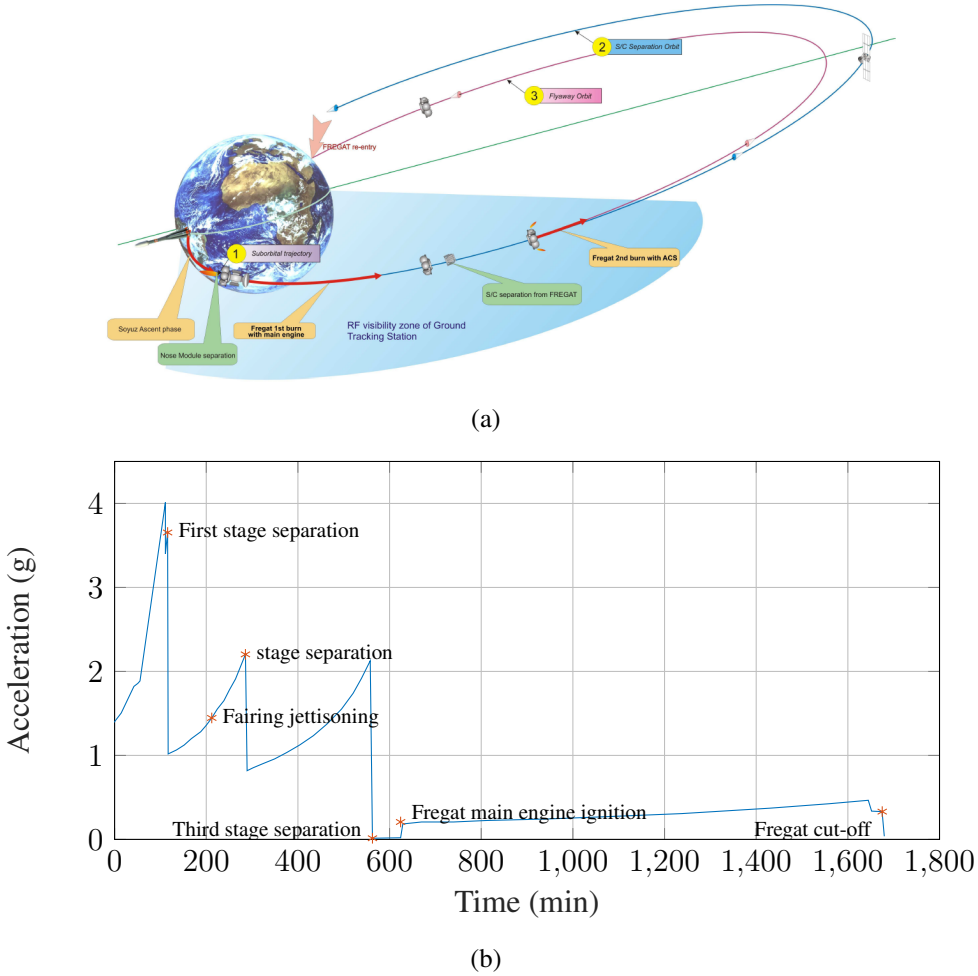

Figure 2.16: Standard geostationary transfer orbit flight manoeuvre of Soyuz launcher: (a) scheme of the mission profile and (b) typical longitudinal acceleration. Source [97].

the broadband vibrations generated by the propulsion system of the launcher. During the test, the DUT is subjected to a pseudo-random vibration with a specific Amplitude Spectral Density (ASD) defined by the launchers company and the governmental space agencies.

According to the ECSS-E-ST-10-03C standard [89], the test bench must avoid resonances to the extent possible, and the applied vibration should not present slopes greater than $25\,\mathrm{dB/octave}$. The standard [89] also states a safety margin of $3\,\mathrm{dB}$ above the vibration levels established by the launcher company. Conversely, NASA specify their own MW for random vibration tests [98]. Figure 2.18 shows the MW defined by the NASA, as well as the ASD of the most used launchers of the market considering the $3\,\mathrm{dB}$ security margin defined by the ESA.

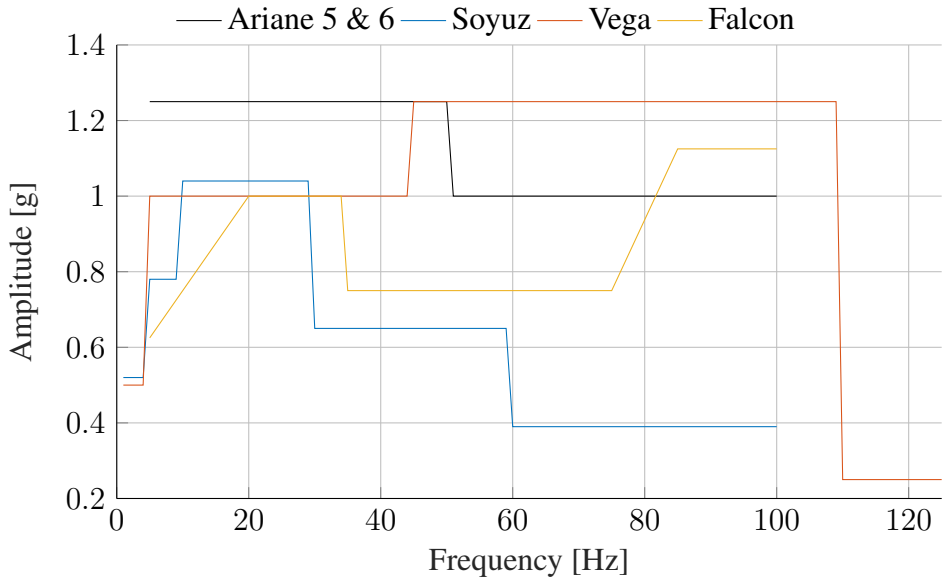

Figure 2.17: Minimum workmanship for sinusoidal sweep tests derived from measurements taken during the operation of commonly-used space shuttles.

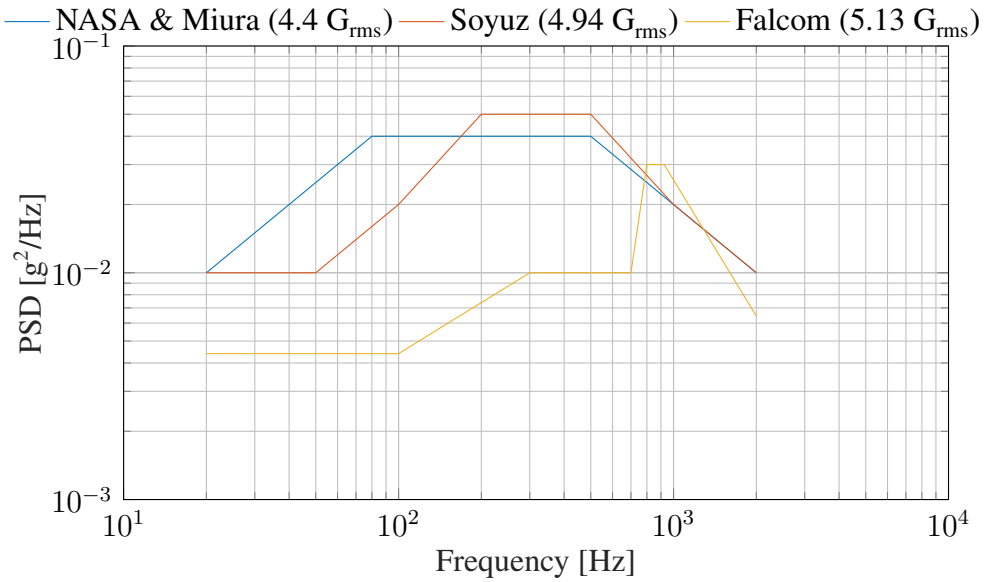

Figure 2.18: Minimum workmanship requirements for random vibration tests derived from measurements taken during the operation of commonly-used space shuttles.

The random vibration test has been replaced by an acoustic test in Ariane group launchers (Ariane 5, Ariane 6, and Vega). Unfortunately, since we lack access to a test bench capable

of conducting this type of test, it will not be studied.

The vibration tests should be performed for the three main axes of the parts, and the natural resonance frequency of DUTs shall be characterised before and after each test. The natural frequency is a key parameter of the mechanical reliability of the DUT as any change in the part geometry (e.g. cracks, bends or parts displacements), no matter how small it is, produces a substantial change in its natural frequency. The standard ECSS-E-ST-10-03C [89] specifies the success criteria for the natural frequency as a maximum variation of less than $5\,\%$ in frequency and less than $20\,\%$ in amplitude.

2.2.5 Power Handling Issues

Communications satellites have to work with high-power signals to compensate for propagation losses. This is especially important for high-altitude orbits where the distance between the transmitter and receptor is very high. However, new LEO constellations also need to handle high-power signals to boost the channel capability. Thus, when designing communication devices for the satellite output chain, designers have to consider the harmful effects of high-power RF signals: heating problems, multipactor effect and corona discharge.

2.2.5.1 Heating problems: average power handling capability

The different loss mechanisms of communication devices produce heat when they are fed by a continuous-wave high-power signal. This heat increases the temperature of the devices, which could generate a high thermal stress that can destroy or deform them. The increase in heat depends on several factors, such as the loss mechanisms of the DUT, input power, and the temperature control system, making its study quite complex.

2.2.5.2 Peak power handling capability: multipactor phenomenon

The multipactor effect refers to an avalanche increase in the number of free electrons that occurs in devices that operate with high-power signals under low pressure. This phenomenon only occurs under vacuum or very low-pressure conditions, where the free electrons can travel through the "empty" volume of the device without impacting any atom. When a high-power electric field accelerates free electrons under vacuum conditions, they can impact the metallic walls of the device. This impact can start three different reactions in the conductor, depending on the energy of the impact and the properties of the material: the material might absorb the incident electrons, the electron might be reflected, or more electrons may be released from the surface, see Figure 2.19.

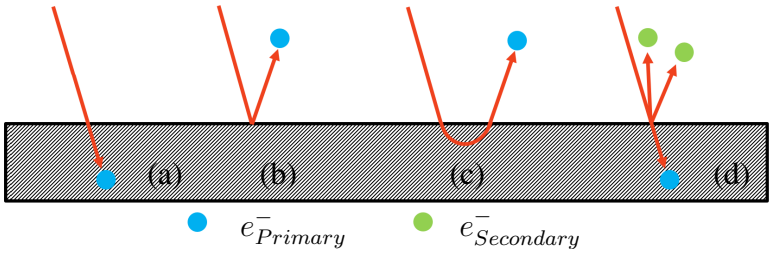

Figure 2.19: Four possible interactions between electron and matter: (a) Electron absorption, (b) Elastic reflection, (c) Inelastic reflection and (d) True secondary emission.

If the power of the RF signal is high enough to release more electrons from the material (secondary electrons), and it occurs when the harmonic field reverses direction, the process is in resonance with the RF signal and the free electrons are accelerated towards the opposite direction, impacting other surfaces and releasing more electrons. If the process is sustained in time, more electrons will be released in each cycle, producing a self-stimulated growth of free electrons as seen in Figure 2.20.

The resulting cluster of free electrons produced by the multipactor phenomenon can result in several harmful effects [99]. Free electrons generated by multipactor increase the electric noise, reducing the signal to noise ratio. This is significantly negative for small satellites with limited power and modulation schemes. The cloud of electrons can behave as a short circuit reflecting the input power, which is especially dangerous when it happens in devices of the output stage since a high power can be reflected to the output amplifier resulting in its destruction. Ultimately, the impact of electrons generates heat with the consequent thermal problems. If this heat evaporates part of the device, the multipactor phenomenon can trigger an even more destructive corona discharge.

Multipactor may damage vital communication equipment putting at risk the survivability of the satellite. For this reason, satellite equipment susceptible to multipactor discharge needs extensive analysis and testing of this phenomenon. However, multipactor is a very complex phenomenon that depends on several factors, and the prediction of its threshold power is a complex process that requires extensive analysis.

Traditionally, the theoretical study of the multipactor phenomenon has been simplified to obtain an analytical solution. One of the most popular models of the two-surface multipactor interaction is the parallel-plate model depicted in Figure 2.20 and studied by Hatch and Williams in [100]. This model is particularly useful for predicting multipactor discharge in rectangular waveguides and capacitive parts of combline filters and, being more general, in any device where the impacting surfaces are two parallel plates. This model allows us to the-

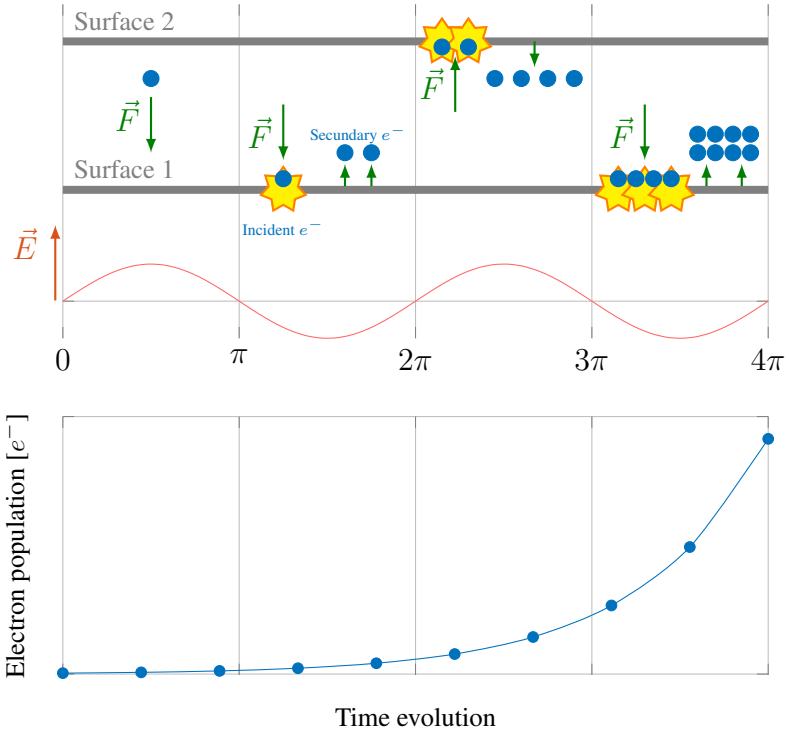

Figure 2.20: Scheme of a multipactor discharge. Blue circles depict free electrons, while the arrows $\vec{E}$ and $\vec{F}$ represent the electric field and Lorentz force, respectively. The bottom figure shows the exponential evolution of the electron population in a multipactor discharge.

oretically determine the threshold power needed to obtain a sustained multipactor discharge as a function of the material properties, the gap between the two plates and the signal frequency. In practice, the parallel-plate case has been solved for a series of materials obtaining the Hatch and Williams chart shown in Figure 2.21.

The Hatch and Williams chart has been employed to define safe multipactor limits in the NASA and ESA standards [101] due to its simplicity. However, this methodology provides a very conservative prediction for most applications since it considers a continuous wave excitation, a homogeneous distribution of the electric field within the plates, and a perfect resonance of the electrons and the RF signal. This implies over-demanding design specifications for microwave devices, increasing the design complexity, cost, volume and weight of the devices. Although it has not been a problem in the space sector in the past years, it is especially problematic for new satellites as they increase the transmitted power and push up their operative frequency to improve their performance. This trend implies a higher concentration of electric fields in smaller devices, resulting in lower breakdown power thresholds. Thus,

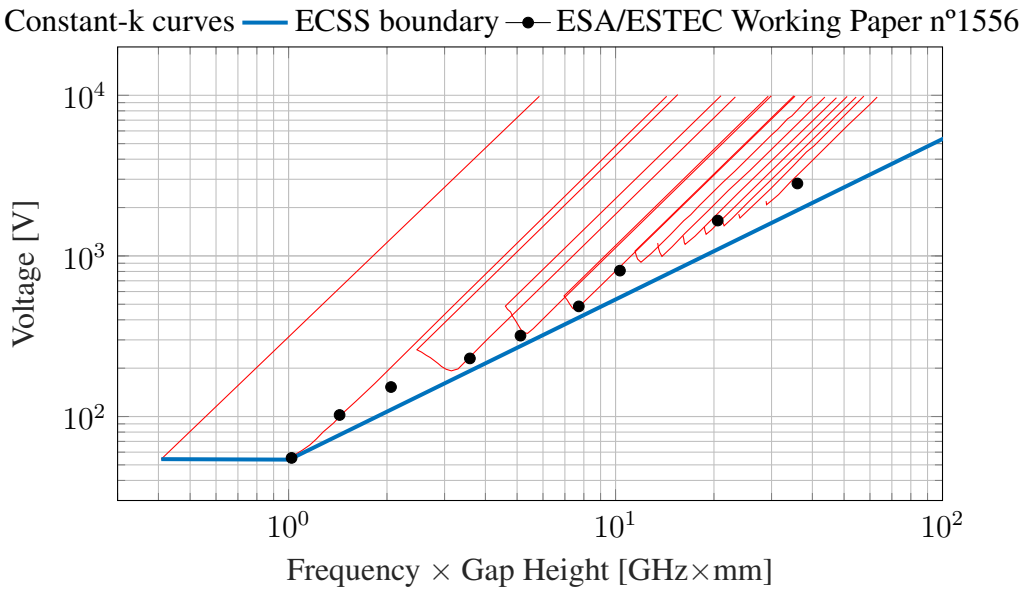

Figure 2.21: Multipactor susceptibility chart for the constant-k in the parallel-plate model of standard copper.

particle simulators are more popular nowadays since they provide a more accurate prediction for a particular structure and modulation.

2.2.5.3 Peak power handling capability: corona discharge

A corona discharge is an electric discharge caused by the ionization of the gas that surrounds the conductors of high-power devices. In this effect, the pressure inside the device must be higher than in the multipactor discharge. Thus, free electrons inside the device will hit the gas particles, forcing the release of secondary electrons, which ionize the gas. Under particular conditions, the density of free electrons can increase in an avalanche manner, turning an isolating gas into conducting plasma.

Since corona discharge occurs at higher pressures than multipactor, it should be considered for components that are expected to work under low pressure, e.g. ground segment equipment or satellites orbiting at very low altitudes. In practice, the corona analysis and prediction are studied using particle simulators, as in the case of multipactor discharge.

Chapter 3

Additive Manufacturing of Microwave Filters

The spectrum saturation and the rapid development of their competitors have forced the space sector to reduce costs and increase its data management capability in order to remain profitable. As a consequence, the focus of the space business is shifting towards new schemes based on high-throughput GEO satellites or mega-constellations of small to medium size LEO satellites. These new systems lower the cost per bit, being economically more efficient, but they also require communication devices with better performance and smaller sizes. Additionally, as the number of satellites in mega-constellation increases, all their parts, including microwave filters, need to be efficiently produced for medium and high volume production. Traditional filters based on conventional waveguides or planar transmission lines do not meet these requirements because they are either too bulky or do not have the desired performance at an affordable price.

The idea of Substrate Integrated Circuit (SIC) was developed in the late 1990s by Ke Wu and Deslandes, D. in [3] as a solution to the space communications needs of that time. The general idea behind this technology is to develop waveguide or coaxial transmission lines using a stack up of PCBs. This approach allows mass production and reduces the mass and size of devices compared to traditional waveguides while maintaining excellent electrical performance. However, the stack of PCBs imposes limits in the geometric complexity and design flexibility, making it difficult to implement the complex designs that require the current space sector.

On the other hand, Additive Manufacturing (AM) is a straightforward technology that provides an unprecedented design flexibility. This technology can easily and affordably manufacture complex geometries. AM is particularly well-suited for small and medium production volumes and uses lightweight materials. This makes it ideal for both high-throughput

satellites and smaller and simpler satellites, making it a promising candidate for addressing the current and future needs of the space industry.

The main objective of this chapter is to explore the application of AM techniques in the development of low-loss filters, offering significant weight and cost reduction compared to conventional solutions. The main idea is to combine this new manufacturing technology with Surface-Mount Technology (SMT) to develop easy integrable filters, thereby leveraging the design flexibility and lightweight advantages of AM along with the seamless integration of SMT. This innovative approach has the potential to compete with traditional substrate-integrated circuits.

The chapter is organised as follows. Section 3.1 provides a comprehensive overview of additive manufacturing, offering essential background information. Section 3.2 outlines the manufacturing approach developed throughout this thesis. In Section 3.3, we delve into the fundamental aspects of the SMT transition and explore the application of different resonant topologies. Sections 3.4 and 3.5 focus on the design and analysis of various filter topologies. Lastly, in Section 3.6, we examine the space qualification tests conducted on the developed filters.

3.1 Additive Manufacturing at Microwave Frequencies

AM offers numerous advantages over traditional manufacturing processes that rely on subtractive techniques. This relatively new manufacturing technique builds 3D objects by adding material layer by layer, allowing for a high degree of geometric complexity in the final part. The use of AM reduces the strict geometrical constraints of traditional manufacturing methods, which have historically limited the electromagnetic performance of microwave devices. This unprecedented design flexibility allows for the integration of multiple components into a single monolithic part and enables the adaptation of parts' geometry to meet specific requirements, such as reducing material usage or minimising mass and size while ensuring correct operational performance.

However, since additive manufactured parts consist of a stack of layers with a finite thickness, they are always an approximation of the original 3D model. This makes the tolerances of traditional manufacturing processes about one order of magnitude better to AM techniques ($0.01\,\mathrm{mm}$ of CNC vs $0.10\,\mathrm{mm}$ of 3D printing).

The application of AM in the microwave and RF sector has enormous potential, especially in the space industry where mass and size are critical. However, the application of this new manufacturing technology in this field is still in an early stage, presenting a promising area for future research and development.

3.1.1 Type of AM Techniques

Additive Manufacturing is a wide-ranging field encompassing multiple technologies, each with a different working mechanism. The standard ISO/ASTM 52900:2015 [102] defines five technologies based on the technique used to execute the 3D printing process: extrusion-based systems, vat photopolymerization, Powder Bed Dusion (PBF), Material Jetting (MJ), and Binder Jetting (BJ) systems.

3.1.1.1 Extrusion-based systems

Extrusion-based systems selectively dispense the material through a nozzle that traces the shape of the part layer by layer. The most extended technology is the Fused Deposition Modelling (FDM), where a plastic filament is melted and extruded through a hot nozzle. The nozzle moves along the three axes, precisely depositing the melted plastic at specific locations where it solidifies and bounds to previously printed layers, giving rise to the 3D object.

FDM has been traditionally based on the use of solid plastics, such as acrylonitrile butadiene styrene (ABS), polycarbonate (PC), polyamide (PA) and polylactic acid (PLA). Additionally, there is a wide variety of composite materials that mix plastic and a reinforcement material that can include copper, iron, and fibreglass, among others.

Fused deposition technology is widely accessible and offers many options for both professional and amateur users, primarily due to the low cost of its printers and materials. Nonetheless, some drawbacks limit its suitability for end-user applications. The layer thickness results in a poor surface finish and usually provides a low resolution of approximately $150\,\mu\mathrm{m}$. Furthermore, FDM often results in low adherence between layers, leading to parts with highly anisotropic mechanical properties.

3.1.1.2 Vat photopolymerization processes

This process creates parts by using a Ultraviolet (UV) light to selectively solidify liquid photopolymer resins. The part is typically built from the bottom up on a building platform submerged in a vat filled with photo-sensible resin. The building platform leaves a gap between it and the light source, allowing the selective solidification of the pattern of the layer. As the building platform is raised, the next layer is cured and fused to the previous one. Parts printed with this technology normally have to undergo two final post-processing steps: a cleaning bath to remove excess of uncured resin and a hardening process in an UV oven.

Vat Photopolymerization houses different printing technologies, including Stereolithography Apparatus (SLA), Direct Light Processing (DLP) and Masked Stereolithography Apparatus (MSLA). SLA employs a small laser spot that traces the shape of the layers to build

the object. Although this technique offers high precision, it can be time-consuming as the laser spot must travel across the entire surface of each layer. In contrast, DLP and MSLA use a projected image of the desired layer pattern to solidify the entire layer at once. Both technologies offer a reduced accuracy compared to SLA but significantly shorten the overall printing time.

Vat photopolymerisation processes can only use photopolymer resins. Similarly to FDM technology, novel composite materials with a wide range of fillers have appeared on the market during the last few years. However, the optical nature of Vat Photopolymerization does not allow the use of metal fillers, a limitation not present in the FDM technology.

Vat Photopolymerization technology offers high printing accuracy of approximately $0.15\,\mathrm{mm}$, high repeatability, and smooth finishing. This printing technique allows using very thin layers ($25\,\mu\mathrm{m}$), resulting in printed parts with surface finishes similar to those obtained through injection moulding.

However, the technology also has limitations. Parts always need support structures to attach suspended areas to the existing structure, limiting the geometry complexity of the printed parts. Additionally, the material of printed parts is normally sensitive to UV light, leading to variations in their mechanical properties over time.

3.1.1.3 Powder Bed Fusion

In PBF, parts are produced by selectively melting powdered particles to form each layer of the printed part. First, a thin layer of powder is spread over the building platform, and then the printing area is heated near the material's melting temperature. A laser or electron beam is then used to fuse and bind the powder particles together. Notably, this technology does not require support structures, as the unused powder material supports the subsequent layers.

PBF can employ a vast range of materials, including nylon, polypropylene, polycarbonate, and polyamide. They are all robust plastics traditionally used for manufacturing functional parts with traditional manufacturing techniques. The technology also allows for using metal alloys as building material, enabling the production of metal devices.

This technology does not require support structures, allowing for the fabrication of more complex geometries than vat photopolymerization and extrusion-based systems. However, this technology offers lower resolutions and accuracies than vat photopolymerization. Additionally, since parts are printed from powder material, they have a very rough finishing. Despite these limitations, the ability to produce strong and durable parts makes PBF the preferred technology for producing low and medium volumes of end-user parts in many industries.

3.1.1.4 Material Jetting

Material Jetting (MJ) works in a similar way as standard 2D ink printers. In this technology, a printer head selectively jets tiny droplets of a liquid polymer, following the desired pattern of the layer. The droplets are solidified using ultraviolet light or heat, forming one layer of the part. Then, a new layer is jetted over the freshly printed layer, and the process is repeated.

Among the MJ technologies, PolyJet (PJ) is the first to appear in the market and remains the most widely used, leading to the term PJ being broadly used to describe Material Jetting as a whole.

PolyJet (PJ) and most material jetting technologies typically utilise acrylic and wax photopolymers as their low viscosity allows precise jetting. Currently, research groups and manufacturers are exploring new materials that include ceramics and metals in their composition. However, these new materials tend to be too viscous and have large particles, making it challenging to jet through the small nozzles of the printer head.

Material jetting technique is highly precise, although their surface roughness is typically higher than the obtained with vat photopolymerisation. One of the strong points of this technology is that it can print with different materials simultaneously to produce full-colour and multi-material prints. This allows using soluble material to print easy-to-remove support structures.

Material Jetting is a costly process and is considered one of the most expensive manufacturing techniques. Despite this, it offers high dimensional accuracy and good surface finish, making it the only viable method when colourful, multi-material printing and good finishing are required.

3.1.1.5 Binder Jetting

Similarly to PBF, this process spreads a thin layer of powder material on a building platform. Then, a printer head selectively deposits a binding agent in the desired pattern that binds the powder particles together and forms the layer.

BJ is a versatile technology that can use a wide variety of materials, including metals, ceramics, sands, and polymers. However, the resulting parts tend to be porous and fragile, requiring additional processes such as sintering or infiltration to enhance their density and robustness. Additionally, while BJ can use metal particles, the final product has no electrical conductivity as the metal particles are bonded with a non-conductive material. The sintering and infiltration overcome this problem by obtaining fully conductive parts, but these processes tend to reduce the dimensional accuracy and repeatability.

As with other techniques, the unused powder material serves as a natural support structure, allowing for the creation of complex geometries. Binder jetting can produce parts with high accuracy, but the final precision is difficult to predict as sintering can cause a substantial and non-homogeneous shrinkage of up to $40\,\%$. Moreover, although sintered parts are almost fully dense, their mechanical resistance is not comparable to traditionally machined parts. The surface roughness is generally better than that obtained with most PBF processes, but it is lower than that obtained with vat photopolymerization or MJ.

Binder jetting represents a cost-effective alternative to more expensive techniques, including MJ and PBF. Although it may offer limited accuracy and mechanical resistance, it is currently the fastest and most affordable method for producing metal and ceramic parts.

3.1.2 Additive Manufacturing Techniques for Microwave Applications: Requirements and Considerations.

Since its inception, additive manufacturing has been widely used in both the industry and research communities for creating conceptual models and exhibition parts. However, over the past decade, AM has made significant progress, gaining the attention of the industrial and research communities. Today, AM is no longer limited to producing prototypes [6].

The focus of research in this area has primarily been on the development of micro and millimeter-wave devices that use bulky guiding technologies such as waveguides and coaxial cables. In this context, the use of AM can significantly reduce the mass and cost of developed devices for medium to low production runs while maintaining high-performance levels. However, the application of additive manufacturing at microwave frequencies requires dealing with stringent requirements in terms of dimensional accuracy, surface roughness, and some material considerations.

3.1.2.1 Dimensional accuracy

Many passive devices, particularly filters that operate at microwave and millimetre-wave, require manufacturing techniques with thigh tolerances. Even slight deviations in the dimensions of a filter's geometry can result in significant deviations in its electrical response. Although the microwave industry has developed various tuning mechanisms to allow for relaxed tolerance constraints, the use of more precise manufacturing techniques is preferable since tuning can be complex and its design process can be challenging.

3.1.2.2 Surface roughness

The same holds for the surface finish, which can increase the ohmic loss of devices, especially at high frequencies where the skin depth is comparable to the surface roughness. When the size of the roughness deformations is small compared to the skin depth, most of the RF current can flow in a straight line (the wave does not "notice" the deformation), resulting in no additional losses. However, as the surface roughness Root Mean Square (RMS) value (R_q) approaches the skin depth, the currents are forced to follow a different path than in a smooth conductor (the wave does "notice" the deformation), causing an increase in ohmic loss. Hammerstad and Jensen [103] derived an empirical formula to model this effect, expressing the increase in ohmic loss as follows:

$$\alpha_c' = \alpha_c \times K_{SR} \qquad \text{where} \qquad K_{SR} = 1 + \frac{2}{\pi} \times \arctan\left(1.4\left(\frac{R_q}{\delta}\right)^2\right) \tag{3.1}$$

, where α_c' is the ohmic attenuation coefficient including roughness effects, α_c is the ohmic attenuation coefficient for smooth perfect conductor, K_{SR} is the roughness multiplier, and δ is the skin depth. We utilized the aforementioned roughness model to simulate the increase in ohmic losses of a microstrip transmission line operating at 11 GHz in order to illustrate the significance of this phenomenon. The results of this simulation are presented in Figure 3.1.

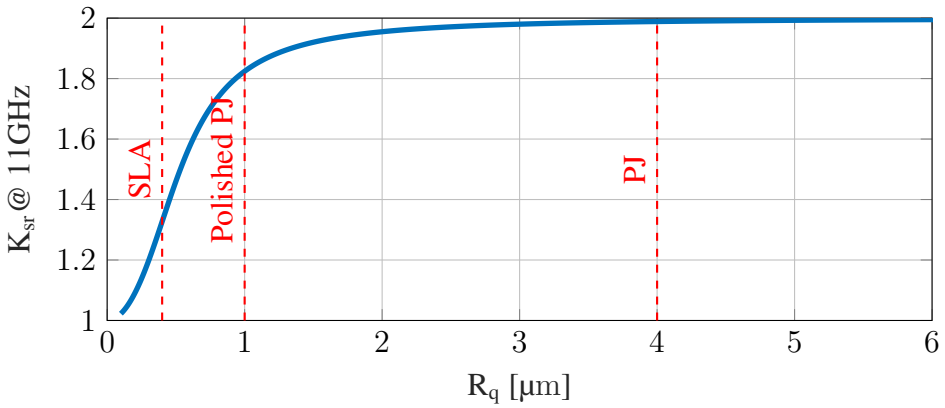

Figure 3.1: Roughness multiplier for the ohmic loss of a copper microstrip computed at 11 GHz. The markers used to represent the different printing technologies are average values obtained from personal measurements using printing samples and a contact profilometer.

The roughness multiplier K_{SR} equals one at low frequencies, where the R_q is much

smaller than δ, and asymptotically approaches two at high frequencies where $\delta << R_q$. More elaborate roughness models have demonstrated that K_{SR} can take even higher values when the roughness dimension is much bigger than the skin depth [104, 105]. This highlights the significance of achieving a surface that is as smooth as possible, as roughness can have a significant impact on the ohmic losses of a device.

3.1.2.3 Material considerations

In addition to surface smoothness, other secondary aspects such as the mechanical properties, Heat Deflection Temperature (HDT), Coefficient of Thermal Expansion (CTE), and the outgassing rate of the materials used in microwave devices are also crucial. These properties need a special attention in highly demanding applications such as the space segment of satellite communication systems.

3.1.2.4 Conclusion

Based on the requirements of microwave devices and the fundamental properties of each AM technology discussed in the previous sections, the following conclusions can be drawn. While FDM is the most affordable technique and can work with a wide range of materials, it does not provide the required accuracy and finish for the microwave band. Thus, it can only be used as an auxiliary technology to develop prototypes or sample parts. In contrast, PBF systems have good dimensional accuracy for microwave frequencies but do not provide a good surface finish. Moreover, direct metal printing requires expensive equipment and materials, so we have to discard this type of technology for research purposes. On the other hand, vat polymerisation and material jetting stand out among the available printing technologies due to their superior surface finish, moderate pricing, and excellent printing accuracy. Furthermore, their compact size makes them suitable for integration into small laboratory setups. These two technologies have been specifically chosen for this thesis as they are deemed the most suitable techniques for developing components with high precision and a superior finish. Material jetting has been employed to produce exhibition and production prototypes, while vat polymerisation has been used for the production of final devices with specific high thermal requirements.

3.2 Propose Manufacturing Procedure

Microwave devices often require the use of metallic surfaces, but only a limited number of additive manufacturing techniques are capable of printing such materials. Additionally, the

few techniques that do allow printing with metals or other electrically conductive materials tend to be expensive. As a result, two alternative strategies have emerged as feasible options for fabricating microwave devices: direct metal printing and a combination of plastic printing with supplementary plating or coating processes.

Direct metal printing techniques, such as Powder Bed Dusion (PBF), Binder Jetting (BJ), and some Fused Deposition Modelling (FDM) methods, have the potential to fabricate microwave devices directly from electrically conductive materials. This approach may eliminate the need for additional metallisation processes. However, direct metal printing techniques tend to be costly and result in looser manufacturing tolerances and rougher surfaces when compared to their plastic counterparts. Therefore, this solution is primarily relegated to applications that require exceptional mechanical resistance and where traditional manufacturing methods are not feasible due to the geometrical complexity of the part. Nonetheless, numerous examples of this approach can be found in the literature, and private companies are currently using these technologies to develop waveguide devices for the space sector [49].

An alternative approach to direct metal printing is to use conventional AM techniques and materials to print the geometry of the microwave device. Once the plastic part has been printed, it undergoes a metallisation process that covers the part with a thin layer of an electrically conductive material. Since the skin depth at high frequencies is very thin, only a thin conductive layer is needed to achieve a device with the same electromagnetic performance as one entirely made of metal. This approach is popular among academic and research communities, as it provides a straightforward and inexpensive way of fast prototyping, significantly reducing the time between design and publication. This thesis focuses on this approach.

3.2.1 Plating of Plastic Materials

The metallisation process for plastic surfaces typically involves two sequential coating processes. The first step focuses on applying a thin coating layer that adheres well to the plastic surface, while in the second process, the deposited layer is further stabilised and thickened. The coating material of the last metallisation step can differ from the first process to meet specific requirements, such as enhanced conductivity and wear or corrosion resistance.

In the initial plating process, a thin layer of conductive material is attached to the plastic part. This process can be challenging due to the low roughness and surface energy of plastics, resulting in the limited presence of binding sites [106]. This forces the use of additional surface treatments to enhance the roughness and improve the adhesion strength of the coating. The most common deposition methods for directly plating plastics include electrically conductive painting, electroless plating, and Physical Vapor Deposition (PVD).

Physical Vapor Deposition (PVD) is widely used in metallisation processes for AM. It

compasses various deposition methods, where the material to be deposited transitions from a solid to a vapour state in a vacuum chamber. The vaporised material is then directed toward the sample, condensing and forming a metal coating on their surfaces. This method requires a previous plasma etching as a preconditioning treatment [107] to obtain an excellent adhesion. However, PVD requires complex and expensive equipment, and the deposition rate is very slow for medium and high productions. Moreover, while this process is convenient for flat substrates, it is limited for substrates with complex geometries [108], where it can result in a non-uniform coating thickness.

Conductive painting is another widely used method in the academic field. This method involves applying a thin layer of conductive paint to the plastic part. Solvents of the paint solve the exposed layer of the part, achieving an excellent adhesion. However, the coating layer obtained with this technique is non-uniform, and the geometry of the part can cause paint agglomeration in corners or protrusions. Additionally, the conductivity of the paint is usually moderate, requiring additional plating processes.

Electroless plating, also known as autocatalytic plating, is the most common technique in the industry for plating plastic parts with complex geometries. This process chemically reduces metal ions of a liquid solution, allowing them to deposit onto the surface of the object. The resulting layer is even and uniform for any geometry regardless of its complexity [109, 110]. This method is typically more cost-effective than PVD as it does not require expensive equipment. However, the coating may have limited adhesion to certain materials, requiring additional surface preparation for most plastics.

Once a thin layer of conductive material has been applied to the part, it can undergo an electroplating process. In this process, the part is placed in an electrolyte solution containing ions of the metal to be deposited. The part is connected to the negative terminal (cathode), and an electrode made of the metal to be deposited is connected to the positive terminal (anode). When an electric current is passed through the solution, metal ions from the electrode are attracted to the part, giving rise to the coating layer. This last coating process thickens and stabilises the previously deposited layer.

In this thesis, we have employed a combination of electroless and electroplating, which offers a cost-effective solution for achieving a uniform copper coating layer on complex geometries. The optimised process used in this research is described in detail below.

3.2.2 Optimised Electroless Plating Process

We have developed a novel electroless plating process in collaboration with the "Instituto de Tecnología Química (ITQ)" of the "Universitat Politècnica de València (UPV)" that allows the attachment of copper particles to polymeric surfaces without the need for an electric

current. This method is based on the work conducted in [111], and with a few modifications, it can be applied to various materials. Over a hundred plating processes were performed to optimise the procedure for three commonly used plastic materials in 3D printing: bronze and copper-filled PLA, ABS, and different types of SLA resin. This enables us to use different printing technologies, including FDM, PJ, SLA and MSLA.

Figure 3.2 displays the four phases of the plating process. First, the part undergoes a surface treatment to increase the nano-metric roughness, ensuring a robust bond with the metal deposition. Second, a thin layer of a catalytic element is deposited on the surface of the part. In the third step, the catalytic layer is cleaned and prepared for the final stage, where a relatively thick layer of copper is deposited onto the part. An optional passivation step can be applied as a final phase to prevent copper oxidation.

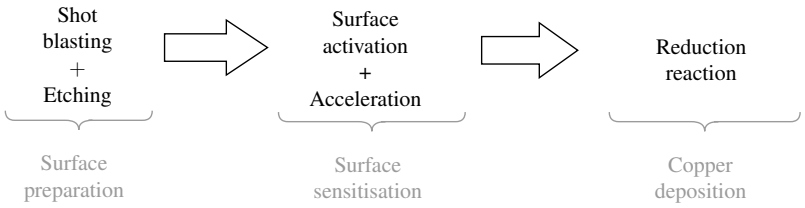

(a)

(b)

Figure 3.2: (a) Schematic of the electroless plating process. (b) Experimental setup for the electroless plating.

1. Etching: Polymer surfaces typically exhibit limited binding sites for metal coatings. In the industry, chemical etching using strong oxidising compounds like chromium salts is used to improve the adhesion of the coating. This aggressive etching enhances surface roughness and oxidises the chemical components of the material, creating a strong mechanical interlocking between the plastic and the coating [106]. However, these strong oxidising compounds are highly corrosive and environmentally hazardous. In our research, we have replaced this costly and polluting process with a double etching technique that consists of shot blasting and chemical etching using a sodium hydroxide solution. The shot blasting process creates a rough surface to improve mechanical interlocking, while the chemical etching step oxidises certain elements of the polymer, increasing the chemical interlock between the plastic and the metal coating. Compared to the conventional approach, this new method is less corrosive and has lower environmental impacts, making it a more sustainable option for industrial applications.

   The first shot blasting is needed only for ABS and SLA resin. We conducted several calibration processes, subjecting different materials to various shot-blasting treatments to determine the optimal combination. Figure 3.3 illustrates metallisation samples printed with PJ using ABS material that underwent different shot blasting processes.

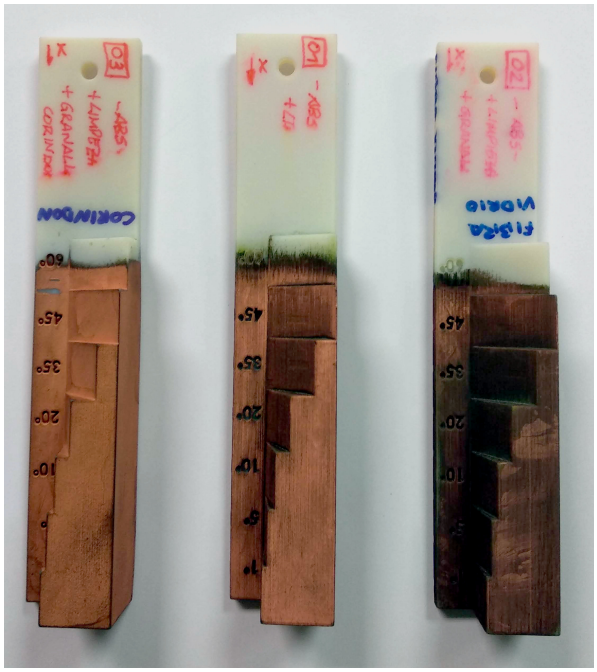

Figure 3.3: Metallisation samples, from left to right: shot blasted with corundum, no shot blasted and shot blasted with glass particles. Samples were made of ABS and were printed with PJ.

Based on the results of our investigation, it was concluded that the corundum shots produce the best finishing. In contrast, the untreated samples and those subjected to glass shots exhibited several uncoated areas, as shown in Figure 3.4. This outcome was consistent across several sample materials evaluated in this study (ABS and SLA resins). As a result, corundum blasting has been consistently used to treat all parts that were printed using MJ, SLA, and MSLA technologies.

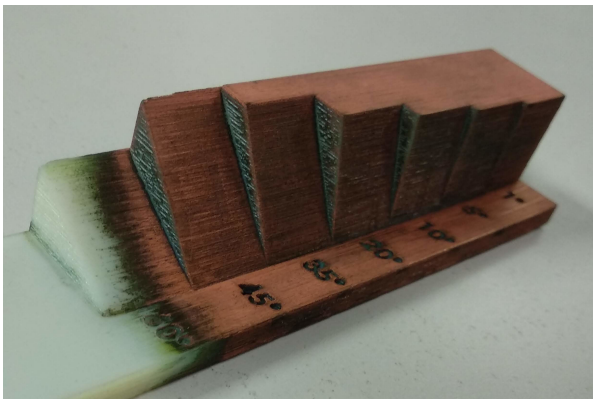

Figure 3.4: Detail of metallisation sample without shot blasting. Black areas are coated with the catalytic material but not with copper.

After shot blasting, parts should undergo a chemical etching process. It involves immersing the parts in a solution of sodium hydroxide ($NaOH$), ethyl alcohol, and distilled water at approximately $50\,^{\circ}\mathrm{C}$. After etching, parts must be rinsed thoroughly to eliminate any possible residues that could spoil the following chemical bath. Notably, this process is much less hazardous and polluting than traditional methods based on chromium, reducing the costs associated with safety and waste management.

2. Activation or surface sensitisation: this step involves immersing the part in an activation solution consisting of $PdCl_2$, $SnCl_2$, and HCl. In this phase, a palladium-tin alloy is attached to the part's surface. The palladium acts as a catalyst for the metallisation reaction, while the tin helps attach palladium particles to the plastic surface [111].

3. Acceleration: The tin particles of the previously deposited catalytic alloy can interfere with the coating reaction. To remove this material and expose the palladium sites, the sample is immersed in an HCl acid solution at $25\,^{\circ}\mathrm{C}$.

4. Copper deposition: the part is finally immersed in a copper-formaldehyde solution. Continuous agitation and intense airing should be ensured to prevent the formation of hydrogen gas bubbles in the copper coating, which would reduce the adhesion strength.

Finally, the thickness of the copper coating can be controlled by adjusting the immersion time.

The optimised metallisation process developed in this section enables the development of passive RF devices using different AM techniques and materials. This method was combined with a final electroplating process conducted on the MiniContact-RS commercial plating system from LPKF Laser & Electronics. These metallisation processes were employed to fabricate the different filter topologies that are discussed in detail in the following sections.

3.3 Design of Surface-Mounted Cavity Filters

As discussed in the previous section, additive manufacturing provides rapid prototyping with reduced mass and cost. Previous studies on this topic have explored the use of this technology for developing complex geometries that could not be fabricated using traditional manufacturing techniques. This chapter aims to investigate the application of AM in the development of Surface-Mount Technology (SMT) filters, combining the advantages of both technologies.

Surface-mounted filters have been extensively studied in microwave engineering due to their numerous advantages compared to traditional waveguide or planar filters. These filters are directly integrated onto a PCB, offering a compact footprint and easy integration with planar subsystems. The combination of surface-mount technology with additive manufacturing presents an excellent opportunity to develop highly integrable devices that deliver high performance within tight volume and mass constraints. This section examines the development of surface-mounted filters using AM technology.

3.3.1 Study of the Surface-Mounted Cavities

Cavity resonators have been widely employed in microwave filters due to their outstanding performance and ease of implementation. They offer a straightforward and economical solution for designing filters with high selectivity and significantly lower loss when compared to planar resonators.

In its simplest form, a cavity resonator consists of a closed conductive container designed to resonate at a specific frequency. The cavity can take various shapes; e.g., rectangular, hexagonal, circular, and spherical; and the cavity's size, shape, and material determine its resonant properties (resonant frequency and unloaded quality factor).

When implemented in a waveguide, cavities exhibit an extremely high quality factor, making them ideal for low-loss and narrow-response filter designs. However, when used in

Substrate Integrated Circuit (SIC) technology, they provide a moderate quality factor that is between that of waveguide cavities and planar resonators while offering reduced size and easier integration. This trade-off between performance and size has been of great interest for low-orbit satellite systems.

The integration of cavity resonators with SMT technology combines the high performance of waveguide resonators with the ease of integration of SIC circuits, being particularly interesting for highly demanding satellite systems. In the subsequent sections, the basic properties of rectangular and circular cavities will be studied, followed by an examination of their SMT implementation.

3.3.1.1 Rectangular cavity

The rectangular cavity resonator is composed of a short-circuited rectangular waveguide, as illustrated in Figure 3.5. This structure has been extensively studied in the literature [64, 69]. However, it is worthwhile to briefly examine its performance in terms of quality factor and Spurious Free Range (SFR) for a better understanding.

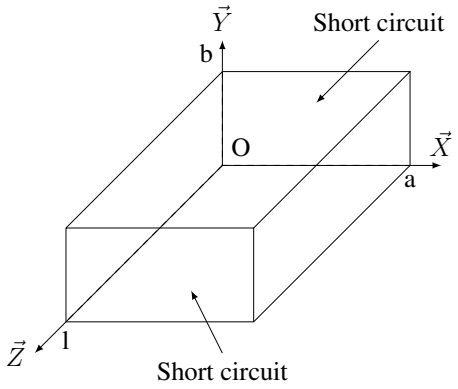

Figure 3.5: Basic structure of a waveguide rectangular cavity.

For standard waveguide structures with $b \leq a \leq l$, the dominant resonant mode is the TE_{101}. Considering this mode, the initial dimensions of the cavity can be calculated using equation 3.2 for $m = 1$, $n = 0$ and $p = 1$ [64].

$$f_{mnp} = \frac{c}{2\pi}\sqrt{\left(\frac{m\pi}{a}\right)^2 + \left(\frac{n\pi}{b}\right)^2 + \left(\frac{p\pi}{l}\right)^2} \tag{3.2}$$

where a, b and l are the width, height and length of the cavity, respectively. Thus, for a waveguide with $a = 19.05\,\mathrm{mm}$ the cavity length for a resonance frequency of $11\,\mathrm{GHz}$ would be approximately $l = 19.5\,\mathrm{mm}$.

After determining the width and length of the cavity, its height (b) must be chosen to achieve a balance between unloaded quality factor (Q_U), SFR and compactness. A higher height yields a better Q_U but reduces the spurious-free range, while a larger height results in a more complex SMT assembly.

The example cavity with a center frequency of 11 GHz ($a = 19.05\,\text{mm}$, and $l = 19.5\,\text{mm}$) was analysed to demonstrate the balance between quality factor and spurious-free range.

Figure 3.6 (a) shows the multimodal analysis of the cavity, including the resonant frequencies of the first four modes in the proposed cavity and its evolution with the cavity height. Figure 3.6 (b) shows the unloaded quality factor (Q_u) of the rectangular cavity. It was calculated as the relationship between the total stored energy and the power dissipation in the cavity walls due to ohmic loss by using the well-known expression $Q = \omega_0(W_e + W_m)/P_c$ from [64].

$$Q_u = \frac{(kal)^3\, b\eta}{2\pi^2 R_s} \frac{1}{(2a^3b + 2bl^3 + a^3l + al^3)} \tag{3.3}$$

where a, b and l ar the width, height and length of the cavity, k is the wavenumber, R_s is the surface resistance, and η is the intrinsic impedance of the medium.

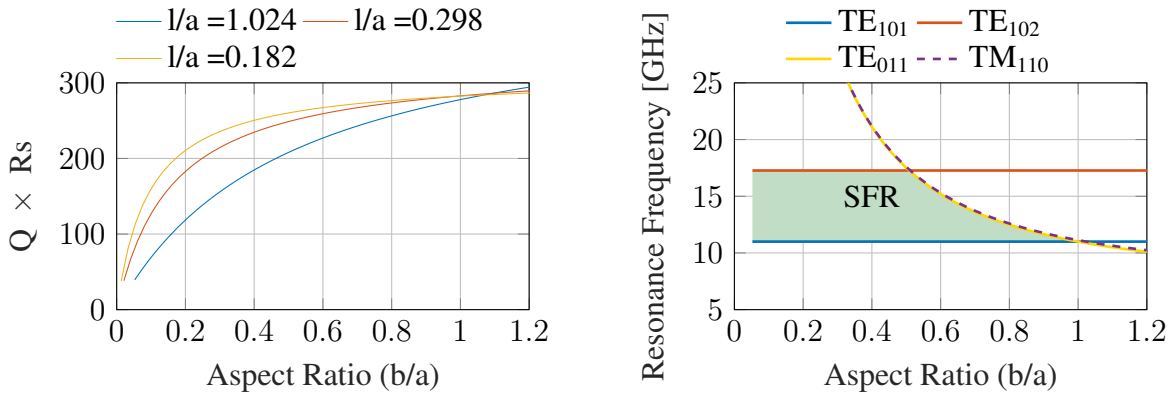

Figure 3.6: (a) Unloaded quality factor of the fundamental mode (TE_{101}) of a rectangular cavity as a function of its height (b) for a resonance frequency of 11 GHz. (b) Resonance frequencies of the first four resonant modes of a standard rectangular cavity with a width of $a = 19.05\,\text{mm}$ and a length of $l = 19.5\,\text{mm}$.

It can be observed that for low b/a ratios, the SFR is limited by the TE_{102} mode. However, with increasing cavity height, the resonance frequency of the TE_{011} mode decreases, approaching and exceeding the TE_{102}. The balance between SFR and Q_u is achieved when

$b = a/2$, as the resonant frequencies of the subsequent modes (TE_{102} and TE_{011}) become equal. Higher cavity heights result in higher Q-factor values, but it inevitably narrows the SFR.

3.3.1.2 Circular Cavity

Figure 3.7 depicts the fundamental structure of a circular cavity resonator. It consists in a circular waveguide that has been short-circuited at both ends. The resonance frequencies of the different TE_{mnp} and TM_{mnp} resonant modes are determined by the following equations:

$$f_{mnp} = \frac{c}{2\pi}\sqrt{\left(\frac{2P'_{mn}}{a_c}\right)^2 + \left(\frac{p\pi}{l}\right)^2} \qquad \text{for } TE_{mnp} \text{ modes.} \tag{3.4}$$

$$f_{mnp} = \frac{c}{2\pi}\sqrt{\left(\frac{2P_{mn}}{a_c}\right)^2 + \left(\frac{p\pi}{l}\right)^2} \qquad \text{for } TM_{mnp} \text{ modes.} \tag{3.5}$$

, where a_c and l refer to the diameter and length of the cavity. The parameter c represents the speed of light in the medium. The terms P'_{mn} and P'_{mn} are the m-th root of the Bessel function of n kind and its derivative, respectively.

This type of cavity can only be surface-mounted on one of its two flat faces, i.e., the top and bottom surfaces of Figure 3.7. This makes the TM_{010} and the TE_{111} modes the most relevant for surface-mount technology.

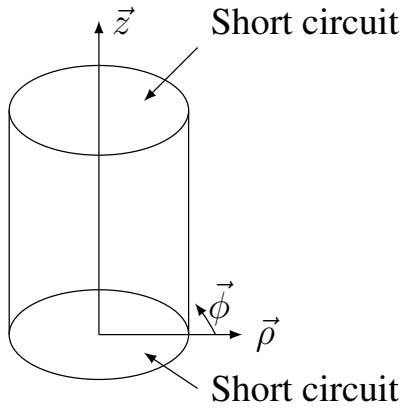

Figure 3.7: Basic structure of a waveguide circular cavity.

On the one hand, the TM_{010} mode exhibits a length-independent resonance frequency that makes it particularly advantageous for SMT applications. The resonance frequency of

this mode is solely determined by the cavity diameter, while the cavity length must be chosen to meet the requirements of compactness and quality factor. The resonant modes immediately above the fundamental one are the TM_{110} and TE_{102}. For low heights, the SFR is limited by the TM_{110} mode, whose resonance frequency only depends on the diameter. In contrast, the TE_{102} mode's resonance frequency is determined by both the diameter and length. As the length increases, its resonance frequency decreases, ultimately narrowing the SFR as is illustrated in Figure 3.8 (b). Thus, the height yielding the highest SFR and Q-factor occurs when the resonance frequencies of bot modes are equal, as per equation 3.6.

$$b_c^{MAX} = \frac{a_c \pi}{2\sqrt{P_{11}^2 - P_{11}'}} \tag{3.6}$$

As in the case of the rectangular waveguide, the quality factor of this mode increases with the cavity length, as demonstrated by the numerical simulations of a weakly coupled cavity of Figure 3.8 (a).

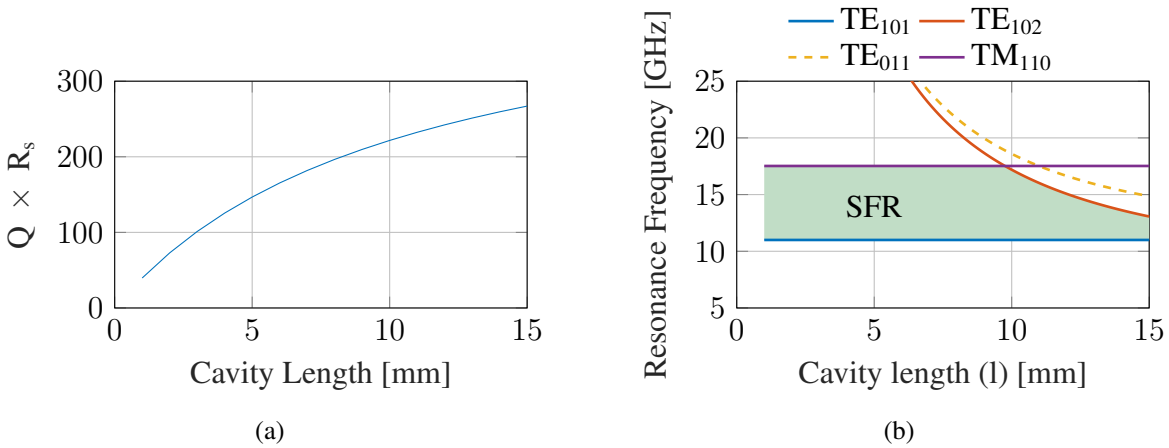

Figure 3.8: (a) Unloaded quality factor of the fundamental mode (TM_{010}) of a circular cavity as a function of its length (l) where the cavity diameter is fixed at $a = 20.87\,\mathrm{mm}$. (b) Resonance frequencies of the first four resonant modes of the same circular cavity with a diameter of $a = 20.87\,\mathrm{mm}$.

On the other hand, the TE_{111} mode is of interest because its surface currents have no components along the longitudinal axis. This property makes it insensitive to non-perfect electric connection between parts, thereby reducing the impact of manufacturing and assembling tolerances. However, the practical use of this mode is limited by the large volume it requires, making it impractical for SMT applications. For this reason, we finally decided to use the TM_{010} mode in SMT applications.

3.3.1.3 SMT transition

This section introduces a novel input/output coupling mechanism developed in this thesis, which enables the integration of rectangular and circular cavity resonators and filters through a simple Surface-Mount Technology (SMT). Figures 3.9 (a) and (b) show the proposed coupling structure for a rectangular and circular cavity resonator, respectively.

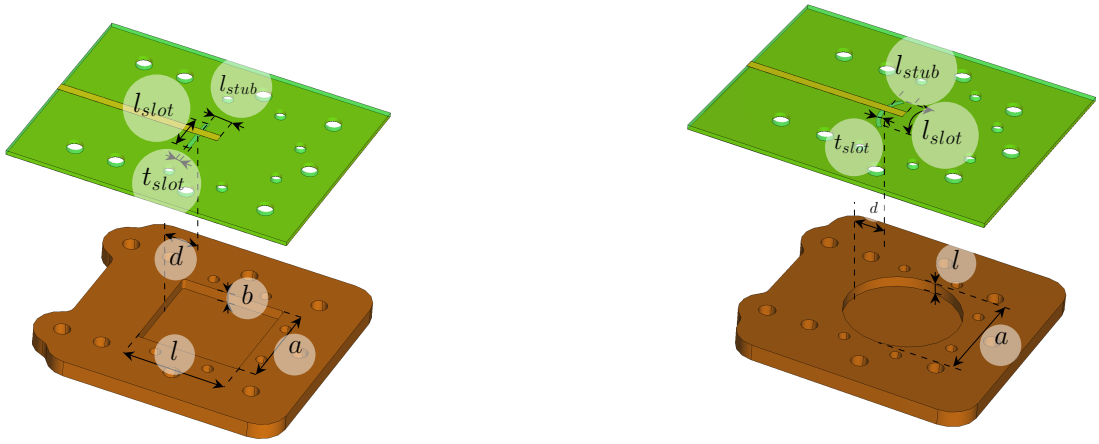

(a) (b)

Figure 3.9: Layout of the SMT assembling: (a) slot coupling for a rectangular cavity resonator and (b) slot coupling for a circular cavity resonator. Metallised 3D-printed parts are represented in brown, dielectric material in green, and copper in yellow.

The coupling element comprises a thin slot aperture fabricated on the ground plane of a Microstrip Line (MSL) that works as a feeding line. The slot cuts the current return path of the line, acting as a magnetic monopole that stimulates the desired mode of the resonator [112].

To maximise the power transfer and, therefore, the coupling value, the slot must be placed at a location where the magnetic fields of both the MSL and the resonator are maximum [113]. Two methods can be used to precisely define a maximum of magnetic field in the the MSL: either short-circuit the end of the microstrip feeding line at the position of the slot ($l_stub = 0$) or add a quarter-wavelength open-ended stub ($l_stub = \lambda/4$). The position and shape of the slot depend on the resonator topology and the preferred resonant mode. For rectangular cavities operating at the TE_{101} mode, the slot should be parallel to and as close as possible to the short-circuited end ($d \simeq 0$) [113]. In contrast, for circular cavities operating at the TM_{010} mode, the slot should draw an arc at approximately $\rho = 0.75a/2$, where a is the diameter of the resonator. In this position, the magnetic field of the TM_{010} mode is maximum. There are no general rules for the other design parameters, l_{slot} and t_{slot}) that have to be optimised in

order to obtain the desired coupling value.

In order to demonstrate the behaviour of this new coupling, two single-loaded resonators, one rectangular and another circular, have been simulated using CST Studio Suite. For this study, the dimensions of the rectangular cavity resonator are $19.05\,\mathrm{mm}$ width and $19.50\,\mathrm{mm}$ length so that the TE_{101} mode resonates at $11\,\mathrm{GHz}$. The diameter of the circular resonator is $20.87\,\mathrm{mm}$ so that the TM_{010} mode resonates at $11\,\mathrm{GHz}$. The height of both resonators was set to $2\,\mathrm{mm}$ and the slot thickness was fixed to $t_{slot} = 0.7\,\mathrm{mm}$. The initial separation between the slot and the short circuit of the resonators is $d = 2\,\mathrm{mm}$, and the initial slot lengths are chosen to be $3.5\,\mathrm{mm}$ for the rectangular resonator and $4\,\mathrm{mm}$ for the circular cavity. The PCB is a RO4003C laminate of $1.524\,\mathrm{mm}$ thickness with $17.5\,\mu\mathrm{m}$ of copper cladding. The microstrip is $3.25\,\mathrm{mm}$ of width ($Z_{MSL} = 50\,\Omega$) and the initial length of the open-ended stub is approximately one-quarter wavelength in the MSL at $11\,\mathrm{GHz}$ ($l_{stub} = 3.95\,\mathrm{mm}$). The external quality factor of the resonators was extracted using the group delay method previously explained in Section 2.1.1.

Figure 3.10 (a) shows the external quality factor of both cavities as a function of the stub length. As was expected, the higher coupling is achieved for a stub length similar to one-quarter wavelength in the MSL. Figure 3.10 (b) shows the external quality factor of both cavities as a function of the parameter d. The highest coupling is achieved when the slot is near the short-circuited end of the rectangular resonator. Regarding the circular cavity, it is maximum when the slot is located at 0.75 times the cavity radius, i.e. $d = 2.60\,\mathrm{mm}$. Finally, it can be observed that the coupling value is higher for longer slot lengths for both resonators, as is depicted in Figure 3.10 (c). This analysis demonstrates the behaviour of the coupling mechanism, where the slot can be modelled as a magnetic monopole that implements a magnetic coupling between the MSL and the resonant cavities.

It should be noted that the proposed structure can also behave as a narrowband transition for developing non-resonant devices. Huang states the principal working mechanism of such transition and proposes an equivalent circuit for its design in [113]. This transition demonstrated a practical operation bandwidth of up to $40\,\%$ for $15\,\mathrm{dB}$ RL [113, 114]. Its performance is relatively inferior compared to more complex transitions implemented in substrate-integrated circuits, such as those presented in [18, 115]. However, the design and manufacturing process of the slot transition is much simpler, being very suitable for developing SMT narrowband devices such as resonators and filters.

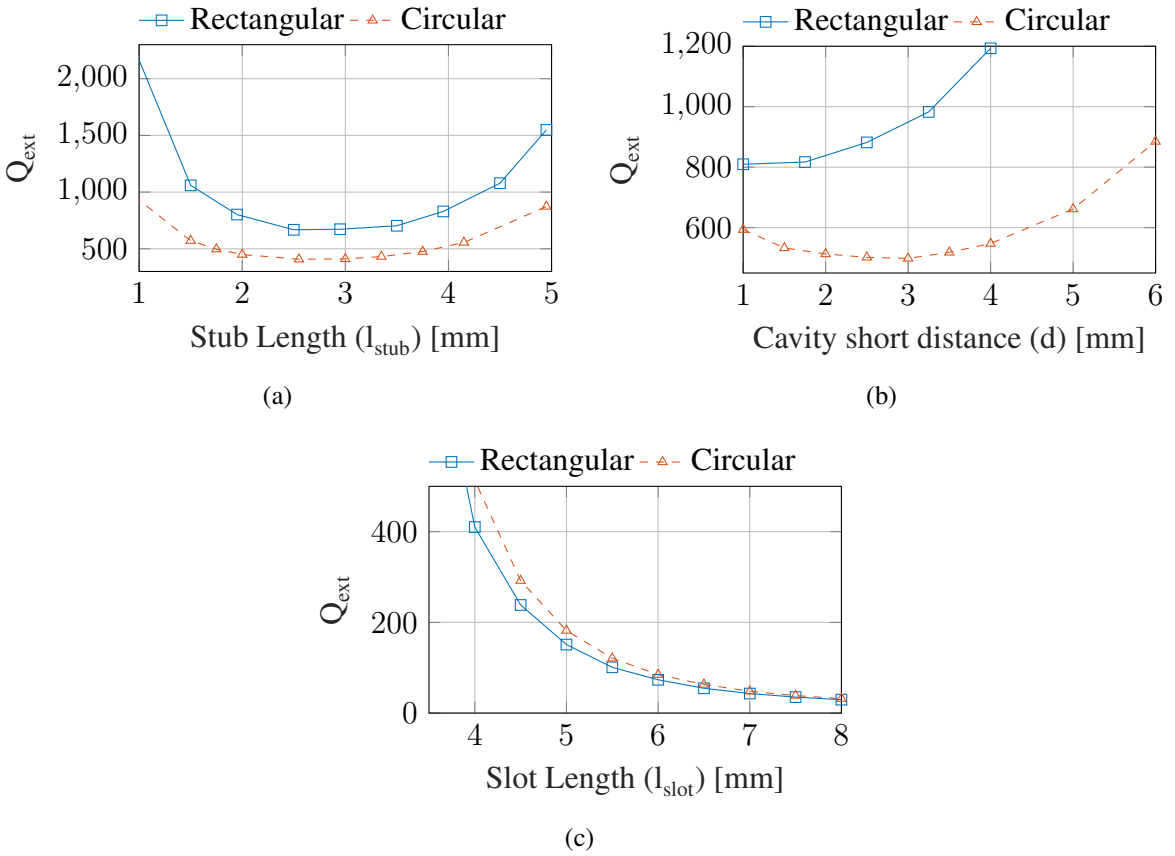

Figure 3.10: Design curves of the slot coupling mechanisms for rectangular and circular cavities. (a) Variation of external Q factor (Q_{ext}) with respect to stub length (l_{stub}). (b) Relationship between Q_{ext} and short circuit distance (d). (c) Q_{ext} as a function of the slot length (l_{slot}).

3.4 Filter Prototypes

In this section, we present the final prototypes that have been designed and manufactured. The design parameters are summarised, and the simulated response is compared with measurements. The prototypes consist of a WR75 waveguide filter and three SMT filters with different topologies. All the prototypes presented in this section were fabricated using the desktop SLA printer Form 2 from Formlabs [116] using Rigid 10K resin and a layer resolution of $25\,\mu\mathrm{m}$. The selection of Rigid 10K resin was based on its high content of solid silica (SiO) particles, ranging from $55\,\%$ to $75\,\%$, which effectively reduces shrinkage forces and enhances printing accuracy [117]. Moreover, this resin offers an exceptionally high Heat Deflection Temperature (HDT) compared to standard SLA resins, making it highly suitable for

demanding applications. To further minimise deformation associated with shrinkage, all parts were printed with a honeycomb reinforcement structure, ensuring acceptable manufacturing tolerances for the production of bandpass filters at microwave frequencies [33, 118].

The 3D-printed parts were metallised using the double-stage plating process explained in Section 3.2, involving the newly developed electroless plating method from this thesis and a final commercial electroplating process. The prototypes were introduced for $15\,\mathrm{min}$ in the final phase of the electroless plating, resulting in a copper cladding thickness ranging from 0.5 to $1.7\,\mu\mathrm{m}$, as shown the Field-Emission Scanning Electron Microscope (FESEM) image depicted in Figure 3.11 (a). The final copper layer obtained after electroplating was thicker, ranging from 6.5 to $12\,\mu\mathrm{m}$, as shown in Figure 3.11 (b). Since the skin depth at $11\,\mathrm{GHz}$ for annealed copper ($\sigma_{\text{copper}} = 58\,\mathrm{MS/m}$) is approximately $0.63\,\mu\mathrm{m}$, the resulting copper layer thickness is more than sufficient to provide excellent electric performance.

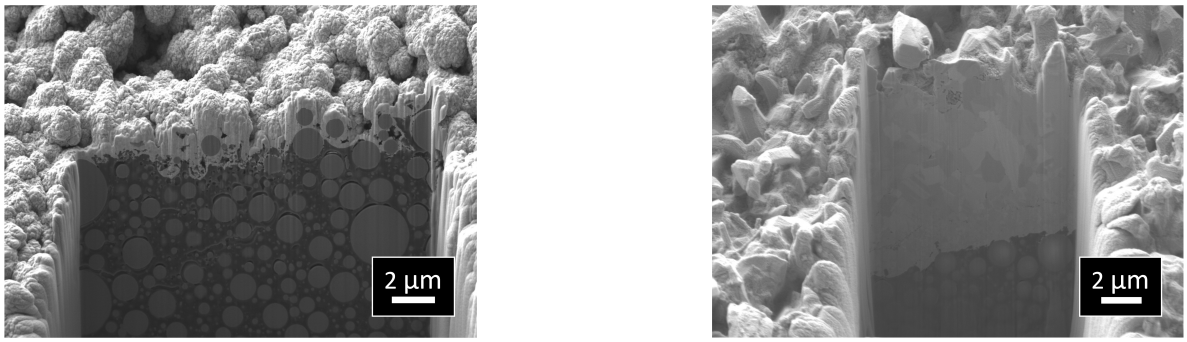

(a) (b)

Figure 3.11: FESEM view of a trench etched on a metallised part. The copper layer is depicted in white, the SLA resin is shown in dark grey, and the light grey spheres are particles of SiO_2. (a) Post electroless plating. (b) Post electroplating.

3.4.1 WR75 Cavity Filter

The first prototype is the four-poles bandpass filter used in Section 2.1.1 to explain the filter design procedure. It has a Chebyshev response centred at $11\,\mathrm{GHz}$ with $300\,\mathrm{MHz}$ bandwidth and $20\,\mathrm{dB}$ in-band return loss. The filter topology is depicted in Figure 3.12. It compasses four rectangular resonant cavities and five inductive apertures that work as resonators' couplings. The resonators are implemented on a standard rectangular WR75 waveguide with $19.050\,\mathrm{mm}$ of width and $9.525\,\mathrm{mm}$ of height, and operate under the TE_{101} mode.

The values of the inverters $K_{I,i+1}$ for the specified filter response are: $\overline{K}_{S,1} = \overline{K}_{4,L} = 0.2143$ and $\overline{K}_{1,2} = \overline{K}_{3,4} = 0.0390$, $\overline{K}_{2,3} = 0.0300$. The elements of the coupling matrix

are $M_{(S,1)} = M_{(L,4)} = 1.035$, $M_{(1,2)} = M_{(3,4)} = 0.911$ and $M_{(2,3)} = 0.700$, while all other elements of the matrix are zero.

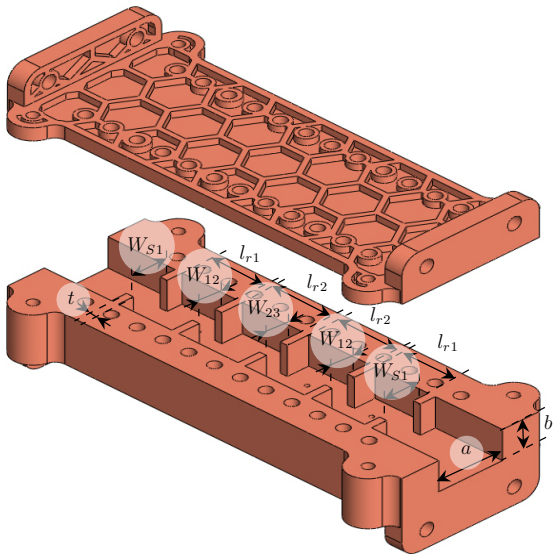

Figure 3.12: Layout of the X-band H-plane directly coupled cavity filter designed within a WR75 rectangular waveguide.

The filter has been developed following the design process developed in Section 2.1.1. Figure 3.13 shows the optimised response, and Table 3.1 list the optimised dimensions.

Table 3.1: Final dimensions of the X-band filter in WR75.

Parameter	**Dimension** [mm]
a	19.05
b	9.53
l_{r1}	15.97
l_{r2}	17.74
t	2.00
W_{S1}	10.21
W_{12}	6.86
W_{23}	6.37
l_{in}	20.00

Two prototypes of this filter were manufactured and tested; Figures 3.14 (a) and (b) show one of the manufactured devices. The filters were fabricated in two parts, using the body and cover strategy. Parts were assembled using bolts and nuts that were specifically located to minimise the effect of non-perfect electric contact between both parts of the filter. Moreover,

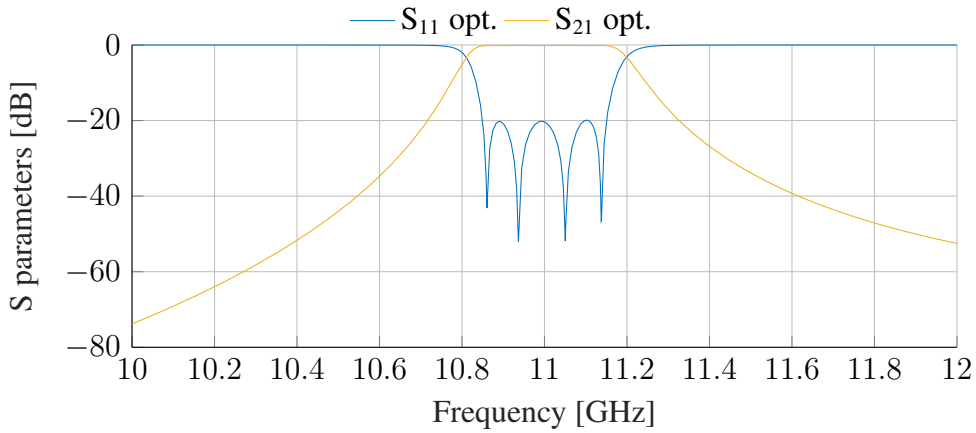

Figure 3.13: Simulated response of the X-band filter in WR75.

a thin ribbon of indium was located in the perimeter of the filters' cavities in order to fill the small gaps and deformations produced during the manufacturing process, see Figure 3.14 (a).

(a) (b)

Figure 3.14: Manufactured prototype of the WR75 filter: (a) Top view of the body part showing the filter cavities and coupling irises. (b) Assembled filter showing the waveguide flange.

The initial structure of the filter shown in Figure 3.12 was modified to fit the requirements of the space tests. Two venting holes of $1.20\,\mathrm{mm}$ diameter are included in each cavity. These holes were positioned on the diagonal of the cavity at a distance of $4.50\,\mathrm{mm}$ from the centre, minimising their impact on the electric field distribution of the cavity. Accordingly, these holes had minimal impact on the response of the resonators, and the design dimensions

specified in Table 3.1 were still valid for this new design.

Figure 3.15 shows the simulated and measured responses of the two prototypes. They were measured using a VNA calibrated with a commercial TRL calibration kit for rectangular waveguide.

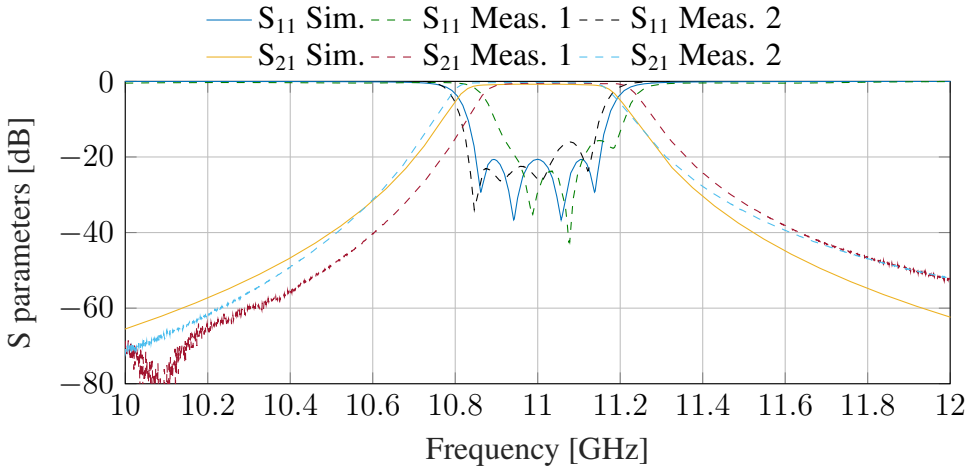

Figure 3.15: Frequency response (simulated and measured) of the X-band filters implemented in WR75 waveguide.

The measurements of both realisations demonstrate an excellent agreement with the simulated response. The realisation 1 exhibits a slight deviation of $-18\,\mathrm{MHz}$ in center frequency and $5.9\,\mathrm{MHz}$ in $-3\,\mathrm{dB}$ bandwidth ($BW_{-3\,\mathrm{dB}}$), exhibiting an extremely low IL of $0.29\,\mathrm{dB}$. In contrast, realisation 2 shows a higher insertion loss ($0.45\,\mathrm{dB}$) and a larger deviation of $51.3\,\mathrm{MHz}$ in center frequency. These slight deviations in frequency and loss could be attributed to potential manufacturing imperfections. Nonetheless, the measured performance of both realisations is excellent, showing high isolation and low loss, meeting the demands of highly demanding applications. The excellent results obtained with these prototypes validate the superior performance of the manufactured technology.

3.4.2 Rectangular SMT (R-SMT) Filter at X Band

To demonstrate the effectiveness of the proposed SMT approach developed in Section 3.3, we designed a 4-pole Chebyshev filter realisation with SMT assembly. The filter is centred at $11\,\mathrm{GHz}$, with a $300\,\mathrm{MHz}$ bandwidth and $20\,\mathrm{dB}$ in-band return loss. The initial dimensions of the rectangular cavity are $a_r = 10.05\,\mathrm{mm}$ of width and $l_r = 19.50\,\mathrm{mm}$ of length. A low cavity height of $b_r = 2.00\,\mathrm{mm}$ was selected for this implementation to enable comparisons with similar structures implemented in SIC technology [18]. Furthermore, the low-profile

resonators can help reduce the overall size of the device, making it easier to integrate into planar systems.

Figure 3.16 shows the layout of this filter realisation. It comprises four rectangular cavities coupled through inductive irises with a thickness of $t_{ri} = 4.00\,\mathrm{mm}$. This thickness was selected to place M2 bolts close to the iris walls, improving the electrical contact between the filter body and the PCB.

The filter is externally coupled to two microstrip feeding lines through the proposed slot coupling introduced in Section 3.3.1.3. The PCB is a RO4003C substrate with $\varepsilon_R = 3.55$, $t_s = 1.524\,\mathrm{mm}$ thickness, and $17.5\,\mu\mathrm{m}$ of top and bottom copper cladding. The microstrip line was designed to have a characteristic impedance of $50\,\Omega$ ($W_{ms} = 3.25\,\mathrm{mm}$).

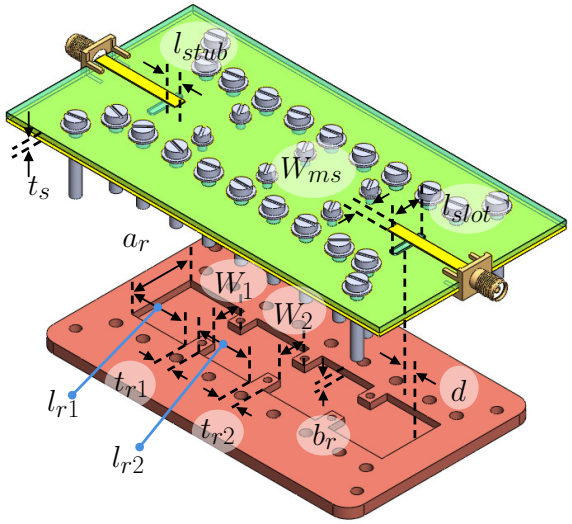

Figure 3.16: Layout of the X-band rectangular Surface-Mount Technology filter. Metallised 3D-printed parts are represented in brown, dielectric material in green, and copper in yellow.

The inverters values of the proposed response for an input/output impedance $Z_s = 50\,\Omega$ are: $\overline{K}_{S,1} = \overline{K}_{4,L} = 0.2143$, $\overline{K}_{1,2} = \overline{K}_{3,4} = 0.0390$, and $\overline{K}_{2,3} = 0.0300$. It corresponds with $Q_{ext} = 34.22$ and the following coupling matrix with $M_{(S,1)} = M_{(L,4)} = 1.035$, $M_{(1,2)} = M_{(3,4)} = 0.911$ and $M_{(2,3)} = 0.700$.

The dimensions of the slot transition were designed following the guidelines of Section 3.3.1.3, and the length of the slot (l_{slot}) was modified to obtain the desired value of external quality factor using the group delay method explained in Section 2.1.1. Similarly, the inter-resonator coupling was determined from the simulated response of two inter-coupled cavities, and it was represented as a function of the iris width (W_{ij}). The curves of Q_{ext} and k_{ij} for the

filter design are presented in Figures 3.17 (a) and (b), respectively.

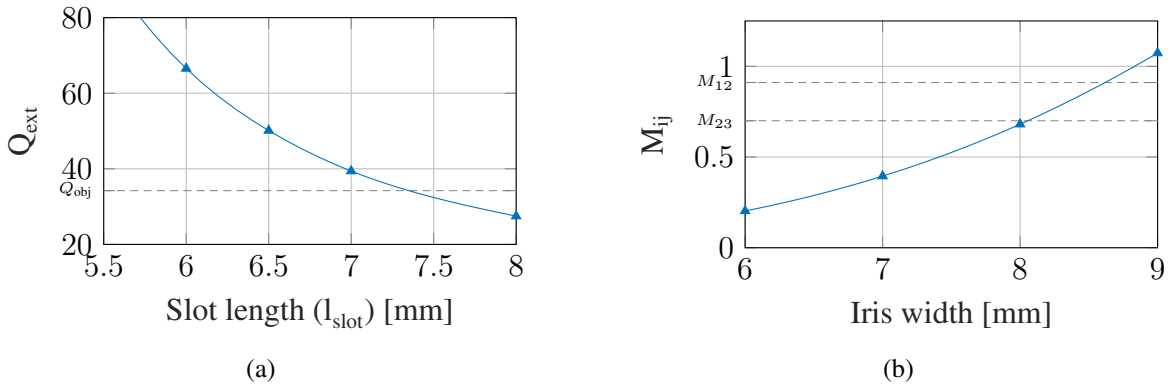

Figure 3.17: Design curves of the X-band rectangular SMT filter: (a) Variation of external Q-factor with respect to slot length (l_{slot}). (b) Coupling as a function of iris width (W_{ij}).

Finally, the complete filter structure was simulated and optimised. The simulated response is shown in Figure 3.18, and their final dimensions are depicted in Table 3.2.

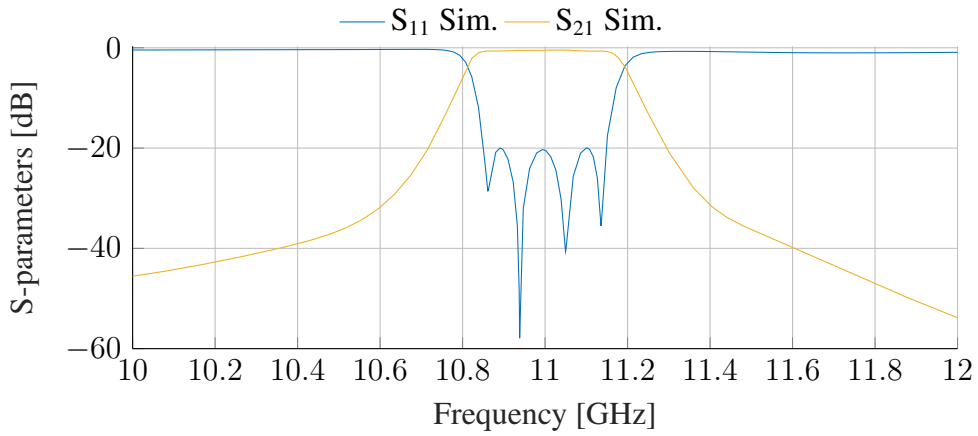

Figure 3.18: Simulated response of the X-band rectangular SMT filter.

Table 3.2: Final dimensions of the X-band rectangular SMT filter.

Parameter	**Dimension** $[\mathrm{mm}]$
a_r	19.05
b_r	2.00
$l_{r1} = l_{r4}$	17.42
$l_{r2} = l_{r3}$	16.88
$t_{r1} = t_{r2}$	4.00
$W_{12} = W_{34}$	8.19
W_{23}	7.75
W_{MSL}	3.25
l_{stub}	3.58
d	2.35
t_{slot}	0.70
l_{slot}	6.95

As shown in Figure 3.16, several holes have been distributed along both parts of the filter for alignment and assembly purposes. These holes have been placed near the centre of the cavities and coupling windows, where the vertical components of the electric currents of the TE_{101} mode are strongest. This arrangement minimises the effect of imperfect contact between parts. Nevertheless, a thin ribbon of indium was placed along the filter perimeter to fill any possible gap.

This filter was manufactured using AM and electroless copper plating techniques. Section 3.2 provides a detailed description of the manufacturing process. Figure 3.19 shows the most representative views of the manufactured part.

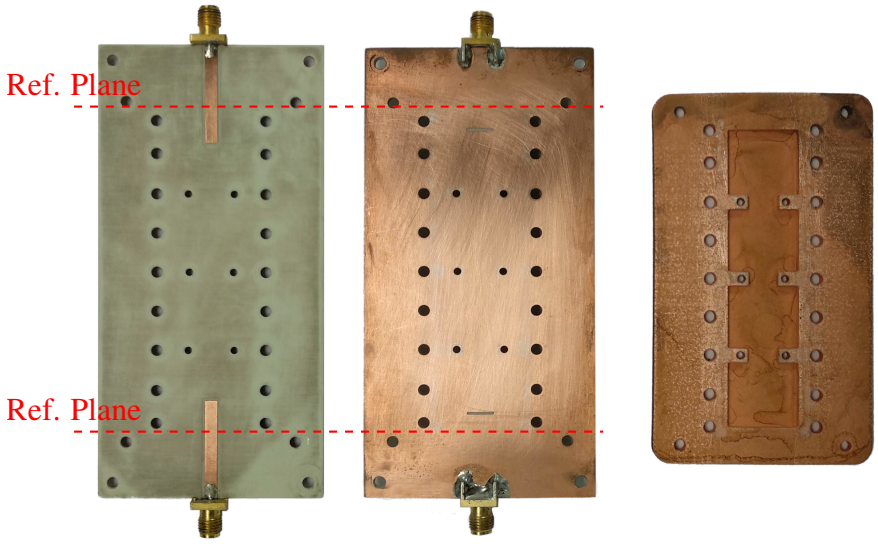

Figure 3.19: Photograph of the manufactured SMT rectangular filter operating at X band. From left to right: top view of the PCB, bottom view of the PCB, and top view of the 3D-printed filter.

Figure 3.20 compares the simulated and measured response of the SMT rectangular filter. Measurements were carried out using a microstrip TRL calibration that compensates for the undesired effects of connectors and feeding lines. The same calibration kit was employed for all the SMT filter realisations of this research.

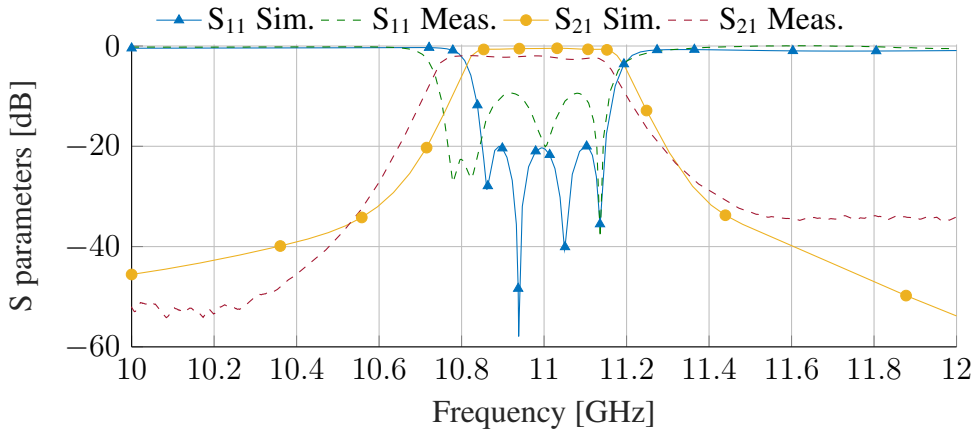

Figure 3.20: Frequency response (simulated and measured) of the SMT rectangular filter operating at X band.

The experimental results of the filter demonstrate noticeable discrepancies compared

to the simulation outcomes. The center frequency exhibits a deviation of approximately $-57.0\,\mathrm{MHz}$ ($-0.4\,\%$), and the $-3\,\mathrm{dB}$ bandwidth shows a variation of $45.3\,\mathrm{MHz}$ ($15.1\,\%$). Moreover, the prototype exhibits an average insertion loss of $2\,\mathrm{dB}$, which is approximately $1.5\,\mathrm{dB}$ higher than the simulated values. These discrepancies in performance are attributed to manufacturing variations that are more pronounced in this specific geometry and a sub-optimal electrical joint between the filter and the PCB. Further details on this matter can be found in Section 3.5.

Figure 3.21 shows the measured response of the filter in a broader bandwidth. The resonance frequency of the second order mode was located at 1.45 times the center frequency. This indicates that no unexpected resonant modes were excited in the microstrip or the waveguide structures. The filter's performance was good and demonstrated its suitability for non-demanding applications.

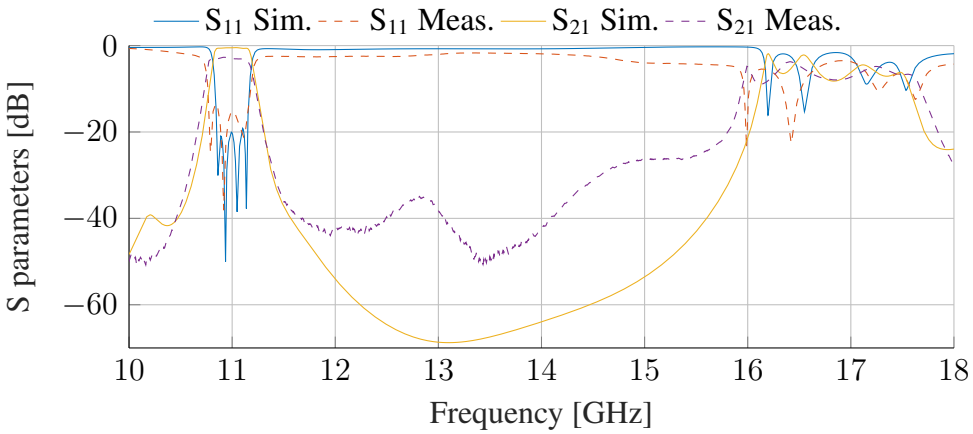

Figure 3.21: Out of band response (simulated and measured) of the SMT rectangular filter operating at X band.

The measured results show a reasonable agreement with simulations, especially if we consider that the geometry of the filter and the employed manufacturing technique ease the integration of tuning elements that can easily compensate for observed deviations. These findings indicate that the filter layout and the developed manufacturing process are appropriate for achieving the desired performance characteristics, and further optimisation could lead to even better outcomes.

3.4.3 Circular SMT (C-SMT) Filter at X Band

In this section, a second SMT Filter is proposed. It is a 4-pole Chebyshev filter with the same filtering response of the previous design, i.e., 11 GHz of center frequency, 300 MHz of bandwidth and 20 dB of in-band return loss. The coupling matrix and the inverter values are unchanged and can be found in the previous filter design.

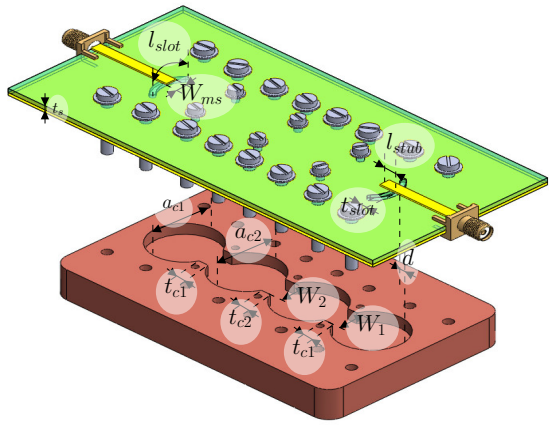

Figure 3.22: Layout of the X-band circular Surface-Mount Technology filter. Metallised 3D-printed parts are represented in brown, dielectric material in green, and copper in yellow.

The filter layout, as depicted in Figure 3.22, consists of four circular cavity resonators with initial dimensions of $a_c = 20.87\,\mathrm{mm}$ in diameter and $b_c = 10.00\,\mathrm{mm}$ in height. The diameter was chosen such that the TM_{010} mode resonates at 11 GHz, and the height was chosen to achieve the highest possible Q-factor while maintaining the broadest SFR using equation 3.6. The cavities are coupled through inductive irises with a thickness of $t_c = 3.00\,\mathrm{mm}$. The filter is coupled to the input/output microstrip through the previously introduced slot transition implemented in a RO4003C substrate with $\varepsilon_R = 3.55$, $t_s = 1.524\,\mathrm{mm}$ thickness, and $17.5\,\mu\mathrm{m}$ of top and bottom copper cladding.

Figures 3.23 (a) and (b) show the design curves for the external quality factor and inter-resonators coupling irises. The optimised dimensions are listed in Table 3.3, and the final filter response is depicted in Figure 3.24.

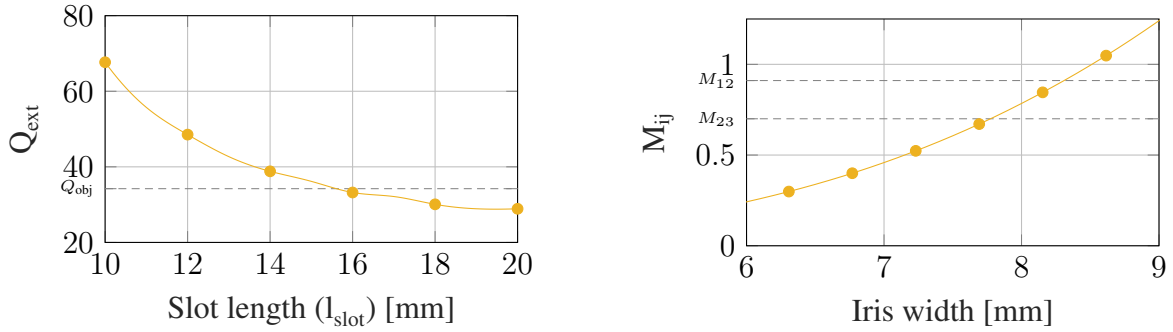

(a) (b)

Figure 3.23: Design curves of the X-band circular SMT filter: (a) Variation of external Q-factor with respect to slot length (l_{slot}). (b) Coupling as a function of iris width (W_{ij}).

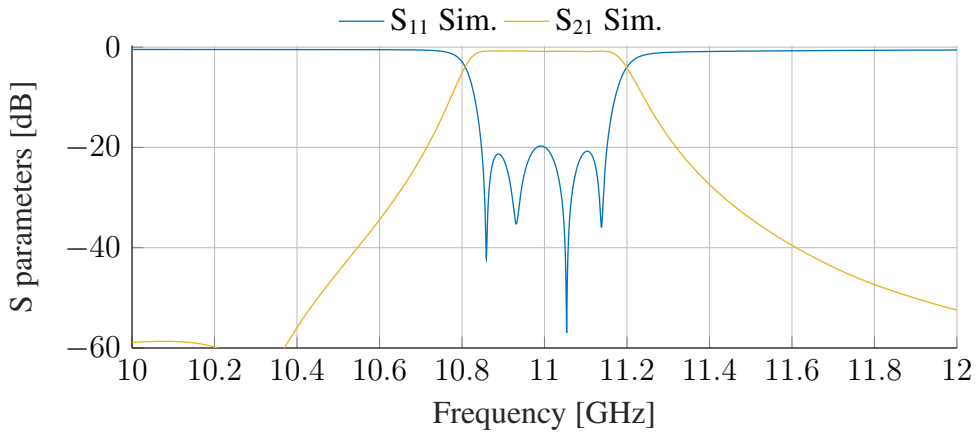

Figure 3.24: Simulated response of the X-band circular SMT filter.

Table 3.3: Final dimensions of the X-band circular SMT filter.

Parameter	**Dimensions** $[\mathrm{mm}]$
b_c	10.00
$a_{c1} = a_{c4}$	20.48
$a_{c2} = a_{c3}$	20.09
$W_{12} = W_{34}$	8.23
W_{23}	7.77
$t_{c1} = t_{c2}$	3.00
W_{MSL}	3.25
l_{stub}	3.95
d	2.5
t_{slot}	0.70
l_{slot}	13.80

Assembling holes were homogeneously distributed along the propagation direction. The filter prototype was additively fabricated with a Form 2 printer, Rigid 10k resin and the metallisation process explained in Section 3.2. Figure 3.25 presents a detailed view of the manufactured prototype. The measured frequency response is compared with simulated data obtained using CST in Figure 3.26. To maintain consistency with the rectangular SMT filter realisation, the same TRL calibration kit was used in this case.

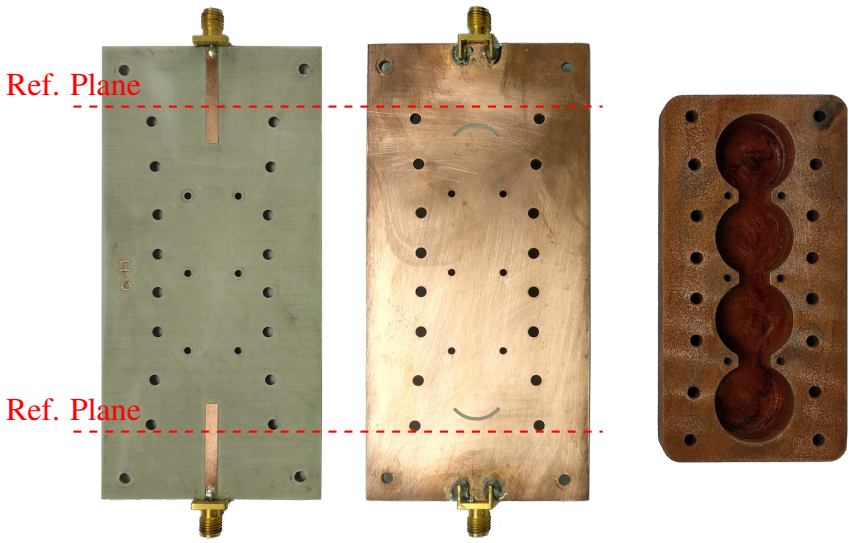

Figure 3.25: Photograph of the manufactured SMT circular filter operating at X band. From left to right: top view of the PCB, bottom view of the PCB, and top view of the 3D-printed filter.

Compared to the rectangular filter, the circular filter exhibits smaller measured deviations. It shows an IL of $1.75\,\mathrm{dB}$, which is only $1.25\,\mathrm{dB}$ higher than the simulated value. The observed frequency shift is minimal, about $-2.2\,\mathrm{MHz}$ ($-0.02\,\%$), and the 3-dB bandwidth deviation is also very small, measuring only $16\,\mathrm{MHz}$ ($4.2\,\%$). These small deviations in the filter response can be attributed to manufacturing tolerances and imperfect joints between the PCB and the filter.

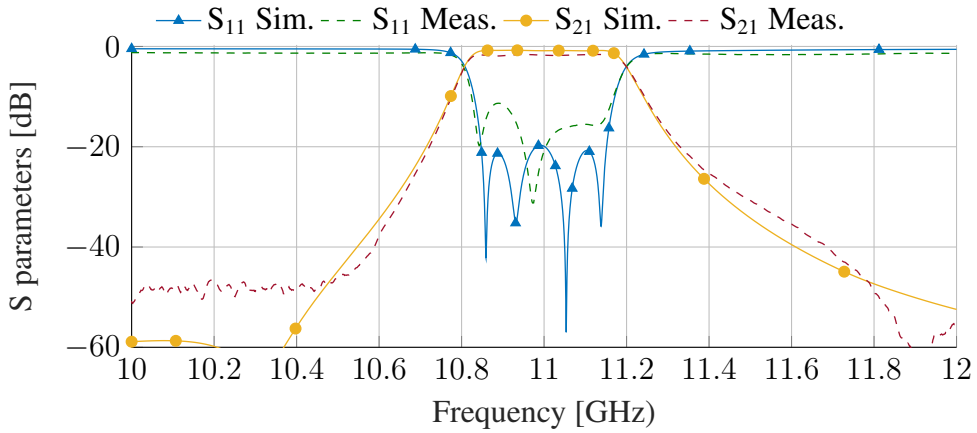

Figure 3.26: Frequency response (simulated and measured) of the SMT circular filter operating at X band.

3.4.4 Circular SMT Filter at C Band

In this section, we present the design of a passband filter for indoor applications of the IEEE 802.11a Wi-Fi standard. The filter is designed with a cross-coupled trisection topology to reject strong interferences from adjacent channels. Refer to Figure 3.27 (a) for the filter layout. The designed filter has a center frequency of $5.25\,\mathrm{GHz}$, a bandwidth of $200\,\mathrm{MHz}$, and $15\,\mathrm{dB}$ of in-band RL.

The proposed filter covers the U-NII-1 and U-NII-2 radio-frequency bands, corresponding to channels 0 to 9 of the IEEE 802.11a standard. The trisection topology allows including a Transmission Zero (TZ) at the upper side of the passband to mitigate the potential interference of the adjacent U-NII-2C band, located from $5.47\,\mathrm{GHz}$ to $5.725\,\mathrm{GHz}$. For this reason, the coupling matrix was optimised to obtain a TZ at $5.492\,\mathrm{GHz}$, resulting in a rejection greater than $30\,\mathrm{dB}$ for the entire U-NII-2C band.

With the given specifications, the required external quality factor and coupling coefficients are $Q_{ext} = 29.364$, $M_{(1,1)} = M_{(3,3)} = 0.075$, $M_{(2,2)} = -0.370$, $M_{(1,2)} = M_{(2,3)} = 0.828$, and $M_{(1,3)} = 0.341$.

$$\begin{pmatrix} 0 & M_{(S,1)} & 0 & 0 & 0 \\ M_{(S,1)} & M_{(1,1)} & M_{(1,2)} & M_{(1,3)} & 0 \\ 0 & M_{(1,2)} & M_{(2,2)} & M_{(2,3)} & 0 \\ 0 & M_{(3,1)} & M_{(2,3)} & M_{(3,3)} & M_{(S,1)} \\ 0 & 0 & 0 & M_{(S,1)} & 0 \end{pmatrix} \tag{3.7}$$

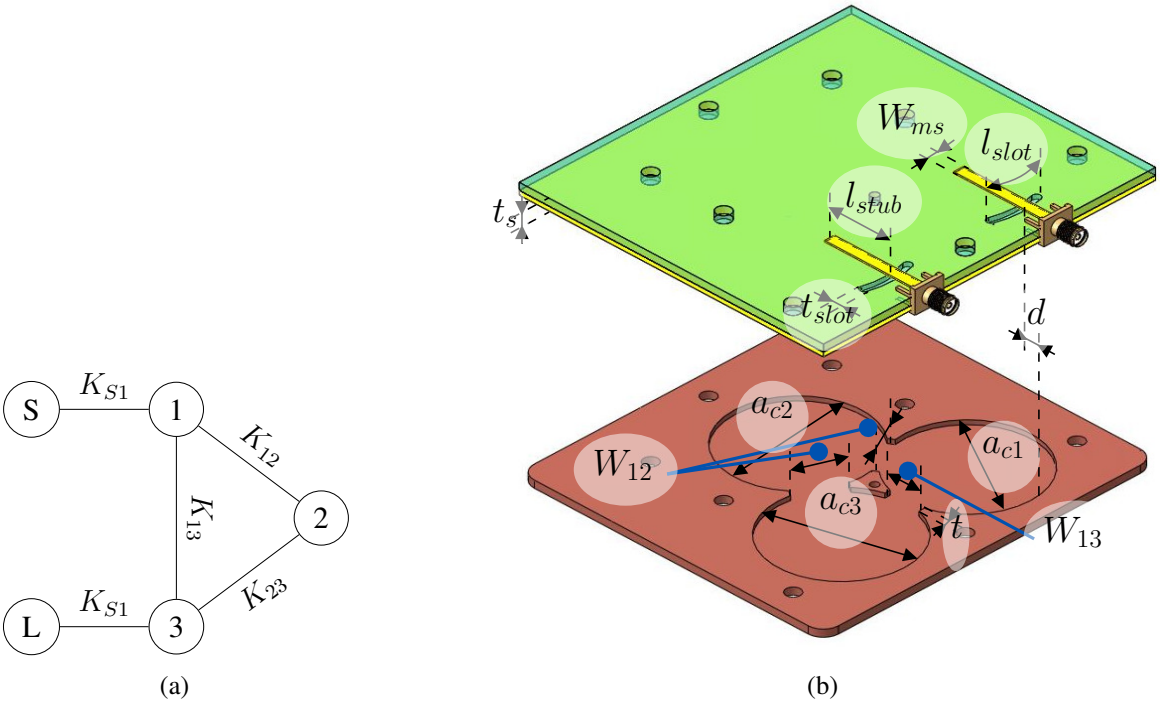

Figure 3.27: (a) Trisection filter topology. (b) Layout of the C-band trisection circular filter in Surface-Mount Technology. Metallised 3D-printed parts are represented in brown, dielectric material in green, and copper in yellow.

The filter is not synchronous due to its asymmetric response, resulting in the following resonant frequencies: $f_{res1} = f_{res3} = 5.242\,\mathrm{GHz}$ and $f_{res2} = 5.286\,\mathrm{GHz}$. For these resonant frequencies, the theoretical diameters of the resonators are $21.88\,\mathrm{mm}$ for the first and third resonators and $21.71\,\mathrm{mm}$ for the second resonator. The cavity height (b_c) was set to $1.524\,\mathrm{mm}$ for comparison purposes with similar filters in the same band [119]. The resonators were inter-coupled through inductive apertures with a thickness of $2\,\mathrm{mm}$. Thinner apertures were selected in this filter realisation as the effect of assembling gaps is not significant at this frequency.

The filter was externally coupled to the same $50\,\Omega$ MSL designed for the other two SMT filters. To achieve the desired external quality factor, the length of the slot was modified, and the other parameters of the slot coupling were kept constant, following the design rules specified in Section 3.3.1.3. Similarly, the width of the irises was adjusted by changing the width of the coupling aperture (W_{ij}) to reach the targeted coupling value (M_{ij}). The design curves are presented in Figures 3.28 (a) and (b).

The optimised dimensions of the filter are listed in Table 3.4, and the final filter response

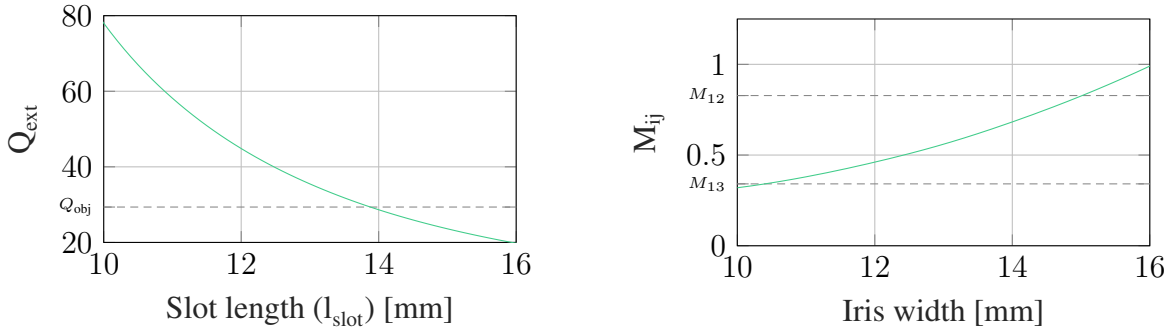

(a) (b)

Figure 3.28: Design curves of the C-band circular SMT filter: (a) Variation of external Q-factor with respect to slot length (l_{slot}). (b) Coupling as a function of iris width (W_{ij}).

is shown in Figure 3.29.

Table 3.4: Final dimensions of the C-band circular SMT filter.

Parameter	**Dimensions** [mm]
b_c	1.53
$a_{c1} = a_{c3}$	41.57
a_{c2}	41.96
$W_{12} = W_{23}$	14.58
W_{13}	11.24
t	2
W_{MSL}	3.25
l_{stub}	8.60
d	3.00
t_{slot}	1.25
l_{slot}	14.27

Figure 3.30 shows the most important views of the manufactured prototype. This filter has been measured using the same TRL calibration kit used for the previous SMT devices. Its frequency response is compared with the simulations in Figure 3.31.

There is a minimal frequency shift due to the manufacturing tolerances of the fabricating process (3D printing, shot blasting and metallisation). Specifically, the frequency deviation is $24\,\mathrm{MHz}$ ($0.46\,\%$), while the shift in the 3-dB bandwidth reaches $13.7\,\mathrm{MHz}$ ($5.10\,\%$). The measured response has an in-band insertion loss of $1.43\,\mathrm{dB}$.

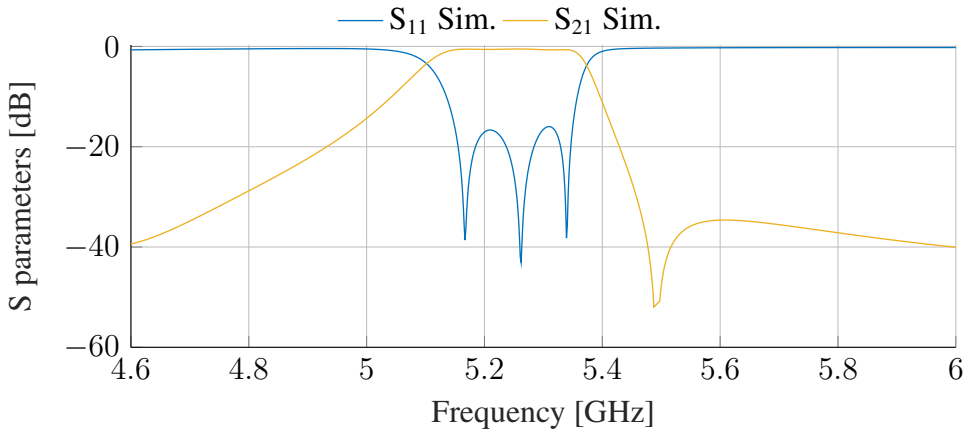

Figure 3.29: Simulated response of the C-band circular SMT filter.

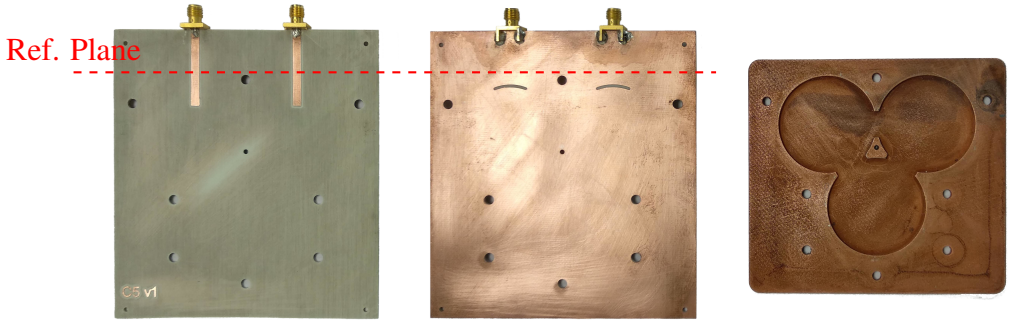

Figure 3.30: Photograph of the manufactured SMT trisection filter operating at C band. From left to right: top view of the PCB, bottom view of the PCB, and top view of the 3D-printed filter.

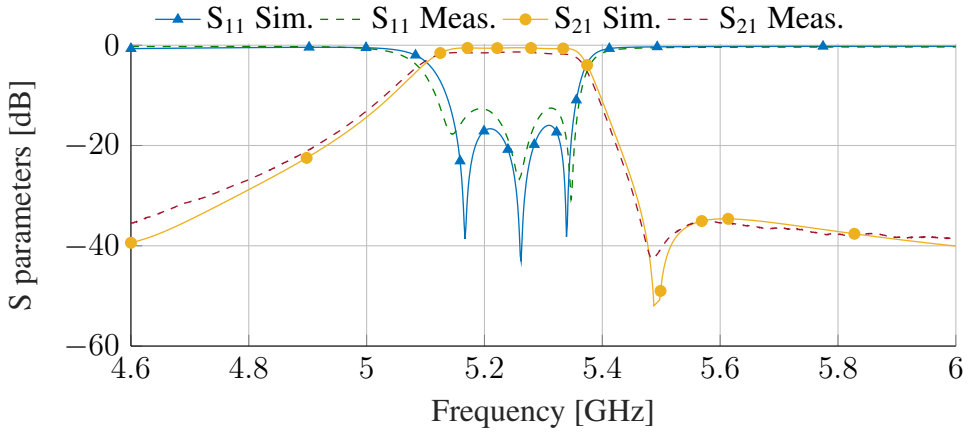

Figure 3.31: Frequency response (simulated and measured) of the SMT trisection filter operating at C band.

3.4.5 Performance Comparison between Prototypes

This section presents a comparison of the measured results for the additively manufactured filters developed in this chapter of the thesis. Table 3.5 summarises the average losses, deviation in center frequency and deviation in $-3\,\mathrm{dB}$ bandwidth of the fabricated prototypes.

Table 3.5: Measured central frequency, bandwidth and insertion loss of additively-manufactured filters.

Prototype	**IL**	f_0	Δf_0	BW_{-3dB}	ΔBW_{-3dB}
WR75 1	$0.29\,\mathrm{dB}$	$10.983\,\mathrm{GHz}$	$-18\,\mathrm{MHz}$ ($-0.16\,\%$)	$391.50\,\mathrm{MHz}$	$5.9\,\mathrm{MHz}$ ($1.53\,\%$)
WR75 2	$0.45\,\mathrm{dB}$	$11.051\,\mathrm{GHz}$	$51.3\,\mathrm{MHz}$ ($0.47\,\%$)	$396.60\,\mathrm{MHz}$	$-16\,\mathrm{MHz}$ ($-4.16\,\%$)
R-SMT (rectangular)	$2\,\mathrm{dB}$	$10.947\,\mathrm{GHz}$	$-57.0\,\mathrm{MHz}$ ($-0.52\,\%$)	$430.30\,\mathrm{MHz}$	$45.3\,\mathrm{MHz}$ ($11.77\,\%$)
C-SMT (Circular)	$1.75\,\mathrm{dB}$	$10.998\,\mathrm{GHz}$	$-2.2\,\mathrm{MHz}$ ($-0.02\,\%$)	$401.00\,\mathrm{MHz}$	$16\,\mathrm{MHz}$ ($4.16\,\%$)
SMT trisection	$1.43\,\mathrm{dB}$	$11.024\,\mathrm{GHz}$	$24\,\mathrm{MHz}$ ($-0.22\,\%$)	$398.7\,\mathrm{MHz}$	$13.7\,\mathrm{MHz}$ ($3.56\,\%$)

The satisfactory results obtained in these filter realisations validate the performance of the manufacturing and assembling approach. The classical rectangular waveguide filters, WR75 realisations 1 and 2, demonstrate lower frequency variation and higher RL within the passband than the SMT realisations. This is because their geometry is less prone to shrinkage deformations that occur during the 3D printing process. Deformations can be more significant for the flatter geometries of the SMT filters, which may explain why the R-SMT and the trisection filter showed higher frequency variation than the C-SMT realisation.

Both realisations of the WR75 filter show low insertion losses (ILs), being very close to the simulated values. However, the SMT filters exhibit higher losses than expected. Specifically, the rectangular filter showed an increase of $1.5\,\mathrm{dB}$ in IL compared to the simulated value. These losses could be attributed to radiation losses resulting from imperfect joints between the filters and the PCBs. Warping deformations resulting from resin shrinkage could have affected this radiation loss, which would explain why flat devices exhibit higher losses. The impact of these unexpected issues on the performance of the filters is further analysed in detail in the following section.

Table 3.6 presents a comparison between the SMT filter realisations and filters from the existing literature, all of which have been manufactured using AM techniques. X-band filter realisations proposed in this thesis exhibit moderate losses that are between those expected by monolithic filters manufactured using SLM and the filters printed with polymeric materials. One significant advantage of our SMT realisations is their significantly lower footprint, comparable only to the multimode realisations [35,45,46]. It is essential to note that our proposed SMT solution facilitates the integration of the filters into planar systems, while other filter realisations may require a waveguide for feeding.

In Table 3.7, we compare the SMT filters with SMT and substrate-integrated filter realisa-

tions from the existing literature. Our filter realisations demonstrate moderate loss values that are between filled and empty substrate-integrated filters and have a similar footprint to empty substrate-integrated structures. The proposed SMT solution allows for easy integration with planar systems, eliminating the need for complex transitions and soldering required by the proposed SIC implementations. Additionally, 3D printing offers unmatched design flexibility and reduces manufacturing costs compared to substrate-integrated circuits, thus breaking free from the design constraints imposed by SIC.

Table 3.6: Comparative analysis of additive manufactured filters and proposed filters in this chapter.

Ref.	**[35]**	**[34]**	**[46]**	**[47]**	**This work**	**This work**	**[45]**	**[37]**	**[38]**	**This work**
Manufacturing technique	SLA	SLA	SLM	SLM	SLA	SLA	SLM	FDM	FDM	SLA
Feeding line	WR90	WR75	WR90	Coaxial	Microstrip	Microstrip	WR112	WR159	Inverted microstrip	Microstrip
SMT assembly	No	No	No	No	Yes	Yes	No	No	No	Yes
Center frequency [GHz]	10	10	11.5	11	11	11	8.23	5.45-5.89	5.45	5.25
FBW [%]	3	5	0.47	1.82	2.73	2.73	5.6	3.93	55	3.8
Filter technology	Spherical Multimode	Spherical monomode	Spherical Multimode	Triangular monomode	Waveguide monomode	Waveguide monomode	Spherical Multimode	Waveguide monomode	Ridge -	Waveguide monomode
IL [dB]	0.25	0.15	1.5	1.75	2	1.43	0.4	2.9-1.6	0.89	1.43
Footprint mm^2	2280	6800*	1500*	3300	1550	1800	4500*	8256	3000*	6500
Height [mm]	31	30*	30*	30	4.5	12.5	31	40.4	5.8*	4

* Estimated values.

Table 3.7: Comparative analysis of substrate-integrated filters and proposed filters in this chapter.

Ref.	**[120]**	**[121] Filt. 1 / Filt. 2**	**[18]**	**[18]**	**This work**	**This work**	**[122]**	**[123]**	**[124]**	**[119]**	**This work**
Manufacturing technique	PCB	PCB	PCB	PCB	SLA	SLA	PCB	PCB CNC	PCB	PCB	SLA
Filter technology	ESIW	Half-mode SIW SIW	ESIW	SIW	Waveguide	Waveguide	SIW	Combline Microstrip	SIW	SIW	Waveguide
Feeding line	Microstrip	Microstrip	Microstrip	Microstrip	Microstrip	Microstrip	Microstrip	Microstrip	Microstrip	CPW	Microstrip
SMT assembly	No	No	No	No	Yes	Yes	No	Yes	No	No	Yes
Center frequency [GHz]	11	9/9	11	11	11	11	8	4	5.8	5.25	5.25
FBW [%]	3	3.9/4.4	2.73	2.73	2.73	2.73	3.35	6.25	2.1	3.8	3.8
Filter order	4	3/3	4	4	4	4	5	6	4	3	3
IL [dB]	2.15	2.13/1.73	0.9	2.5*	2	1.43	2.15	9*	3.2	1.5	1.43
Footprint mm^2	1090*	2570*/2450*	1660*	430*	1550	1800	-	361	1200*	1880*	6500
Height [mm]	2.5*	0.6*/0.6*	4.6	1.5*	4.5	12.5	1*	5	2*	1.5*	4

* Estimated values.

3.5 Manufacturing Issues

3.5.1 Sensitivity Analysis

In general, the SMT filters exhibit a relatively high variation in their electric response due to manufacturing tolerances. These tolerances are associated with various fabrication processes that include PCB milling, 3D printing, copper plating, and part assembling. This section aims to investigate the impact of these manufacturing tolerances on the frequency response of the filters.

To accomplish this, we performed several Monte Carlo (MC) analyses, where the response of each filter was obtained after randomly varying their dimensions. To ensure realistic variations, we treated each dimension as a random variable following a normal distribution. The mean of this distribution was set to the design value of the dimension, and the standard deviation was derived from the associated manufacturing tolerance.

Since the Protomat 103s milling machine from LPKF was used for the PCB milling process, its higher dimensional uncertainty was considered as the standard deviation for the PCB dimensions. The positioning uncertainty of this machine was found to be $\pm 0.02\,\mathrm{mm}$ with a compliance of $95\,\%$. Consequently, a standard deviation of $\sigma = 0.01\,\mathrm{mm}$ was applied for the MC analysis of the PCB dimensions.

For the 3D-printed parts, the accuracy data exposed in the accuracy report of the Form 3 printer from Formlabs [125] was employed. This report observed a standard deviation of $\sigma = 0.03\,\mathrm{mm}$ for details smaller than $9\,\mathrm{mm}$, $\sigma = 0.04\,\mathrm{mm}$ for dimensions between 10 and $20\,\mathrm{mm}$, and $\sigma = 0.055\,\mathrm{mm}$ for dimensions between 30 and $45\,\mathrm{mm}$.

We first conducted an analysis focusing on the deviations observed on the PCBs. 100 simulations were performed varying the value of the most critical dimensions of the PCB of each filter (W_{ms}, l_{stub}, d, t_{slot} and l_{slot}). The result of this study is shown in Figures 3.32.

As can be noticed, the responses of the filters were minimally affected by the expected deviations of the PCB machining. Both circular and rectangular X-band filters exhibited similar frequency deviations, and the circular filter had slightly lower deviations in frequency and IL. This is probably because this particular realisation has thicker and longer coupling slots. The trisection filter was even less sensitive to deviations in PCB milling, as it operates at a lower frequency. The most significant deviation in the frequency response was observed in the RL levels within the bandpass, with a maximum deviation of less than $1\,\mathrm{dB}$ for the X-band filters.

In the second MC analysis, we accounted for the combined impact of deviations in both PCB machining and 3D printing. We conducted 200 simulations, introducing random deviations in the critical dimensions of the filters listed in Tables 3.3, 3.2, and 3.4. The outcomes

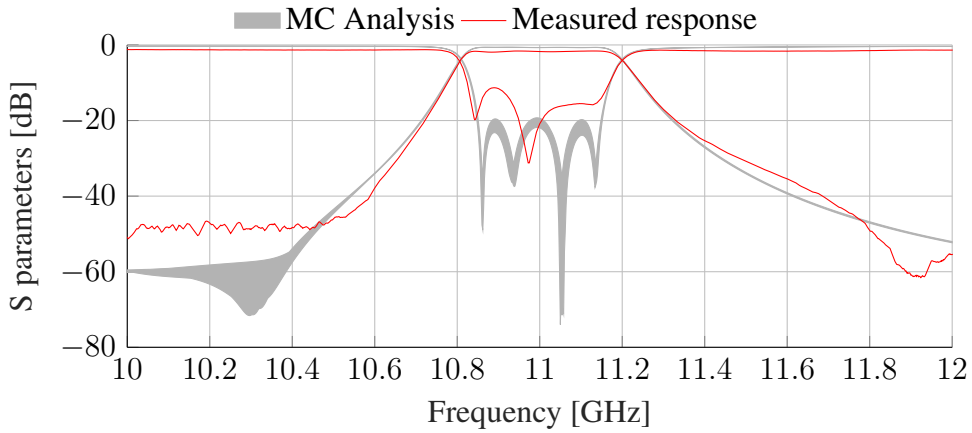

(a)

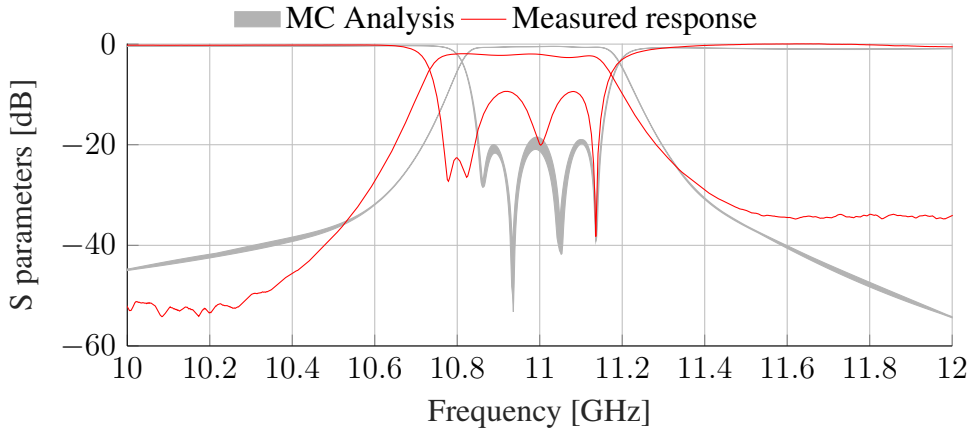

(b)

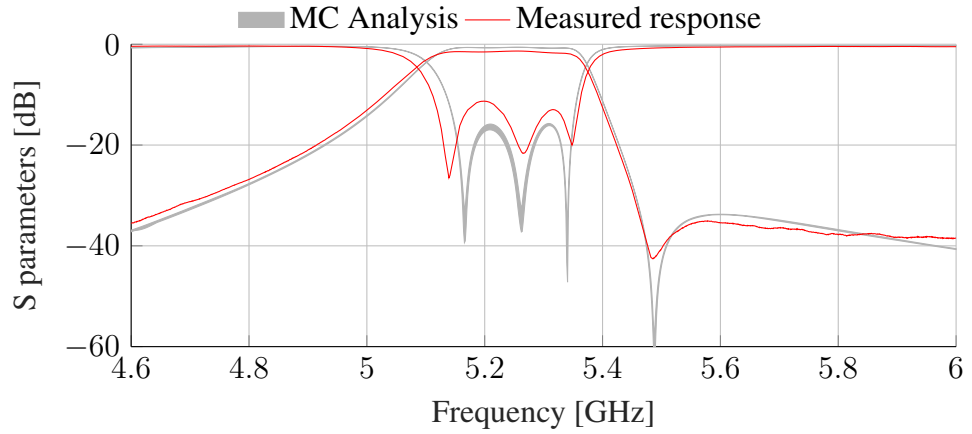

(c)

Figure 3.32: Sensitivity analysis to tolerance deviations of the PCB milling. (a) Circular realisation of the SMT filter. (b) Rectangular realisation of the SMT filter. (c) SMT trisection filter.

of this investigation are depicted in Figure 3.33.

The results indicate that the manufacturing deviations have minimal impact on the electric performance of the filters. The circular, rectangular, and trisection SMT filters exhibited standard deviations of center frequency of $\sigma_{f_0} = 16.8\,\mathrm{MHz}$, $\sigma_{f_0} = 14.1\,\mathrm{MHz}$, and $\sigma_{f_0} = 4.4\,\mathrm{MHz}$, respectively. However, the deviations had a strong effect on the position of the filters' poles, resulting in an increment of the RL levels within the passband.

The analysis has also revealed that the rectangular cavity filter (R-SMT) is technically less sensitive to minor manufacturing deviations than the circular realisation (C-SMT). However, we found a completely different behaviour in the measurements of actual prototypes, where the R-SMT filter exhibited a much higher deviation than the predicted by the MC analyses. This discrepancy could be attributed to the effect of manufacturing deviations that were not considered in the MC analysis, such as warping during printing and the presence of an assembling gap.

A parametric analysis was conducted to investigate the impact of assembling gaps on filters performance. Both X-band filters (R-SMT and C-SMT) were simulated considering a homogeneous gap of thickness ranging from 0 to $50\,\mu\mathrm{m}$. Figures 3.33 (a) and (b) show the simulation results for a gap size of 20 and $40\,\mu\mathrm{m}$. The parametric analysis demonstrated that even a small variation in gap size could result in significant deviations in center frequency, bandwidth, and insertion loss. It also revealed a linear relationship between gap thickness and the deviation observed in many of the considered factors, as shown in Figures 3.34 (a), (b), and (c). The circular filter shown a deviation of $-0.66\,\mathrm{MHz}/\mu\mathrm{m}$ in center frequency, $0.29\,\mathrm{MHz}/\mu\mathrm{m}$ in BW, and $-0.06\,\mathrm{dB}/\mu\mathrm{m}$ in RL. While the deviations observed in the rectangular realisation were systematically higher: $-2.5\,\mathrm{MHz}/\mu\mathrm{m}$ for the center frequency, $0.67\,\mathrm{MHz}/\mu\mathrm{m}$ for the BW, and $-0.13\,\mathrm{dB}/\mu\mathrm{m}$ for the RL.

Figure 3.34 (d) shows the average loss within the bandpass, which is calculated as $1 - (|S_{11}|^2 + |S_{21}|^2)$. As can be noticed, there is an exponential relationship between the loss and gap thickness. However, the radiation loss increases more rapidly in the case of square cavities, where the imperfect joint causes over $55\,\%$ of the total losses for a gap of $40\,\mu\mathrm{m}$. This is in contrast to the circular filter, where radiation loss accounts for only $25\,\%$ of the total losses for the same gap.

In addition, it is noticeable that the assembling gap reduces the out-of-band rejection levels of both filters, but this effect is much more pronounced in the rectangular realisation. This is because the assembling gap acts as a parallel-plate transmission line, increasing parasitic coupling between the input and output feeding lines, as shown in Figure 3.35.

From this, we can conclude that the rectangular filter is more sensitive to the assembling gap than the circular filter, producing a greater mismatch in center frequency and insertion

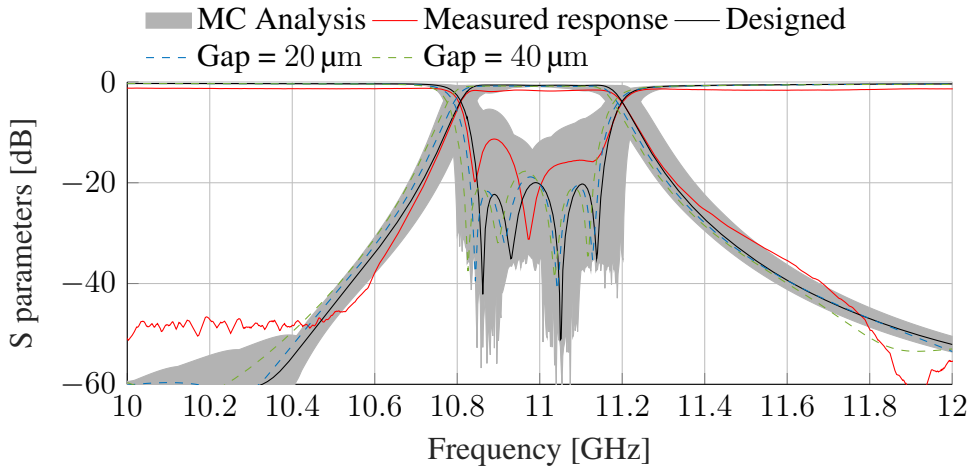

(a)

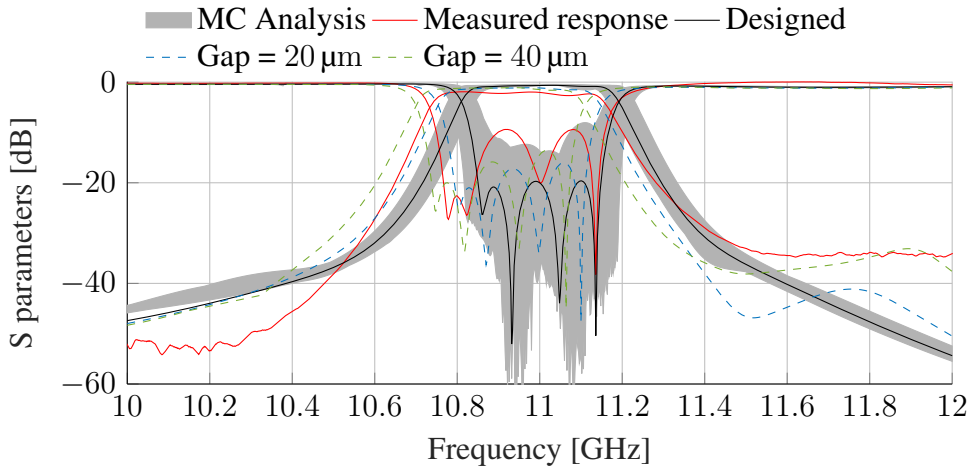

(b)

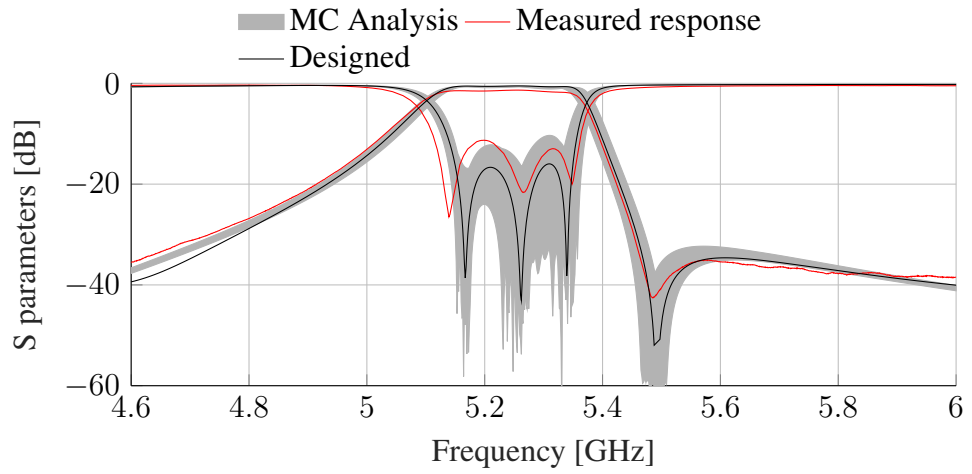

(c)

Figure 3.33: Sensitivity analysis to tolerance deviations of the PCB milling and 3D printing. (a) Circular realisation of the SMT filter. (b) Rectangular realisation of the SMT filter. (c) SMT trisection filter.

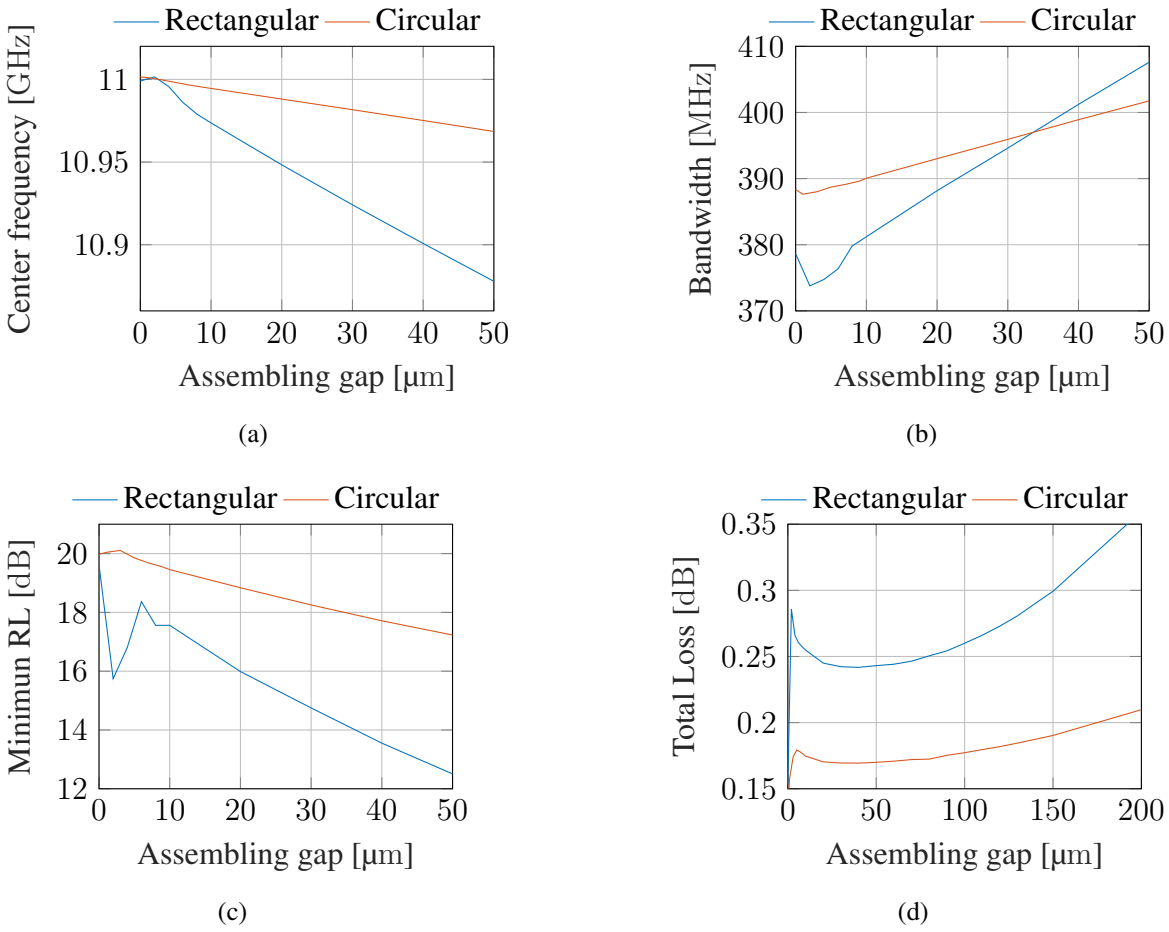

Figure 3.34: Effect of gap between filter and PCB on key filter characteristics. (a) Center frequency (f_0) deviation. (b) Passband bandwidth (BW) deviation. (c) Minimum return loss (RL) deviation within the bandpass. (d) Average insertion loss (IL) deviation within the passband.

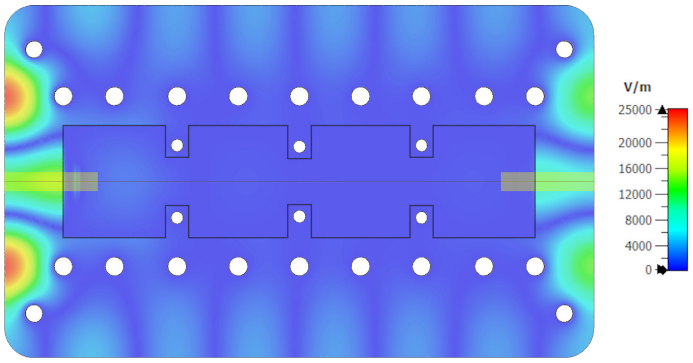

Figure 3.35: Electric field distribution in the gap between the filter and the PCB for the rectangular SMT X-band filter. Simulation performed at 12 GHz for a gap size of 50 μm.

loss. This finding helps to explain why the measured response of the rectangular filter deviates more from predictions compared to the other two filter realisations. Nonetheless, a more comprehensive analysis of the non-considered manufacturing tolerances is given in the following subsections.

3.5.2 Conductivity Analysis

Despite efforts to minimise losses due to assembling gaps, the simulated insertion loss remains lower than the measured values, indicating the presence of unaccounted loss mechanisms. Some of these mechanisms may include oxidation and surface roughness. To precisely assess the performance of the copper deposition, considering the degrading effects of oxidation and roughness, a 3D-printed rectangular cavity resonator was designed and printed.

The cavity resonates at the center frequency of the filters with higher deviation in loss (11 GHz) and operates under the TE_{101} mode. The dimensions of the cavity are a width of $a = 19.05\,\mathrm{mm}$, height of $b = 9.53\,\mathrm{mm}$, and length of $l = 18.46\,\mathrm{mm}$, and it is fed by a WR75 waveguide. The resonator was manufactured using the clamshell strategy to minimise radiation losses resulting from poor electrical connections between parts, as shown in Figure 3.36 (a).

Two resonators were printed under the same conditions as the previously presented filters, including material (Rigid 10K), printing orientation, and post-processing, resulting in similar roughness and oxidation finishing.

One of the fabricated resonators can be seen in Figure 3.36 (b), while Figure 3.37 shows the electric response of both realisations. It is important to note that under-coupled resonators

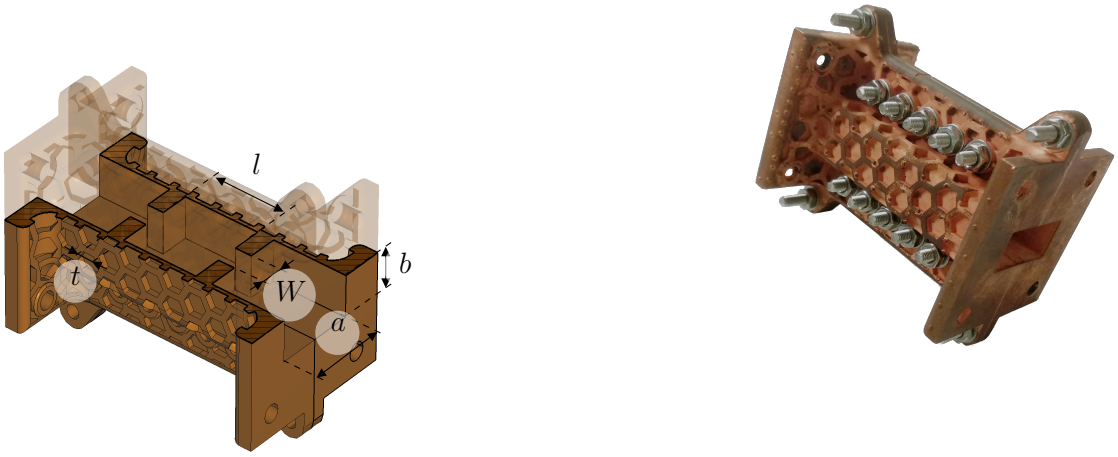

(a) (b)

Figure 3.36: WR75 resonator designed to characterise the electric conductivity of the applied metallisation: (a) layout and (b) photograph of a manufactured device.

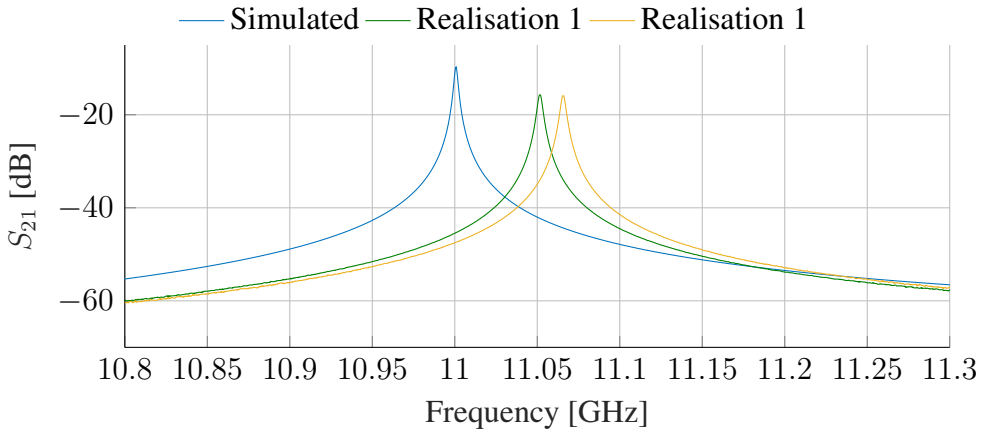

Figure 3.37: Simulated and measured response of the WR75 resonators.

are highly sensitive to manufacturing tolerances, which can lead to significant deviations in measurements of both realisations. However, these deviations in the frequency response have minimal impact on the effective conductivity results.

The effective conductivity of (σ_{eff}) of the copper surface was computed from the quality factor of the resonator. The loaded quality factor (Q_L) was calculated from the measurements using equation 3.8.

$$Q_L = \frac{f_0}{BW_{-3dB}} \tag{3.8}$$

, where f_0 is the resonance frequency and BW_{-3dB} is the $-3\,\mathrm{dB}$ bandwidth.

Subsequently, the unloaded quality factor (Q_u) was determined by using the external quality factor (Q_{ext}), employing equations 3.9 and 3.10.

$$Q_{ext} = \frac{Q_L}{S_{21Max}} \tag{3.9}$$

$$\frac{1}{Q_u} = \frac{1}{Q_L} - \frac{1}{Q_{ext}} \tag{3.10}$$

Then, the surface resistivity can be approximated using the well-known expression of the quality factor for a TE_{101} mode cavity from equation 3.11. Finally, the effective electric conductivity can be derived under the assumption of the good conductor approximation using equation 3.12.

$$R_s = \frac{(kal)^3 b\eta}{Q_u 2\pi^2} \times \frac{1}{2a^3b + 2bl^3 + a^3l + al^3} \tag{3.11}$$

$$\sigma_{eff} = \frac{2\pi f \mu_0}{2R_s^2} \tag{3.12}$$

, where R_s is the surface resistivity, k is the wavenumber, and a, b and l are the cavity's width, height, and length, respectively.

In order to enhance result accuracy, a simulation model was calibrated with the measurement of both resonators. The conductivity of the model was adjusted to align with the measured Q_u. The initial values for the optimisation process were derived from the effective conductivity obtained using equation 3.12. Measured resonance parameters and the corresponding conductivities of the two resonators are detailed in Table 3.8.

Both resonators demonstrate similar conductivity values, with slight variations that might be attributed to differences in oxidation levels and surface roughness. The average effective conductivity of the coating is $17.7\,\mathrm{MS/m}$, which is 4 to 8 times higher than conductivity values reported in similar studies [126, 127], and 20 times higher than the obtained with

Table 3.8: Most important characteristics of the resonators (f_0 and Q_u) along with the associated effective conductivity (σ_{eff}).

Realisation	**Resonance frequency (GHz)**	Q_u	σ_{eff} **from eq. (3.11)** (MS/m)	σ_{eff} **from sim.** (MS/m)
Resonator 1	11.049	3906	17.93	18.55
Resonator 2	11.065	3747	15.67	16.87

binder jetting printed parts infiltrated with copper [48].

3.5.3 Dimensional Analysis of R-SMT Filter

As was depicted in the Monte Carlo (MC) analysis, the measured performance of the rectangular SMT filter realisation (R-SMT) shows a considerable frequency deviation that exceeds the predicted values. Therefore, we conducted a series of dimensional analyses of the filter to identify and understand the cause of these deviations. For the dimensional analysis, three measurements of each filter dimension were taken using a Rown & Sharpe Global C/I 091208ROWN coordinate measuring machine. The results of this analysis and its conclusions are developed below.

3.5.3.1 Erosion of the shot-blasting process

Shot-blasting is an essential step in the metallisation process of SLA resins. This process enhances the surface roughness of the plastic part, creating binding sites for strong adhesion of the copper coating. However, it also removes a thin layer of material, causing the cavities to increase in size and rounding off the sharp corners.

To study the impact of shot blasting on the dimensions of the rectangular SMT filter, we measured its dimensions before and after the process. The resulting erosion was computed as the difference between the dimensions before and after shot-blasting. Results are presented in Figure 3.38.

The analysis revealed that shot-blasting has a different impact on the dimensions of cavities and protrusions (irises). The erosion observed in protrusions is more significant and has a wider variation than that observed in the cavities. It was also observed that cavities on the right-hand side, those with higher n, exhibited systematically higher erosion. This is likely because the filter was placed closer to the blasting jet on its right-hand side.

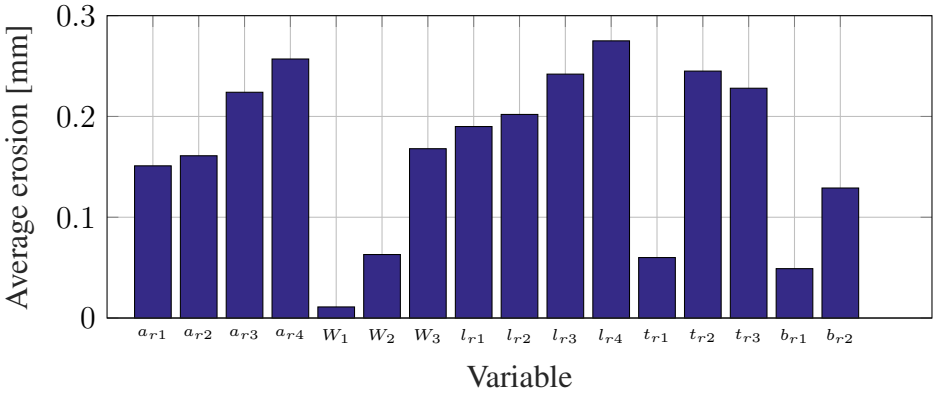

Figure 3.38: Average erosion of the shot blasting: a_n, b_n, and l_{rn} denote the width, height, and length of the nth resonator, while W_n and t_n denote the width and thickness of the iris between the resonator n and n+1.

3.5.3.2 Manufacturing tolerances

A final dimensional analysis was conducted on the metallised filter, which results are included in Table 3.9. The average deviations of the most representative dimensions of the filter are shown in Figure 3.39.

Table 3.9: Results of the dimensional analysis performed on the metallised filter (rectangular SMT filter).

Variable	**Dimension** [mm]	**Variable**	**Dimension** [mm]
a_{r1}	19.177	W_1	8.333
a_{r2}	19.160	W_3	8.367
a_{r3}	19.170	t_{r1}	4.023
a_{r4}	19.143	t_{r2}	4.040
l_{r1}	17.123	t_{r3}	4.037
l_{r4}	17.133	b_{r1}	1.970
l_{r2}	16.500	b_{r2}	2.000
l_{r3}	16.483	b_{r3}	1.977
W_2	7.903	b_{r4}	1.990

Figure 3.39 shows that the error behaviour differs for each of the three axes of the part being studied. For the dimensions arranged in the transverse axis, including the error in width of cavities (a) and iris apertures (W), the deviation is approximately $120\,\mu\mathrm{m}$. Conversely, the dimensions arranged in the longitudinal axis, the length of cavities (l_1 and l_2), exhibit a greater deviation (-0.268 and $-0.352\,\mathrm{mm}$), as well as a more significant variation.

The observed variation in width values can be attributed to multiple factors, including

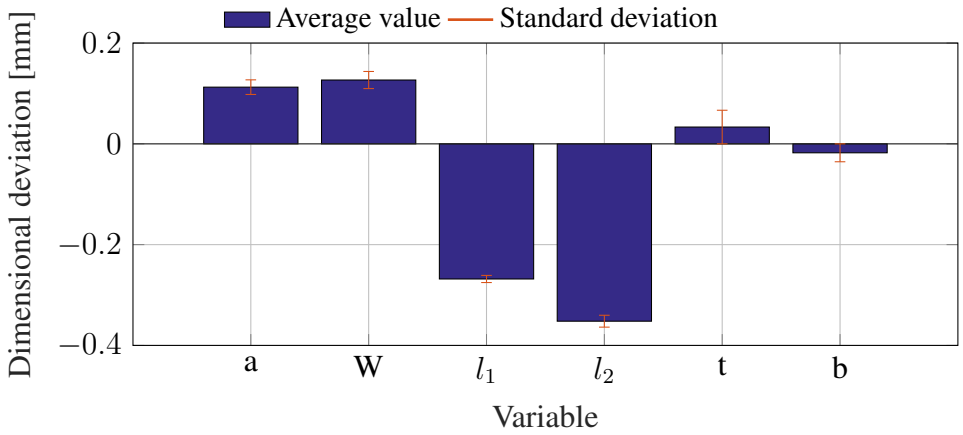

Figure 3.39: Deviation in dimensions of the metallised filter. Here, a and b represent the mean width and height of the filter cavities, W and t denote the mean width and thickness of the irises, l_1 represents the mean length of the first and fourth resonators, and l_2 the mean length of the second and third resonators.

shrinkage, warping, and the effects of shot blasting. However, the greater discrepancy noticed in the length of cavities located in the middle of the part (l_2) compared to the exterior ones (l_1) suggests that warping may be the primary cause of the error. This phenomenon has been reported in similar studies [33, 118], and it's more likely to occur in extremely flat parts like the one being analysed. Figure 3.40 depicts the warping of two flat devices printed with different materials, demonstrating the warping effect.

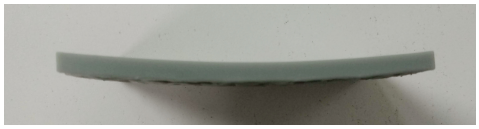

(a)

(b)

Figure 3.40: Warping in rectangular X-band filter prototypes printed with different materials: (a) filter printed with grey resin from Fromlabs, (b) filter printed with Rigid 10K resin from Formlabs. Both filters were manufactured under similar conditions, using a Form 2 printer from Formlabs.

Based on the results obtained in this study, we could conclude that the rectangular SMT filter presents a more significant dimensional deviation than the other filters. This is because its geometry is more prone to deformations. For future studies, this issue could be addressed

by increasing the height of the cavities or the thickness of the reinforcement structure.

3.5.3.3 Impact of manufacturing issues on the filter response

In order to conclude the deviation analysis, a realistic model of the SMT rectangular filter was simulated in CST. This model assumes all the manufactured issues investigated in this section of the thesis. It considers a conductivity of $17.7\,\mathrm{MS/m}$, the dimensions obtained during the dimensional analysis (Table 3.9) and a gap between the PCB and the filtering part of $40\,\mu\mathrm{m}$. This gap was estimated by measuring the thicknesses of the PCB and the 3D printed parts separately and measuring the total thickness of the assembled device. The measurements were conducted using a micrometer screw with an uncertainty of $\pm 2\,\mu\mathrm{m}$. The simulation results can be found in Figure 3.41.

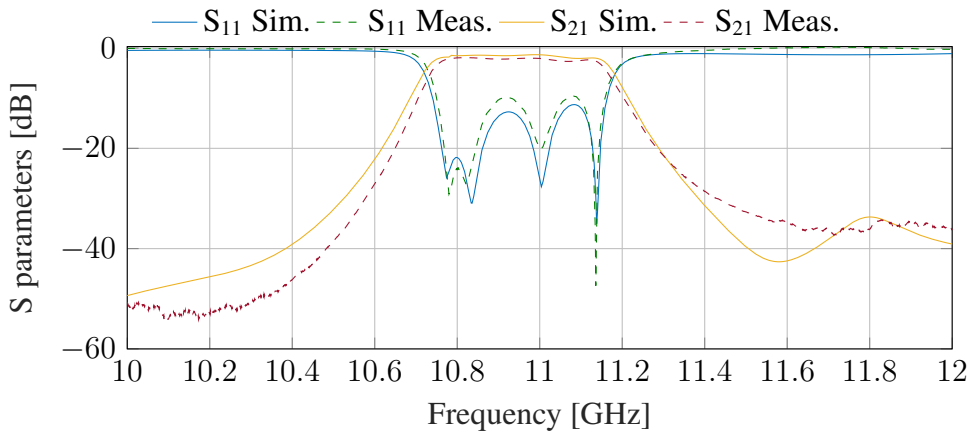

Figure 3.41: Simulation of the realistic model for the SMT rectangular filter. This model includes all the manufacturing issues studied in this section of the thesis, including effective conductivity, printing deviation and deformations, the impact of shot-peening in dimensions and the assembling gap.

The simulation results match well with the measurements, suggesting that warping deformation and imperfect electric contact between the two parts of the structure are responsible for the observed deviations in this particular filter. Additionally, it appears evident that the R-SMT filter prototype is more susceptible to warping deformations due to its highly asymmetric shape, which could explain its higher level of deviations.

3.6 Qualification for Space Applications

Satellites and their payloads are subject to harsh conditions such as extreme temperatures, intense vibrations, and radiation in space. It is crucial that satellites and their equipment

demonstrate proper operation under such conditions. To ensure the reliability of satellites, space agencies and satellite contractors establish a series of tests known as the qualification for space applications. Filters, in particular, must demonstrate their ability to function effectively under extreme vibration, temperature gradients, and high-power operation.

This section will assess the reliability of the additively manufactured filters discussed in the previous section under space conditions. Specifically, we will conduct a qualification for space applications on the WR75 filter developed in Section 2.1.1.2, as well as the rectangular SMT filter (R-SMT) and circular SMT filter (C-SMT) prototypes presented in Section 3.3. The first part of this study will be focused on thermal stability tests, while the second part will cover vibration tests that simulate the extreme vibrations experienced during orbit positioning. Finally, the third part will address the multipactor effect.

3.6.1 Thermal Stability

Temperature tests are essential to validate microwave devices for space applications [89]. These tests evaluate the ability of satellite equipment to withstand the expected temperature ranges that it will experience throughout its operational lifetime. The temperature range of a satellite's payload can vary depending on factors such as orbit, satellite shape, and temperature control system efficiency. Based on the investigations reported in Section 2.2.1, we have determined that filters used in LEO satellites typically operate within a temperature range of --20 to $40\,^{\circ}\mathrm{C}$. However, since the materials used in our filters can withstand more extreme temperatures, we defined a broader temperature range for testing, from -60 to$100\,^{\circ}\mathrm{C}$. This test covers a severe thermal environment that is applicable to higher altitude orbits, such as MEO and GEO. Additionally, to comply with ECSS-E-ST-10-03C, we included measurements at intermediate temperature values, including -60, -40, -20, 0, 20, 40, 60, and $100\,^{\circ}\mathrm{C}$.

3.6.1.1 Theoretical analysis and predictions

Temperature changes can significantly affect the frequency response of filters, sometimes causing them to stop working. However, in most cases, temperature changes only lead to predictable changes in the electrical response of devices. In this study, we investigate the impact of temperature changes on the resonance frequency of filters under study, and propose a theoretical analysis that correlates their center frequency drift with their materials' Coefficient of Thermal Expansion (CTE) that are listed in Table 3.10. The filter deviations were studied as the deviations of one of their resonators, following the approach developed in [128].

Considering the WR75 filter, which is entirely made of Rigid 10K resin, we can assume

Table 3.10: Coefficient of Thermal Expansion (CTE) for the Rigid 10K resin and RO4003C substrate. The horizontal plane of filter and PCB is defined by X-Z axis

Axis	Rigid 10k	RO4003C
X	$41\,\mathrm{ppm/°C}$	$12.5\,\mathrm{ppm/°C}$
Y	$41\,\mathrm{ppm/°C}$	$46\,\mathrm{ppm/°C}$
Z	$41\,\mathrm{ppm/°C}$	$12.5\,\mathrm{ppm/°C}$

a uniform coefficient of thermal expansion of $\delta_{R10K} = 41\,\mathrm{ppm/°C}$ for all spatial directions. Assuming that the devices can expand freely, the deformation caused by a change in temperature $\Delta T = T_2 - T_1$ in the length and width of the rectangular cavities are given by equations 3.13 and 3.14.

$$l^{T_1+\Delta T} = (1 + \delta_{R10K}\Delta T)\, l \tag{3.13}$$

$$a^{T_1+\Delta T} = (1 + \delta_{R10K}\Delta T)\, a \tag{3.14}$$

T_1 represents the reference temperature at which the device was manufactured (reference temperature), and l and a are the length and width of the cavity at the reference temperature. By substituting equations 3.13 and 3.14 into the resonance frequency of the TE_{101} mode of the rectangular cavity, given by equation 3.2, we can derive the new resonance frequency of the cavity for a given temperature change:

$$f_r^{T_1+\Delta T} = \left(\frac{1}{1+\delta_{R10K}\Delta T}\right)\frac{c}{2\pi}\sqrt{\left(\frac{m\pi}{a}\right)^2 + \left(\frac{n\pi}{b}\right)^2 + \left(\frac{p\pi}{l}\right)^2} = \left(\frac{1}{1+\delta_{R10K}\Delta T}\right) f_r^{T_1} \tag{3.15}$$

Then, the frequency drift $\Delta f_r = f_r^{T_2} - f_r^{T_1}$ due to the temperature change can be derived as follows:

$$\Delta f_r = \frac{f_r^{T_1}}{1+\delta_{R10K}\Delta T} - f_r^{T_1} = \frac{-\Delta T \delta_{R10K} f_r}{1+\Delta T\delta_{R10K}} \tag{3.16}$$

And we can define the frequency variation with respect to the temperature change, or temperature drift, as follows:

$$\delta_{f_r} = \frac{\Delta f}{f_r^{T_1}\Delta T} \tag{3.17}$$

Substituting equation 3.16, the temperature drift can finally be expressed as:

$$\delta_{f_r} = \frac{-\delta_{R10K} \cdot 10^6}{(\delta_{R10K}\Delta T + 1)} \quad [\mathrm{ppm/^\circ C}] \tag{3.18}$$

For small CTE, which is the typical case, the denominator of 3.18 is near one, and the frequency drift is approximately the CTE with an opposite sign.

SMT filters are more complex to analyse because the PCB and the 3D-printed part have different Coefficient of Thermal Expansion (CTE) values. The RO4003C substrate used in the PCBs has an average CTE of $\delta_H = 12.5\,\mathrm{ppm/^\circ C}$ for the horizontal plane and $\delta_V = 46\,\mathrm{ppm/^\circ C}$ for the vertical direction. In contrast, the filter body has a uniform CTE of $\delta_{R10K} = 41\,\mathrm{ppm/^\circ C}$. This results in a non-uniform CTE for the SMT filters. As both parts of the filters can not expand freely, a temperature change may result in deformations similar to those observed in bimetal unions. However, we can obtain an equation for the temperature drift of both filters by assuming that screws limit the deformation of the 3D-printed part. In this case, it can be considered that SMT filters would exhibit the CTE of the PCB for the horizontal axes, and the CTE of Rigid 10K for the vertical direction.

With these assumptions, the frequency drift of the C-SMT filter can be derived similarly to the WR75 filter. The change in diameter and length of the circular cavity with a temperature change can be expressed using equations 3.19 and 3.20.

$$a_c^{T_1+\Delta T} = (1 + \delta_H \Delta T)\, a_c \tag{3.19}$$

$$L_c^{T_1+\Delta T} = (1 + \delta_V \Delta T)\, L_c \tag{3.20}$$

, where a_c and L_c are the diameter and length of the cavity at the reference temperature. As the TM_{010} mode of the circular resonator is length-independent, the temperature drift of the resonance frequency can be calculated using equation 3.21.

$$f_r^{T_1+\Delta T} = \left(\frac{1}{1 + \delta_H \Delta T}\right)\left(\frac{c}{2\pi}\frac{2P_{01}}{a_c}\right) = \left(\frac{1}{1 + \delta_H \Delta T}\right) f_r^{T_1} \tag{3.21}$$

Finally, the temperature drift can be derived, obtaining equation 3.22. The expression for the temperature drift is the same for both the C-SMT and WR75 filters, which indicates that the TM_{010} mode of the circular resonator and the TE_{101} mode of the rectangular resonator are equally sensitive to temperature deformation.

$$\delta_{f_r} = \frac{-\delta_H \cdot 10^6}{\delta_H \Delta T + 1} \quad [\text{ppm}/^\circ\text{C}] \tag{3.22}$$

The frequency drift of the R-SMT filter can be derived similarly to the previous one, obtaining precisely the same relationship of the C-SMT realisation, equation 3.22.

Table 3.11 summarises the temperature drifts of the three filter realisations within the test temperature range. The frequency responses of the different realisations are equally sensitive to temperature deformation. However, SMT filters exhibit a lower frequency drift than the WR realisation. This analysis predicts the frequency variation of the filters proposed in this chapter and can be used to develop temperature compensation systems in future analyses.

Table 3.11: Theoretical predictions for frequency drift resulting from a temperature change of $\Delta T = 100 - (-60) = 160\,^\circ\text{C}$.

	WR75	**R-SMT**	**C-SMT**
Dimensions	$a = 19.05\,\text{mm}$ $l = 19.50\,\text{millim}$ $b = 9.53\,\text{mm}$	$a = 19.05\,\text{mm}$ $l = 19.50\,\text{millim}$ $b = 2\,\text{mm}$	$a = 20.87\,\text{mm}$ $l = 10.00\,\text{millim}$
CTE	Uniform $\delta_{R10K} = 41\,\text{ppm}/^\circ\text{C}$	Horizontal plane: $\delta_H = 12.5\,\text{ppm}/^\circ\text{C}$ Vertical direction: $\delta_V = 41\,\text{ppm}/^\circ\text{C}$	Horizontal plane: $\delta_H = 12.5\,\text{ppm}/^\circ\text{C}$ Vertical direction: $\delta_V = 41\,\text{ppm}/^\circ\text{C}$
ΔT	$160\,^\circ\text{C}$	$160\,^\circ\text{C}$	$160\,^\circ\text{C}$
δf_r	$-40.75\,\text{ppm}/^\circ\text{C}$	$-12.48\,\text{ppm}/^\circ\text{C}$	$-12.48\,\text{ppm}/^\circ\text{C}$

After analysing the predictions, it was decided to test only one of the two SMT filters as they have similar temperature drift. The circular design was ultimately selected for testing as it was found to have superior performance.

3.6.1.2 Experimental setup and measurement procedure

The temperature tests were carried out following the technical specifications for testing space engineering systems and devices [89] at the high-power radiofrequency space laboratory of the European Space Agency (ESA)-Valencian Space Consortium (VSC). These tests were conducted under atmospheric pressure, as our investigations developed in Section 4.3.1 shown that there is no significant difference in the thermal response of isolated devices between tests conducted under atmospheric or high-vacuum conditions [95].

The measurement setup for the temperature tests is shown in Figure 3.42 (a). It comprises a temperature chamber (Vötsch VT70010), a Data Acquisition System (DAQ), and a VNA.

One device was tested at a time. The DUT was introduced into the thermal chamber and connected to the VNA, as depicted in Figure 3.42 (b). Several temperature sensors were placed on various areas of the climatic chamber and devices to monitor the temperature of the DUTs. The thermal chamber adjusted the temperature of the DUT to a specific profile, and the response of the devices was measured and stored once the target temperatures were achieved.

Figure 3.42: (a) Measurement setup diagram for vacuum temperature tests. (b) WR75 filter inside the climatic chamber.

The measurement setup was not calibrated before measuring the filters since the properties of the test bench can change with temperature. To address this, the standards of the calibration kits were also submitted to the thermal test, and the resulting measurements were used to calibrate the response of the two devices by following the procedure outlined in [129].

3.6.1.3 Experimental results

Figures 3.43 and 3.44 illustrate the transmission coefficients of both filters at the different temperatures of the test. Figure 3.45 shows the temperature drift in center frequency along with the predicted response. We performed three measurements at $20\,^{\circ}\mathrm{C}$ at the start, middle, and end of the thermal cycle in order. The results revealed a minimal deviation in these measurements, providing evidence of no permanent changes in the devices due to the thermal shock.

The frequency drift of the WR75 filter was inversely proportional to temperature, as expected. This proportion exhibits a linear relationship, with a temperature drift of $-38.67\,\mathrm{ppm}/^{\circ}\mathrm{C}$, which is very similar to the theoretical value of $-40.75\,\mathrm{ppm}/^{\circ}\mathrm{C}$. The predicted deviation in frequency fits very well the measurements except for $-60\,^{\circ}\mathrm{C}$ The insertion loss exhibits an inverse relation with temperature ($-0.0064\,\mathrm{dB}/^{\circ}\mathrm{C}$) as a result of a reduction of the assembling gap. An increase in temperature leads to material expansion,

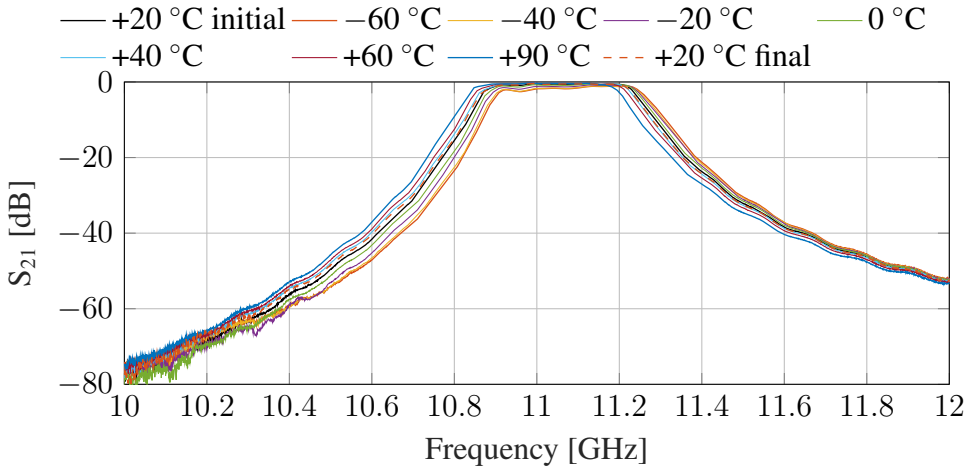

Figure 3.43: WR 75 filter response during the temperature test.

reducing the gap between both parts and, therefore, the associated radiation loss.

Similarly, the C-SMT filter exhibits a temperature drift of $-16.28\,\mathrm{ppm/°C}$, which is slightly higher than the predicted value of $-12.48\,\mathrm{ppm/°C}$. The predicted deviation in frequency, Figure 3.45, fits very well the measured results for low temperatures. Notably, the IL of the SMT filter increased with temperature with a rate of $0.003\,\mathrm{dB/°C}$. This effect may be attributed to a warping deformation produced by the non-homogeneous CTE of the filter. This deformation can result in an increased assembling gap at higher temperatures with the associated increase in radiation loss and reduction of the resonance frequency.

The WR75 and C-SMT filters showed similar behaviour in the evolution of their center frequency and insertion loss with temperature. They both showed an inverse linear relationship between their center frequency and temperature, with values similar to theoretical predictions. It is worth noting that devices behaved excellently and did not show any failure that could affect their performance at any temperature between $-60\,°\mathrm{C}$ and $100\,°\mathrm{C}$.

3.6.2 Vibration Tests

Mechanical vibration tests aim to ensure the integrity of a satellite and its components when subjected to intense mechanical waves or vibrations. Vibrational stress is an inherent aspect of any space application due to the intense vibrations that occur during take-off and orbit positioning.

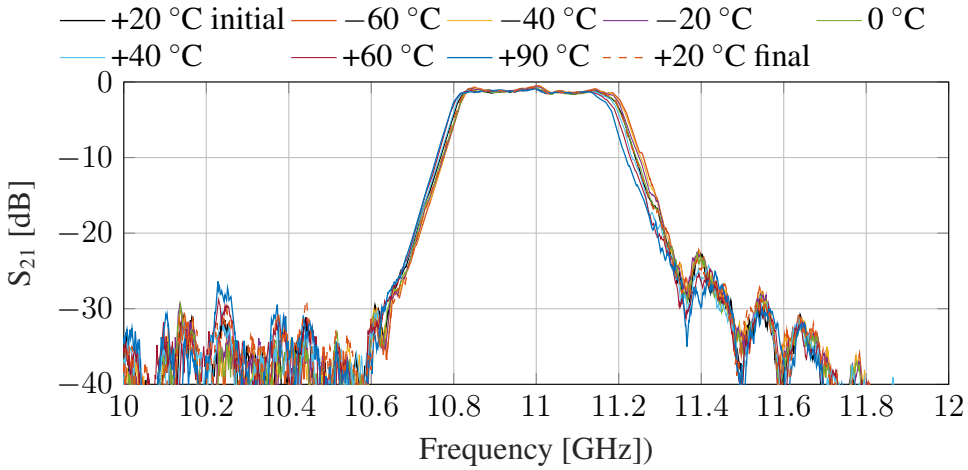

Figure 3.44: C-SMT filter response during the temperature test.

3.6.2.1 General test considerations and test bench

For these filters we considered the WR75, C-SMT, and R-SMT filter prototypes developed for the X Band. The test bench was compliant with the ECSS-E-ST-10-03C standard [89]. Filters were secured to a $25\,\mathrm{mm}$ thick aluminium plate in the same manner they would be fixed in an actual satellite to simulate real working conditions; see Figure 3.46. The dimensions of the vibration plate were chosen specifically to avoid resonances within the frequency range of the tests, and different mounting fixtures were employed at various positions of the plate to assess the filters' performance along their three spatial axes.

The following tools were used for the excitation and measurements:

- Electrodynamics vibration exciter LDS V721: this, combined with a PA1000 amplifier, served as the vibrating bed that transmitted stress waves to the vibration plate and filters.

- Triaxial accelerometer PCB 356A16 ($100\,\mathrm{mV/g}$): this was used to monitor the applied vibration and was placed either on the vibrating bed or on the aluminium plate, depending on the test.

- Ultralight accelerometers PCB 352C22 ($10\,\mathrm{mV/g}$): we placed this precision accelerometer at the centre of each filter to measure their natural frequency. Although this accelerometer has low vibration sensitivity, its weight of $0.5\,\mathrm{g}$ ensures minimal interference with the natural frequency of the DUT.

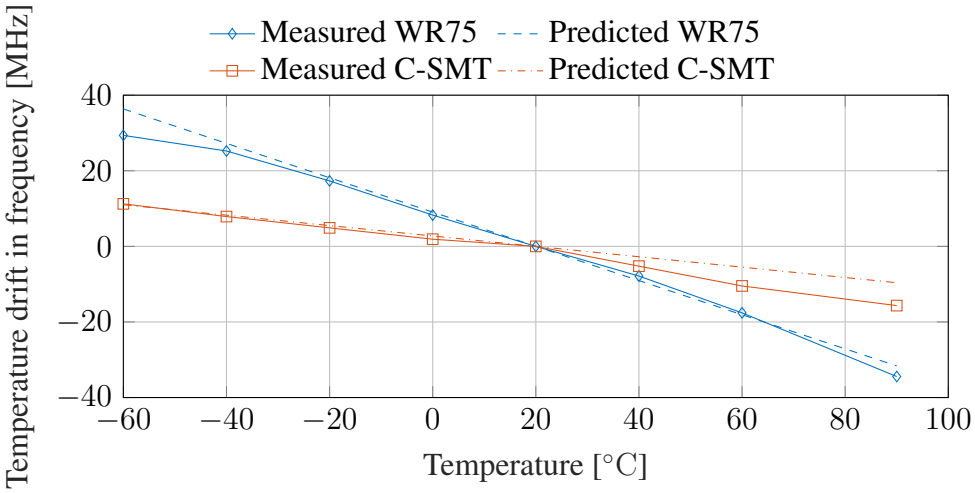

Figure 3.45: Measured and predicted temperature drift for the center frequency of the WR75 and C-SMT filters.

- National Instruments PCI 4451 card for excitation management and measurement in the random vibration test.
- P8020 Analyzer and Prosig DATS 7.0 software for measuring natural frequencies.

3.6.2.2 Sinusoidal sweep test

The sinusoidal sweep test involved applying narrow-band stress waves to the filters. This test simulates the low-frequency vibrations that occur during the atmospheric flight of the space launcher. This test entails applying an incremental and decremental frequency sine vibration to the DUTs. The energy of the applied vibrations should surpass those measured during typical space launcher flights. To this end, we considered the vibration experienced in Ariane 5 and 6, Soyuz, and Vega shuttles and defined the testing ASD accordingly (refer to Figure 3.47).

3.6.2.3 Random vibration test

During the random vibration test, the DUTs are subjected to a pseudo-random vibration signal, which ASD should be above the desired MW. In this test, the MW was designed to cover the specifications of the NASA and measurements of the Ariane and Soyuz launchers, resulting in the ASD depicted in blue in Figures 3.48 (a) and (b).

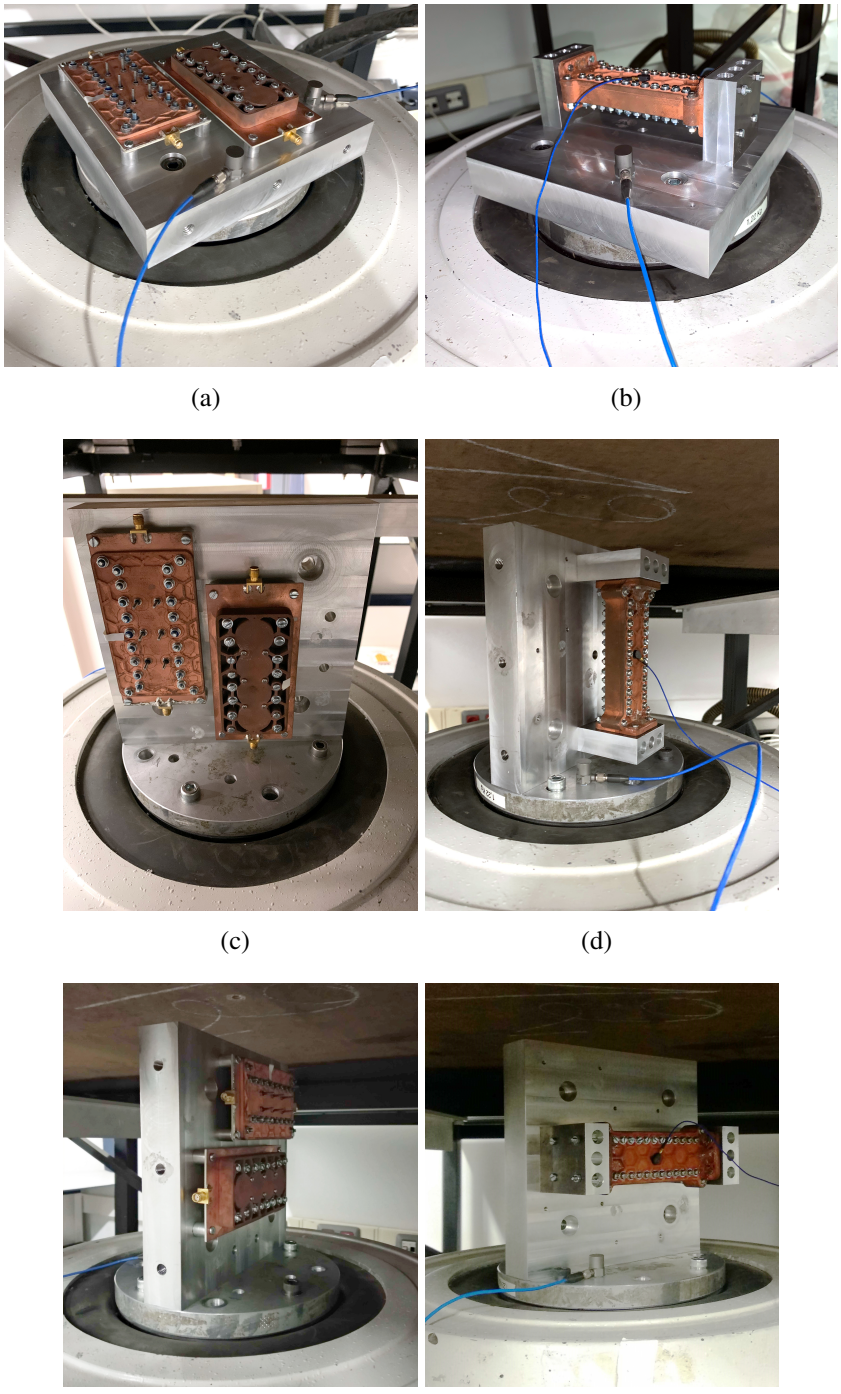

(a) (b)

(c) (d)

(e) (f)

Figure 3.46: Setup for vibration tests: (a) SMT filters on Y-axis measurement configuration, (b) WR75 filter on Y-axis measurement configuration, (c) SMT filters on Z-axis measurement configuration, (d) WR75 filter on Z-axis measurement configuration, (e) SMT filters on X-axis measurement configuration, (f) WR75 filter on X-axis measurement configuration.

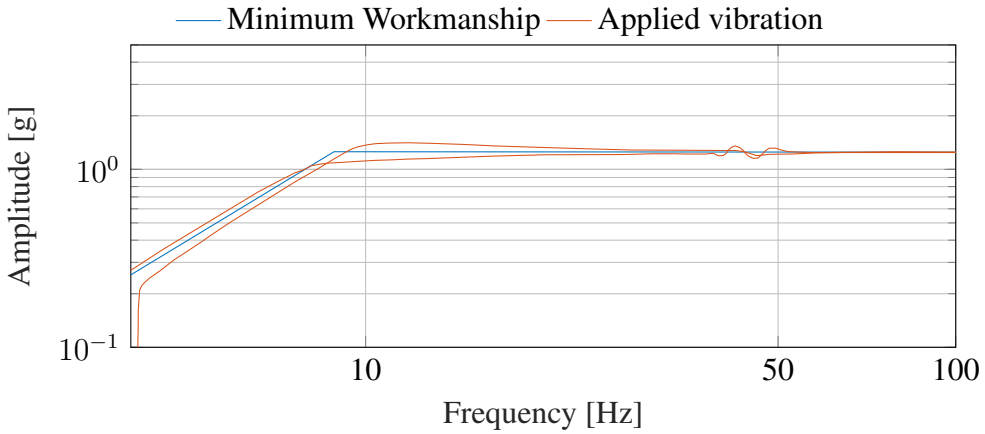

Figure 3.47: Amplitude spectral density of vibration measured during the sinusoidal sweep test.

WR75, R-SMT, and C-SMT filters underwent the vibration test along their three axes. The duration of the applied vibration was $2\,\mathrm{min}$ for each axis, and the root mean square power value was $7.5\,\mathrm{g}$. The power of the applied vibration was monitored during the test by recording the acceleration of the vibrating plate. The results are shown in Figures 3.48 (a) and (b).

During the tests of both SMT filters, the applied vibration was consistently above the minimum workmanship, and no resonances were detected in the measurement setup. However, resonances above $1000\,\mathrm{Hz}$ were observed during tests of the WR75 filter for the X and Z axes. These resonances are probably due to the aluminium supports that hold the device. Nonetheless, it was concluded that these specific resonances did not significantly impact the test, and the results were still valid despite them.

3.6.2.4 Experimental results

The resonant mode is a crucial parameter that represents the structural integrity of the DUT. The ECSS-E-ST-10-03C standard uses this factor as an indicator of test failure, setting a maximum deviation in the natural frequency of $5\,\%$ in frequency and $20\,\%$ in amplitude. In our case, the first mechanical resonant mode of the filters was characterised before and after undergoing both tests, providing an inherent safety margin to the standard, as the variation is due to two vibration tests and not only one.

Table 3.12 compares the natural frequency and amplitudes of the mechanical resonant mode of the three filters. As can be noticed, none of the filters experienced variations greater than the established limits. The C-SMT filter showed a variation in the amplitude of the resonant mode close to the limit. However, as this filter had to be disassembled to perform

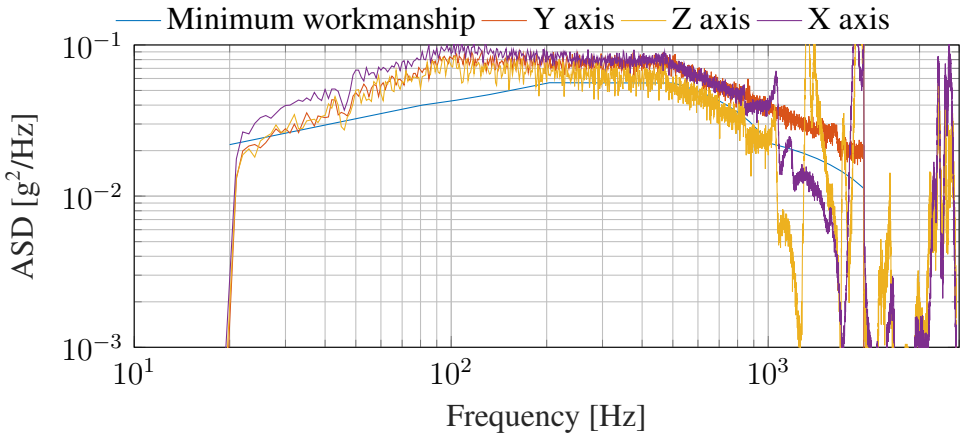

(a)

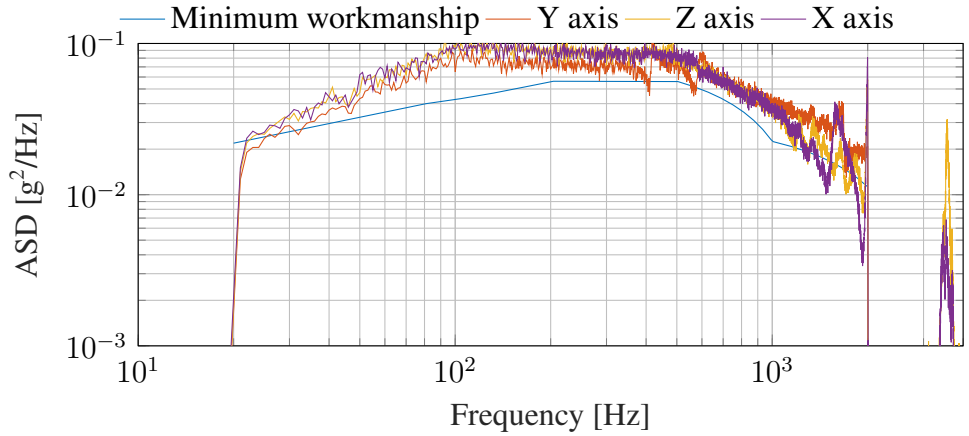

(b)

Figure 3.48: Amplitude spectral density of vibration measured during the random vibration test of the: (a) WR75 filter and (b) SMT filters.

the tests in the different axes, the variation was likely due to a change in the tightening torque of the fixing screws rather than a critical change in the integrity of the device.

The frequency response of each filter was measured before and after the vibration tests using two TRL calibration kits, eliminating the effect of connectors and feeding lines. The resulting measurements are presented in Figures 3.49 (a), (b), and (c). No significant changes were observed in any filter response, and minor deviations could be attributed to a repetition of the measurement rather than the effect of the vibration tests.

In conclusion, the vibration tests performed on the three filters demonstrate that they can successfully withstand the mechanical disturbances generated by the most widely used space shuttles. The frequency response measurements also indicated that the different vibrations

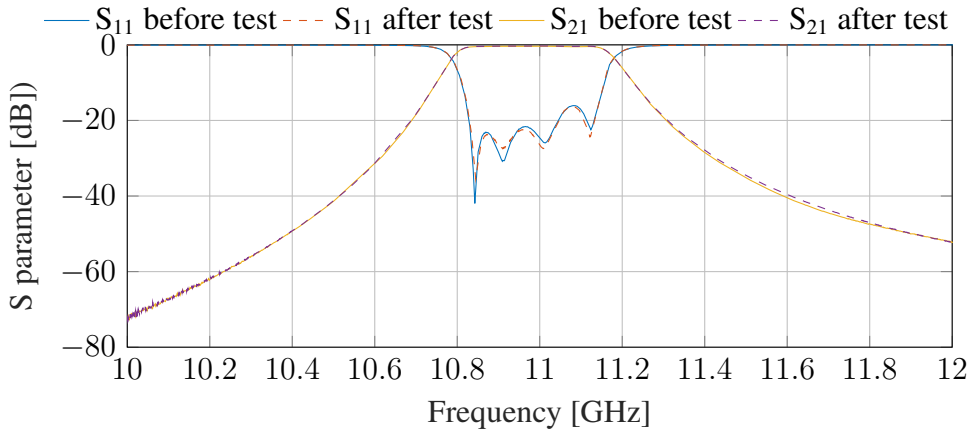

(a)

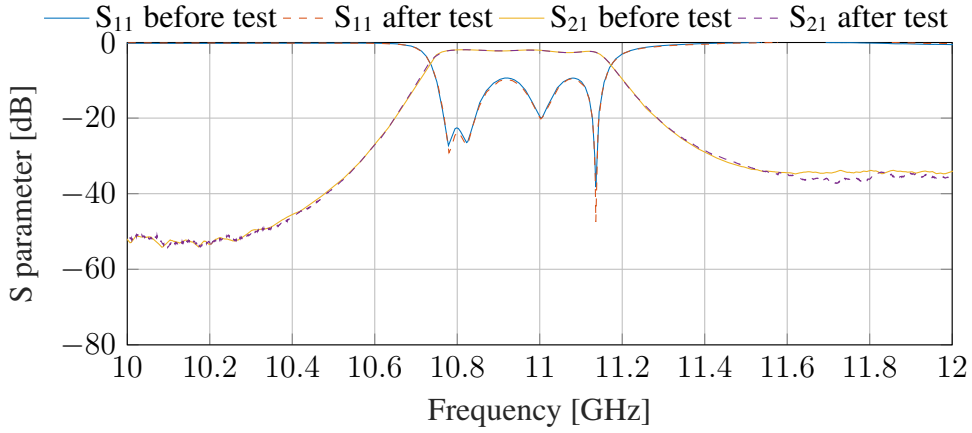

(b)

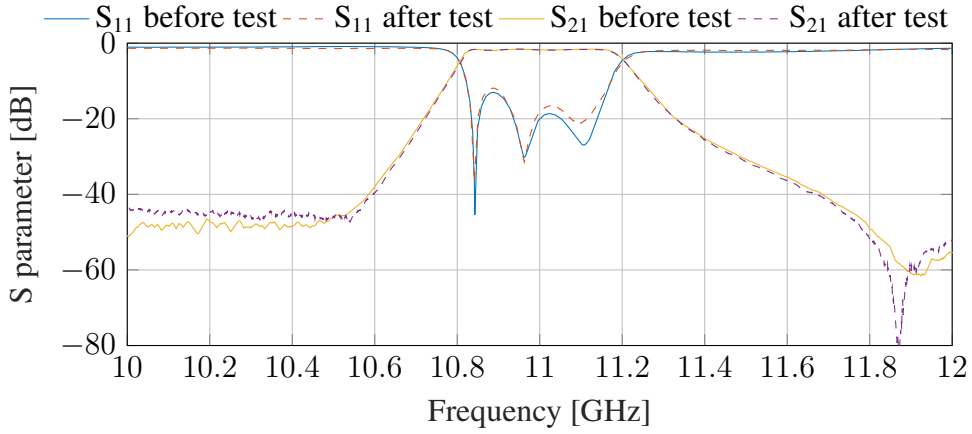

(c)

Figure 3.49: Frequency response of the filters under study before and after the vibration tests: (a) WR75 filter, (b) R-SMT filter, and (c) C-SMT filter.

Table 3.12: Natural frequency variations of filters after sinusoidal and random vibration tests.

Filter	Natural Frequency (Hz)	Δf (%)	Amplitude	ΔAmp. (%)
R-SMT	433-432	-0.2	223.4-235.6	5.5
C-SMT	615-621	1.0	198.2-170.0	-14.2
WR75	1772-1768	-0.2	220.5-202.5	-8.2

did not affect the filters' performance, demonstrating their suitability for space applications.

3.6.3 Multipactor

The Multipactor phenomenon is a discharge of electrons that occurs in RF devices that operate with high-power RF signals under low-pressure conditions. In such situations, a cluster of free electrons can resonate with the RF field, causing a self-stimulated growth in the electron population. This phenomenon can lead to effects, including increased electric noise, extreme heating, and the creation of virtual shorts that can cause undesired reflections. Since this phenomenon is potentially destructive, its prediction and testing are paramount to ensure the correct operation of the satellite throughout its lifetime.

In this section, we will predict and test the multipactor power threshold of two filters based on rectangular cavities: the WR75 and R-SMT. To achieve this, we will begin by studying the properties of the novel materials used in our filters. Subsequently, we will investigate the power distribution in both filters to predict the power required to trigger the multipactor discharge. Finally, the predictions will be verified by conducting an actual multipactor test campaign.

3.6.3.1 Thermo gravimetric analysis

As the multipactor effect occurs under high vacuum conditions, the materials used in the proposed devices need to prove their viability to work under this specific condition. The most important concerns when working under high vacuum conditions is the release of volatile species as they can condense in different places, causing unwanted contamination of sensitive equipment. Moreover, the presence of gas in an area that is likely to initiate a multipactor discharge can transform this phenomenon into an even more harmful corona discharge that can destroy the devices [130].

To determine whether the Rigid 10K resin used in our filters can release contaminating gases, we performed a Thermogravimetric Analysis (TGA). This test quantifies the generation of volatile species when a material is heated to a specific temperature. For this test, we first preconditioned two samples of Rigid 10K resin at room temperature with a relative

humidity of $55 \pm 5\,\%$ for $72\,\mathrm{h}$. The purpose of this conditioning is to achieve a consistent moisture level in the samples, allowing us to determine the portion of the mass lost during the test that is attributed to moisture loss. Then, the TGA was conducted in a nitrogen atmosphere to avoid moisture accumulation. The test consists in heating the piece at $125\,^{\circ}\mathrm{C}$ for a certain period of time, while the weight of the samples is continuously monitored. The temperature was held constant at $125\,^{\circ}\mathrm{C}$ until the mass loss stabilized, which took approximately $90\,\mathrm{min}$.

The results of this test are shown in Figure 3.50. Both samples lost a small amount of mass of approximately $0.11\,\%$ during the first few minutes of the test. Then, as the temperature exceeded $100\,^{\circ}\mathrm{C}$, the mass rapidly decreased until reaching a steady state, resulting in a total mass loss of approximately the $0.4\,\%$.

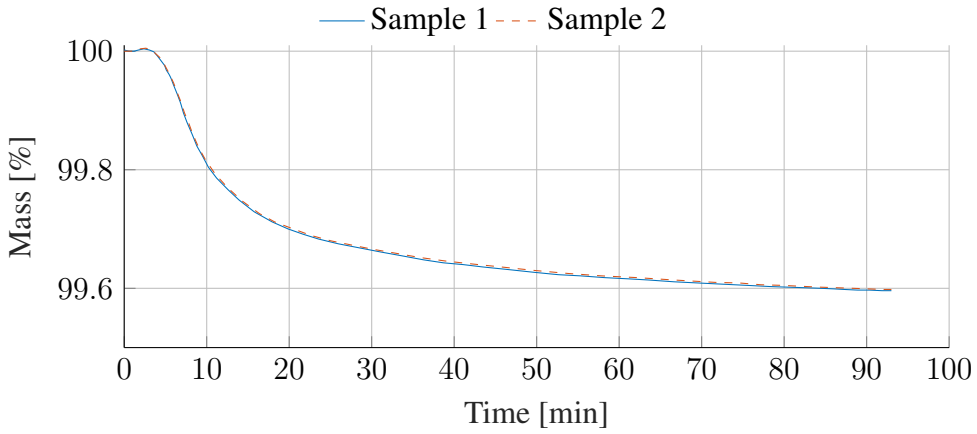

Figure 3.50: Mass loss during Thermogravimetric Analysis (TGA) of two Rigid 10K resin samples. The samples underwent typical postprocessing: UV curing and thermal treatment.

The mass loss experienced by both samples during the TGA was significantly below the $1\,\%$ limit established by the ECSS-Q-ST-70-02C standard [131]. Additionally, after a final conditioning at a controlled humidity level, both samples regained the same amount of mass lost during the test. This suggests that the loss was caused by moisture evaporation rather than by the evaporation of the resin itself. The ECSS-Q-ST-70-02C standard indicates that water vapour is not a significant concern for vacuum instruments as it can be prevented through proper drying. In light of the results obtained, we can confirm that Rigid 10k resin is suitable for high vacuum environments.

3.6.3.2 Secondary emission yield measurement

Multipactor is a complex phenomenon that strongly depends on the SEE property of the surfaces involved in the electron resonance. This effect is challenging to characterise as it

exhibits a random nature that depends on several factors, such as the material of the surface, its roughness, and the presence of impurities. This means that Secondary Emission Yield (SEY) curves for standard materials cannot be generally applied to specific devices, and it is highly recommended to measure the SEY of the specific materials of the devices under test [132].

Filters used in the experiment have a uniform height and the TE_{101} mode exhibits a vertical electric field polarisation. This makes that free electrons in the device are accelerated toward the top and bottom surfaces of the filters, interacting with the copper deposition of the plated Rigid 10K resin and the copper ground plane of the RO4003C substrate. Thus, the SEY study was focused on the different surface finishing of these materials, resulting in the study of the following samples:

- A sample of RO4003C substrate with a standard $18\,\mu\mathrm{m}$ electro-deposited copper cladding.
- A sample of RO4003C substrate with the standard electro-deposited coating that underwent an additional copper electro-deposition in our facilities.
- A sample of Rigid 10K resin with a first electroless copper deposition.
- A sample of Rigid 10K with the first electroless copper cladding and the additional electro-deposited cladding applied in our facilities.

The SEY samples were produced following the same processes employed for the filters under study so that they represent their surfaces accurately. The SEY measurements were performed in the European high power space materials laboratory of VSC-ESA. Figure 3.51 shows the obtained results.

It is important to note that the SEY curves of the different samples are considerably higher than the SEY of oxygen-free copper proposed in the ECSS-E-20-01 standard for multipactor prediction and testing, which underlines the importance of characterising this factor for the specific surfaces of each DUT. These results will be employed in the following sections for predicting the multipactor power threshold.

3.6.3.3 Filter analysis and redesign

Observing the SEY results of Figure 3.51, it is expected that the mutipactor power threshold of the R-SMT filter exceeds the average power handling capacity of standard end-launch connectors. This presented a potential issue, as the connectors could overheat or initiate a multipactor discharge during the test run. Moreover, the multipactor prediction needs to be

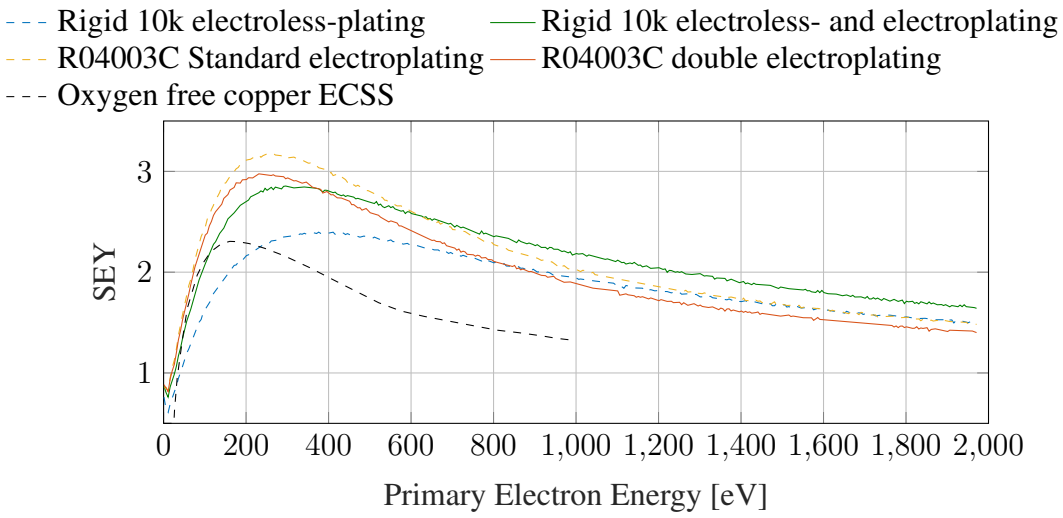

Figure 3.51: SEY curves of the materials under test for a normal incident angle of the primary electrons. The SEY curve of standard oxygen-free copper is also depicted.

done on the final design, as it involves several time-consuming numerical analyses. Consequently, it was decided to develop a representative model of the R-SMT filter specifically for testing purposes.

In the multipactor model of the R-SMT filter, henceforth known as the low-profile filter, the slot coupling was replaced with an input/output coupling iris. This iris is fed by a WR75 waveguide through a broadband transition. The height of this new filter is the same as the SMT prototype, and a PCB cover was designed to shield the critical areas for multipactor discharge. This design replicates the multipactor conditions of the SMT design without the power limitations imposed by coaxial connectors. Furthermore, because the same guiding structure feeds both the low-profile and the WR75 filters, the same test bench can be utilised for both filters. Figure 3.52 (a) and (b) illustrate the proposed filter's structure and the manufactured prototype.

The broadband transition of the low-profile filter was designed as a three-stage Chebyshev matching transformer of third order by following the designing procedure described in [64]. It consists of three waveguide sections whose heights and lengths have been optimised to achieve an RL of $40\,\mathrm{dB}$ within the filter passband. Figure 3.53 presents the simulated response of the back-to-back transition.

The PCB cover of the filter was designed with venting holes to ensure proper venting, reducing the risk of corona discharge during multipactor testing. Additionally, electron seeding areas were included to facilitate the penetration of high-power electrons into the cavities of the filter, simulating the presence of free electrons in space components. These features

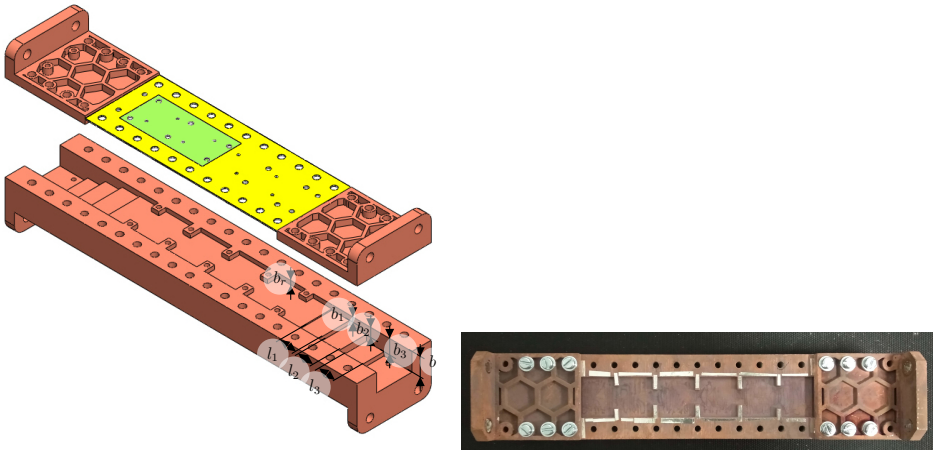

(a) (b)

Figure 3.52: Low-profile filter for multipactor testing. (a) Layout and assembling. Metallised 3D-printed parts are represented in brown, dielectric material in green, and copper in yellow. (b) Photograph of the manufactured device.

streamlined multipactor testing, significantly reducing testing time and cost. The final dimensions of the low-profile filter are listed in Table 3.13, and Figure 3.54 shows the frequency response of the manufactured prototype. As with other filter realisations, a ribbon of indium was used around the perimeter of the filter to improve the electrical connection at the junction between the filter body and the cover.

3.6.3.4 Multipactor prediction analysis

Multipactor analysis involves three main steps — first, identifying the critical frequencies and regions, which are the regions and frequencies of the device in which the multipactor discharge is most likely to occur with the lowest input power — second, estimating the worst-case multipactor power using a simple model—and finally, determining an accurate power threshold for the critical frequency.

As the Multipactor phenomenon is more likely to appear in small gaps with high field strength, one way to find the critical regions and frequencies is to numerically obtain the electric field distribution of the devices at different frequencies. This method is easy but computationally intensive and time-consuming, requiring multiple simulations.

An alternative and faster method to determine critical frequencies and areas is to analyse the TASE of individual filter resonators. The TASE describes how the electric and magnetic energies are distributed across different resonators. For filters with a homogeneous multi-

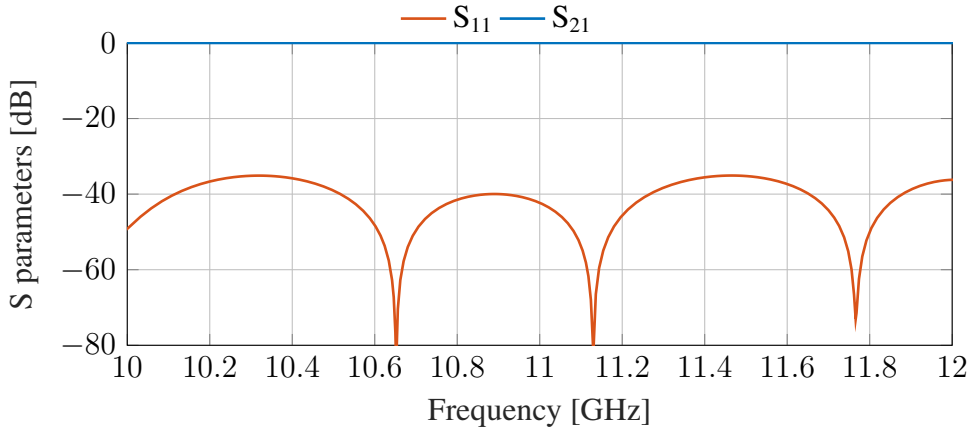

Figure 3.53: Simulated response of the broadband transition between the low-profile waveguide and a standard WR75 waveguide.

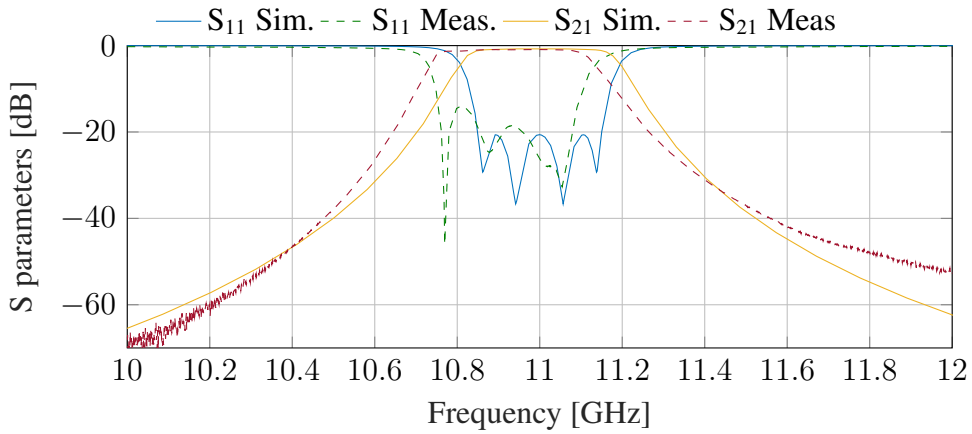

Figure 3.54: Frequency response (simulated and measured) of the low-profile filter.

pactor gap, such as those under consideration, the TASE is directly proportional to the voltage, so identifying the critical frequencies and resonators can be accomplished by identifying the highest TASE values.

We used the methodology developed in [66, 133] to compute the TASE distribution of both filter realisations. The procedure involves extracting the coupling matrix from the measured filter response, which was accomplished using the filter designer module of CST. The resulting matrices for WR75 and low-profile filters are shown in 3.23 and 3.24, respectively.

Table 3.13: Final dimensions of the low-profile filter.

Parameter	**Dimensions** [mm]
a	19.05
b_r	2.00
$l_{r1} = l_{r4}$	14.81
$l_{r2} = l_{r3}$	16.82
t	4
$W_{S1} = W_{4L}$	11.34
$W_{12} = W_{34}$	8.26
W_{23}	7.78
b_1	2.57
b_2	4.44
b_3	7.60
b	9.53
l_1	9.52
l_2	9.05
l_3	9.53

$$\begin{pmatrix} 0 & 1.019 & 0 & 0 & 0 & 0 \\ 1.019 & -0.398 & 0.868 & 0 & 0 & 0 \\ 0 & 0.868 & -0.413 & 0.674 & 0 & 0.008 \\ 0 & 0 & 0.674 & -0.382 & 0.863 & -0.141 \\ 0 & 0 & 0 & 0.863 & 0.086 & 1.045 \\ 0 & 0 & 0.008 & -0.141 & 1.045 & 0 \end{pmatrix} \tag{3.23}$$

$$\begin{pmatrix} 0 & 1.083 & 0 & 0 & 0 & 0 \\ 1.083 & 0.348 & 0.939 & 0 & 0 & -0.001 \\ 0 & 0.939 & 0.452 & 0.730 & 0 & 0.004 \\ 0 & 0 & 0.730 & 0.405 & 0.930 & -0.133 \\ 0 & 0 & 0 & 0.930 & 0.682 & 0.997 \\ 0 & -0.001 & 0.004 & -0.133 & 0.997 & 0 \end{pmatrix} \tag{3.24}$$

Then, the admittance matrix of the bandpass prototype ($\boldsymbol{Y}$) of the filters was computed as follows:

$$\boldsymbol{Y} = \boldsymbol{G} + j\omega'\boldsymbol{C} + j\boldsymbol{M} \tag{3.25}$$

, where $\boldsymbol{G}$ contains the input/output admittances of the filter ($G_S = 1/R_S$ and $G_L = 1/R_L$), $\boldsymbol{C}$ is a diagonal matrix that represents the capacitors of the low-pass filter prototype;

which normalised values are one; and ω' denotes the frequency transformation from low-pass to band-pass of equation 2.3.

Afterwards, the voltage at each node of the circuit can be computed from the excitation current by equation 3.26.

$$\boldsymbol{V} = \boldsymbol{Y}^{-1} \cdot \boldsymbol{I} \tag{3.26}$$

$\boldsymbol{V}$ and $\boldsymbol{I}$ are column vectors that denote the peak voltage and excitation current at each resonator. For a CW excitation of 1 W of mean power at the port one, the only non-zero element of the excitation current vector ($\boldsymbol{I}$) is the first one, whose value is $I_0 = \sqrt{8G_S}$.

Finally, the TASE of the n-th resonator can be computed as the stored energy in the corresponding capacitor multiplied by the scale factor of the frequency transformation [133]. For bandpass filters, the TASE of the n-th resonator reads as follows:

$$TASE_{1W,n} = \frac{|V_n|^2 C_n}{4} \frac{d\omega'}{d\omega} \tag{3.27}$$

The computed TASE distributions for the resonators of both filter realisations are presented in Figures 3.55 (a) and (b). These figures emphasise the non-uniform distribution of fields, which tend to concentrate on specific resonators near the cutoff frequencies.

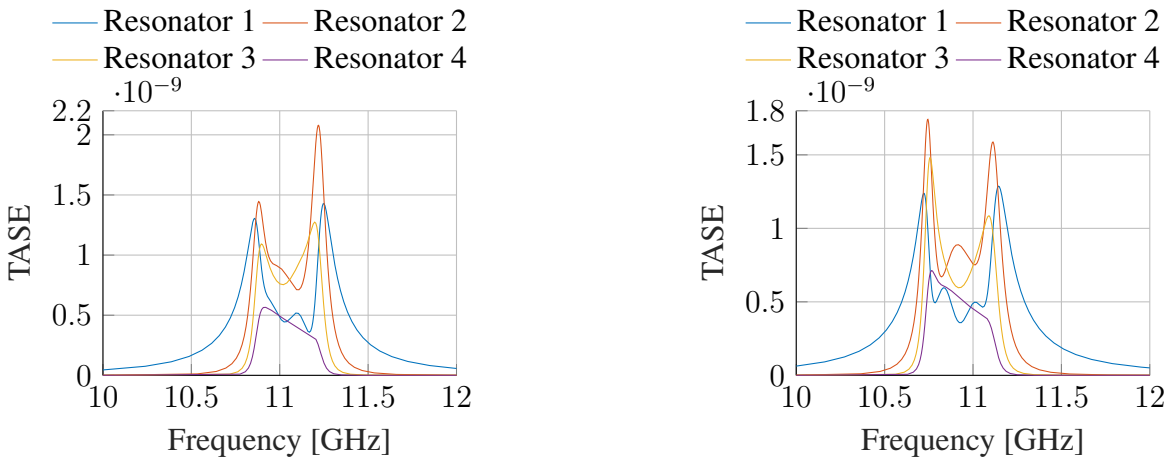

Figure 3.55: Time-Average Stored Energy (TASE) of each resonator for both filters under study: (a) WR75 filter and (b) Low-profile filter.

The energy distribution of the low-profile filter indicates that the critical frequency is the lower cutoff frequency, and the second resonator is the critical region. However, for

the WR75 resonator, the critical frequency is not so simple as the upper cut-off frequencies exhibit a higher energy concentration than the lower ones. Thus, a study of the multipactor phenomenon at both cut-off frequencies of the WR75 filter was undertaken, with the second resonator identified as the critical region for both frequencies.

After identifying the frequencies and areas where multipactor can appear, the power threshold needed to trigger a discharge can be estimated using the infinite parallel-plate approach, referred to Section 2.2.5. To accomplish this, the electric field of both filters was computed at their respective critical frequencies using CST.

Using the electric field distribution, the Voltage Magnification Factor (VMF) can be easily calculated as the ratio of the voltage at the critical area and the voltage at the input port (VMF $= V_{max}/V_{in}$). With this information, the input power required to produce a multipactor discharge can be approximated using the following equation [100]:

$$P_{in}^{th} = \frac{|V_{th}|^2}{2Z_0 \text{VMF}^2(1-|S_{11}|)^2} \tag{3.28}$$

, where V_{th} is the threshold voltage needed for a multipactor discharge in the equivalent parallel plate model. It can be obtained from the multipactor susceptibility chart for pure copper provided by the ESA in the ECSS multipactor tool software [100]. $|S_{11}|$ is the measured modulus of the S_{11} parameter, and Z_0 denotes the equivalent TEM impedance of the TE_{10} mode that can be computed as follows:

$$Z_0 = \eta \frac{2b}{a} \frac{\lambda_g}{\lambda} \tag{3.29}$$

, where a and b are the horizontal and vertical dimensions of the rectangular waveguide, λ the wavelength in free space, λ_g is the wavelength in the waveguide, and η is the intrinsic impedance of free space.

Table 3.14 presents the predicted power threshold values for the critical frequencies of both filters. Based on this preliminary approximation, the input power threshold for the WR75 filter is approximately $586\,\text{W}$, whereas for the low-profile realization, it is $242\,\text{W}$. Furthermore, the analysis indicated that the critical frequency of the WR75 filter is the lowest cutoff frequency, and the hot spot of both filters is situated in the centre of the second resonator.

The parallel plates approach is a valuable tool for obtaining a preliminary power threshold and identifying critical frequencies and regions. However, It represents the worst-case scenario for multipactor discharge, providing a very conservative threshold. In order to obtain a more accurate prediction, we performed a multipactor study on SPAK3D (2021 SP5 - Jun 28 2021). This simulator models the electron movement produced by the electromagnetic

Table 3.14: Power Threshold values for multipactor effect obtained using the parallel plates approximation.

Filter realisation	**Low-profile filter**	**WR75 filter**	
Frequency [GHz]	10.744	10.882	11.219
V_{max} [V]	63.88	118.49	128.11
VMF	3.19	4.74	4.42
V_{th} [V]	1160	5597	5770
Z_0 [Ω]	116.25	545.76	528.88
P_{in}^{th} [W]	242.95	586.34	793.95

fields and the SEE of the surfaces of the device to quantify the electron multiplication over several wave cycles. The simulation parameters and analyse frequencies considered in this study were the following:

- **Seeding electrons:** this field represents the initial electron population in the simulation, with $30\,000$ electrons assigned to the low-profile filter and $50\,000$ to the WR75 filter. In order to ensure that critical areas were identified, the particles were distributed homogeneously throughout the entire device.
- **Multipactor discharge criterion:** a multipactor discharge was detected by the simulator when the population of electrons was augmented by an automatically determined factor.
- **Initial power:** $50\,\mathrm{W}$ for the low-profile filter and $500\,\mathrm{W}$ for the standard WR75 realisation. Both power values were lower than the expected power threshold obtained with the parallel plates model.
- **SEY:** we utilised the SEY curves shown in Figure 3.51. Specifically, we used the SEY of the Rigid 10k resin with two plating processes and the SEY of the RO4003C with the first electro-deposited copper layer.
- **Frequency:** the test bench used for multipactor testing cannot work with RL values higher than $14\,\mathrm{dB}$ as these reflections can produce potentially destructive effects in the test bench. Based on this criterion and the TASE analysis, we decided to analyse and test the multipactor effect at the lower edge of the practical bandwidth for $RL > 14\,\mathrm{dB}$ and at the center frequency of both filters, i.e. 10.917 and $11.199\,\mathrm{GHz}$ for the standard WR75 filter and 10.775 and $10.940\,\mathrm{GHz}$ for the low-profile filter.

Simulated results for both filters at their lowest analysis frequencies are presented in Figure 3.56. This chart illustrates the evolution of the electron population over time for a

certain input power. For low input power levels, the electron population decreases, showing that multipactor did not appear. However, the electron population increases for high input power levels, indicating the presence of a sustained multipactor discharge. The multipactor threshold is defined as the minimum input power required to trigger an exponential increase in the electron population.

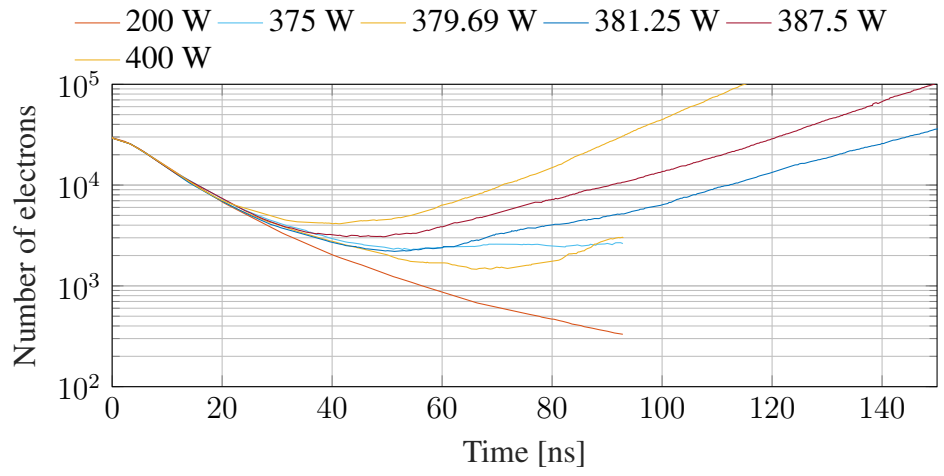

(a)

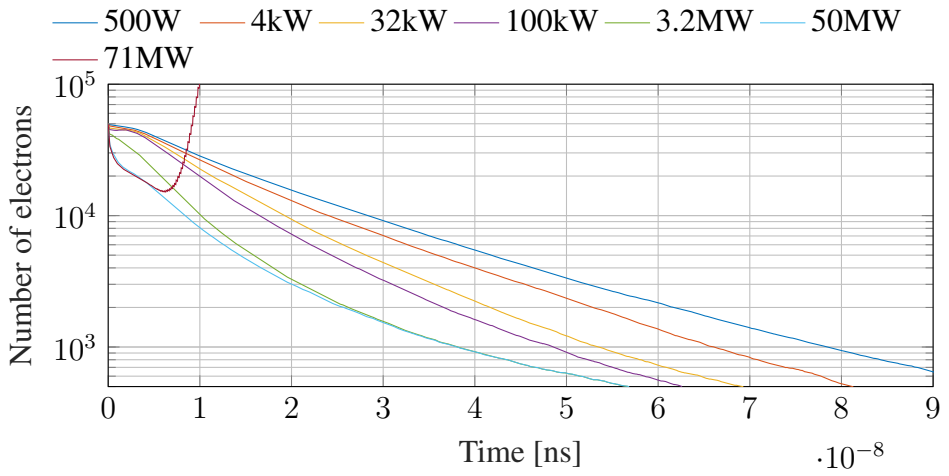

(b)

Figure 3.56: Evolution of electrons population at lowest analysis frequency for the: (a) WR75 filter and (b) low-profile filter.

The numerical analysis also helps to identify the critical areas of the filters. Figures 3.57(a) and 3.57(b) depict the electron distribution at the start and conclusion of the particle simulation for the low-profile filter fed by a $10.775\,\mathrm{GHz}$ frequency continuous wave signal with a power of $400\,\mathrm{W}$. Results show a notable increment of the electron population in the

second resonator while the number of electrons in other areas decreases, indicating that it is the critical area. Similar results were obtained in the multipactor analyses performed on the WR75 filter, demonstrating that the critical area of both filters is the centre of the second resonator.

(a) (b)

Figure 3.57: Distribution of electrons population in the low-profile filter for an $10.775\,\mathrm{GHz}$ input signal with a power of $400\,\mathrm{W}$. (a) Initial distribution of 3000 electrons. (b) Electron distribution after $80\,\mathrm{n\,sec}$. Electrons are depicted in white over the electric field distribution of the filter.

Table 3.15 summarises the results of the multipactor analysis obtained with the particle simulations. The analyses show that the WR75 filter has an exceptionally high power threshold of over $70\,\mathrm{MW}$ for all analysed frequencies, while the low-profile version exhibits a threshold power of approximately $380\,\mathrm{W}$ for the critical frequency.

Table 3.15: Power threshold values for multipactor effect obtained using the SPARK 3D particle simulator.

Filter realisation	**WR75 filter**			**Low-profile filter**	
Frequency [GHz]	10.917	11.051	11.199	10.775	10.940
Simulated multipactor threshold	71 MW	$>$ 90 MW	83 MW	380 W	844 W
Critical resonator	2nd	2nd	2nd	2nd	2nd

3.6.3.5 Multipactor testing and experimental results

The multipactor tests conducted in this work adhered to the technical specifications outlined in the ECSS-E-ST-20-01C standard for multipactor design and testing [101]. Tests were performed in the high power radio-frequency laboratory of the ESA-VSC using the test bench depicted in Figure 3.58 (a).

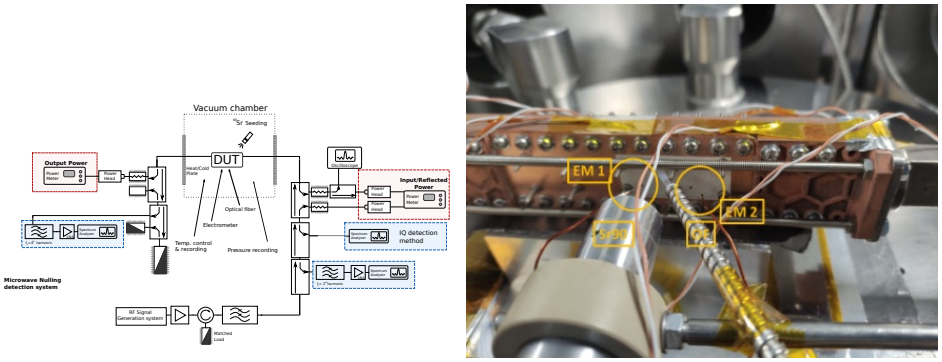

(a) (b)

Figure 3.58: (a) Multipactor measurement setup. (b) Detail of the low-profile filter in the multipactor test bench.

The DUTs were introduced into a high vacuum chamber and connected to the test bench. Before each test, the test bench was validated and verified using test samples with known breakdown thresholds. This verification allows for discarding the presence of multipactor discharges along the test bench. To simulate the free electrons present in space, a strontium-90 (^{90}Sr) radioactive source was directed towards the critical area of the filters; see Figure 3.58 (b). DUTs were fed with a pulsed continuous wave of increasing power until some evidence of multipactor was detected.

Several multipactor detection methods were employed during the tests, including two General Detection Method (GDM) and two different Local Detection Method (LDM). The general detection methods were an IQ detection method and two harmonic detection methods. Additionally, we employed the following local detection methods: an optical fibre situated in the second resonator and two electron probes pointing to the second and third resonators. General detection methods are used to detect the presence of a multipactor discharge within the entire test bench, while local methods are focused on detecting a multipactor discharge in specific areas of the device. According to the ECSS standard [101], a combination of at least one general and one local detection method are needed to confirm the occurrence of a multipactor even.

The test procedure is as follows. DUTs are fed with a continuous wave signal, with power gradually increased until a discharge is detected. The power is then reduced until no further discharges are observed and then increased again until a new multipactor event confirms the discharge. The lowest input power of both discharges is recorded as the power threshold. If there is no second discharge, the test should be halted to determine the cause of the initial multipactor discharge. Table 3.16 shows the results of the multipactor tests.

Table 3.16: Simulated and measured multipactor threshold power.

Filter realisation	**WR75 filter**			**Low-profile filter**	
Frequency [GHz]	10.917	11.051	11.199	10.775	10.940
Simulated multipactor threshold	71 MW	> 90 MW	83 MW	380 W	844 W
Critical resonator	2nd res.	2nd res.	2nd res.	2nd res.	2nd res.
Measured multipactor threshold	6 kW (only detected by GDM)	No Discharge	No Discharge	398 W	950 W
Discharge location	Not observed	Not observed	Not observed	2nd res.	2nd res.

The power thresholds for the low-profile filter were comparable to the SPARK-3D estimations. The local detection methods located the multipactor events in the second resonator for both test frequencies, confirming the predictions. For the WR75 realisation, a weak multipactor discharge was detected only by one detection method and for an input power of 6 kW. This discharge was not identified by any local detection method and it was not confirmed during a second multipactor test that was performed as verification. Since simulations indicated a much higher power threshold and the maximum power capacity of the test bench is 6 kW, it is inferred that the multipactor event noticed during the WR75 filter test must have occurred somewhere in the test bench.

Chapter 4

Substrate Integrated Circuits

4.1 Introduction

Radiofrequency circuits are commonly based on a hybridisation of planar technologies, such as microstrip and coplanar waveguides, and classical 3D guiding structures, like coaxial cables and hollow waveguides.

On the one hand, coaxial cables and metallic waveguides have very low transmission loss, high-quality factor, high-power handling, low noise sensitivity, and high electromagnetic shielding. However, their closed structure hardens the integration of active devices. Additionally, they are heavy and bulky, which limits their use in the consumer sector and relegates them to more stringent areas such as space and defence sectors [79].

On the other hand, planar transmission lines (microstrip, coplanar, and stripline) allow a natural integration with lumped elements and active devices due to their planar topology and Transverse ElectroMagnetic (TEM) mode. Moreover, the improvements in manufacturing techniques and dielectric substrates have enabled a high degree of miniaturisation and accurate impedance performance. Nevertheless, planar lines exhibit higher loss (low Q), strong parasitic couplings (leakage), low power handling, and high sensitivity to manufacturing tolerances. These issues become increasingly pronounced at higher frequencies [79]. Consequently, planar transmission lines are a better choice for end-user devices operating at "low" frequencies in less stringent fields, such as mobile and domestic communications.

Planar transmission lines and 3D guiding structures are complementary and combining them provides incredible flexibility and performance. However, it was not until the early 2000s that both structures were combined onto the same substrate [3], giving rise to what was later known as substrate-integrated circuits (SICs). The point of SICs is to develop hybrid circuits that combine planar and non-planar transmission lines within the same substrate.

This technology benefits from the low-cost mass production capability of planar transmission lines and the high electrical performance of non-planar guiding technologies, enabling the use of waveguides and coaxial lines in end-user applications [79]. Some of the most used SIC structures are presented below, including descriptions of their structure, fabrication and design equations.

4.1.1 Substrate-Integrated Waveguide (SIW)

The concept of Substrate Integrated Waveguide (SIW) was first introduced in 2001 [3]. It involves producing a rectangular waveguide structure within a dielectric substrate. This is achieved by incorporating two rows of periodically metallised holes that connect the top and bottom ground planes of a PCB. Properly selecting the diameter and spacing of these metallised holes allows them to function as continuous metallic walls, emulating the characteristics of a dielectric-filled rectangular waveguide.

Figure 4.1 illustrates the fundamental structure of a SIW. It encompasses five essential design parameters: the relative dielectric constant (ε_r), the substrate thickness (t), the diameter of plated holes (d), the separation between holes (p), and the separation between rows or SIW width (a). The selection of these parameters determines factors like the cutoff frequency of the propagation modes, the single-mode bandwidth, wave impedance, and radiation losses.

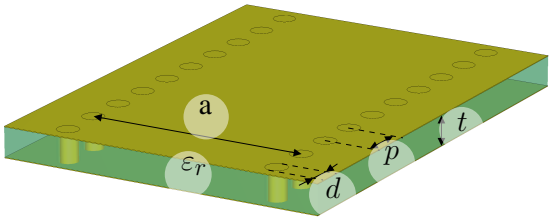

Figure 4.1: Structure of a Substrate Integrated Waveguide (SIW) consisting of a rectangular waveguide implemented in a Printed Circuit Board (PCB) by means of two parallel rows of plated through holes. Copper is depicted in yellow, and the substrate material is represented in green.

The separation between adjacent plated holes (p) should be minimal to ensure that the SIW operates as a rectangular waveguide. In the work presented in [134], the concept of surface impedance was used to model the rows of plated through holes of the SIW, obtaining the following design guidelines:

$$p > d \tag{4.1}$$

$$0.05 < \frac{p}{\lambda_c} < 0.25 \tag{4.2}$$

$$\tag{4.3}$$

After the substrate design is finalised and an appropriate combination of hole diameters and spacing is selected, the subsequent relation can be employed to provide an approximation for the effective width of the equivalent rectangular waveguide [135]:

$$a_{eff} = a - 1.08\frac{d^2}{p} + 0.1\frac{d^2}{a} \tag{4.4}$$

, where a_{eff} denotes the width of an equivalent rectangular waveguide with solid walls filled with the same dielectric as the SIW structure. This equivalent waveguide serves as a valuable tool for approximating the wave impedance and the monomode bandwidth of the substrate-integrated waveguide.

Compared to planar transmission lines, SIW exhibit lower ohmic and leakage loss, and similar dielectric loss. The substrate-integrated waveguide has improved shielding and similar integration to microstrip, but has a reduced monomode bandwidth and a larger footprint. Compared to classical waveguides, SIW has higher losses due to the dielectric substrate. However, it exhibits an easy integration and low cost.

Over the past decade, various substrate-integrated waveguide configurations have emerged to enhance the SIW's performance in terms of its footprint, operational bandwidth, and transmission loss. In pursuit of a narrower profile, the Half-Mode SIW was introduced [84]. Similarly, the Ridge SIW, proposed in [85], enhances the single-mode bandwidth of the SIW. Finally, empty and air-filled versions of the SIW appeared as a solution to mitigate or eliminate the dielectric loss [18, 136].

4.1.2 Empty Substrate-Integrated Waveguide (ESIW)

The empty SIW (ESIW) and Air-filled SIW (AFSIW) were introduced in 2014 [18, 136]. Both topologies proposed an empty or quasi-empty version of the SIW topology. The ESIW uses a stack of three PCBs, in which an empty cavity is milled in the centre layer to synthesise a hollow rectangular waveguide. The side walls of the waveguide can be implemented by metallising the side walls of the empty cavity (ESIW) or by performing two rows of metallised holes (AFSIW). When the three layers are assembled and soldered, the structure

operates as a rectangular waveguide, as illustrated in Figure 4.2.

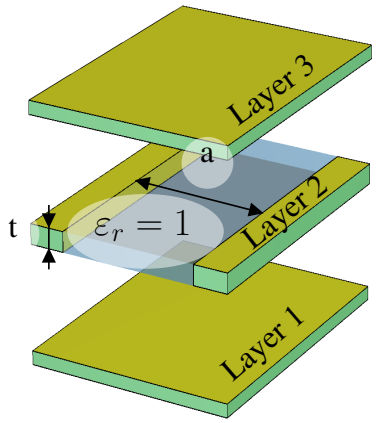

Figure 4.2: Structure of an Empty Substrate Integrated Waveguide (ESIW) developed in three layers of PCB. Copper components are represented in yellow, the substrate material in green, and empty areas in blue.

The lack of dielectric material in the ESIW results in a significant reduction in transmission loss compared to the standard SIW. However, this advantage comes at the cost of increased manufacturing complexity and a large footprint. To address these issues, new empty topologies have emerged, including the ridge ESIW and the half-mode ESIW,

Compared to classical waveguides, the ESIW has higher transmission loss as the electric currents flow in a reduced area, but it presents a good integrity and an affordable manufacturing process.

4.1.3 Empty Substrate Integrated Coaxial Line (ESICL)

The ESICL technology emerged in 2015 as a promising option for achieving a low-loss SIC topology suitable for low frequencies where the size of empty substrate-integrated waveguides makes them impractical [87]. This technology involves implementing a rectangular coaxial cable in a stack of five PCBs, as shown in Figure 4.3. The active conductor of the rectangular coaxial is located in layer three, while layers two and four act as separators, and layers one and five serve as the bottom and top covers. Due to the current distribution of the TEM mode, soldering is not necessary, and the different layers can simply be assembled using bolts.

As the fundamental mode of the ESICL is the TEM, this transmission line exhibit a very wide monomode bandwidth and a simple integration with lumped and active devices without

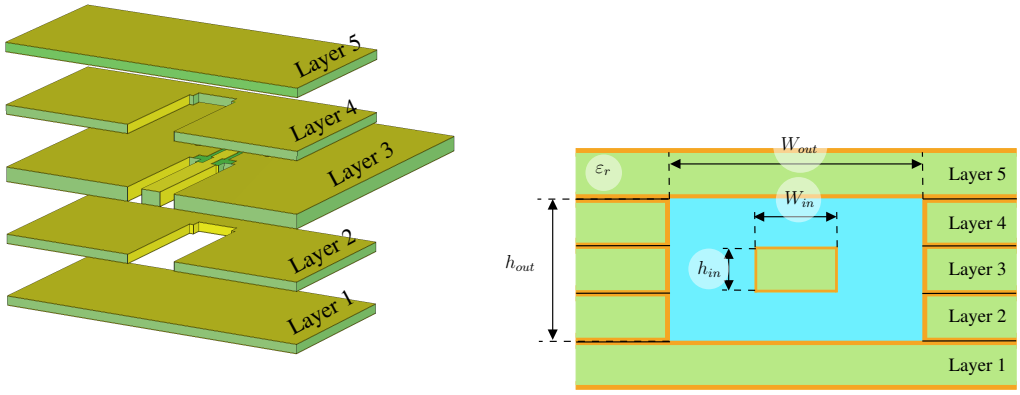

(a) (b)

Figure 4.3: Structure of an Empty Substrate Integrated Coaxial Line (ESICL): a) exploded view, and b) cross-section view. The first and fifth layers serve as covers, while the second, third, and fourth layers form the ESICL.

the need for changing to a planar transmission line.

Dimensions of the ESICL; the width of the inner conductor W_{in}, the height of the inner conductor h_{in}, the width of the outer conductor W_{out}, and the height of the outer conductor h_{out}; control the characteristic impedance of the line (Z_0). The expression developed in [137] can be used to approximate these dimensions without the need for full-wave simulators:

$$Z_0 = \frac{\eta}{4}\left[\frac{1}{\frac{w_{out}}{h_{out}}\left(1-\frac{h_{in}}{h_{out}}\right)} + \frac{2}{\pi}\ln\left(\frac{1}{1-\frac{h_{in}}{h_{out}}} + \coth\left(\frac{\pi}{2}\frac{w_{out}}{h_{out}}\right)\right)\right] \tag{4.5}$$

This expression is only valid for ESICL and rectangular coaxial structures with a centred inner conductor.

4.2 Substrate Integrated Filters

In this section, we delve into the design of four Ku band bandpass filters. These filters are realised within four different SIC topologies and share a common Chebyshev response, enabling us to compare their performance. The filter specifications are: order N =5, 13 GHz of center frequency, 300 MHz of bandwidth, and an in-band ripple of 0.1 dB, which correspond to a return loss of 25 dB.

The proposed response has the following inverter values: $\overline{K}_{S,1} = \overline{K}_{5,L} = 0.2134$, $\overline{K}_{1,2} = \overline{K}_{4,5} = 0.0353$, and $\overline{K}_{2,3} = \overline{K}_{3,4} = 0.0247$. This corresponds to $Q_{ext} = 34.493$ and the

following coupling matrix: $M_{(S,1)} = M_{(L,5)} = 1.1208$, $M_{(1,2)} = M_{(4,5)} = 0.9738$ and $M_{(2,3)} = M_{(3,4)} = 0.6825$. As can be noticed from their coupling matrix, the filters have an in-line topology.

4.2.1 SIW Filter

As previously stated, the SIW is an equivalent waveguide implemented on a microwave substrate. Two rows of plated through holes behave as the vertical walls of the waveguide, while the top and bottom metallic planes of the PCB act as the top and bottom covers of the equivalent waveguide. For this filter, it was decided to use a SIW with two rows of metallized vias with a diameter (d_v) of $0.7\,\mathrm{mm}$, a separation (p_v) of $1.0\,\mathrm{mm}$, and a width (a) of $8.93\,\mathrm{mm}$. The design was intended for a RO4003C substrate with $\varepsilon_r = 3.55$, a thickness of $0.813\,\mathrm{mm}$, and a copper cladding thickness of $17.5\,\mu\mathrm{m}$. The dimensions were calculated to achieve a cutoff frequency of $9.5\,\mathrm{GHz}$ for the fundamental mode of the SIW following the design guidelines presented in Section 4.1.1.

4.2.1.1 Topology and design

A linearly tapered microstrip transition was designed to connect the microstrip line with the SIW filter. This transition was originally proposed in [3], and its design equations were introduced in [138]. Figure 4.4 depicts the transition structure.

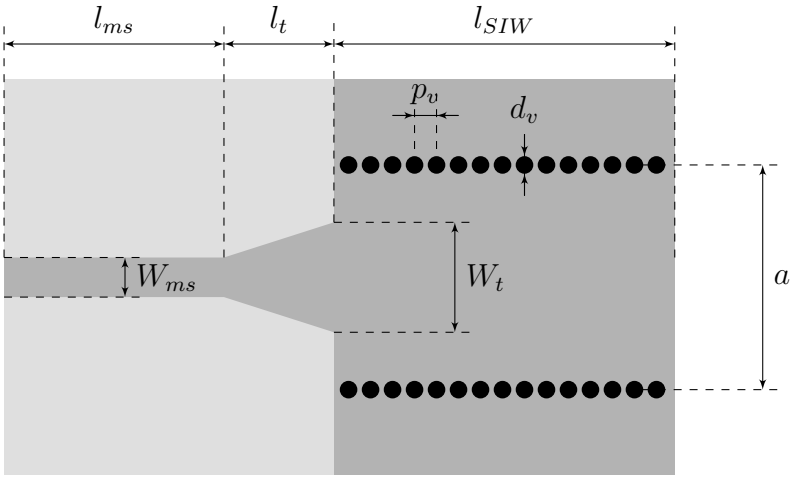

Figure 4.4: Layout of the SIW taper transition. The dielectric substrate is shown in light grey, the copper metallisation on top of the substrate is depicted in dark grey, and the metallised vias are shown in black.

To determine the dimensions of the microstrip taper, namely W_t and l_t, the substrate-integrated waveguide can be modelled as a TEM waveguide with an equivalent width of W_e. Previous research [138] has established that the optimum adaptation between the microstrip and the SIW occurs when the relationship between the permittivity and width ratios is given by:

$$\frac{a_{eff}}{W_e} = 4.38e^{\left(-0.627\frac{\varepsilon_r}{\varepsilon_{eff}}\right)} \tag{4.6}$$

, where: a_{eff} is the effective width of the equivalent waveguide that models the SIW, and W_e is the width of the TEM equivalent of the same SIW.

Now, the width of the tapered microstrip can be calculated by equating the impedance of the microstrip tapper and the impedance of the equivalent TEM model of the SIW, obtaining the following expression:

$$Z_{TEM} = \sqrt{\frac{\mu}{\varepsilon_0\varepsilon_r}}\frac{h}{W_e} = Z_{ms} = \begin{cases} \frac{60}{\sqrt{\varepsilon_{eff}}\ln\left(8\frac{h}{W_t}+0.25\frac{W_t}{h}\right)} & \text{for } W_t/h < 1 \\ \frac{120\pi}{\sqrt{\varepsilon_{eff}}[W_t/h+l.393+0.667\ln(W_t/h+1.444)]} & \text{for } W_t/h > 1 \end{cases} \tag{4.7}$$

where h is the height of the substrate, Z_{ms} is the impedance of the microstrip taper, and Z_{TEM} is the impedance of the equivalent TEM waveguide.

The equations mentioned above provide an estimation of the width of the tapered transition (W_t). The length of the taper (l_t) was set to a quarter of the wavelength. Next, the dimensions (W_t and l_t) were optimised using CST to maximise the return loss. Table 4.1 lists the resulting dimensions obtained from this process. These dimensions have been calculated for a RO4003C substrate with $\varepsilon_r = 3.55$, a dielectric thickness of $0.813\,\mathrm{mm}$, and a copper cladding thickness of $17.5\,\mu\mathrm{m}$.

Table 4.1: Dimensions of the linearly tapered transition from microstrip to SIW.

Parameter	**Dimension** [mm]
a	8.93
d_v	0.70
p_v	1.00
l_{siw}	10.00
W_{ms}	1.85
l_{ms}	10.00
W_t	2.81
l_t	2.97

Figure 4.5 depicts the simulated response of the optimised transition. It can be seen that the return loss exceeds $25\,\mathrm{dB}$ for the mono-mode bandwidth of the SIW and is over $30\,\mathrm{dB}$ for the filter bandwidth.

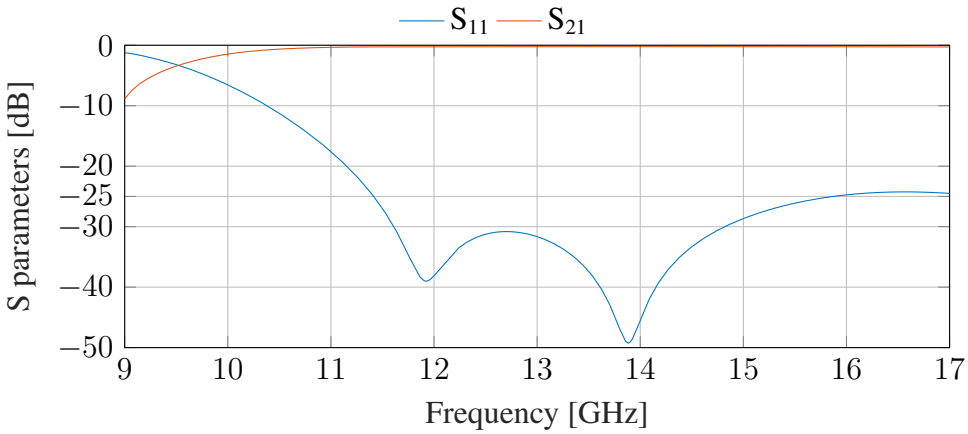

Figure 4.5: Simulated response of the linearly tapered transition from microstrip to SIW.

The layout of the filter is illustrated in Figure 4.6. It consists of five SIW resonators working under the TE_{101} mode. Resonators are coupled through inductive irises implemented with two rows of plated vias.

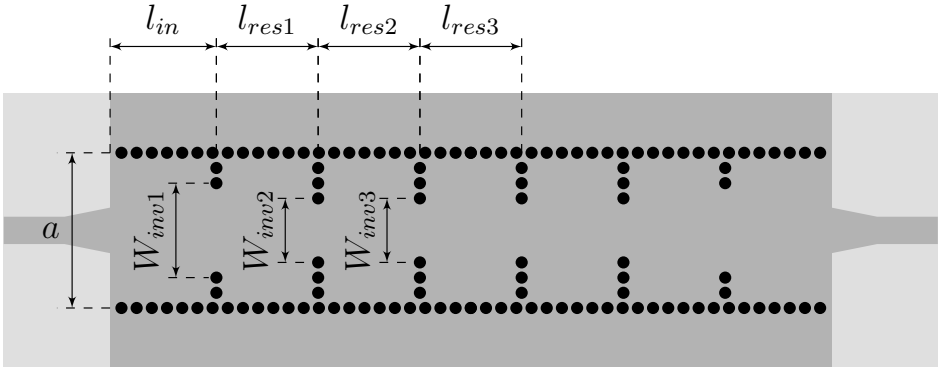

Figure 4.6: Layout of the SIW filter. The dielectric substrate is shown in light grey, the copper metallisation on top of the substrate is depicted in dark grey, and the metallised vias are shown in black.

The coupling matrix design procedure outlined in Section 2.1.1 was used to design the filter. Table 4.2 presents the final dimensions of the filter and the optimised response is illustrated in Figure 4.7.

It can be observed that the SIW filter exhibits higher loss compared to the surface mount

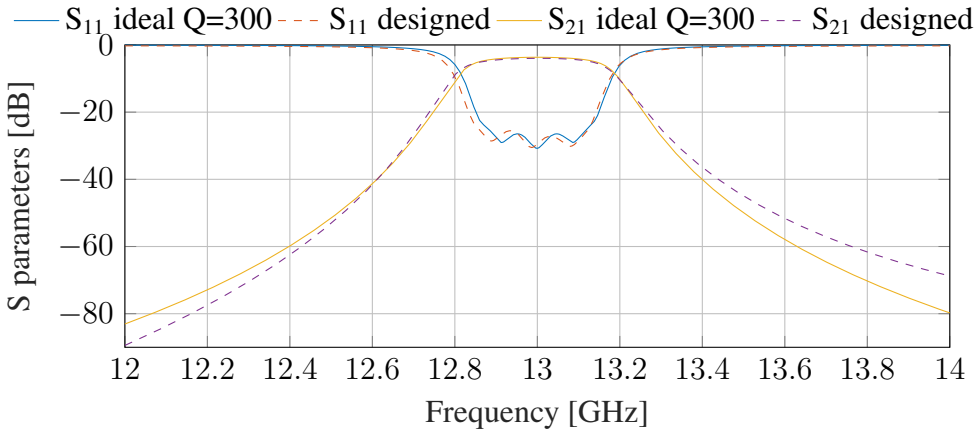

Figure 4.7: Simulated response of the SIW filter. The ideal response was computed by considering a quality factor of 300 for all resonators.

Table 4.2: Final dimensions of the SIW filter.

Parameter	**Dimension** [mm]
l_{in}	10
l_{res1}	8.08
l_{res2}	8.90
l_{res3}	8.98
W_{inv1}	4.28
W_{inv2}	2.66
W_{inv3}	2.36

technology (SMT) filters developed in Section 3.4. The simulated quality factor of the SIW filter is 277 , which was estimated using equation 4.8 from [139]:

$$Q = \frac{4.343 f_0}{\mathrm{IL}_{f0}(f_2 - f_1)} \sum_{n=1}^{N} g_n \tag{4.8}$$

, where f_0 is the center frequency of the filter, $f_2 - f_1$ is the passband bandwidth, IL_{f0} is the insertion loss at the center frequency, and g_k are the Chebyshev coefficients of the low-pass prototype.

4.2.1.2 Experimental results

Figure 4.8 shows the manufactured prototype. The fabrication process consists of drilling the vias using a mechanical milling machine. Then, the substrate is metallised using an electro-deposition system, and the top layer is milled to perform the transition layout.

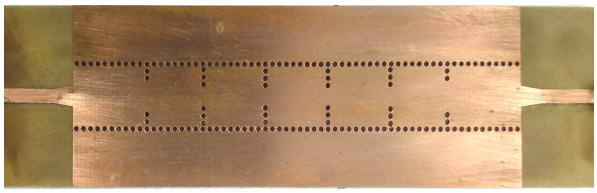

Figure 4.8: Top view of the SIW filter prototype.

Figure 4.9 compares the measured response of the filter with the simulated results obtained with CST. Measurements were obtained with a vector network analyser and a TRL calibration kit, which corrects for errors in the measurement system and compensates for the impact of wires and connectors. This calibration locates the reference plane at the end of the feeding microstrip line. The measured insertion loss is higher than expected ($5.57\,\mathrm{dB}$), corresponding to a quality factor of approximately 176. The measured results also show a reduced rejection, likely due to undesired coupling between the input/output microstrip lines. These deviations are likely due to small manufacturing deviations in both the transition and filter.

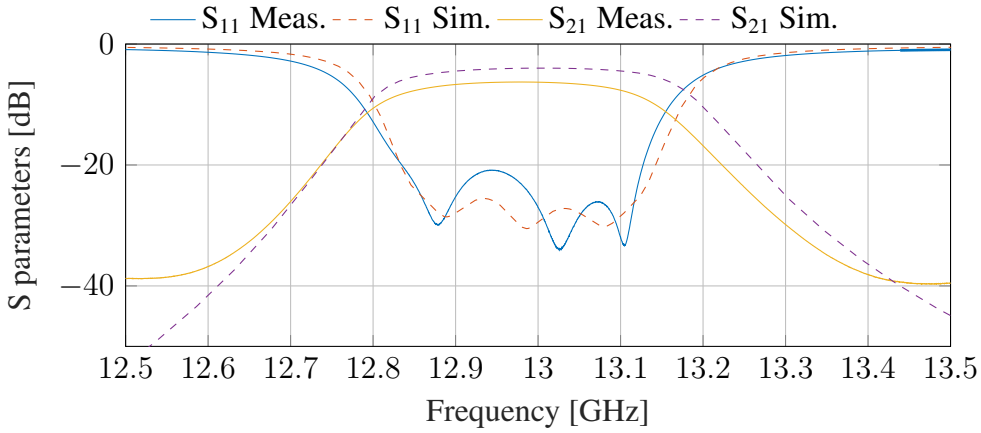

Figure 4.9: Comparison of simulated and measured response of the SIW filter.

4.2.2 ESIW Filter

The ESIW is an empty variation of the SIW that is implemented on a stack of three PCBs. In this configuration, the side walls of the equivalent waveguide are formed by metallised cuts made in the centre layer, while the top and bottom PCBs act as its top and bottom covers. The resulting structure acts as an empty waveguide that can guide electromagnetic waves in the same way as the SIW.

The proposed ESIW was designed to exhibit a cutoff frequency of approximately $9.5\,\mathrm{GHz}$ for a RO4003C substrate of $0.813\,\mathrm{mm}$ thickness and a copper cladding of $17.5\,\mu\mathrm{m}$.

4.2.2.1 Topology and design

It was decided to use the substrate slab transition proposed in [140] to interconnect the microstrip line and the ESIW. The transition is formed by a linear microstrip taper and a dielectric slab. The slab penetrates in the ESICL and its width decreases with the distance z from W_{ti} to W_{tf} according to the following formula:

$$W(z) = \frac{W_{ti}\left(e^{-cl_t} - e^{-cz}\right) + W_{tf}e^{(-cz-1)}}{e^{-cl_t} - 1} \tag{4.9}$$

, where c is the parameter that controls the reduction velocity of the slab width, l_t is the length of the slab, and W_{ti} and W_{tf} are the initial and final width of the slab, respectively. This dielectric slab, along with the linear microstrip taper, gradually adapts the impedance of the feeding microstrip line to the impedance of the equivalent rectangular waveguide.

In [115], the transition was improved by including two lateral incisions of width d_f and length l_f. These incisions help to delimit the width of the input iris W_{ir} that tend to have large manufacturing tolerances in other configurations. Finally, metallised vias of diameter d_v and separation p_v are included to prevent the propagation of leaky waves outside the ESIW. The layout of this transition is illustrated in Figure 4.10.

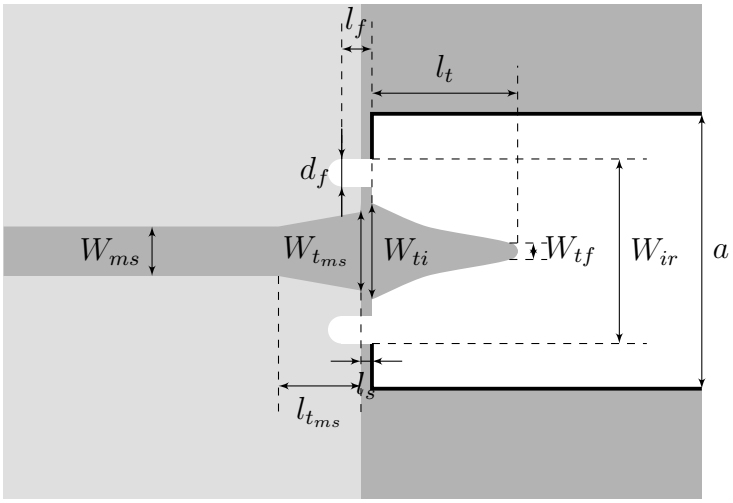

Figure 4.10: Layout of the ESIW taper transition. The dielectric substrate is shown in light grey, the copper metallisation on top of the substrate is depicted in dark grey, and the metallised vias and the border copper metallisation are shown in black.

Esteban et al., in their work [115], offer equations for deriving a practical initial point for the design parameters, as elaborated in equation 4.10:

$$\begin{aligned} l_t &= \frac{\lambda_{g_{(f_0)}}}{4} \\ W_{ti} &= 1.2W_{t_{ms}} \\ W_{ir} &= \frac{a + W_{ti}}{2} \\ c &= \frac{2}{l_t} \\ l_{t_{ms}} &= \frac{\lambda_{ms_{(f_0)}}}{4} \\ W_{t_{ms}} &= 4W_{tf} \end{aligned} \tag{4.10}$$

, where $\lambda_{g_{(f_0)}}$ represents the wavelength at the center frequency within the waveguide, and $\lambda_{ms_{(f_0)}}$ denotes the wavelength in the microstrip at the same frequency.

The transition was initially designed with expressions 4.10 and optimised to maximise the return loss. The optimised dimensions are listed in Table 4.3, and the simulated response is shown in Figure 4.11. The final return excess $25\,\mathrm{dB}$ for the entire mono-mode bandwidth of the ESIW.

Table 4.3: Final dimensions of the transition from microstrip to ESIW.

Parameter	**Dimension** [mm]	**Parameter**	**Dimension** [mm]
a	15.80	d_f	1.00
l_{in}	10	l_f	0
W_{ms}	1.85	l_s	0.50
l_{ms}	10.00	W_{ti}	2.90
d_v	0.70	W_{tf}	0.50
p_v	1.00	l_t	5.99
$W_{t_{ms}}$	2.45	c	0.26
$l_{t_{ms}}$	2.18	W_{ir}	6.81

The layout of the filter is shown in Figure 4.12. It comprises five ESIW cavities operating in the TE_{101} mode, which are coupled by inductive irises of thickness l_{invn} and width W_{invn}. Table 4.4 shows the final dimensions of the filter, and Figure 4.13 depicts the optimised response. In this case, simulation fits very well the ideal response, showing an unloaded quality factor of approximately 1500 .

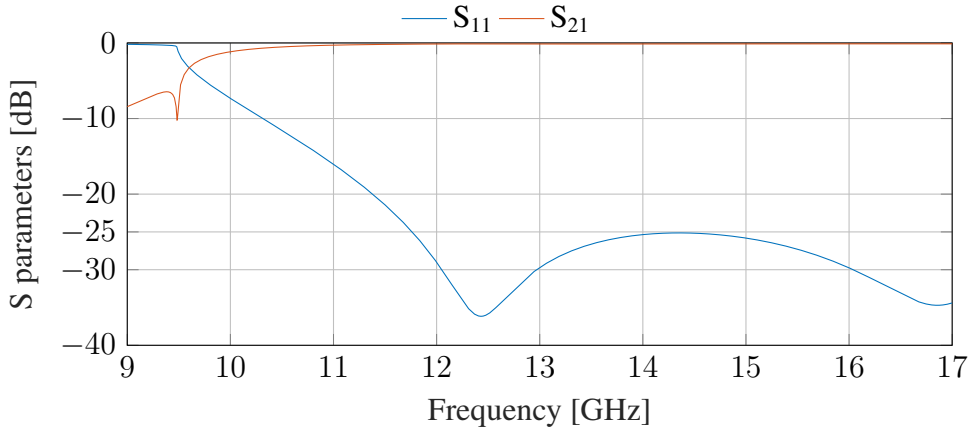

Figure 4.11: Simulated response of the transition from microstrip to ESIW.

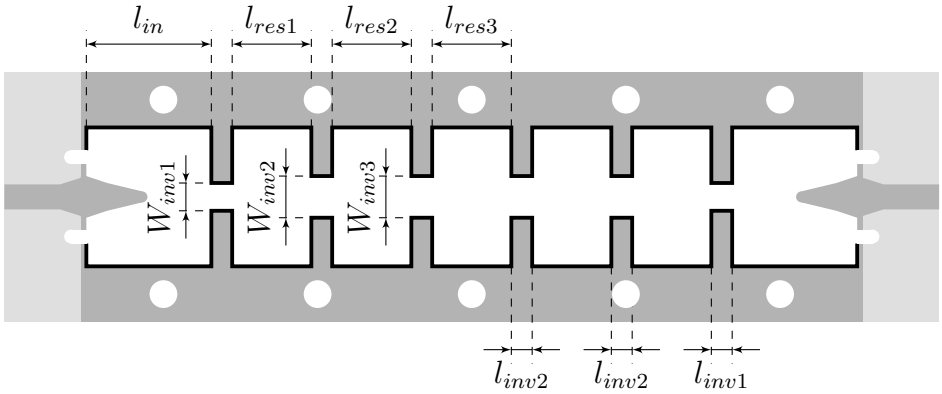

Figure 4.12: Layout of the centre layer in the ESIW filter. The dielectric substrate is shown in light grey, the copper metallisation on top of the substrate is depicted in dark grey, and the metallised vias and the border copper metallisation are shown in black.

4.2.2.2 Experimental results

A prototype of the ESIW filter was manufactured using RO4003C substrate with a thickness of $0.813\,\mathrm{mm}$, and a copper cladding of $17.5\,\mu\mathrm{m}$ for all layers. Figure 4.14 shows a top view of the centre layer of the manufactured device. The fabrication involves drilling vias using a mechanical milling machine and cutting the ESIW cavities using a laser milling machine. Then, the substrate is metallised using an electro-deposition system, and the top copper cladding of the centre layer is milled to create the transition layout. Finally, the different layers are fastened and soldered using bolts and tin solder paste to ensure good electrical contact between layers.

The measured response of the prototype is compared with the simulated response in Fig-

Table 4.4: Final dimensions of the ESIW filter.

Parameter	Dimension [mm]	Parameter	Dimension [mm]
l_{in}	10	$l_{inv1} = l_{inv2} = l_{inv3}$	2
l_{res1}	13.64	W_{inv1}	8.91
l_{res2}	15.35	W_{inv2}	5.10
l_{res3}	15.53	W_{inv3}	5.43

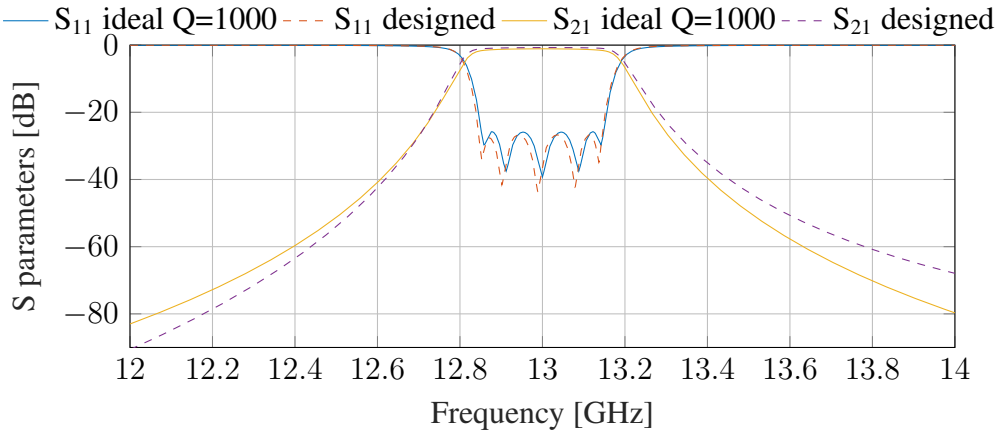

Figure 4.13: Simulated response of the ESIW filter. The ideal response has been computed considering resonators with Q= 1000 .

ure 4.15. The measurement setup underwent calibration using the same microstrip TRL calibration kit employed for the SIW, eliminating the degradation effects of connectors and feeding lines.

The measured insertion loss is 1.21 dB, corresponding to a quality factor of approximately 644 . The measured return loss shows a significant increase of 5 dB compared to the simulation, which could be attributed to manufacturing tolerances in the dimensions of the transition. Similarly to the SIW filter, the measured rejection levels are lower than the simulated values. This is probably due to the propagation of leaky waves between the top and bottom cladding of the top cover.

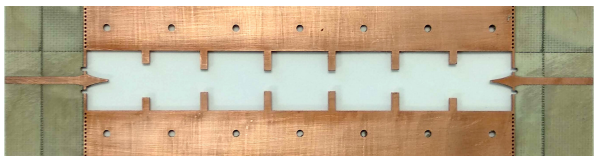

Figure 4.14: Top view of the centre layer of the ESIW filter prototype.

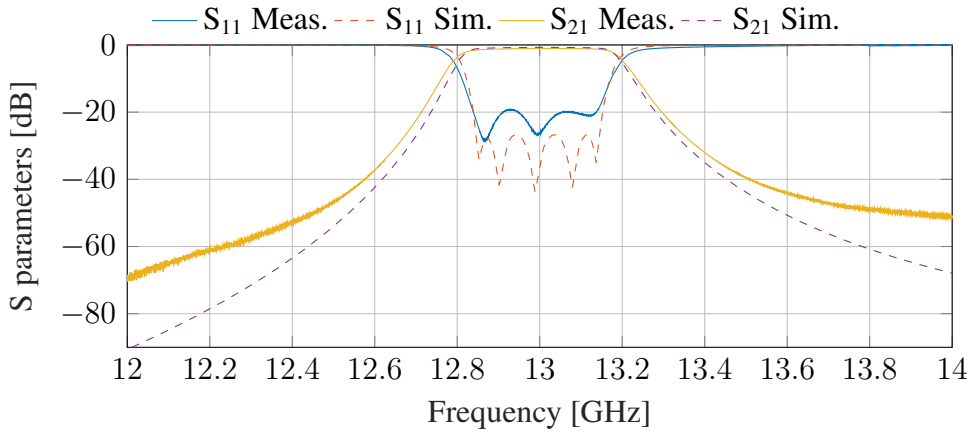

Figure 4.15: Comparison between simulated and measured response of the ESIW filter.

4.2.3 ADLS Filter

The ADLS filter is composed of rectangular SIW resonators operating the TE_{101} mode. These resonators are coupled by sections of ESIW lines that operate below their cutoff frequency, behaving as immittance inverters. This topology is similar to the dielectric filters presented in Section 2.1, and it strikes a balance between SIW and ESIW filters, resulting in a moderate loss and footprint.

4.2.3.1 Topology and design

The layout of the proposed filter is depicted in Figure 4.16. It is composed of five SIW sections that behave as resonators and six ESIW sections that implement the coupling elements. The filter uses the same linearly tapered transition developed for the SIW filter in Section 4.2.1.

Table 4.5 list the optimised dimensions of the filter, and Figure 4.17 shows the simulated response. The simulations show an insertion loss of $3.45\,\mathrm{dB}$ at the center frequency, which corresponds with a quality factor of $Q = 319$.

4.2.3.2 Experimental results

A prototype was fabricated using RO4003C substrate with a thickness of $0.813\,\mathrm{mm}$ and a copper cladding of $17.5\,\mu\mathrm{m}$ for all the layers. The fabrication process consisted of drilling the vias of the SIW sections and cutting the cavities of the ESIW sections in the centre layer. Then, the substrate is metallised using an electro-deposition system. Afterwards, the top copper cladding of the centre layer is milled to perform the microstrip transition. Finally,

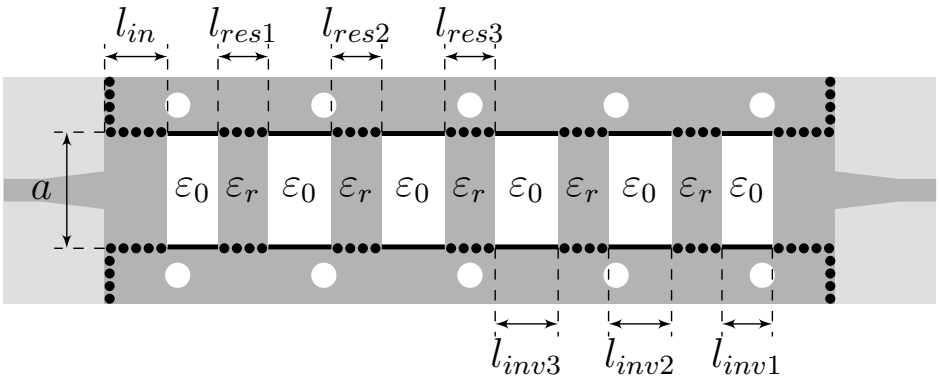

Figure 4.16: Layout of the centre layer in the ADLS filter. The dielectric substrate is shown in light grey, the copper metallisation on top of the substrate is depicted in dark grey, and the metallised vias and the border copper metallisation are shown in black.

Table 4.5: Final dimensions of the ADLS filter.

Parameter	**Dimension** [mm]
l_{in}	10
l_{res1}	3.19
l_{res2}	3.11
l_{res3}	3.11
a	8.38
a_{vias}	8.93
l_{inv1}	4.76
l_{inv2}	10.64
l_{inv3}	11.93

the different layers are fastened and soldered. Figure 4.18 shows the centre layer of the manufactured prototype.

Figure 4.19 compares the simulated and measured responses. The same TRL calibration kit employed for the previous filters locates the measurement reference plane at the end of the microstrip feeding line. The Filter response shows large deviations due to manufactured tolerances. It is centred at $13.05\,\mathrm{GHz}$, and has an IL of $5.28\,\mathrm{dB}$ that corresponds to a quality factor of approximately 220 . Finally, the return loss excess $15\,\mathrm{dB}$ within the filter passband.

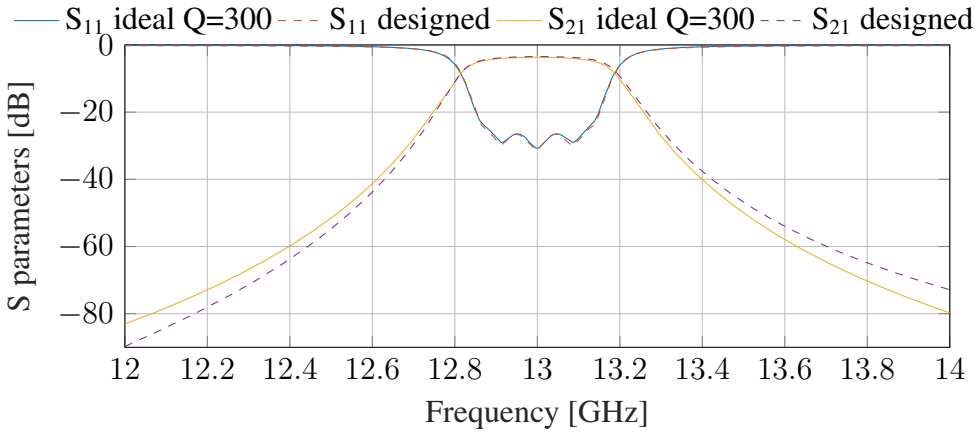

Figure 4.17: Simulated response of the ADLS filter. Ideal response has been computed considering resonators with Q= 300 .

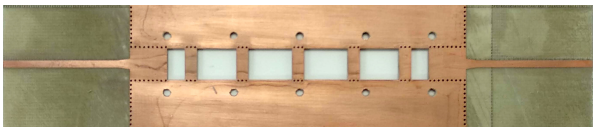

Figure 4.18: Top view of the centre layer of the ADLS filter prototype.

4.2.4 ESICL Filter

The ESICL structure is built by stacking five PCBs, which are processed to form a rectangular coaxial line. For this study, RO4003C substrates with a thickness of $0.813\,\mathrm{mm}$ and a copper cladding of $17.5\,\mu\mathrm{m}$ were used for all the layers. The dimensions of the resulting line are $2.65\,\mathrm{mm}$ of height and $6.00\,\mathrm{mm}$ of width for the outer conductor, and $0.813\,\mathrm{mm}$ of height and $1.82\,\mathrm{mm}$ of width for the inner conductor. Dimensions were chosen considering the final thickness of the stack-up and a characteristic impedance of $50\,\Omega$ [141].

4.2.4.1 Topology and design

Figure 4.20 shows the most representative views of the transition between microstrip and ESICL [141]. The design was based on the transition between a grounded coplanar waveguide and a ESICL developed in [87, 142]. It consists of a feeding microstrip line connected to the final ESICL through a two-step transition. The microstrip line is connected to a quarter wavelength stripline section performed in layers 3 and 4. This stripline feeds a short section of a suspended stripline performed in layers 2, 3, and 4. Finally, the suspended stripline is connected to the ESICL. Depending on the material and dimensions of the inner conductor, several plated vias should be introduced at the beginning of the inner conductor of the ESICL

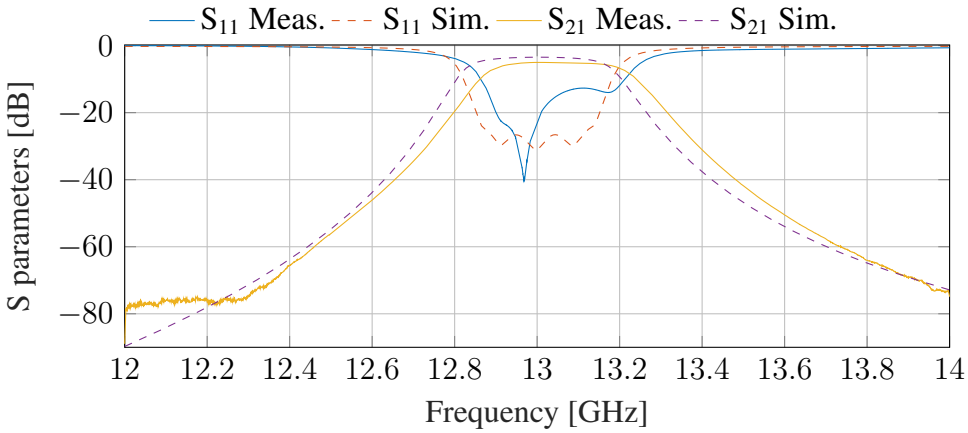

Figure 4.19: Comparison between simulated and measured response of the ADLS filter.

to avoid the propagation of undesired leaky waves between the input and output ports.

The design procedure consists of the following steps. First, the dimensions of the ESICL, the microstrip, the stripline, and the suspended stripline are selected to achieve a $50\,\Omega$ impedance. The theoretical dimensions can be fine-tuned using a numerical simulator (CST) to obtain a more precise result. Initially, the length of the coplanar is set to a quarter of the wavelength in the stripline at the center frequency, and the length of the suspended stripline is chosen to be as short as possible, typically $5\,\mathrm{mm}$. Next, the parameter b_c is chosen to be lower than W_{out}, and W_{cut} is set to a value that can be easily fabricated and ensure the mechanical stability of the design. Finally, W_c, W_t, and l_c are optimised to maximise the return loss in the desired bandwidth, in this case from 0 to $20\,\mathrm{GHz}$.

The dimensions of the optimised transition are listed in Table 4.6, and its frequency response is depicted in Figure 4.21. As can be noticed, the simulated return loss excess $25\,\mathrm{dB}$ for the entire band of interest and $35\,\mathrm{dB}$ for the filter passband.

Table 4.6: Dimensions of the transition from microstrip to ESICL.

Parameter	**Dimension** [mm]	**Parameter**	**Dimension** [mm]
W_{in}	1.82	p_v	0.77
h_{in}	0.813	b_c	3.09
W_{out}	6.00	W_c	1.01
h_{out}	2.65	l_c	2.00
l_{in}	10	W_t	0.82
W_{ms}	1.85	l_t	0.50
l_{ms}	10.00	d_c	0.50
d_v	0.50		

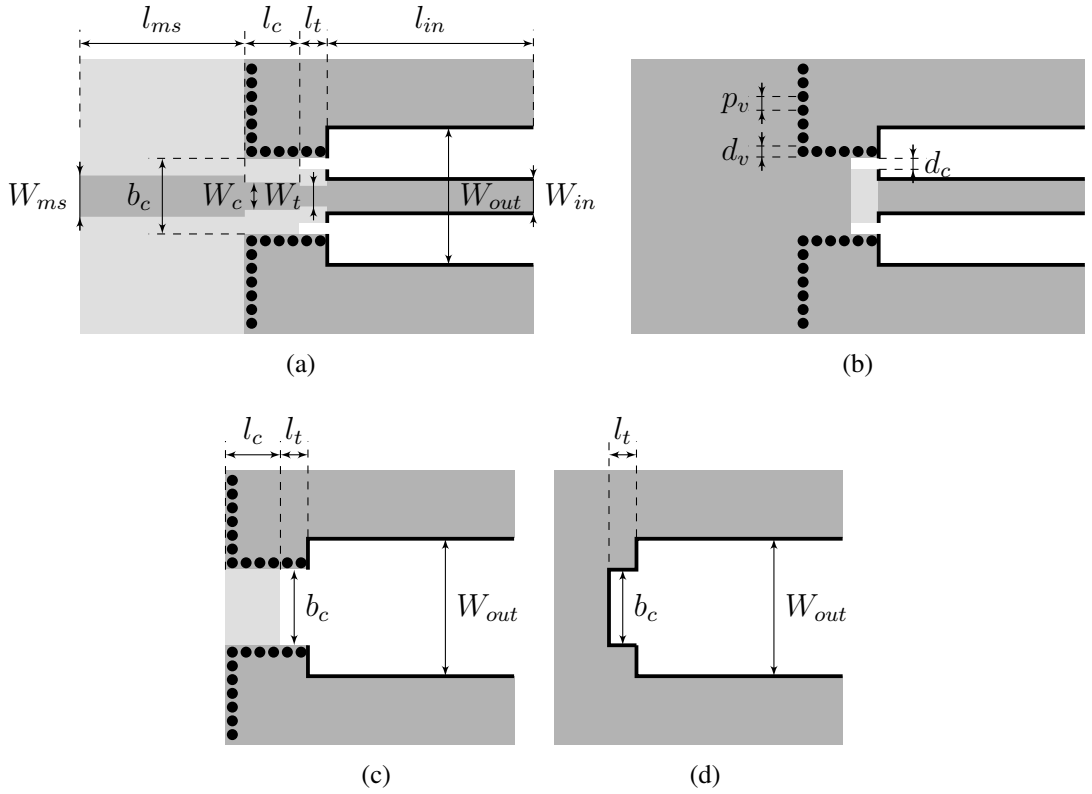

Figure 4.20: Layout of the transition between microstrip and ESICL. (a) Top view of the 3rd layer. (b) Bottom view of the 3rd layer. (c) Bottom view of the 4th layer. (d) Top view of the 2nd layer. The dielectric substrate is shown in light grey, the copper metallisation on top of the substrate is depicted in dark grey, and the metallised vias and the border copper metallisation are shown in black.

The layout of the filter is presented in Figure 4.22. The design is based on the filter developed in [19]. This topology utilises half wavelength short-circuited sections of ESICL as resonators. These resonators are coupled through shunt inductances that are implemented by short-circuiting the active and ground conductors of the ESICL in the centre layer (See Figure 4.22). The shunt inductances act as impedance inverters whose value can be controlled with the length of the short connection L_{invn}.

The dimensions of the filter are in Table 4.7, and its results are shown in Figure 4.23. The simulated response has an insertion loss of $0.90\,\mathrm{dB}$ at the center frequency, corresponding to a quality factor of approximately 1220.

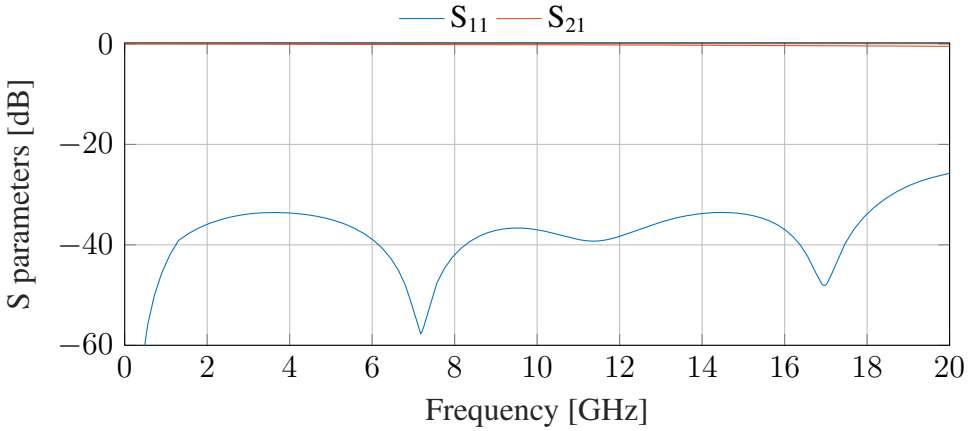

Figure 4.21: Simulated response of the transition from microstrip to ESICL.

Table 4.7: Final dimensions of the ESICL filter.

Parameter	**Dimension** [mm]
l_{in}	10
l_{res1}	9.19
l_{res2}	9.32
l_{res3}	9.32
l_{inv1}	1.32
l_{inv2}	5.20
l_{inv3}	6.02

4.2.4.2 Experimental results

A prototype of the proposed filter was manufactured using RO4003C substrate with a thickness of $0.813\,\mathrm{mm}$ and a copper cladding of $17.5\,\mu\mathrm{m}$ for all layers. Figure 4.24 shows a top view of the centre layer. The fabrication process consists of drilling the vias and cutting the cavities of all layers. Then, the different layers are metallised using an electro-deposition system, and the copper claddings of the third and fourth layers are milled and cut to perform the transition layout. Finally, the different layers are fastened and soldered.

Figure 4.25 compares the measured and simulated response of the prototype. The same TRL calibration kit used for the other filters was employed, locating the measurement reference plane at the end of the microstrip feeding line.

The measured insertion loss is $2.11\,\mathrm{dB}$, corresponding to a quality factor of approximately 536. It seems that the manufacturing tolerances strongly impact the return loss within the filter passband. The filter is centred at $12.97\,\mathrm{GHz}$, exhibits a return loss that excess the $15\,\mathrm{dB}$, and has a minimum rejection level of $35\,\mathrm{dB}$.

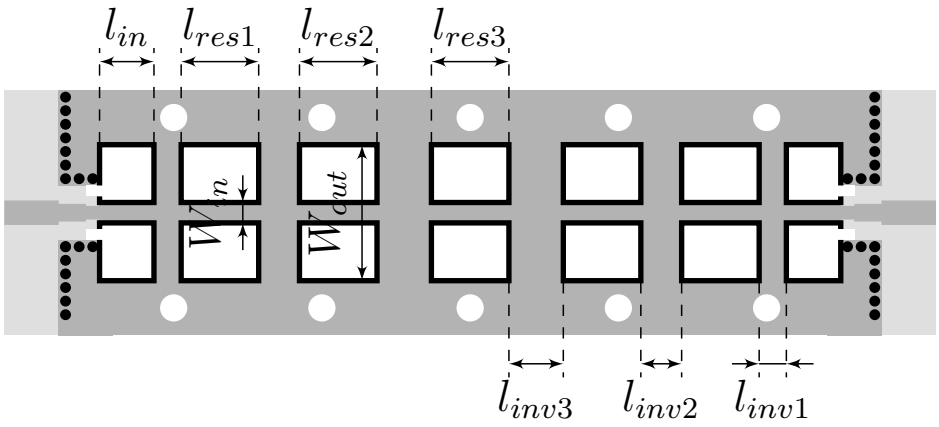

Figure 4.22: Layout of the centre layer in the ESICL filter. The dielectric substrate is shown in light grey, the copper metallisation on top of the substrate is depicted in dark grey, and the metallised vias and the border copper metallisation are shown in black.

4.2.5 Comparison between Prototypes

This section provides a comparison of the measured results for the four fabricated prototypes. Table 4.8 provides a summary of the simulated and measured quality factors, as well as the deviations in central frequency and $-3\,\mathrm{dB}$ bandwidth of the measurements.

Table 4.8: Measured central frequency, bandwidth and insertion loss of SIC filters.

Filter prototype	**Simulated** Q_u	**Measured** Q_u	**Center frequency deviation** [MHz]	**BW$_{\text{-3dB}}$ deviation** [MHz]	**Footprint** [mm × mm]
SIW	277	176	−26.45	−35.27	25 × 90
ADLS	319	221	48.89	4.96	25 × 113
ESIW	1518	644	−5.00	26.30	40 × 140
ESICL	1221	536	−32.29	8.89	20 × 116

All prototypes have demonstrated good performance. However, there has been a degradation in the simulated quality factor for all the filter realisations. The empty filter structures (ESIW and ESICL) demonstrate significantly higher quality factors compared to the filled structures (SIW and ADLS), at the cost of increasing the footprint. Based on these results, empty filters would be suitable for high-performance applications, while the filled realisations can be used in applications where miniaturisation is critical.

Considering frequency deviation, the ESIW filter has the lowest frequency shift, whereas the other realisations show similar deviations. It is interesting to note that the ADLS and

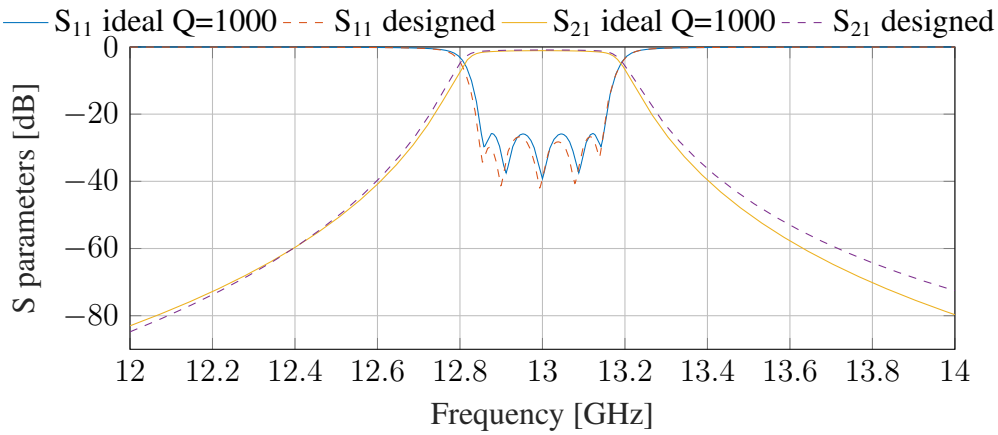

Figure 4.23: Simulated response of the ESIW filter. Ideal response has been computed considering resonators with Q$=1000$.

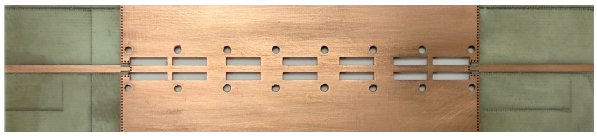

Figure 4.24: Top view of the centre layer of the ESICL filter prototype.

ESICL realisations have a significantly lower deviation in bandwidth. This is because these topologies utilise larger elements for synthesising the coupling elements, making them less sensitive to manufacturing deviations than the other structures. This effect can be explored in future works to develop filters with a lower sensitivity to manufacturing tolerances.

4.3 Qualification for Space Applications

This section assesses the reliability and performance of the SIC filters developed in the previous section under the harshest space conditions. The study is divided into three main parts: the first section focuses on thermal stability tests, the second covers vibration tests, and the final part addresses the multipactor effect.

4.3.1 Thermal Stability

In this section, we analyse the effect of temperature gradients in the response of the SIW, ESIW, ADLS and ESICL filters introduced in the last section. Firstly, we estimate the deviations in the filter response produced by a temperature change using numerical models of the filter topologies. Then, we present the results of two thermal cycling tests: one performed un-

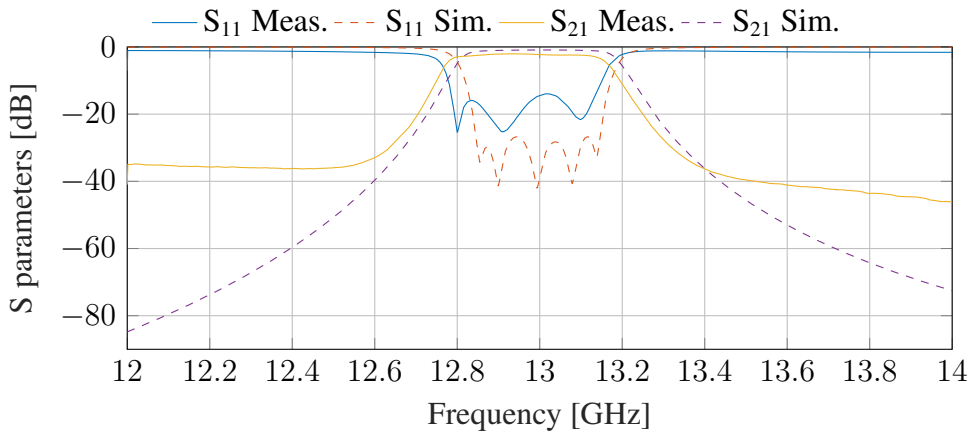

Figure 4.25: Comparison between simulated and measured response of the ESICL filter.

der atmospheric pressure and another performed under high vacuum conditions. These tests were performed per the ECSS-E-ST-10-03C standard [89] and aim to evaluate the ability of the filters to withstand the temperatures that will experience throughout their operational lifetime.

4.3.1.1 Thermal analysis and predictions

Temperature fluctuations can significantly impact the frequency response of filters, leading to predictable changes in their electrical performance. As discussed in Section 3.6.1, temperature variations can induce expansions and contractions in the filter dimensions, ultimately affecting their frequency response. Fortunately, the temperature expansion and its effect on the filters' performance can be predicted. In this context, we conducted a series of numerical simulations to estimate potential deviations in the frequency response of the filters across a range of temperatures, ranging from -60 to $95\,^{\circ}\mathrm{C}$. Simulations considered the coefficient of thermal expansion of the RO4003C substrate ($\delta_x = 11\,\mathrm{ppm}/^{\circ}\mathrm{C}$, $\delta_y = 14\,\mathrm{ppm}/^{\circ}\mathrm{C}$, and $\delta_z = 46\,\mathrm{ppm}/^{\circ}\mathrm{C}$ for the X, Y, and Z direction) as well as the thermal coefficient of the substrate permittivity ($\delta_\varepsilon = 40\,\mathrm{ppm}/^{\circ}\mathrm{C}$ for the RO4003C substrate).

Figure 4.26 illustrates the simulated frequency response of the filters, and Figures 4.27 (a) and (b) depict the frequency and BW$-3\,\mathrm{dB}$ shifts with respect to temperature, considering a reference temperature of $25\,^{\circ}\mathrm{C}$. In general, the IL and BW$-3\,\mathrm{dB}$ exhibit minimal changes with temperature. The computed frequency drift (δf_0) for the SIW, ADLS, ESIW, and ESICL filters are $-32.75\,\mathrm{ppm}/^{\circ}\mathrm{C}$, $-27.95\,\mathrm{ppm}/^{\circ}\mathrm{C}$, $-13.36\,\mathrm{ppm}/^{\circ}\mathrm{C}$, and $-9.72\,\mathrm{ppm}/^{\circ}\mathrm{C}$, respectively. As expected, the dielectric-filled implementations show a more significant variation in all the factors due to the variation in the permittivity of the dielectric substrate.

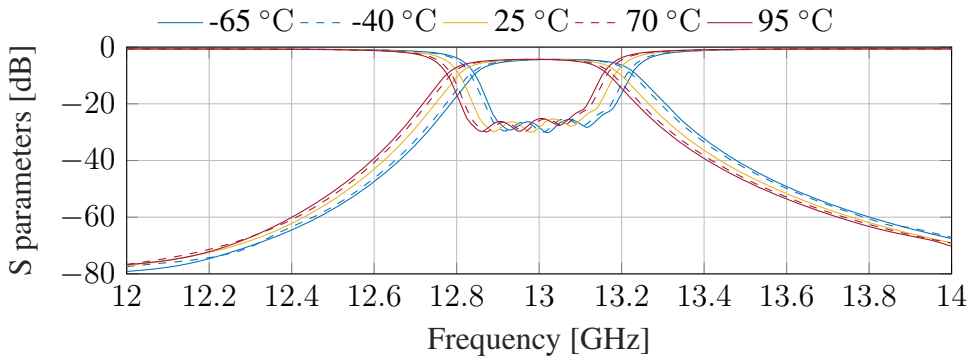

(a)

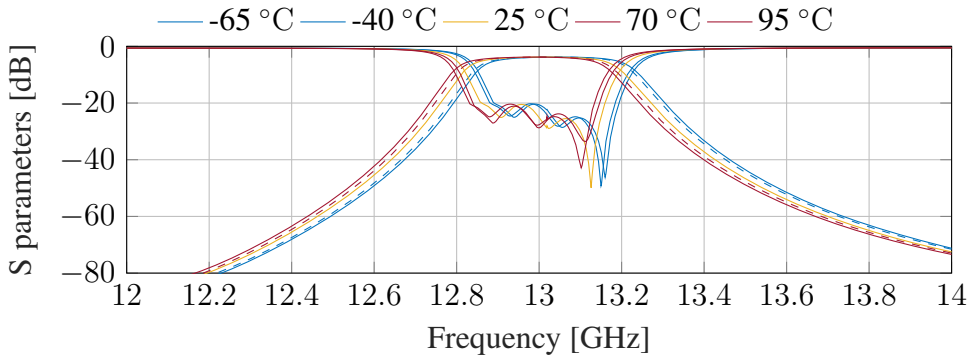

(b)

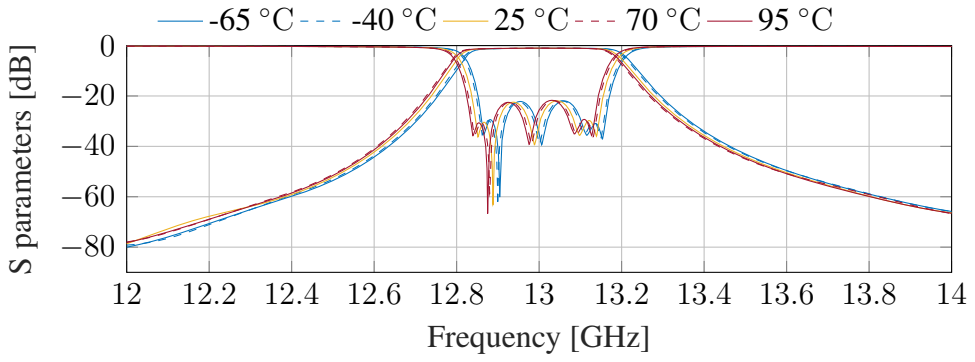

(c)

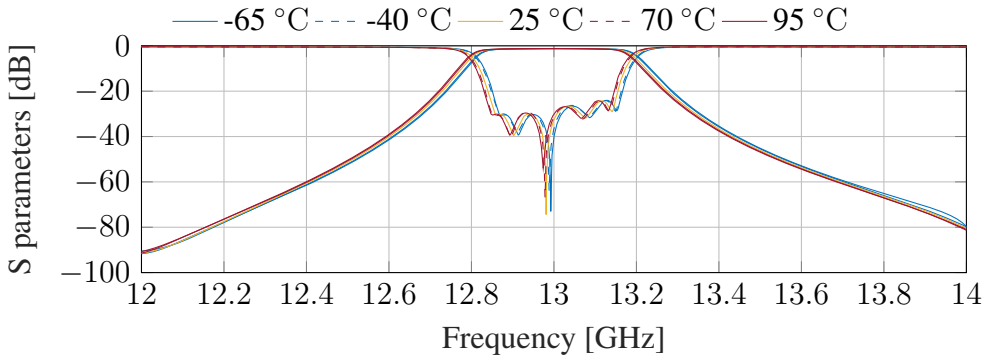

(d)

Figure 4.26: Simulation results for different temperatures and filters. (a) SIW filter, (b) ADLS filter, (c) ESIW filter, and (d) ESICL filter.

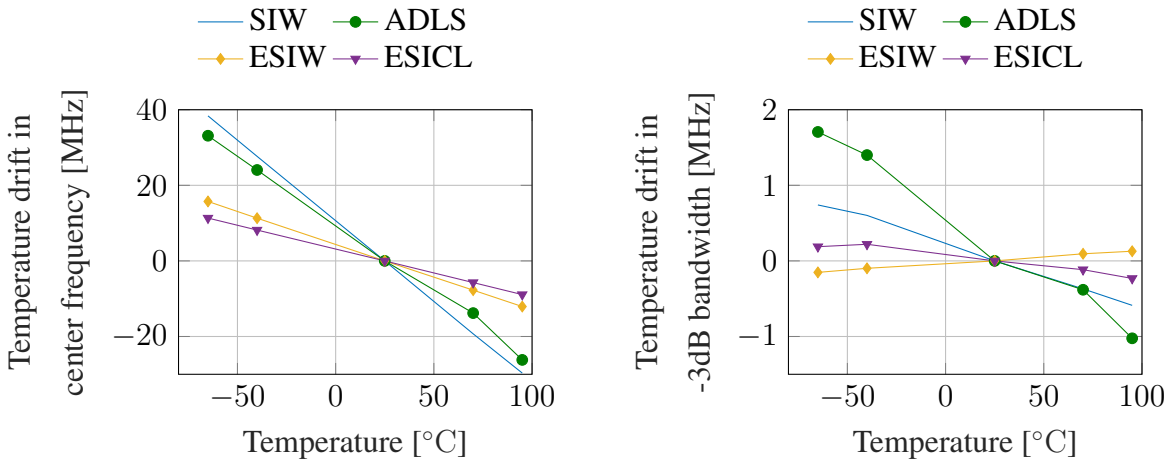

Figure 4.27: Simulated variations in: (a) center frequency and (b) $-3\,\mathrm{dB}$ bandwidth with temperature.

4.3.1.2 Experimental setup and measurement procedure

The studied filters underwent two distinct tests: a thermal cycling test conducted under atmospheric pressure and another thermal cycling test performed under high vacuum conditions. These experiments were carried out at the high-power radiofrequency space laboratory of the European Space Agency (ESA)-Valencian Space Consortium (VSC), in compliance with the technical criteria outlined for evaluating space engineering systems and equipment [89].

The experimental setup for the thermal cycling test under atmospheric pressure was the same as the one employed for testing the additive-manufactured filters in Section 3.6. This configuration encompassed a temperature chamber (V"otsch VT70010), multiple temperature sensors, a Data Acquisition System (DAQ), and a VNA. Numerous temperature sensors were strategically positioned on the devices to monitor their temperature. The temperature of the devices was adjusted to a predefined profile using the thermal chamber, and their responses were measured and recorded once specific temperatures were attained. The temperature range considered for the thermal cycling under atmospheric pressure spanned from -40 to $70\,^{\circ}\mathrm{C}$, while the temperature range for the test under vacuum conditions extended from -60 to $95\,^{\circ}\mathrm{C}$. Both tests included measurements at intermediate temperatures: -40, -35, -25, 25, 60, and $70\,^{\circ}\mathrm{C}$.

To conduct both thermal cycling, the calibration procedure outlined in [129] was followed. This procedure necessitates subjecting all standards within the calibration kits to both

thermal tests and employing the resulting measurements for calibrating the measurement system. The calibration standards included in the TRL calibration kit are displayed in Figure 4.28 (b).

The vacuum test was conducted within a custom-designed vacuum chamber equipped with a dual pump system that maintained a pressure below 10^{-5} hPa. Given that conduction is the primary heat transfer mechanism under vacuum conditions, various test jigs were meticulously designed to ensure effective heat conduction from the thermal base of the vacuum chamber to the prototypes.

- Figures 4.28 (a) and (b) display two aluminium test jigs created to accommodate the filters. These supports work very well for relatively big devices, but they were unsuitable for the elements of microstrip TRL as the microstrip could not be covered.

- To resolve this issue, the microstrip TRL calibration kit's standards were soldered onto thin copper sheets called thermal "bridges," illustrated in Figure 4.28 (c). Copper was preferred as it ensured a good heat transfer. Two cuts were performed on the extremes of the thermal "bridges" to allow fastening them to the thermal plate of the vacuum chamber.

Subsequently, we conducted an initial temperature cycling experiment to assess the efficacy of the aluminium jigs and thermal bridges. In this evaluation, mock-up devices were securely affixed to an aluminium jig and soldered onto a thermal bridge. These assemblies were subjected to a comprehensive temperature cycling process spanning from -80 to $95\,^{\circ}\mathrm{C}$ under vacuum conditions. The outcomes of this evaluation are depicted in Figure 4.29, providing valuable insights into the performance of the employed thermal setup.

While the aluminium jigs and thermal bridges demonstrated effectiveness for larger devices, they faced certain limitations in achieving the lowest temperature required for the test's open standard of the calibration kit. This led us to limit the temperature range of the vacuum test to temperatures above $-65\,^{\circ}\mathrm{C}$, ensuring the reliability and accuracy of the test.

4.3.1.3 Experimental results

The measured response of the filters during the thermal cycling is shown in Figures 4.30 (a)-(d) for test under atmospheric pressure, and in Figures 4.31 (a)-(d) for high vacuum.

Figures 4.32 (a) and (b) summarise the evolution of frequency and insertion loss with temperature observed in the two thermal tests. The deviations observed during both tests are consistent for all filters, except for the ESICL realisation, which exhibits inconsistent results under vacuum conditions. Additionally, the results at $-60\,^{\circ}\mathrm{C}$ were ignored due to the

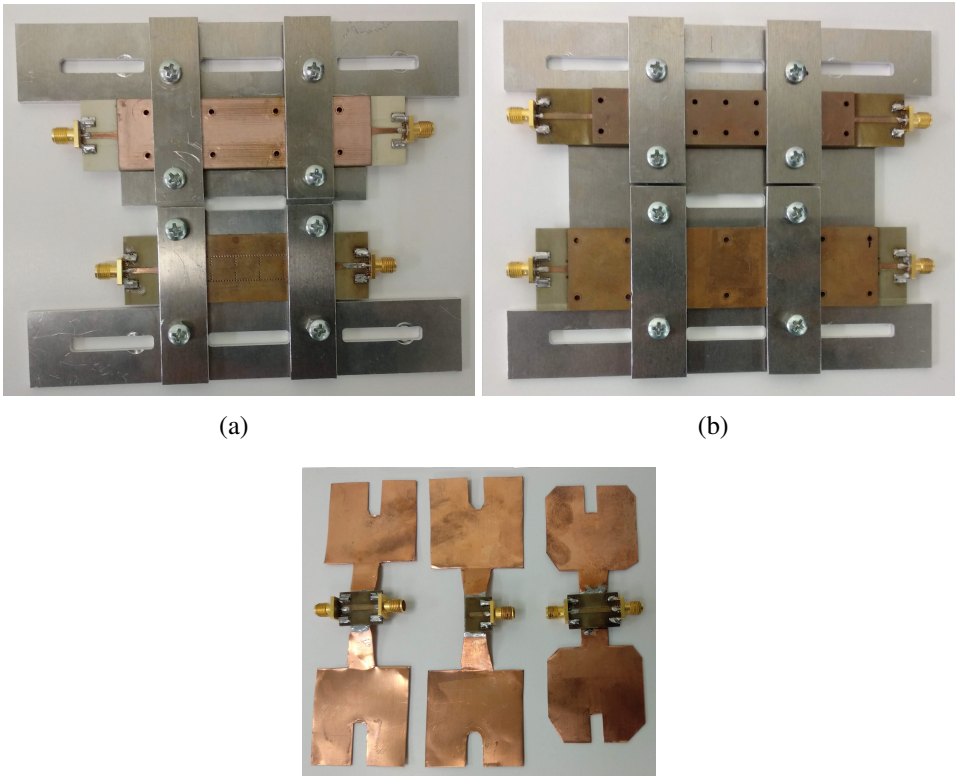

(a) (b)

(c)

Figure 4.28: Test jigs used for the thermal cycling tests at high vacuum conditions. (a) Aluminum jig used for testing ADLS and SIW filters. (b) Aluminum jig used for testing ESICL and ESIW filters. (c) Microstrip calibration kit standards soldered onto thermal "bridges"; from left to right: through, reflect (open) and line.

deviations observed in all parameters at that specific temperature, which could be due to a failure of any part of the measurement setup.

Table 4.9 summarises the simulated and measured frequency drift of the filters. As can be noticed, simulated and measured results are aligned for all filters except for the ESICL realisation that exhibits a deviation closer to the ESIW result. Furthermore, it is worth noting that there are no significant differences between the results obtained under atmospheric pressure and high vacuum conditions.

The filled topologies exhibit a higher loss drift compared to the empty realisations. The maximum deviation observed in the filled filters (SIW and ADLS) is about $\pm 1\,\mathrm{dB}$ for the considered temperature range (-40 to $95\,^{\circ}\mathrm{C}$), whereas for the empty realisations (ESIW and ESICL), it is around $\pm 0.3\,\mathrm{dB}$. This is attributed to the variation of the dielectric loss tangent of the RO4003C substrate with temperature.

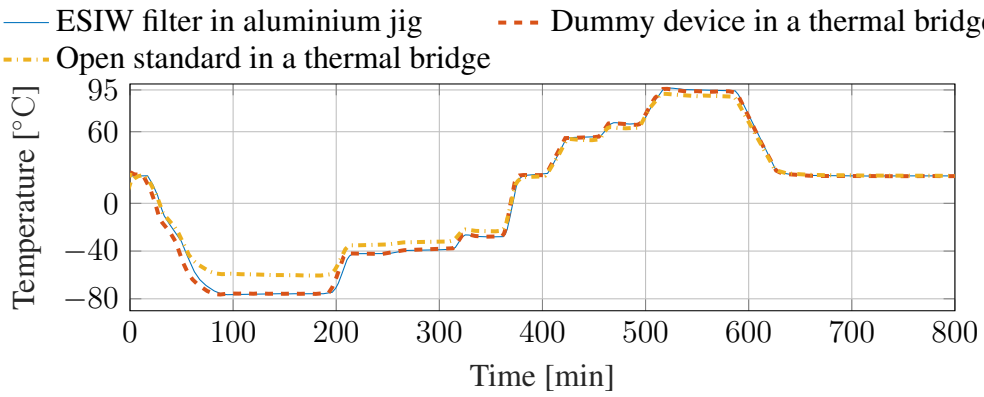

Figure 4.29: Measured temperature profiles for evaluating the performance of DUT jigs for the thermal cycling at high vacuum conditions.

Table 4.9: Temperature drift of SIC filters.

Filter Realisation	Simulation	Atmospheric pressure	Vacuum conditions
SIW	$-32.75\,\mathrm{ppm/°C}$	$-27.21\,\mathrm{ppm/°C}$	$-27.42\,\mathrm{ppm/°C}$
ADLS	$-27.95\,\mathrm{ppm/°C}$	$-21.93\,\mathrm{ppm/°C}$	$-21.43\,\mathrm{ppm/°C}$
ESIW	$-13.36\,\mathrm{ppm/°C}$	$-13.95\,\mathrm{ppm/°C}$	$-17.18\,\mathrm{ppm/°C}$
ESICL	$-9.72\,\mathrm{ppm/°C}$	$-15.35\,\mathrm{ppm/°C}$	$-7.36\,\mathrm{ppm/°C}$

An iterative optimisation approach was employed to estimate the thermal coefficient of the RO4003C loss tangent. This process involved conducting 3D electromagnetic simulations of both the SIW and ADLS filters using CST. The aim was to match the observed loss variation within the temperature range of -40 to $95\,°\mathrm{C}$.

The electromagnetic simulations encompassed the thermal expansion and permittivity fluctuations of the RO4003C substrate, as well as the thermal coefficient for the resistivity of standard copper ($\delta_\sigma = 3930\,\mathrm{ppm/°C}$). Commencing with the thermal coefficient derived from the measured insertion loss (i.e., $1700\,\mathrm{ppm/°C}$ for the SIW filter and $2000\,\mathrm{ppm/°C}$ for the ADLS variant), we employed the Trust Region Framework to optimise the thermal coefficient for the loss tangent. This iterative process culminated in a final thermal coefficient value of $2000\,\mathrm{ppm/°C}$ for both filter realisations.

4.3.1.4 Comparison and discussion

Table 4.10 compares the temperature stability of the four SIC filters presented in this section. It also includes results of similar filters implemented in waveguide and similar SIC structures.

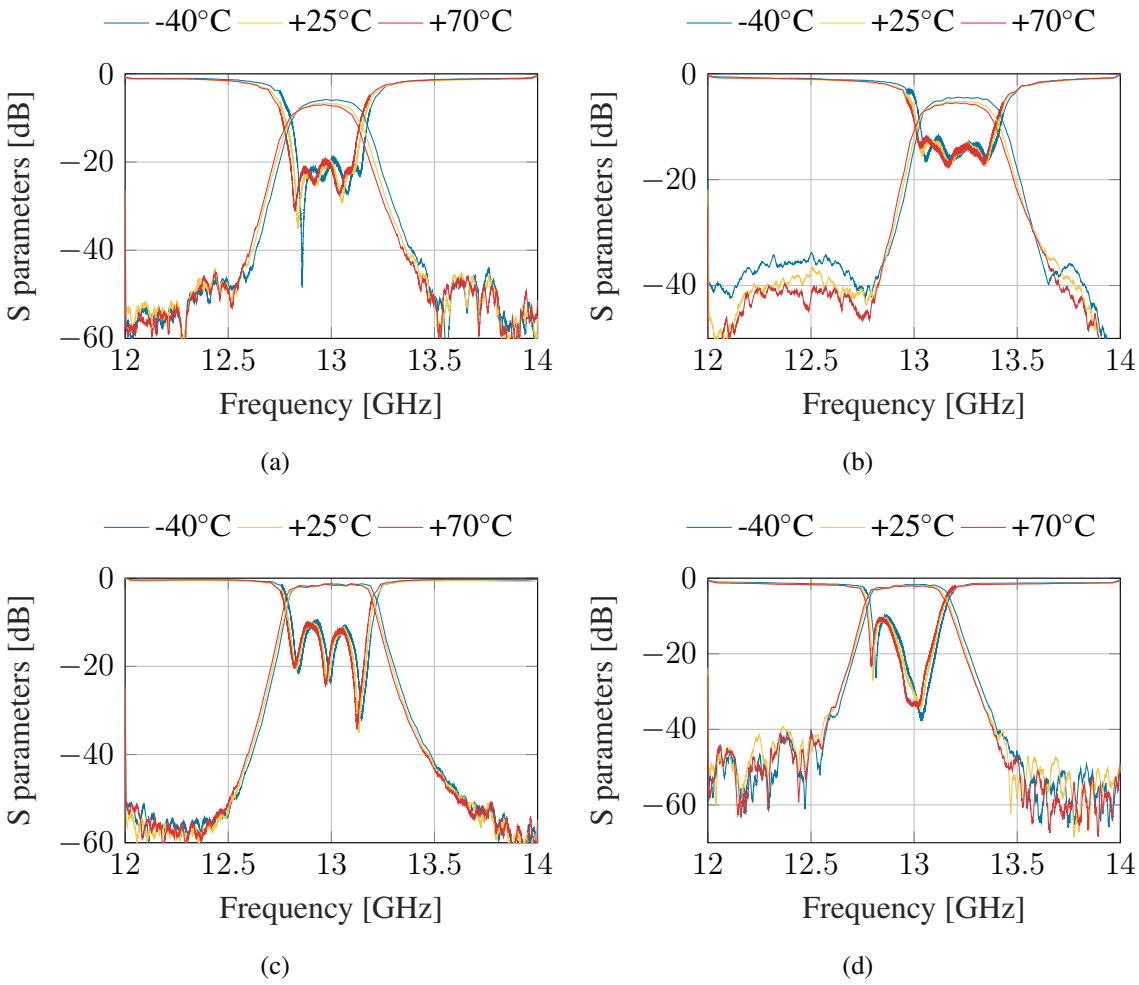

Figure 4.30: Measured response of filters during the thermal cycling under atmospheric pressure: (a) SIW filter, (b) ADLS filter, (c) ESIW filter, and (d) ESICL filter.

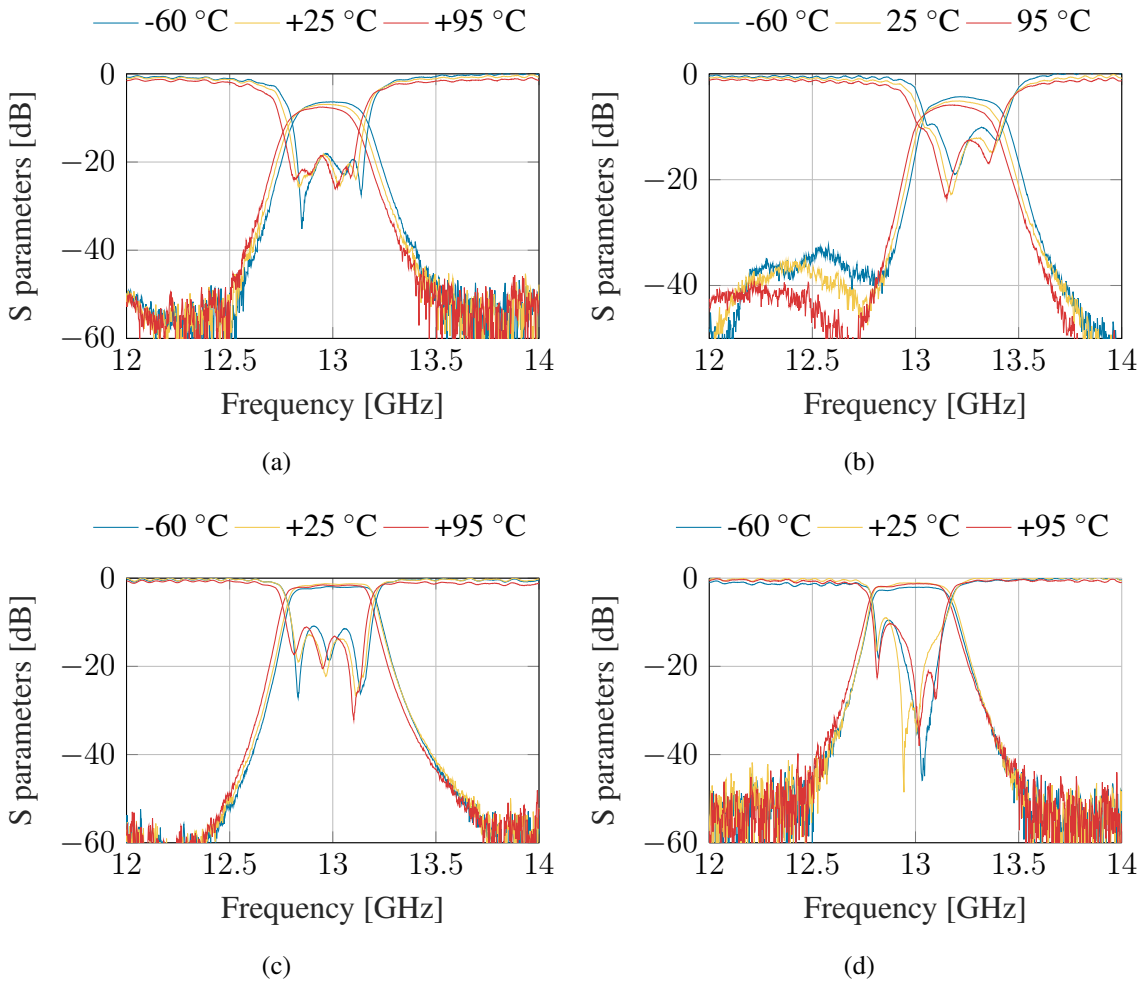

Figure 4.31: Measured response of filters during the thermal cycling under vacuum conditions: (a) SIW filter, (b) ADLS filter, (c) ESIW filter, and (d) ESICL filter.

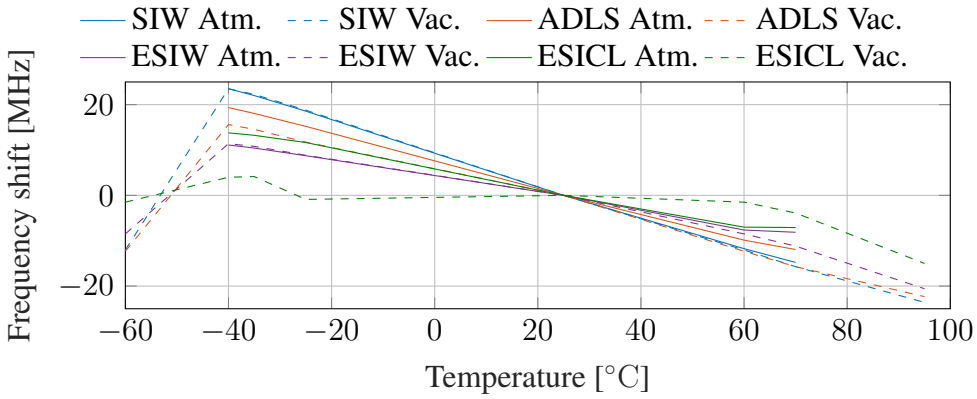

(a)

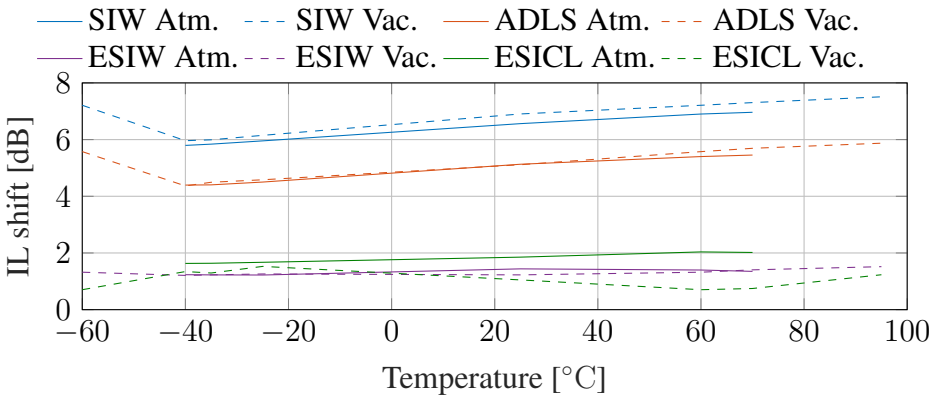

(b)

Figure 4.32: Induced variation in (a) frequency and (b) $-3\,\mathrm{dB}$ bandwidth during thermal cycling for the different filters under test.

The temperature stability exhibited by the filters developed in this section is comparable to that of other filter implementations that do not include a temperature-compensation mechanism, regardless of the guiding technology employed—whether waveguides [93, 129] or substrate-integrated technology [93].

Nonetheless, it is worth noting that the frequency shift observed in the proposed filters is twice that of temperature-compensated implementations detailed in [92, 93]. These compensated filters employ a substrate with a negative thermal coefficient of permittivity, so the effect of the permittivity variation counterbalances the impact of thermal expansion.

Importantly, it should be highlighted that the compensated AFSIW and SIW filters are not fully integrated into planar technologies, whereas our filters are seamlessly integrated into such platforms.

Table 4.10: Comparison of deviations due to temperature gradients in different filter implementations.

Ref.	Filter technology	Planar integration	Filter order	Center frequency [GHz]	FBW [%]	IL [dB]	Temp. [°C]	Δf_0 [%]	Δ BW [%]	Δ IL [%]	Vacuum test
[129]	WR42	No	2	18.38	2.47	0.39	100	-0.13	0.19	9.78	No
[92]	Compensated SIW	Yes	4	10.07	11.6	0.5	-40 80	-0.06 0.05	-4.22 -3.97	-40 -40	No
[93]	Compensated AFSIW	No[2]	4	21.00	1.60	1.08	-40 80	-0.02 0.01	2.38 0.60	-23.14 6.48	No
[93]	ESIW	No[2]	4	21.00	1.59	0.70	-40 80	0.11 -0.11	-0.90 -0.30	-12.86 5.71	Yes
This work	SIW[1]	Yes	5	12.97	2.42	6.08	-60 95 -40 70	0-17 -0.19 0.18 -0.11	2.55 -2.55 4.5 0.20	-8.35 9.06 -11.28 5.57	Yes
This work	ESIW[1]	Yes	5	12.99	3.12	0.63	-60 95 -40 70	0.12 -0.16 0.09 -0.06	1.48 0.49 1.09 -0.24	47.46 23.77 -14.23 -3.52	Yes
This work	ADLS[1]	Yes	5	13.21	2.7	4.47	-60 95 -40 70	0.15 -0.17 -0.17 -0.09	4.49 -1.68 2.81 -2.09	-14.22 14.08 -13.62 5.49	Yes
This work	ESICL[1]	Yes	5	12.98	2.94	0.80	-60 95 -40 70	-0.01 -0.11 0.11 -0.05	-1.57 -3.66 0.16 -0.53	66.82 12.24 -8.82 7.43	Yes

[1] The insertion loss due to transitions has been removed from measured data. As was demonstrated by Belenguer et al. in [18], transitions introduce an average loss of 1 dB.

[2] Compensated AFSIW and SIW filters in [93] do not include transition to any planar line.

4.3.2 Vibration Tests

These tests encompassed sinusoidal sweep and random vibration evaluations, intending to evaluate the impact of mechanical vibrations on the structural integrity and operational efficacy of the filters. Through this evaluation, we aim to determine the viability of deploying these filters within space-based applications.

4.3.2.1 General test considerations and test bench

The SIW, ESIW, ESICL, and ADLS filter prototypes were submitted to two vibration tests specified in the ECSS-E-ST-10-03C standard [89]: the sinusoidal sweep and random vibration tests. Additionally, Two prototypes for the ESIW and ESICL realisations were examined, each featuring different lengths of microstrip feeding lines. This approach allowed us to comprehensively assess the influence of the length of the feeding line on the overall reliability of the prototypes. The mechanical stability of all filters was evaluated by measuring their natural frequency before and after the tests. The test bench was designed in compliance with the ECSS-E-ST-10-03C standard [89].

The filters were attached to a $21\,\mathrm{mm}$ thick methacrylate plate using the holes of their surface-mounted connectors, as shown in Figure 4.33. To prevent any impacts during the tests, we bolted the filters to the vibration plate maintaining a minimum distance between them and the plastic support. As shown in Figure 3.46, we were able to position the methacrylate support in different orientations to facilitate testing for all the three spatial axes.

The same test bench used for testing additively manufactured filters and described in Section 3.6.2 was utilised for these tests.

4.3.2.2 Sinusoidal sweep test

To perform this test, we subjected the device to a sinusoidal sweep vibration between 5 and $140\,\mathrm{Hz}$. The vibration amplitude was set at $1\,\mathrm{g}$, while the sweep speed was set at 2 octaves per minute, following the NASA space testing criteria [98]. The maximum displacement amplitude of the vibration actuator was limited to $5\,\mathrm{mm}$ between 5 and $7\,\mathrm{Hz}$ to ensure the electrodynamics exciter's integrity. As a result, the applied acceleration at these frequencies was limited to $0.5\,\mathrm{g}$, gradually increasing until reaching $1\,\mathrm{g}$ at $7\,\mathrm{Hz}$.

4.3.2.3 Random vibration test

In the random vibration test, the devices under test were exposed to a pseudo-random vibration with a particular ASD. Figure 4.34 displays the measurement of the applied ASD

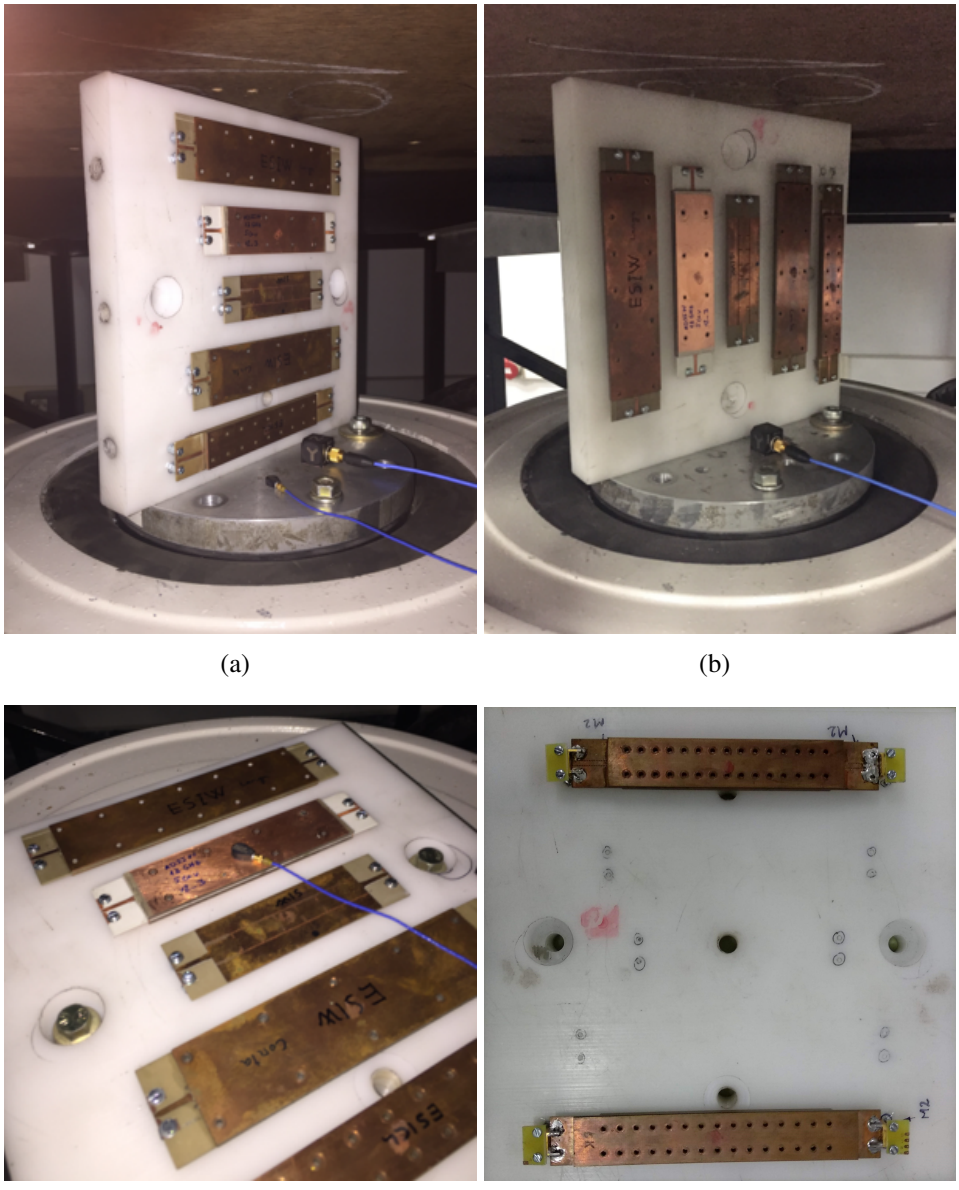

(a) (b)

(c) (d)

Figure 4.33: Setup for vibration tests with the filters under test bolted to the vibration plate: (a) vibration on the X-axis, (b) vibration on the Z-axis, (c) vibration on the Y-axis, and (d) vibration of two ESICL filters with different lengths.

in this test for all three spatial axes. The vibration was applied for $2\,\mathrm{min}$ for each axis, with a root mean square power value of $7.1\,\mathrm{g}$.

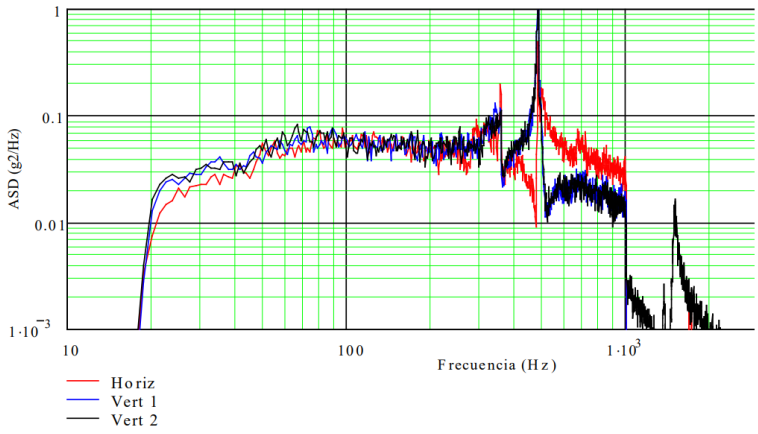

Figure 4.34: Amplitude Spectral Density (ASD) of vibration measured during the random vibration test of the SIC filters.

4.3.2.4 Shock test

During shock testing, devices under test are exposed to high-energy mechanical vibrations of up to $1000\,\mathrm{g}$. This test attempts to simulate the mechanical stress experienced during orbit correction manoeuvres. Due to the high energy needed to perform this test, shock testing could not be carried out. Instead, we present an analysis of possible structural challenges that could arise specifically for substrate-integrated filters.

The structure of the SIW filter is unlikely to be damaged, except in the rare case of a severe breakout of the PCB. Such a strong impact would also affect other parts of the entire communication system, so the integrity of the filter itself would not be a problem.

In contrast, ESIW and ADLS filters can suffer from a separation of their welded layers. Even small gaps between layers can lead to significant resonators detuning and increased insertion loss. On the other hand, the risk of PCB breakout is lower than for the SIW topology since the stack-up of layers is mechanically more robust than a single layer.

For the ESICL filter, the separation of the welded parts is far less critical since the electric current distribution differs from ESIW and ADLS topologies, having no vertical components. This makes the ESICL structure more robust to gaps between layers. Nevertheless, the risk of a breakout of the PCB layer is always present.

4.3.2.5 Natural frequency

To comply with the ECSS standard, it is necessary to measure the natural frequency of the devices under test before and after each vibration test. The standard stipulates that there should be no more than a $5\,\%$ deviation in frequency and no more than a $20\,\%$ deviation in amplitude. However, the size of the devices under test was too small to accurately characterise the deviation in the amplitude of the resonance, so only frequency deviations will be considered in this study.

As in the previous study included in Section 3.6.2, the natural frequency was characterised before and after conducting both the sinusoidal and random vibration tests. The fact that two tests were conducted instead of one provides an additional safety margin for meeting the ECSS standard.

4.3.2.6 Experimental results

The filters' frequency response was evaluated before and after the vibration test. Measurements were done using the TRL calibration kit designed for the filters, compensating the effects of connectors and feeding lines. Figure 4.35 shows the frequency response of the filters. The changes in the frequency response were found to be negligible, only presenting significant variations in the values of the return loss. No important deviations in frequency or insertion loss were observed in any case.

To study the effect of the length of the feeding line of the devices on their response under extreme vibration, the vibration tests were carried out for two different lengths of the ESIW and ESICL filters. Table 4.11 lists the dimensions and natural frequencies of the filters under test.

Table 4.11: Natural frequency deviation of the filters after the vibration test campaign.

Filter	Height [mm]	Width [mm]	Total length [mm]	Initial Freq. [Hz]	End freq. [Hz]	Freq. deviation [%]
SIW	1	25	90	424	425	+0.2
ESIW Short	3	40	130	349	348	+0.3
ESIW Long	3	40	140	303	289	+4.6
ADLS	3	25	113	494	478	+3.2
ESICL Short	4	20	116	435	434	-0.2
ESICL Long	4	20	136	355	345	+0.3

The deviation in natural frequency before and after the tests did not exceed the established limit of $5\,\%$. The extended length ESIW filter exhibited the highest variation, followed by the ADLS filter. The remaining filters showed variations below $0.3\,\%$, demonstrating their

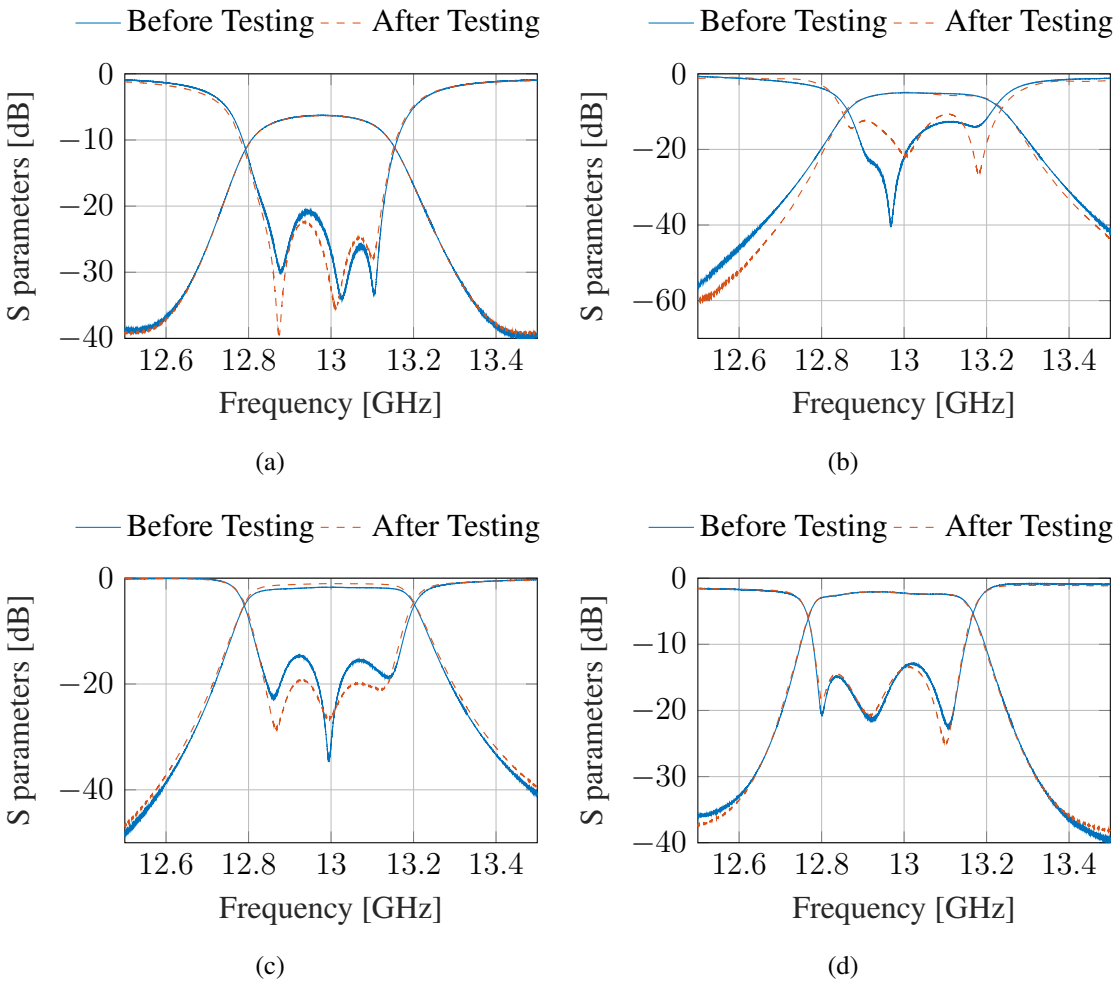

Figure 4.35: Frequency response of filters before and after the test campaign: (a) SIW filter, (b) ADLS filter, (c) ESIW filter, and (d) ESICL filter.

structural strength. It is interesting to note that longer versions of the filters exhibited lower natural frequencies and higher variations after tests, but all results remained under the $5\,\%$ limit. No significant differences were observed between the results obtained for filters of different lengths in terms of their deviation in natural frequency or frequency response. Thus, the length of the feeding line is not a significant parameter regarding mechanical reliability.

The vibration tests conducted on the substrate-integrated filters demonstrated their capability to withstand mechanical disturbances generated by orbit allocation. Additionally, frequency response measurements showed that the vibrations did not affect the filters' performance, indicating their suitability for space applications.

4.3.3 Multipactor

As previously mentioned, the multipactor effect can cause a self-stimulated avalanche of electrons that limits the device's maximum power handling capability. This section presents the predictions of the multipactor effect on the substrate-integrated filters developed in this part of the thesis, including the estimation of maximum input power values, as well as the identification of critical areas and frequencies. Only the ESIW, ESICL, and ADLS filters that are totally or partially empty will be studied, as the multipactor effect requires a high vacuum condition to appear.

The measured response of the SIC filters exhibits a significant deviation that makes it impossible to accurately approximate them using a circuit-based model (using the coupling matrix prototype) or a simulation model (using a combination of CST and Spark 3D). As a result, it is impractical to analyse the multipactor phenomenon using the approaches developed in Section 3.6.3. In this case, the multipactor power threshold was estimated using the simple parallel plate model and the ideal response of the filters.

4.3.3.1 Multipactor prediction

For the study of the multifactor effect, the parallel plate model developed by Hatch and Williams has been used, whose procedure for finding the multipactor threshold is explained below.

First, the distribution of the electric field along the filters is obtained, and the voltage in the area where the electric field is at its maximum is calculated as a function of frequency. The electric field distribution of the ESIW and ADLS filters was examined at the centre of the waveguide where the TE_{01} mode has the maximum electric field. In the case of the ESICL, the electric field was computed at the centre of the top gap, where the electric field intensity is higher.

Figure 4.36 illustrates the frequency distribution of the electric field in the different filters. The different filter implementations show similar electric field distribution. The maximum field intensity is situated in the centre of the second resonator near the upper ($13.2\,\mathrm{GHz}$) and lower ($12.8\,\mathrm{GHz}$) cutoff frequencies.

Next, the maximum voltage in each guided medium (waveguide or coaxial line) was calculated by integrating the electric field along its trajectory. In the case of the ESIW and ADLS filters, this voltage was determined by multiplying the waveguide's height with the electric field, given that the TE_{01} mode's electric field is uniformly distributed along this axis. Conversely, for the ESICL filter, the voltage calculation involved integrating the electric field along its path due to the radial attenuation of the TEM mode's electric field. Figures 4.37 (a), (c), and (e) show the frequency dependence of the maximum voltage for the empty areas of the ESIW, ESICL and ADLS filters. As anticipated, the voltage distribution across all filter variations exhibits a consistent pattern, attaining its peak near the cut-off frequencies.

Then, the Voltage Magnification Factor (VMF) was calculated for each frequency point. This factor is defined as the ratio between the maximum voltage at the specific frequency and the input voltage (V_{in}). The voltage at the input of the device (V_{in}) was obtained by integrating the electric field at the input port.

Finally, the threshold power can be obtained using equation 4.11. This expression relates the VMF, the characteristic impedance of the fundamental mode of the guide Z_0, and the maximum voltage required for multipactor discharge in the parallel plate equivalent Vth to threshold input power [74, 143].

$$P_{in}^{th} = \frac{|V_{th}|^2}{2Z_0 \mathrm{VMF}^2 (1 - |S_{11}|)^2} \tag{4.11}$$

We already know the value of all these variables, except for the threshold voltage Vth that can be obtained from the Hatch and Williams susceptibility charts provided by the ECSS multipactor calculator tool of the European Space Agency. Figures 4.37 (b), (d), and (f) show the maximum input and output power for each filter as a function of the frequency. The maximum input power was computed with equation 4.11, and the output power equation was calculated as $P_{out}^{th} = P_{in}^{th} \cdot |S_{21}|^2$

Table 4.12 summarises the critical areas and frequencies of the different filter topologies. The critical area is the centre of the second resonator for the ESIW and ESICL filters and the interface between the second inverter and the second resonator for the ADLS filter. The critical frequencies are $13.17\,\mathrm{GHz}$ for the ESIW filter and $12.85\,\mathrm{GHz}$ for the ESICL and ADLS filters.

When it comes to critical input power thresholds, the ESIW filter registers $247\,\mathrm{W}$, the ADLS realisation reads $270\,\mathrm{W}$, and the ESICL topology registers $186\,\mathrm{W}$. Notably, these

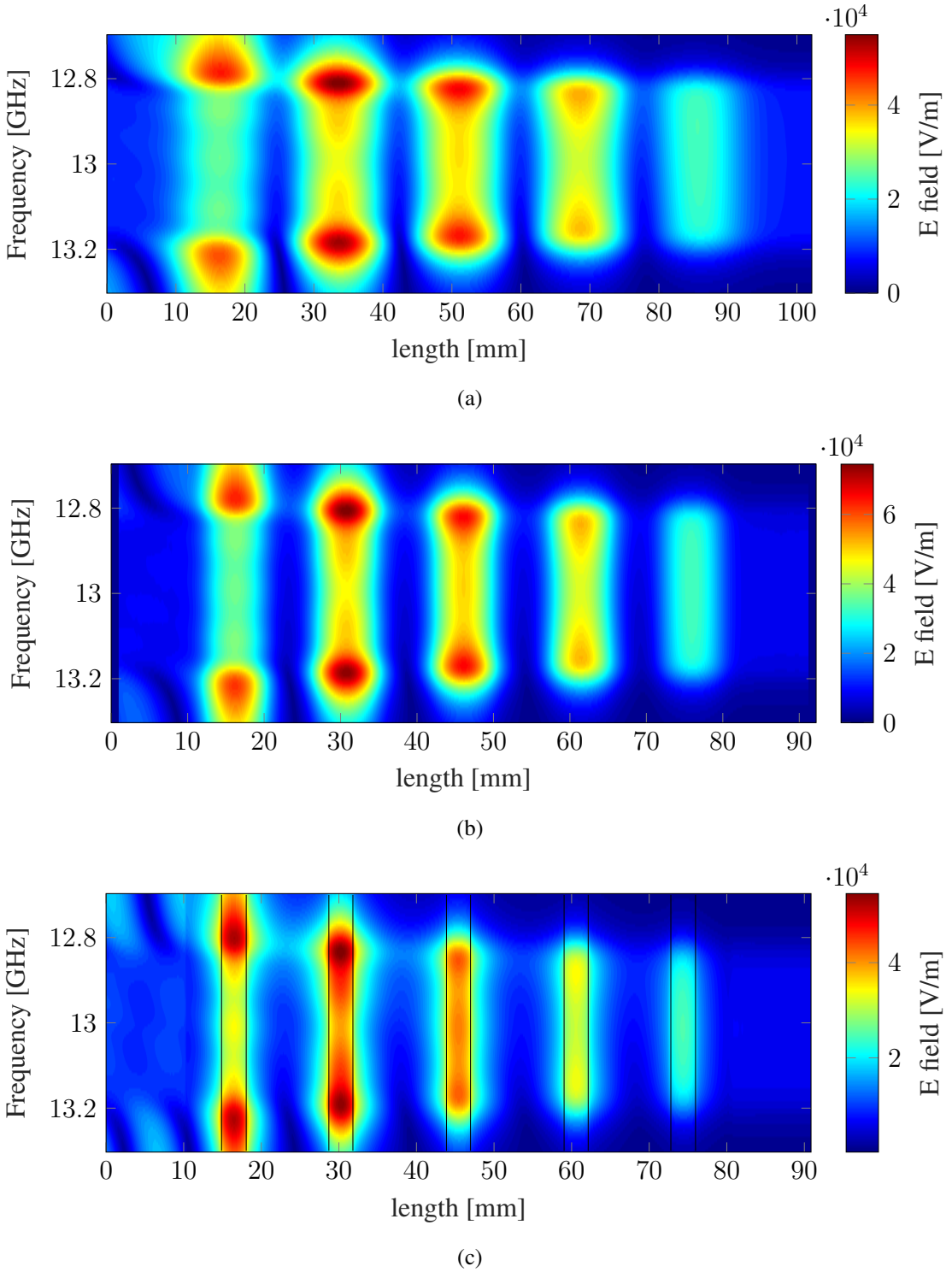

Figure 4.36: Electric field distribution in the different filters along their central line: (a) ESIW filter, (b) ESICL filter, and (c) ADLS filter. The figures show the distribution of the electric field for different frequencies along the length of the filters at the position with maximum field intensity.

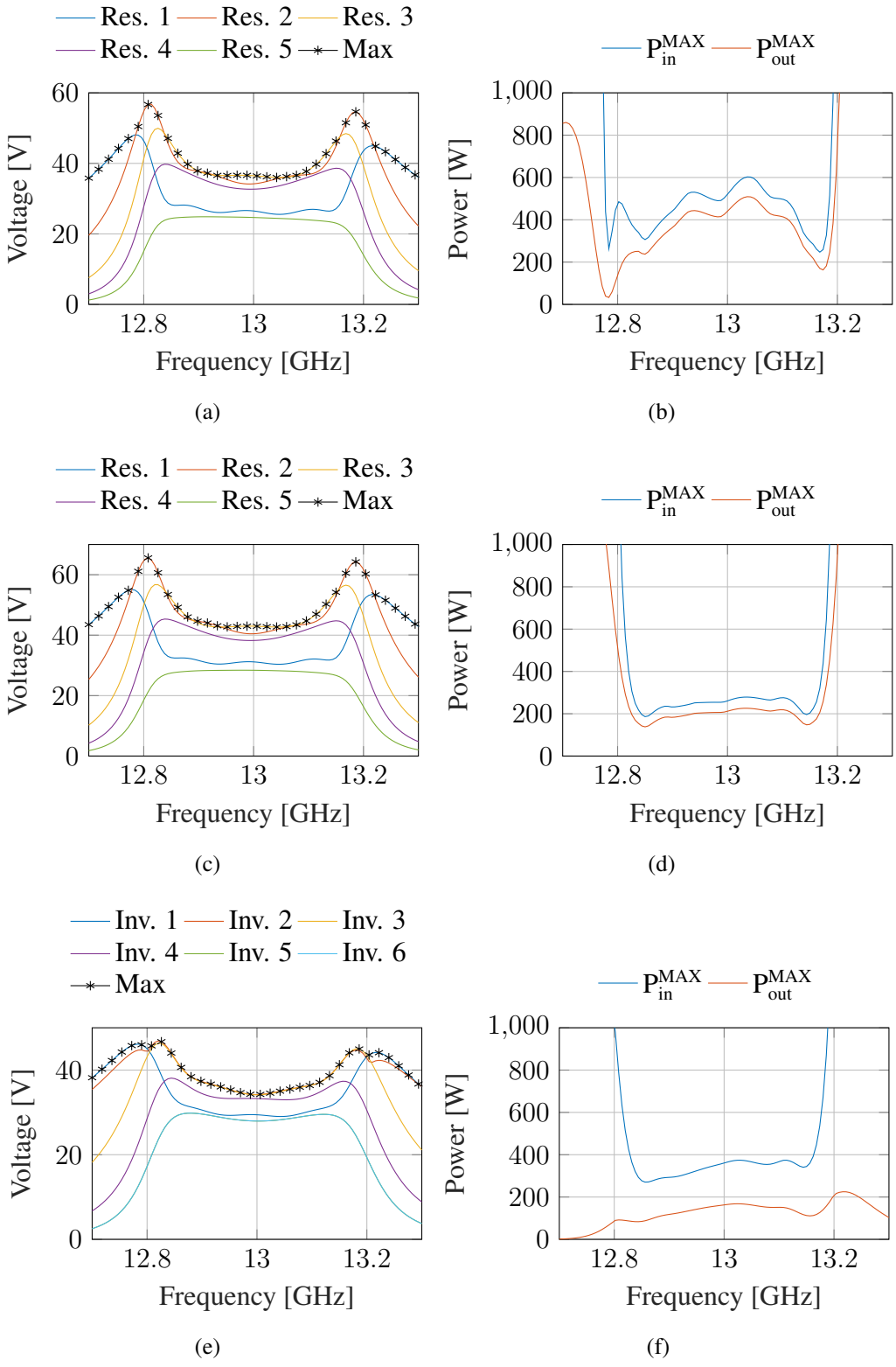

Figure 4.37: (a) Voltage distribution of the ESIW resonators, (b) maximum power of the ESIW filter, (c) voltage distribution of the ESICL resonators, (d) maximum power of the ESICL filter, (e) voltage distribution of the ADLS inverters, (f) maximum power of the ADLS filter.

values were calculated with the parallel plate model, which assumes a uniform electric field distribution between the two plates. While this assumption aligns well with the field distribution of the ESIW and ADLS filters, it is less apt for the field distribution of the ESICL filter. As a result, the prediction for this topology is probably much more conservative than those of the other filter realisations. However, considering that the parallel plate model sets up a worst-case scenario, the yielded threshold values (exceeding $200\,\mathrm{W}$) are sufficiently high for most space communications systems based on LEO and MEO orbits.

Table 4.12: Most important data for multipactor analysis of SIC filters.

Filter	**ESIW**	**ESICL**	**ADLS**
Critical frequency (GHz)	13.17 / 12.78	12.85	12.85
Maximum Voltage (V)	54.34 / 56.77	65.57	46.87
Critical resonator	2nd / 2nd	2nd	2nd
Maximum input power (W)	247 / 263	186	270

4.4 Substrate-Integrated Dividers

The low-loss and wide operation bandwidth of the ESICL makes it especially suitable for low-frequency applications. Compared to other transmission lines, such as the microstrip or the coplanar waveguide, the ESICL exhibits lower insertion loss and high electromagnetic shielding. These factors make it very suitable for demanding and high-power applications at C-band, including research pico- and nano-satellites applications or high-throughput mobile communication systems operating at low frequencies. This section presents three demonstrator models of redistribution elements broadly used in the industry: a T-junction divider, a Wilkinson divider, and a 90° hybrid directional coupler. Moreover, a new design of ESICL with a broader operational bandwidth and its associated transition to coplanar waveguide are presented.

4.4.1 ESICL Design and Transition

Section 4.1.3 introduced the structure and design equations of the Empty Substrate Integrated Coaxial Line (ESICL). However, this study omits a comprehensive analysis of its multimode behaviour. While every transmission line inherently supports multiple modes

of propagation, operating within the single-mode bandwidth is highly recommended. Consequently, this section delves into a numerical multimode analysis of the ESICL structure, encompassing its associated transition to a grounded coplanar waveguide.

Figure 4.38 depicts the electric field distribution of the first four modes of a square ESICL. The fundamental mode is a TEM mode with a cut-off frequency of $0\,\mathrm{GHz}$. The other three high-order modes that propagate through the structure are TE modes, whose cut-off frequencies mainly depend on the width and height of the inner and outer conductors.

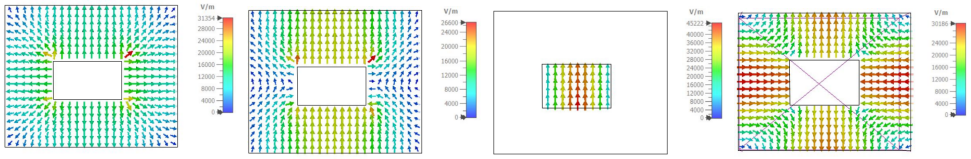

(a) TEM (b) TE (c) TE_{10} (d) TE

Figure 4.38: Field distribution for the four lowest order modes of the Empty Substrate Integrated Coaxial Line.

With this in mind, the dimensions of the ESICL were optimised to obtain not only a $50\,\Omega$ line impedance but also a broad monomode bandwidth, resulting in the dimensions of Table 4.13.

Table 4.13: Dimensions for the proposed Empty Substrate Integrated Coaxial Line (ESICL). W_{inner} is the width of the inner conductor, W_{outer} is the width of the outer conductor, H_{inner} is the height og the inner conductor, and H_{outer} is the height of the outer conductor.

Parameter	Designed ESICL [mm]	ESICL design from [87] [mm]
W_{inner}	0.960	1.917
H_{inner}	0.584	0.933
W_{outer}	2.124	6.000
H_{outer}	1.748	2.733

The cut-off frequencies (f_c) of the first four modes of the proposed ESICL are compared with a previous design [87] in Table 4.14, whose dimensions are also included in Table 4.13. As can be noticed, the proposed line exhibits a monomode bandwidth of $58.9\,\mathrm{GHz}$, more than twice the bandwidth of the previous design.

The proposed ESICL is built in a stack-up of RO4003C substrates with a relative permittivity of $\varepsilon_r = 3.55$. The layer 3 is $0.508\,\mathrm{mm}$ thick, while layers 2 and 4 are $0.406\,\mathrm{mm}$ thick.

Table 4.14: Cut-off frequencies (f_c) of the first four modes of the Empty Substrate Integrated Coaxial Line (ESICL) structures for two designs.

Mode	f_c of the proposed ESICL [GHz]	f_c of the ESICL proposed in [87] [GHz]
TEM mode	0	0
2nd mode (TE)	58.9	21.5
3th mode (TE)	61.9	39.1
4th mode (TE)	105.9	51.2

All substrates have a $17.5\,\mu\mathrm{m}$ copper cladding on the top and bottom layers that are thickened during the manufacturing process, obtaining a final metallisation thickness of approximately $57.5\,\mu\mathrm{m}$ on both sides.

The proposed design offers an improved single-mode bandwidth, yet it does face a significant challenge: the cross-section area of the inner conductor is small, potentially compromising its mechanical strength. To address this concern, the transition developed in [87] was modified to enhance the mechanical integrity of the junction where the inner conductor and the transition meet. Figure 4.39 displays the new layout of the transition. Similar to the previous design, it consists of a grounded coplanar waveguide, a quarter-wavelength stripline, and a short section of suspended stripline with an input iris for feeding the ESICL. Notably, the suspended stripline in this version no longer includes the side cuts seen in the earlier design, which were used to accurately define the input iris's width. Instead, the new layout employs a series of metallised vias to implement the input iris, strengthening the connection while precisely defining the width and length of the input iris.

The transition design procedure is described in [87]. Firstly, the dimensions of the different phases of the transition are chosen to achieve a $50\,\Omega$ impedance. The length of the stripline is selected as a multiple of a quarter wavelength, and the length of the suspended stripline is chosen to be as short as possible (in this case, $0.5\,\mathrm{mm}$). These initial dimensions are then fine-tuned using CST to obtain the desired impedance over the operational bandwidth that, in this case, goes from 0 to $20\,\mathrm{GHz}$. Finally, the transition is optimised to maximise the return loss, resulting in the dimensions presented in Table 4.15.

A transition prototype was developed using a mechanical milling machine and an electroplating system, and the different layers were assembled. This prototype employed no soldering as the distribution of the TEM electrical currents makes this structure insensitive to gaps between layers.

Figure 4.40 shows the assembled prototype and Figure 4.41 depicts the simulated and measured response. Measurements results fit the simulations. The transition exhibits a return loss higher than $14\,\mathrm{dB}$ from $0\,\mathrm{GHz}$ to $20\,\mathrm{GHz}$. This transition was used in all the technology

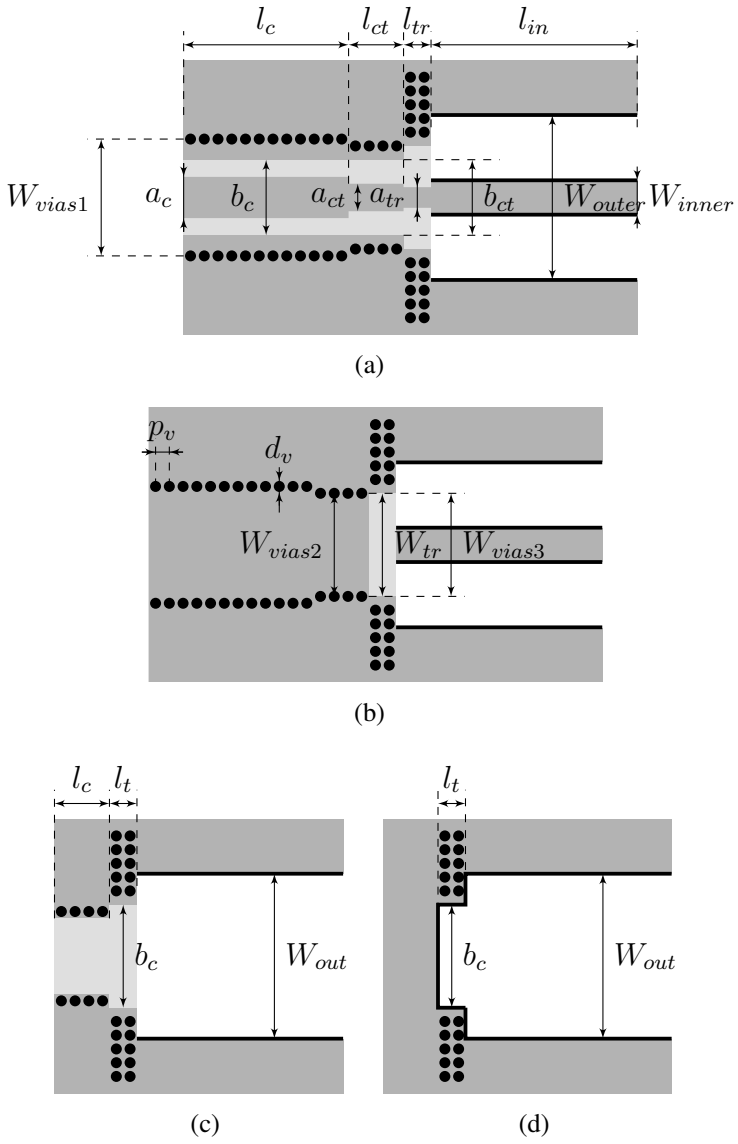

Figure 4.39: Layout of the modified transition between coplanar and ESICL. (a) Top view of the 3rd layer. (b) Bottom view of the 3rd layer. (c) Bottom view of the 4th layer. (d) View of the 2nd layer. In light grey the dielectric substrate, in dark grey the copper metallisation on top of the substrate, and in black the metallised vias and the border copper metallisation.

Table 4.15: Dimensions for the proposed four-stage transition from grounded coplanar waveguide to ESICL.

Parameter	Dimension [mm]	Parameter	Dimension [mm]
a_c	0.84	b_c	1.34
L_c	14.70	L_{ct}	3.50
a_{ct}	0.57	b_{ct}	1.34
W_{vias1}	2.34	W_{vias2}	3.24
W_{ct}	2.34	d_{via}	0.50
a_{tr}	0.92	W_{tr}	1.46
W_{vias3}	2.46	p_{via}	0.70
L_{tr}	1.00		

demonstrators presented in this section of the thesis.

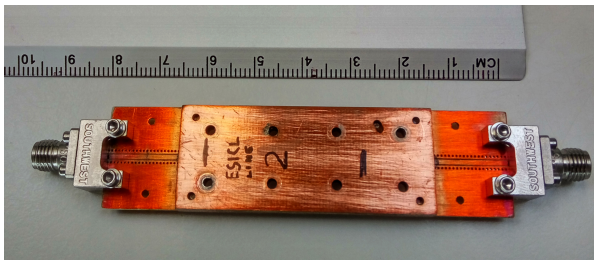

Figure 4.40: Manufactured prototype of the back-to-back transition from grounded coplanar waveguide to ESICL.

4.4.2 ESICL Power Divider

The first technology demonstrator is a T-junction power divider, operating at $5\,\mathrm{GHz}$, which layout is shown in Figure 4.42.

This divider is composed of two transmission lines with a characteristic impedance of $50\,\Omega$ connected to a quarter-wave impedance transformer line with a characteristic impedance of $50/\sqrt{2}\ \Omega$ designed to adapt the two output ports to an input impedance of $50\,\Omega$. The impedance transformer features two linear tapers with an angle of $\alpha = 27°$ to enhance the overall performance. With this configuration, the input port of the divider is adapted to operate as a divider instead of a combiner.

The three arms of the divider were equally oriented in a $120°$ disposition [64] to minimise the capacitive effects of the joint and obtain a wider bandwidth. Finally, the length of the impedance transformer, the transitions, and the joint angle of the output ports were fine optimised to maximise the return loss while maintaining a good output balance. The final dimen-

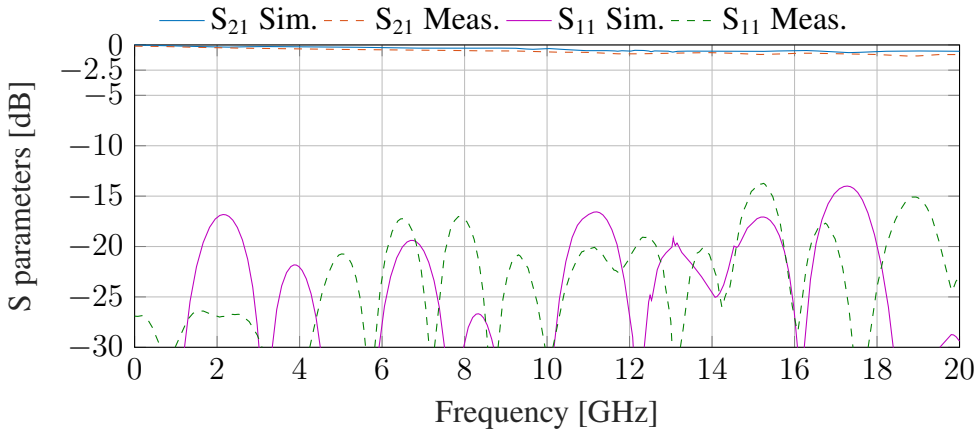

Figure 4.41: Simulated and measured response of the back-to-back transition from grounded coplanar waveguide to ESICL.

sions of the design are: $W_{i1} = 0.96\,\mathrm{mm}$, $W_{i2} = 1.88\,\mathrm{mm}$, $g = 0.60\,\mathrm{mm}$, $L_m = 12.57\,\mathrm{mm}$, and $L_t = 0.93\,\mathrm{mm}$.

The same substrates and techniques employed in the ESICL transition were utilised for the fabrication of this device. The manufactured prototype includes the transition to coplanar waveguide developed in the previous section. Figure 4.43 shows the most representative views of the different layers of the divider and provides a general perspective of the assembled device.

The frequency response of the prototype was measured using a calibrated VNA, and the results are shown in Figure 4.44. It is worth noting that a commercial SOLT calibration was employed, which does not compensate for the effect of connectors and transitions. Figure 4.44 compares the measured parameters of the manufactured device with its simulated counterpart.

As observed from Figure 4.44, the power divider demonstrates good matching at the input port, achieving an optimal match at a center frequency of $4.9\,\mathrm{GHz}$. The practical operational bandwidth was reduced from a $65\,\%$ to an approximately $54.8\,\%$ for a return loss of $15\,\mathrm{dB}$. Furthermore, the power division is $S_{21} = -3.4\,\mathrm{dB} \pm 0.3\,\mathrm{dB}$ and $S_{31} = -3.5\,\mathrm{dB} \pm 0.5\,\mathrm{dB}$ across the operational bandwidth.

4.4.3 ESICL Wilkinson Divider

The second technology demonstrator is a Wilkinson power divider designed to operate at $5\,\mathrm{GHz}$. This passive device is ideally reciprocal, matched at all ports, and lossless when the two output ports are well-matched and balanced [64]. These properties are achieved through

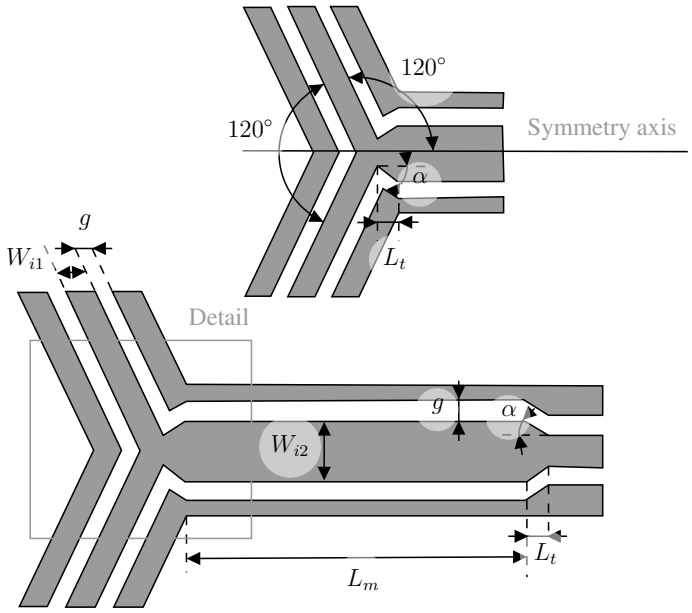

Figure 4.42: Layout of the third layer of the ESICL divider. In grey is the top copper metallisation of the substrate, and in black is the border copper metallisation.

its unique topology, consisting of a $50\,\Omega$ input line connected to two quarter-wavelength transmission lines of $71.7\,\Omega$, between which a lumped resistor of $100\,\Omega$ is connected [64].

Figure 4.45 depicts the layout of the proposed implementation. Implementing the connection of the lumped resistor in shielded transmission lines whose active conductor is encapsulated by the ground is challenging. However, as the ESICL technology is composed of multiple substrate layers, it is possible to mill two striplines in layers three and four that connect the two output ports, enabling the connection of the resistor. This is one of the advantages of SIC structures as they enable the hybridisation of technologies, i.e., the combination of planar and 3D transmission lines.

Implementing the Wilkinson divider with the stripline connection complicates the manufacturing process and increases reflections. A complex process of milling and metallisation was necessary to include the stripline and the surface-mounted resistor. The active conductor of the stripline was milled in the third layer, and the copper cladding of the bottom side of layer four was milled to prevent short-circuiting the stripline. In addition, a hole was made in layers four and five to accommodate the surface-mounted resistor, as shown in Figures 4.46 (a) and (b). Figure 4.45 shows the top view of the third layer, and the manufactured device is displayed in Figure 4.47.

The separation between the output arms was found to be inversely proportional to the input port's matching level. So it was decided to set a minimum separation of $5\,\mathrm{mm}$ between

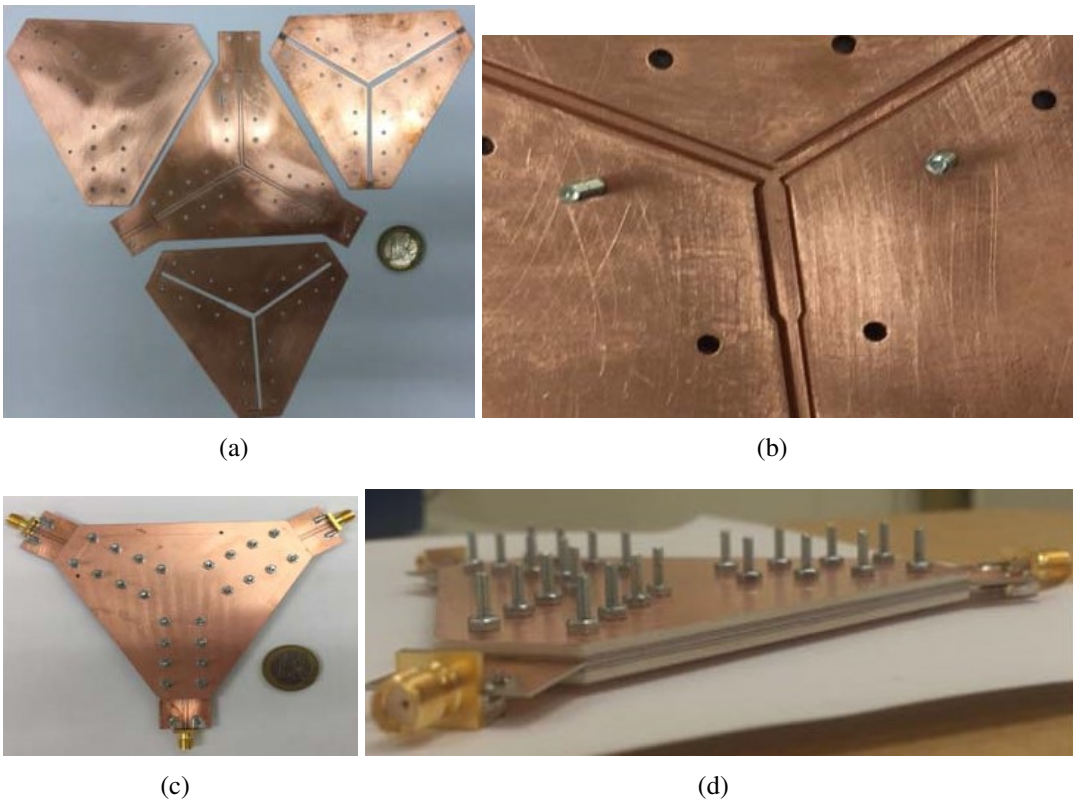

(a) (b)

(c) (d)

Figure 4.43: Most representative views of the divider: (a) Top view of the first, second and third layers, (b) top view of the assembled device without the top layer, (c) top view of the assembled divider, and (d) detail of the device.

output arms and bends at the end of the output lines. These bends were introduced to accommodate the end-launch connectors. Subsequently, an optimisation process was initiated, prioritising achieving optimal input port matching and effective output port isolation rather than focusing on output port matching. In this optimisation process, several key parameters were taken into account, including the lengths of the output transmission lines (L_c), the width of the $50\,\Omega$ characteristic impedance (W_b), the resistor position (L_{smd}), the length of the transition between lines with different impedance (L_t), and the width of the strip line (W_{smd}).

The final dimensions of the Wilkinson power divider are listed in Table 4.16, and its frequency response is shown in Figures 4.48 (a) and (b).

The frequency response of the manufactured device demonstrates an exceptional performance. The relative bandwidth of the input port matching is $20.4\,\%$ for a return loss threshold of $15\,\mathrm{dB}$, while the relative bandwidth for an isolation between the output ports of $15\,\mathrm{dB}$ is $57\,\%$. The measured insertion loss is below $0.5\,\mathrm{dB}$ for the entire bandwidth, and the maxi-

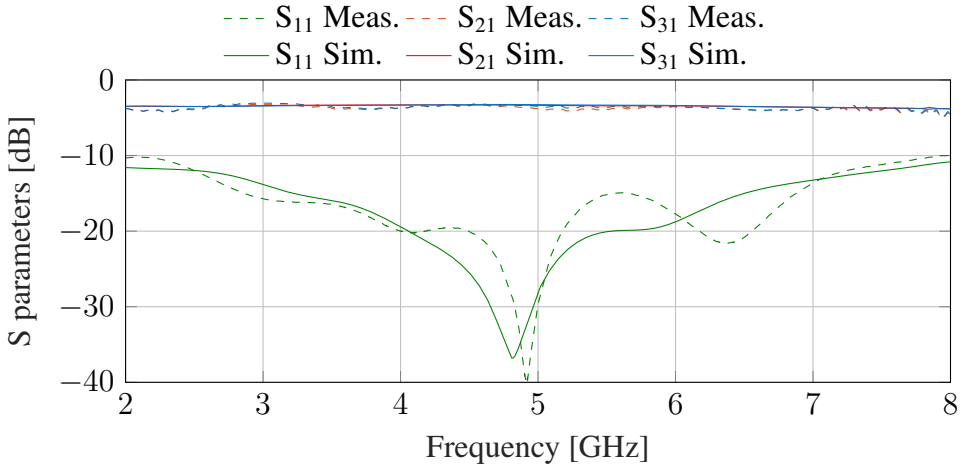

Figure 4.44: Simulated and measured response of the ESICL divider.

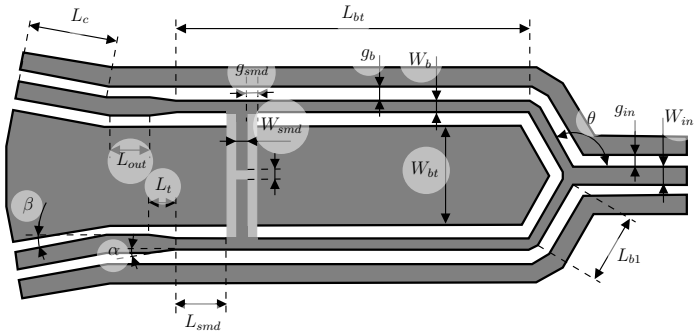

Figure 4.45: Layout of the third layer of the Wilkinson divider. In grey the copper metallisation on top of the substrate, and in black the border copper metallisation.

mum power unbalance is only $0.2\,\mathrm{dB}$. Additionally, the phase unbalance remains below $0.5°$ within the entire operational bandwidth.

A comparison between the proposed Wilkinson divider and a prior design based on a similar substrate-integrated waveguide technology [144] is presented in Table 4.17. The comparison reveals a noteworthy enhancement in terms of operational bandwidth and loss in the proposed design. These results clearly demonstrate the potential of ESICL technology in the development of high-performance components operating in the C band.

4.4.4 ESICL Hybrid Directional Coupler

The third technology demonstrator is a $90°$ hybrid directional coupler with a branch-line topology designed to operate at $5\,\mathrm{GHz}$. The layout of this device is presented in Figure 4.49.

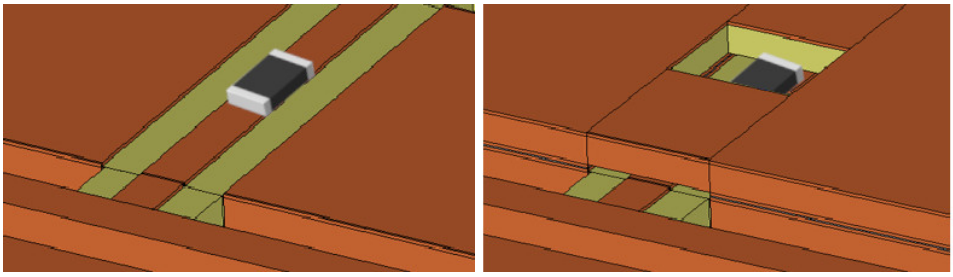

(a) (b)

Figure 4.46: Detail view of the surface-mount resistor: (a) Top view of the third layer and (b) top view of the assembled device without the top cover.

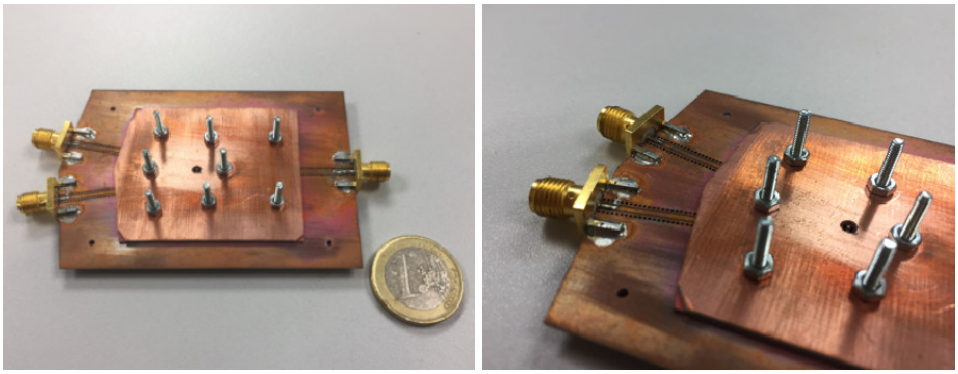

(a) (b)

Figure 4.47: Manufactured prototype of the Wilkinson divider: (a) top view of the device and (b) detail of the coplanar feeding waveguides.

This four-port network divides the input signal between the direct and the coupling ports (ports 3 and 4), while isolating port 2. Additionally, it introduces a phase shift of 90° between the direct and coupled ports. The device comprises four quarter-wavelength transmission lines, where the two vertical lines have a $50\,\Omega$ impedance, and the two horizontal ones have a $50/\sqrt{2}\Omega$ impedance, ensuring equal power distribution between the direct and coupled ports.

The dimensions of the vertical and horizontal transmission lines were optimised using an ideal transmission line model developed in AWR, prioritising the matching at all ports and an equal power distribution between the direct and coupled ports. The optimal electrical response was achieved by selecting a characteristic impedance of $48.26\,\Omega$ for the vertical lines (W_{iv}) and $34\,\Omega$ for the horizontal lines (W_{ih}). These dimensions were then incorporated into the 3D model of the ESICL, and the dimensions of the structure were fine-tuned to obtain the final dimensions listed in Table 4.18.

During the manufacturing of this device, a significant challenge emerged: the disruption

Table 4.16: Final dimensions of the Wilkinson divider.

Parameter	Dimension [mm]	Parameter	Dimension [mm]
L_{in}	6 mm	W_b	0.64 mm
L_{out}	2 mm	W_{bt}	5.2 mm
L_{b1}	3.63 mm	W_{smd}	0.56 mm
L_{b2}	18.63 mm	g_{in}	0.542 mm
L_{smd}	2.76 mm	g_b	0.704 mm
L_c	9.5 mm	g_{smd}	0.52 mm
L_t	1.41 mm	β	10°
W_{in}	0.96 mm	θ	120°
α	7°		

Table 4.17: Performance comparison of the proposed Wilkinson divider.

Parameters	**ESICL**	**Bilayered SIW** (9,75 GHz) [144]
Bandwidth for $S_{11} < -15\,\mathrm{dB}$	20.4 %	not reaching $-15\,\mathrm{dB}$
Bandwidth for $S_{32} < -15\,\mathrm{dB}$	57 %	15.3 %
Bandwidth for $S_{22} < -15\,\mathrm{dB}$	from 1 to $5.2\,\mathrm{GHz}$	not reaching $-15\,\mathrm{dB}$
Insertion loss [dB]	0.5	0.75
Phase unbalance [deg]	0.5	5
Power unbalance [dB]	0.2	Not included
Dimensions [mm]	$42.90 \times 12.55 \times 2.67$	$12.47 \times 12.47 \times 0.76$

of electrical contact between the inner square of the device and the broader PCB, leading to difficulties in achieving proper metallisation during the fabrication process. This problem was overcome by producing the inner square as a separate part, which can be affixed later to the rest of the device using bolts. Other than this challenge, the same substrate materials and fabrication methods used in the production of the ESICL transition were used in the manufacturing process of this device.

Figure 4.51 (a) presents a comparison between the simulated and measured results of the manufactured 90° hybrid directional coupler, demonstrating that the frequency response of the device aligns with the simulations and exhibits a fractional bandwidth of $22\,\%$ for a return loss higher than $15\,\mathrm{dB}$. The average measured insertion loss is lower than $0.7\,\mathrm{dB}$, and the maximum amplitude imbalance within the operating bandwidth is $1\,\mathrm{dB}$. Furthermore, Figure 4.51 (b) illustrates the simulated and measured phase shift, indicating that the device provides a phase shift of $89.5^\circ \pm 1^\circ$ for the operating bandwidth.

Table 4.19 provides a comparison of the 90° hybrid coupler with similar couplers implemented in a waveguide and a substrate-integrated coaxial line [145]. It is important to note

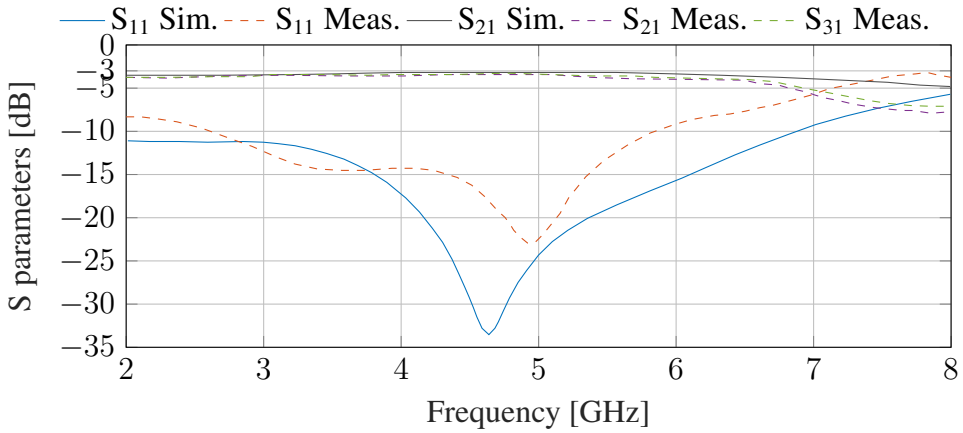

(a)

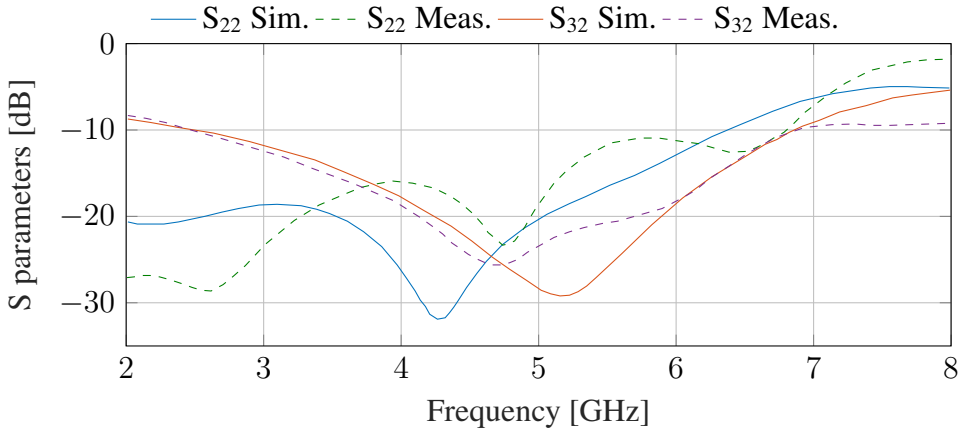

(b)

Figure 4.48: Simulated and measured response of the ESICL Wilkinson divider.

that the reported data for these two references did not include the effect of transitions and connectors. For a proper comparison, the loss due to connectors (1 dB) has been removed for the measurements of the ESICL device.

The bandwidth values for the ESICL and substrate-integrated coaxial line devices correspond to return loss values greater than 15 dB, while the value for the waveguide device corresponds to a return loss greater than 26 dB. Compared to the waveguide hybrid, the ESICL hybrid coupler is significantly lighter and smaller. The performance of the ESICL hybrid coupler is comparable to that of the substrate-integrated coaxial line proposed in [145]. Our implementation shows lower insertion loss, wider operational bandwidth, and similar unbalance, demonstrating the potential of ESICL technology for applications that require a balance between electrical performance, size, and mass.

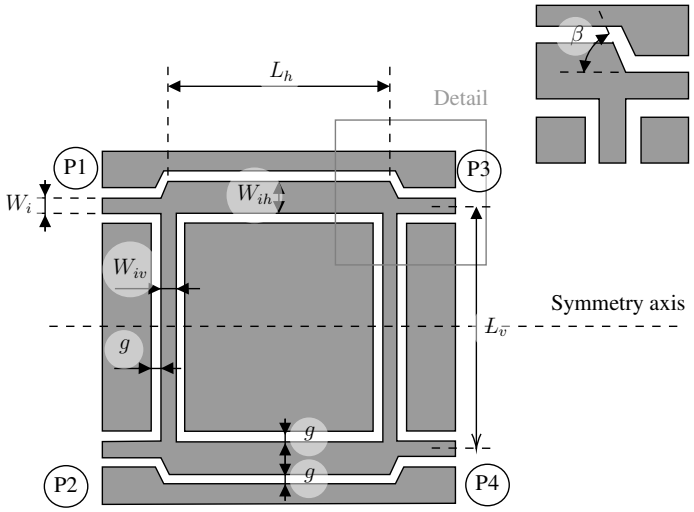

Figure 4.49: Layout of the third layer of the $90°$ hybrid directional coupler. In grey the copper metallisation on top of the substrate, and in black the border copper metallisation.

Table 4.18: Dimensions of the $90°$ directional coupler.

Parameter	Dimension $[\mathrm{mm}]$
W_{iv}	$1.05\,\mathrm{mm}$
W_{ih}	$1.98\,\mathrm{mm}$
W_{i1}	$0.96\,\mathrm{mm}$
g	0.6
L_H	$15.36\,\mathrm{mm}$
L_v	$15.94\,\mathrm{mm}$
β	$62°$

Table 4.19: Comparison of the $90°$ hybrid directional coupler.

Parameter	ESICL	Waveguide	Substrate-Integrated Coaxial Line [145]
Dimensions $[\mathrm{mm}]$	20x37x4.8	153x267x63.5	14x24x0.5
Weight $[\mathrm{g}]$	48.28	900	(not reported)
Center frequency $[\mathrm{GHz}]$	5	5	5.5
Relative bandwidth $[\%]$	22	14	16
Insertion loss $[\mathrm{dB}]$	0.5	(not reported)	0.8
Power unbalance $[\mathrm{dB}]$	$\pm$ 0.98	$\pm$ 0.25	$\pm$ 1

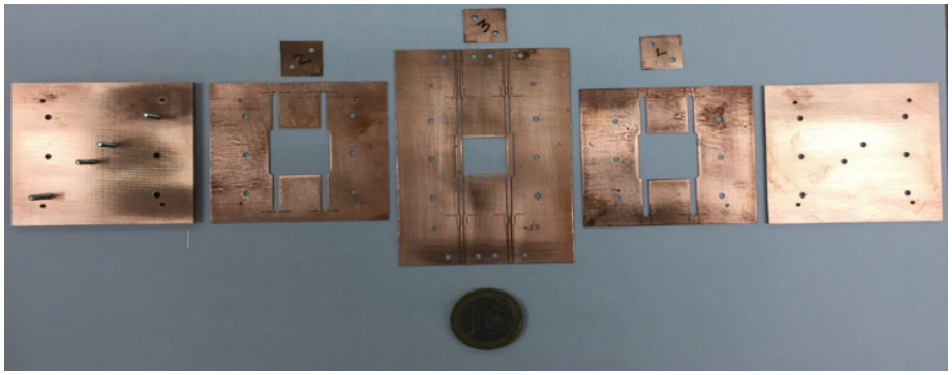

(a)

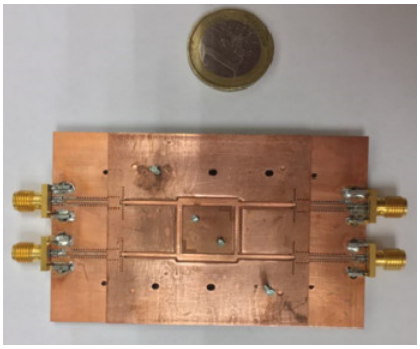

(b)

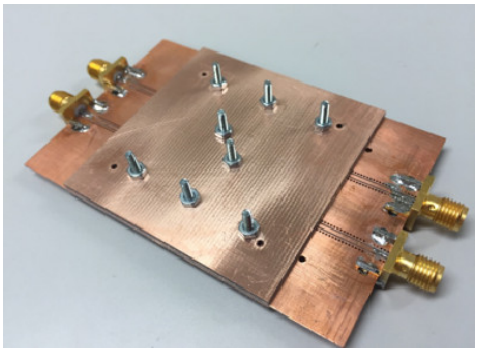

(c)

Figure 4.50: Most representative views of the 90° hybrid directional coupler: (a) top view of layers one, two, three, four and five, (b) top view of the assembled divider without the top cover, and (c) detail of the assembled device.

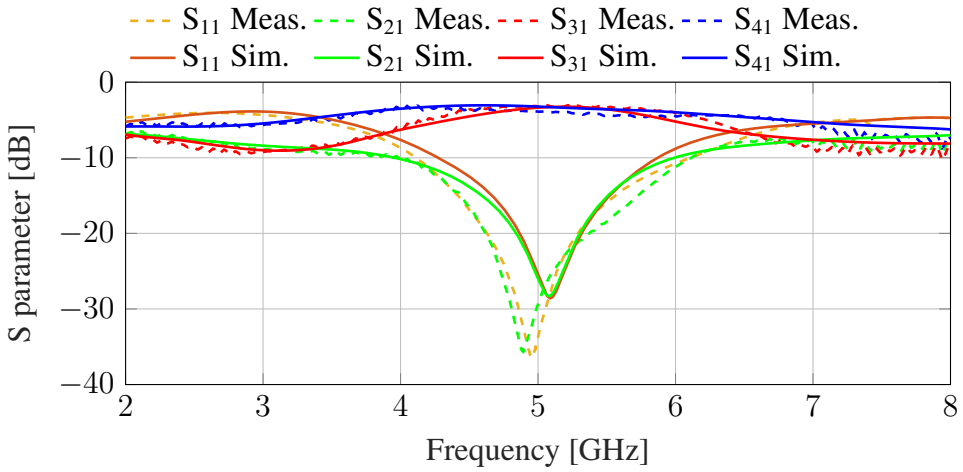

(a)

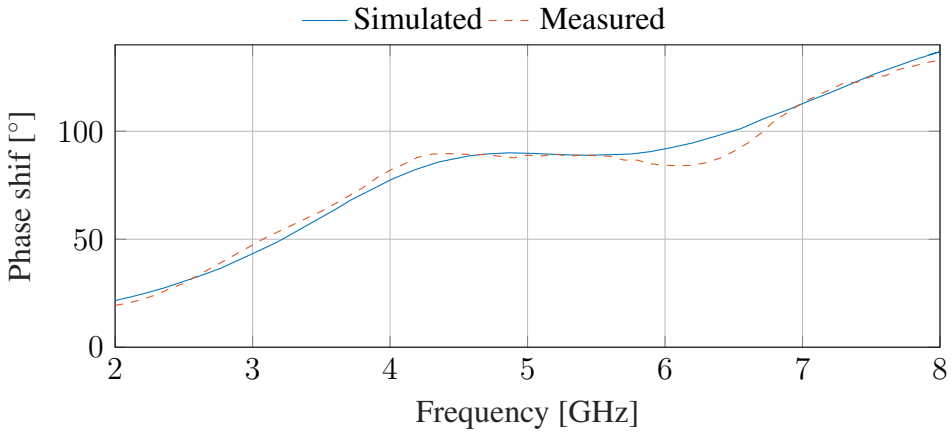

(b)

Figure 4.51: Simulated and measured response of the ESICL directional coupler: (a) S parameters and (b) phase shift between direct and coupled port.

Chapter 5

Reconfigurable Devices Based on Liquid Crystal

As described in Chapter 1, reconfiguration is one of the challenges in the current state-of-the-art of microwave technology. This need has led to the development of different reconfiguration strategies, as discussed in Section 1.2.2. Among these strategies, functional materials, and particularly liquid crystals, have emerged as promising candidates. Functional materials offer the ability to control their electromagnetic properties (permittivity, permeability, or conductivity) through an external stimuli (heat, electric fields, magnetic fields, or biased electric currents).

Compared to other reconfiguration methods like RF-micro-electro-mechanical systems or diodes, which offer discrete reconfiguration states, functional materials provide continuous reconfiguration capabilities. Moreover, while traditional reconfiguration methods are typically implemented in lumped elements, making their integration into non-planar and multilayer structures challenging, functional materials can be distributed throughout the device. These advantages have generated a growing interest in using functional materials at microwave and millimetre-wave frequencies, driving the application of liquid crystals at these frequencies.

However, the application of liquid crystals at microwave frequencies faces a fundamental challenge: the lack of characterisation. Liquid crystals have been extensively used at optical frequencies, as evidenced by the wide range of liquid crystal displays available in the market. However, there is limited information available on the behaviour of such materials at lower frequencies, particularly in the microwave band. This chapter addresses this gap by presenting two novel characterisation methods that can be used to extrapolate the dielectric anisotropy, splay deformation constant, and rotational viscosity of commonly used liquid crystal mixtures.

On the one hand, the anisotropy of the four liquid crystal mixtures will be characterised, including the GT3-23002 mixture from Merck KGaA and the QYPDLC-142, QYPDLC-36 and QYPDLC-193 mixtures from Qingdao QY Liquid Crystal Co. The dielectric properties of these mixtures (permittivity and loss tangent) at their two polarisation extremes will be approximated using a split-cylinder-cavity resonator. For this purpose, three cavities operating at $5\,\mathrm{GHz}$, $9.5\,\mathrm{GHz}$, and $11\,\mathrm{GHz}$ were designed and fabricated. In this method, the liquid crystal samples are placed in glass cells that enable the orientation of the LC molecules in a preferred direction. As a result, the dielectric permittivity and loss tangent of the liquid crystal can be obtained at the two polarisation extremes without the need for external biasing fields. The cells do not require conductivity, additional polarisation patches, magnets or coils, simplifying the measurement setup.

On the other hand, some of the most important mechanical properties of the GT3-23002 mixture, including the splay deformation constant (K_{11}) and rotational viscosity (γ_{11}), will be measured using a substrate-integrated waveguide resonator. This resonator includes two polarisation patches in a substrate-integrated cavity implemented within three PCBs. These polarisation patches are used in conjunction with an anchoring layer to accurately control the orientation of the liquid crystal molecules, allowing for a continuous tunability of the resonator. This structure enables the determination of the dielectric properties of the LC sample under different polarisation states, as well as the approximation of its splay deformation constant and rotational viscosity.

Lastly, the concluding section of this chapter presents a new tunable phase shifter implemented with a liquid crystal filled section of an ESICL. This device and the previously mentioned reconfigurable resonator serve as technology demonstrators to illustrate the benefits of using LC at microwave frequencies.

The structure of this chapter is as follows. The first section delves into the properties of the liquid crystals. The second section provides a brief introduction to the fundamentals of material characterisation at microwave frequencies. The third section presents the split-cylinder-cavity characterisation method, including the obtained results for the samples under study. In the fourth section, the structure of the substrate-integrated waveguide resonator is described, along with the methodology employed to approximate the dielectric anisotropy and mechanical properties of the GT3-23002 liquid crystal. Finally, the fifth section showcases the design and results of the LC-filled ESICL phase shifter.

5.1 Liquid Crystal Theory

The term Liquid Crystal (LC) refers to a class of materials that share properties of both crystalline solids and isotropic liquids, giving them a liquid-like appearance. Liquid crystal molecules are purposefully designed to exhibit mechanical, dielectric, electric, and magnetic anisotropy.

The mechanical anisotropy of their molecules grants liquid crystals both the high fluidity and free molecular mobility of liquids and the long-range orientation order of crystalline solids. Liquid crystal molecules can be oriented in a specific direction, resulting in high orientation order, while they also can freely move in particular directions, resulting in low positional order. Additionally, the magnetic and electric anisotropy of liquid crystals can be used in conjunction with their dielectric and optic anisotropy, resulting in an agile material whose dielectric properties can be controlled by means of an electric or magnetic field. An external electric or magnetic field can be employed to rotate and reorient the LC molecules, which allows the control of the electromagnetic properties of the material. These characteristics have allowed for the creation of agile devices, including liquid crystal displays, optic communication components, and, recently, millimetre and microwave frequency devices [146].

Liquid crystal molecules have an asymmetric geometry, with calamitic LCs having an elongated or rod-shaped structure and discotic LCs having a disk-like shape. The asymmetry in their geometry and molecular construction is responsible for their unique properties. The molecules of calamitic LCs typically consist of a rigid core, a flexible tail, and a head with a permanent dipole. The head dipole provides electric and magnetic anisotropy, which is used to orient the molecules using an external electric or magnetic field. The cylindrical or ellipsoidal rigid core contributes to the dielectric, optical, and mechanical anisotropy (high orientation order), while the flexible tail enhances molecular mobility, reducing positional order. As a result, LC molecules exhibit a combination of properties that make it a functional material. Figure 5.1 shows the simplified scheme of a nematic LC molecule and a representation of the 4-Octyl-4-biphenylcar-bonitrile molecule.

5.1.1 Anisotropy and Reconfigurability

The LC molecules exhibit a high dielectric anisotropy. The dielectric anisotropy ($\Delta\varepsilon_r = (\varepsilon_{\parallel} - \varepsilon_{\perp})$) represents the difference between the dielectric permittivity of a material under different electric polarisation. When the same electromagnetic field is applied to two LC molecules that are perpendicularly polarised; one oriented in parallel to the electric field and the other perpendicular; the free charges of the molecules move, producing a dipole moment in opposition to the electric field. As can be seen in Figure 5.2, the dipole moment of

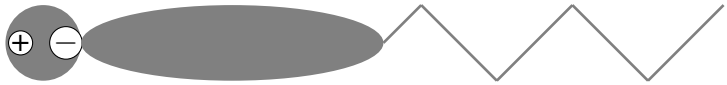

(a)

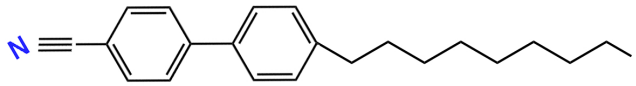

(b)

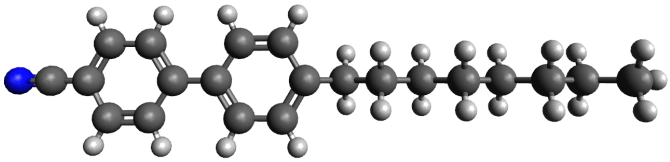

(c)

Figure 5.1: Calamitic Liquid Crystal molecule: (a) functional scheme of a typical molecule, (b) scheme of a molecule of 4-Octyl-4-biphenylcar-bonitrile, and (c) 3D view of a molecule of 4-Octyl-4-biphenylcar-bonitrile.

the molecule oriented parallel to the electric field is greater than that of the molecule oriented perpendicular to the field [147]. This difference results in different dielectric permittivity values for both polarisations. The permittivity of the LC material when its molecules are aligned with the electric field is denoted by $\varepsilon_{\parallel}$. In contrast, the permittivity when the molecules are perpendicular to the electric field is denoted by $\varepsilon_{\perp}$. Intermediate polarisation angles would result in varying permittivity values.

Macroscopically, the electromagnetic properties of LCs are those of an uniaxially anisotropic material, whose molecules' orientation axes are described by the director $\vec{n}$. Therefore, the dielectric permittivity of liquid crystals can be defined as a tensor. For an x-oriented LC volume and a y-oriented electric field, the permittivity tensor can be described as follows 5.1:

$$\varepsilon_r = \begin{pmatrix} \varepsilon_{\parallel} & 0 & 0 \\ 0 & \varepsilon_{\perp} & 0 \\ 0 & 0 & \varepsilon_{\perp} \end{pmatrix} \tag{5.1}$$

Figure 5.3 illustrates the cross-section of a liquid crystal cell, consisting of two parallel surfaces separated by a small distance filled with liquid crystal. This topology has been

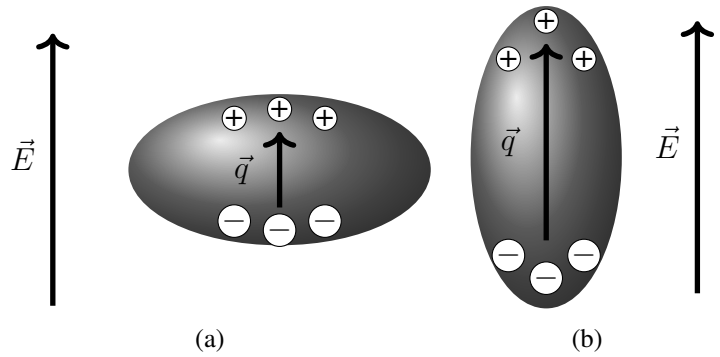

Figure 5.2: Dipole moment induced in a molecule of LC under the presence of an electric field: (a) the molecule is perpendicularly polarised and (b) the molecule is parallelly polarised.

commonly used in the literature because it is the basic building block of a liquid crystal display.

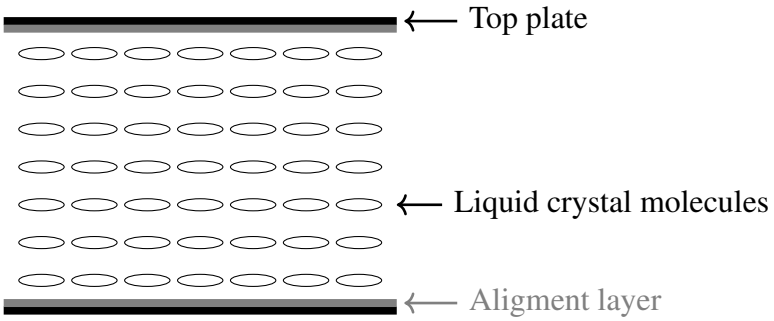

Figure 5.3: Schematic cross-section of an LC cell.

Although liquid crystals exhibit a high order of orientation, the molecules in a high volume of liquid crystal tend to be oriented in small domains. To achieve a homogeneous alignment throughout the entire volume, it is necessary to force the alignment of the liquid crystal molecules in the desired direction by applying some external force. Otherwise, the different polarisation domains will result in an equivalent isotropic material with an average effective permittivity $\varepsilon = (\varepsilon_{\parallel} + \varepsilon_{\perp})/2$ [148].

The molecules of a liquid crystal can be aligned using two methods: an anchoring layer and an electric or magnetic field. The alignment by anchoring layer involves creating a textured coating layer with microscopic grooves on the walls of the LC cell. The molecules of the liquid crystal align with the direction of these grooves to reduce their total energy [148].

In contrast, the alignment by an external field involves applying an electric or magnetic field that induces forces on the permanent dipoles of the LC molecules, forcing their orientation.

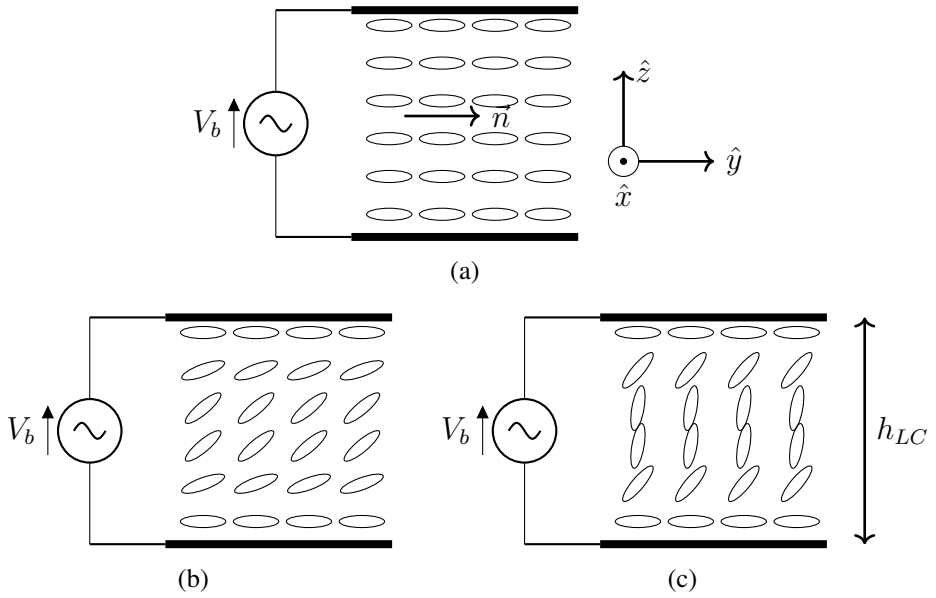

Figure 5.4: Alignment and polarisation of an LC cell under different bias voltages (V_b): (a) $V_b < V_{th}$, (b) $V_b > V_{th}$, and (c) $V_b >> V_{th}$.

Both alignment methods are typically combined to create a material medium with varying permittivity. Figure 5.4 depicts the different polarisation states of an LC cell under various biasing voltages (V_b). The cell is coated with an anchoring layer that enables the LC molecules to align parallel to the surface. When a voltage is applied between the two surfaces, the force induced in the dipole of the molecules causes them to rotate and align with the field. This force is perpendicular to the alignment force generated by the anchoring layer, which attempts to keep the molecules parallel to the cell surfaces. When the voltage is null or very low, the molecules remain parallel to the cell's surface. However, when the voltage increases, the electric force exceeds the anchoring force, and the molecules rotate until an equilibrium state is achieved. The needed voltage to exceed the anchoring force is known as the threshold voltage or voltage of Fréedericksz and can be determined using the following expression [148]:

$$V_{th} = \pi \sqrt{\frac{K_{11}}{\varepsilon_0 \Delta\varepsilon}} \tag{5.2}$$

, where K_{11} is the elastic splay constant or constant of Frank, and $\Delta\varepsilon$ is the dielectric anisotropy of the LC at the frequency of the biasing voltage.

When the voltage is strongly increased, the force induced by the voltage dominates over the anchoring force, and the molecules are orientated parallel to the voltage. Finally, when the applied voltage is reduced, the anchoring force begins dominating, and the liquid crystal molecules reduce their angle with the cell surface.

This mechanism, known as Fréedericksz transition, has been widely used to develop reconfigurable devices at optical frequencies, and it is being explored to develop agile devices at microwave frequencies. However, commercial liquid crystal mixtures are not well-characterised at such low frequencies. For this reason, one of the objectives of this thesis is to characterise the most important properties of these materials at low frequencies, specifically the X and C bands. The following sections present an overview of the existing characterisation methods, along with the introduction of two novel characterisation techniques.

5.2 Liquid Crystal Characterisation

In the case of dielectric materials, their interaction with electric fields is described by the dielectric permittivity ($\varepsilon = \varepsilon' - j\varepsilon''$). This interaction encompasses various microscopic and macroscopic phenomena: at low frequencies, the interaction is dominated by ion conductivity, while at higher frequencies, such as millimeter-wave frequencies, it is associated with atomic and electronic polarisations. In the microwave and millimeter-wave range, dipolar relaxation becomes the main contributor to the permittivity [149]. Consequently, the permittivity and loss tangent ($\tan\delta = \varepsilon''/\varepsilon'$) of materials exhibit a strong frequency dependence. Figure 5.5 depicts the typical behaviour of the complex dielectric permittivity along frequency.

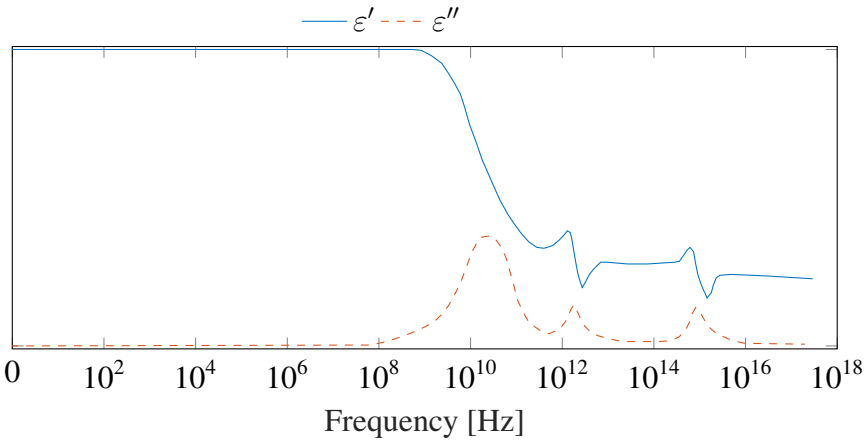

Figure 5.5: Evolution of dielectric permittivity with frequency for a typical dielectric material. Data extracted from [149].

As can be noticed, the investigation of the electromagnetic properties of materials is essential for designing and developing electromagnetic devices across various frequency ranges. Liquid crystals, which have found extensive applications in the optical domain, are now being explored for their potential at millimetre and microwave frequencies. However, the electromagnetic properties of these materials remain relatively unexplored at these frequency ranges. This section briefly overviews some dielectric characterisation methods employed for analysing this material in the context of their electromagnetic behaviour.

5.2.1 Dielectric Characterisation Methods

The literature describes various microwave methods for characterising electromagnetic materials. These methods are based on the principle that the properties of microwave devices are determined by their geometry and the electromagnetic properties of their materials. Thus, knowing these properties, it is possible to deduce the electromagnetic characteristics of the material under test from the measured response of the device. Dielectric characterisation techniques at microwave frequencies are typically divided into two categories, depending on the response of the devices used for the assessment: resonant methods and non-resonant methods.

Resonant methods rely on the measurement of the properties of microwave resonators, i.e. resonant frequencies and quality factors, to extract the electromagnetic properties of the material. These methods provide precise results for a single frequency or a few discrete frequencies at best. Examples of resonant methods include the use of cavity resonators, waveguide resonators, and dielectric resonators. These methods offer high accuracy but are limited to specific frequencies or narrow frequency ranges.

In contrast, non-resonant methods provide less accurate results over a broad frequency range. These methods involve measuring scattering parameters (S parameters) or transmission/reflection coefficients of the material under test. The electromagnetic properties (permittivity or permeability) can be determined by analysing the frequency-dependent behaviour of these parameters. Non-resonant methods are often used in conjunction with resonant methods to obtain accurate results over a wide frequency bandwidth.

The dielectric characterisation of liquid crystals involves obtaining their complex permittivity at a continuous set of orientation states, or at least at their two extreme orientations: parallel ($\varepsilon_{\parallel} = \varepsilon'_{\parallel} - j\varepsilon''\|$) and perpendicular ($\varepsilon_{\perp} = \varepsilon'_{\perp} - j\varepsilon''_{\perp}$) to the electric field. In order to do so, molecules of the liquid crystal need to be aligned in a preferred direction and rotated to achieve different polarisations. Multiple methods can be used to align and rotate the liquid crystal molecules; including anchoring layers, electric fields, and magnetic fields; but commonly, a combination of more than one alignment method is needed to control the

molecule orientation precisely. This anisotropic behaviour and complex polarisation of liquid crystals make their electromagnetic characterisation more intricate and introduce more significant measurement uncertainty. In the following sections, we briefly describe the operating principles of some permittivity characterisation methods commonly used in the literature to study the electromagnetic properties of liquid crystals.

5.2.1.1 Resonant method

In resonant methods, the material under test is integrated into a microwave resonator, so its permittivity and permeability are extrapolated from their resonant properties (resonance frequency and quality factor). These methods are commonly preferred over their counterpart due to their high accuracy and sensitivity.

There are several examples of resonant methods applied to characterise liquid crystals in the literature [150]. In [151], a rectangular cavity resonator with a small dielectric tube was used to characterise the permittivity of a liquid crystal at $30\,\mathrm{GHz}$. In this method, the LC was introduced into the tube, and the orientation of their molecules was achieved by using a strong magnetic field of $0.35\,\mathrm{T}$ created by two permanent magnets. In [152], Gaebler proposed an evolution of the characterisation method. Three orthogonal resonant modes of the rectangular resonator, TE_{011}, TE_{101}, and TM_{120}, were employed to characterise the dielectric properties of the liquid crystal under three orthogonal polarisations at the same time. However, a strong magnetic field was still needed to orientate the molecules of the material in a preferred direction. Both methods introduced a small volume of liquid crystal in the cavity to apply the perturbation technique, simplifying the analysis. However, this also reduces the sensitivity of the method, increasing the uncertainty of the results.

In [153], a split-post dielectric resonator was used to extract the dielectric permittivity of a liquid crystal mixture. It employed LC cells with an anchoring layer that promotes the orientation of the molecules in a linear direction. By applying a significant voltage across the cell plates, the orientation of LC molecules could be manipulated, thus enabling the characterisation of parallel and perpendicular permittivity states. However, as the initial orientation of the liquid crystal is not aligned with the electric field pattern of the resonant mode, the method yields an average LC permittivity ($(\varepsilon_{\parallel} + \varepsilon_{\perp})/2$) at zero voltage. Additionally, the method appears to be highly sensitive to variations in the thickness of the liquid crystal cells [150], significantly restricting its practical applicability.

While resonant methods are typically based on high-quality factor resonators, and therefore, they are commonly implemented on empty cavities, there are also some examples in the literature that use planar resonators. For instance, in [154], a ring resonator implemented on an inverted microstrip was used, while in [155,156], rectangular and circular patch resonators

were employed. The planar topologies of these structures allow for the use of anchoring layers to promote the orientation of the liquid crystal molecules along a particular direction. The two-conductor structures of the inverted microstrip and patch resonators allow for the application of a high-voltage biasing signal that rotates the liquid crystal molecules and controls their orientation. However, these methods generally achieve lower accuracy than the previous methods based on empty cavities as they exhibit higher ohmic and radiation losses, resulting in a reduced quality factor. Additionally, planar resonator structures typically lack precise analytical solutions, requiring accurate simulations to extract the dielectric permittivity of the material under test.

5.2.1.2 Non-resonant method

In non-resonant methods, the material under test is typically integrated into a transmission line, and the permittivity or permeability of the sample is obtained from the transmission and reflection coefficients of the structure [149]. These methods can be used over the entire operational bandwidth of the transmission line, enabling the determination of permittivity or permeability over a wide range of frequencies.

There are several examples of non-resonant methods employed for liquid crystal characterisation. In [157, 158], a coaxial line partially filled with liquid crystal was proposed. The coaxial line allows for the extraction of the permittivity over a very wide frequency range using the scattering parameters of the line. During measurements, the molecules of the liquid crystals were polarised using a combination of magnetostatic and electrostatic fields. Toroidal magnets placed around the coaxial structure forced the molecules to align along the propagation direction while a biasing voltage induced a parallel orientation with the electric field. The combination of electric and magnetic forces enables a continuous reconfiguration range of the liquid crystal. This method is convenient for extrapolating the dielectric constant of the liquid crystal over a broad frequency band. However, the use of bulky and heavy permanent magnets and the requirement of a high voltage are practical limitations that limit its application to laboratory devices.

In contrast, an inverted microstrip configuration was employed in [159]. This method determines the complex permittivity of a liquid crystal mixture from $15\,\mathrm{GHz}$ to $65\,\mathrm{GHz}$. The flat and homogeneous structure of the inverted microstrip is very convenient for the use of an anchoring layer, and its TEM mode facilitates the application of a polarisation bias voltage, allowing a continuous reorientation of the LC molecules. However, the relatively high radiation loss of the inverted microstrip at such frequencies and its sensitivity to the substrate thickness strongly affect the accuracy of the results.

5.2.1.3 Conclusions

As previously mentioned, both resonant and non-resonant methods have advantages and disadvantages. Resonant methods employ electromagnetic structures whose parameters are easier to be theoretically analysed than non-resonant methods, offering higher accuracy. On the other hand, non-resonant methods can provide permittivity data across a broad frequency band. Moreover, these methods tend to be more compact than the resonant ones and allow the use of biasing voltage and anchoring layers to achieve a molecule rotation. In this thesis, two resonant methods are proposed.

In the first approach, liquid crystal is introduced in a liquid crystal cell previously treated with an anchoring layer. This enables the simple alignment of the liquid crystal molecules, achieving the use of simple polarisation methods in traditional resonant methods.

In the second method, a substrate-integrated cavity is used as a resonator. This design facilitates the creation of an anchoring layer and the application of biasing voltages for precise molecule alignment and rotation. This approach strikes a balance between planar and non-planar resonators, achieving a higher quality factor than planar resonators while reducing the size compared to non-planar resonators.

Both methods represent a significant improvement over previous work, which either relied on non-planar resonators necessitating complex polarisation systems or employed planar resonators with low-quality factors.

5.2.2 Split-Cylinder-Cavity Method

The split-cylinder-cavity method was originally proposed by Kent in 1996 [160]. It uses an empty cylindrical cavity divided into two sections. When a flat material sample is positioned between the two parts of the cylinder, as depicted in Figure 5.6, the resonance frequency and quality factor of the cavity are affected by the dielectric properties (permittivity and loss tangent) of the material. This technique allows the determination of the material's dielectric properties by analysing the resonant characteristics of both the empty and filled cavities. For precise results, an accurate characterisation of the dimensions and properties of the cavity, as well as the thickness of the material sample during the calibration process, is crucial.

This method is well-suited for characterising liquid crystal cells due to their thin and flat nature. Moreover, this liquid crystal cell allows the efficient alignment of the liquid crystal molecules by including a simple anchoring layer, as depicted in Figure 5.3.

The selection of a resonant mode in the split-cylinder-cavity method is crucial to ensure the accurate and reliable characterisation of the material under test. The resonant mode

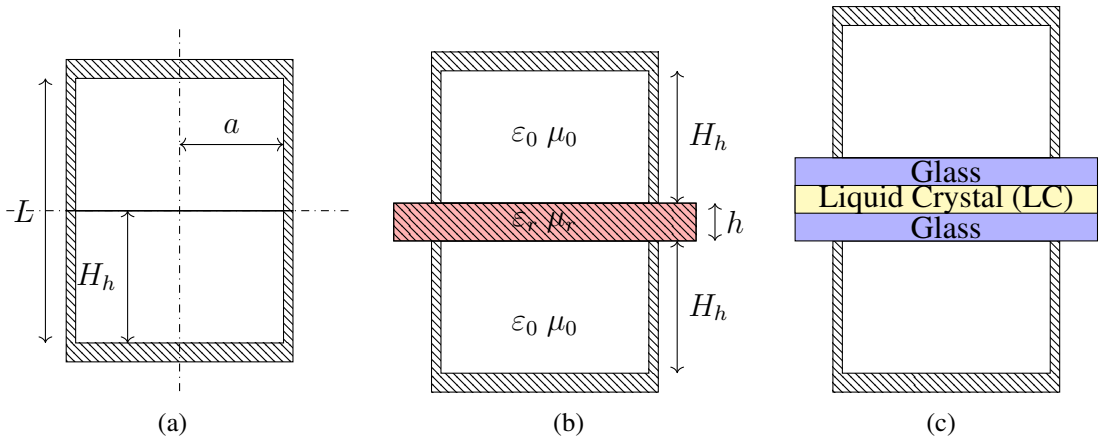

Figure 5.6: Cross-section of a split-cylinder-cavity resonator: (a) empty cavity, (b) cavity filled with a homogeneous material, and (c) cavity filled with an LC cell.

should fulfil two critical requirements: a high-quality factor with low sensitivity to the separation between the two parts of the cavity and an appropriate electric field pattern with a high linearity. Figure 5.7 shows the electric field distribution in the cross-section of the two most important modes of a cylindrical resonator.

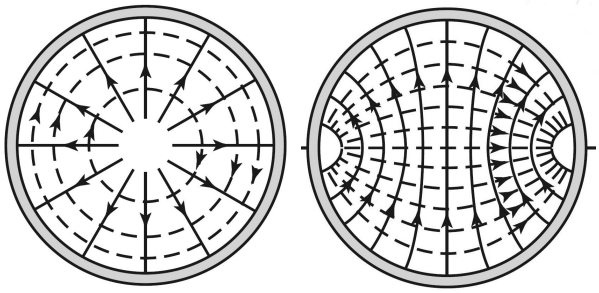

(a) TM_{01} (b) TE_{11}

Figure 5.7: Transverse field distribution for the most representative modes of the split-cylinder-cavity [64]. The electric field is depicted in solid lines, and the magnetic field is depicted in dashed lines.

For isotropic materials, the TM_{01m} mode is commonly employed as it exhibits a high quality factor that is practically unaffected by the gap between the two parts of the cavity. However, the electric field distribution of the TM_{01m} mode is radial, as shown in Figure 5.7 (a). This field pattern is impractical for characterising anisotropic materials like liquid crystals because the electric field would interact with both polarisations of the liquid crystal

molecules.

To address this issue, we selected the TE_{111} resonant mode. The transverse electric field distribution of this mode, depicted in Figure 5.7 (e), is almost linear in the centre of the cavity, allowing the interaction with only one polarisation of an anisotropic material and enables the accurate characterisation of the parallel and perpendicular polarisations of the liquid crystal. Furthermore, the longitudinal field distribution of the TE_{111} mode exhibits a maximum electric field and a minimum magnetic field in the region of the sample, facilitating the characterisation of the dielectric permittivity and minimising radiation losses occurring in the gap between the two parts of the split cylinder.

By selecting the TE_{111} mode, the split-cylinder-cavity method offers an appropriate combination of high-quality factor, linear electric field distribution, and reduced radiation losses, making it a suitable choice for characterising the electromagnetic properties of liquid crystals.

A notable advantage of the split-cylinder resonator is that it allows the determination of the parallel and perpendicular polarisation states of the liquid crystal by manually rotating the LC cell. This eliminates the requirement for complex electrical or magnetic polarisers, simplifying the measurement setup and making it more convenient to obtain the desired polarisations.

The electric and magnetic fields of the TE_{nmp} modes in the empty split-cylinder cavity can be determined by imposing the boundary conditions of the resonator on the Maxwell equations. The electric field expression, $E_{TE_{nmp}}$, and the magnetic field expression, $H_{TE_{nmp}}$, for the TE_{nmp} modes can be given as follows:

$$\begin{aligned} H_\rho &= -j\tfrac{\beta}{k_c} J_n(k_c\rho)' \left[A\sin(n\phi) + B\cos(n\phi)\right] \\ H_\phi &= -j\tfrac{\beta n}{{k_c}^2\rho} J_n(k_c\rho) \left[A\cos(n\phi) - B\sin(n\phi)\right] \end{aligned} \tag{5.3}$$

$$\begin{aligned} E_\rho &= Z_{TE} H_\phi \\ E_\phi &= Z_{TE} H_\rho \end{aligned} \tag{5.4}$$

, where β stands for the propagation constant, k_c symbolizes the cut-off wavenumber, $J_n(x)$ represents the n-th order Bessel functions, $J_n(x)'$ represents the first derivative of the n-th order Bessel functions, and Z_{TE} is the modal impedance of the TE mode.

The resonant frequency for the TE_{nmp} mode, $(f_r)_{mnp}^{TE_{mnp}}$, can be determined using the following equation:

$$(f_r)_{mnp}^{TE_{mnp}} = \frac{1}{2\pi\sqrt{\mu\varepsilon}} \sqrt{\left(\frac{P'_{nm}}{a}\right)^2 + \left(\frac{p\pi}{2L}\right)^2} \tag{5.5}$$

, where μ and ε are the magnetic permeability and electric permittivity of the cavity, respectively, a and L are the radius and total length of the cylindrical resonator, and P'_{nm} is the m-th root of the first derivative of the Bessel function of order n.

These equations provide the mathematical expressions for the electric and magnetic fields and the resonant frequency of the TE_{nmp} modes in the split-cylinder cavity. By solving them, one can determine the specific mode characteristics required for the analysis and characterisation of material samples within the split-cylinder cavity. These equations can be simplified in various ways, leading to the development of different characterization approaches.

5.2.2.1 Design of the split-cylinder cavity

Three split-cylinder-cavity resonators were used to characterise liquid crystal samples at different frequencies. We designed two Split-Cylinder-Cavity resonators operating at $5\,\mathrm{GHz}$ and $11\,\mathrm{GHz}$, respectively, and used a previously designed cavity resonating at $9.5\,\mathrm{GHz}$.

The equation 5.5 establishes a relationship between the resonant frequency of the desired mode (the TE_{111}) and the dimensions of the resonator (the radius of the cavity a, and the length of the cylinder $L = 2 \cdot H_h$). However, one can find multiple combinations of lengths and radii of the cavity to a specific resonant frequency. We conducted a parametric analysis to determine a combination of radius and length that exhibited low sensitivity to dimensional deviations. Figure 5.8 presents the results of this analysis for the resonance frequencies of $5\,\mathrm{GHz}$, $9.5\,\mathrm{GHz}$, and $11\,\mathrm{GHz}$, along with the designed dimensions of the manufactured prototypes.

As can be derived from Figure 5.8, there is an instability region for short lengths where the response of the resonator is highly sensitive to small dimensional deviations. Therefore, the proposed designs operate within the stable range, where the relationship between radius and length remains consistent, obtaining designs with a reduced sensitivity to manufacturing deviations.

The $5\,\mathrm{GHz}$ cavity has a diameter of $40\,\mathrm{mm}$ and a total length ($L = 2 \cdot H_h$) of $64\,\mathrm{mm}$. The $11\,\mathrm{GHz}$ cavity has a diameter of $20\,\mathrm{mm}$ and a total length of $22.4\,\mathrm{mm}$. The $9.5\,\mathrm{GHz}$ cavity has a diameter of $30.08\,\mathrm{mm}$ and a total length of $20\,\mathrm{mm}$. As can be noticed from Figure 5.8, the $5\,\mathrm{GHz}$ and $11\,\mathrm{GHz}$ resonators operate on the above-mentioned stable zone. However, the $9.5\,\mathrm{GHz}$ resonator operates near the unstable area. This is because this resonator was initially designed to operate under a different resonant mode for a previous project.

Cavity feeding was accomplished using two coaxial cables with a final loop that operated as a spire. The loop acts as a magnetic monopole, exciting the magnetic field of the TE_{111} mode within the cavity, as depicted in Figure 5.9. By adjusting the penetration of the loop into the cylinder, the coupling coefficient can be controlled, enabling the adaptation of the

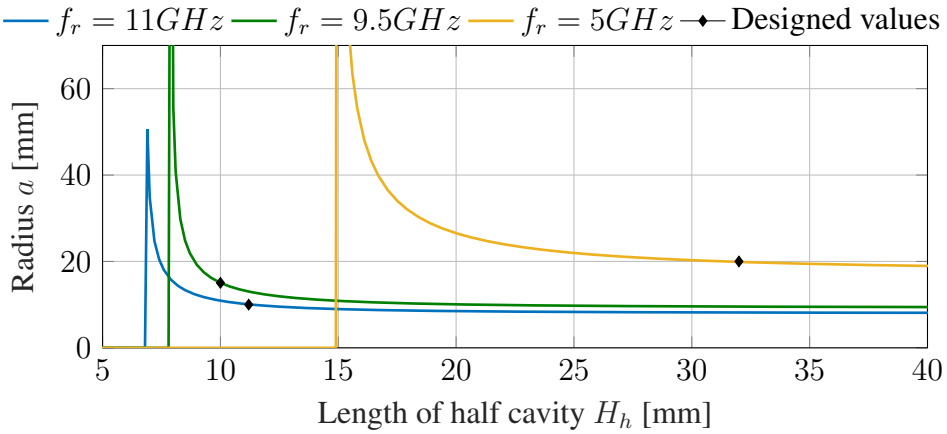

Figure 5.8: Ratio of cavity radius and height to excite a TE_{111} mode at the desired frequency.

measuring conditions to the specific requirements of each material sample.

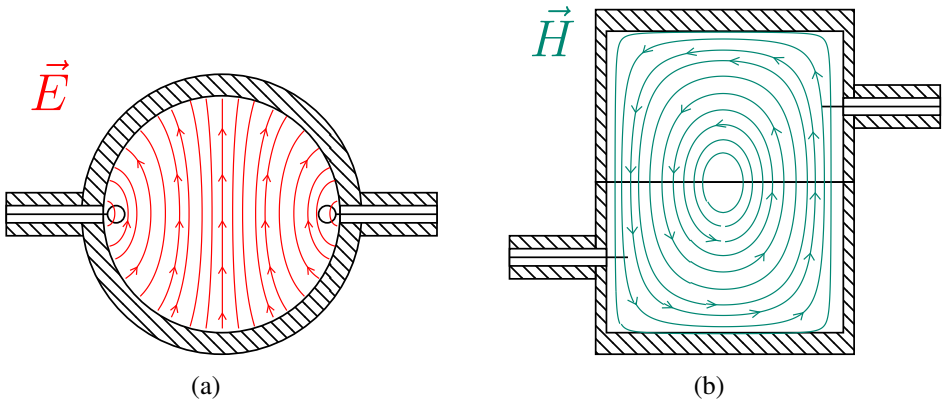

Figure 5.9: Feeding configuration of the split-cylinder-cavity resonators: (a) cross-section view and (b) longitudinal-section view. The electric field is depicted in red and the magnetic field is depicted in green.

The prototypes were manufactured in brass, and an external alignment structure was machined in aluminium, as shown in Figure 5.10. All parts were manufactured in the mechanical workshop of the Technical University of Cologne.

5.2.2.2 Characterisation procedure

The split-cylinder-cavity resonator technique is based on a simple idea: the dimensions and electromagnetic properties of the material sample influence the resonant properties of the resonator. When we insert a material sample in the resonator, its electromagnetic pattern

Figure 5.10: Manufactured prototype of the 11 GHz split-cylinder-cavity resonator.

changes, affecting its resonant frequency and quality factor. This change can be measured and analysed to determine the complex permittivity of the material under test using an analysis method. The most extended analysis method is the Kent method [160]. It assumes some simplifications, assuming the sample is electrically small and the split cylinder is completely closed (not considering the gap between parts). This method is highly convenient due to its simplicity. However, the Kent method can only be used to determine the dielectric properties of homogeneous materials, being unsuitable for studying non-homogeneous materials like the proposed LC cells. For this reason, we had to employ different analysis methods. In particular, we employed two methods: one based on a modal analysis and the other based on a numerical analysis of the resonator.

The characterisation procedure is as follows:

First, the response of the empty resonators is measured to calibrate the measurement setup. The calibration involves adapting the dimensions of the analysis models (cavity diameter and length) and their electromagnetic properties (electric conductivity) to correspond with the actual measured response of the resonators. This calibration aims to align the electrical performance of the analysis models of the split cylinder with its measured response.

Next, the liquid crystal cells were characterised. The thickness of each glass forming the cells is measured, and their dielectric properties (permittivity and loss tangent) are determined using one of the previously mentioned analysis methods. In this case, it was employed the Kent method [160]. Once glasses have been thoroughly characterised, the liquid crystal cells are assembled, and the thickness of the liquid crystal volume in each cell is measured.

Once the dimensions and permittivity of liquid crystal cells are characterised, they are

filled with different liquid crystal mixtures. Then, the filled cells are introduced into the resonator in their two orthogonal orientations, i.e., with their molecules parallel and perpendicular to the electric field, allowing for measuring the permittivity of their two extreme polarisation states. Finally, the frequency response of these two measurements is used to calculate the complex dielectric permittivity of the liquid crystal using a modal and a numerical analysis method.

5.2.2.3 Analysis methods

We have used three different analysis methods throughout the characterisation process. The Kent method was employed to obtain the permittivity of the glass plates that form the liquid crystal cells, and modal and numerical analysis methods were used to compute the complex permittivity of the liquid crystal samples. Below, we present a brief overview of these analytical methodologies.

Kent method The Kent method, described in [160, 161], can only be used to characterise homogeneous samples, so it was only used to compute the permittivity of the glass plates of the liquid crystal cell.

The analysis process begins with the calibration of the analytical model of the resonator. To accomplish this, the response of the empty cavity is measured, obtaining its resonant frequency and loaded quality factor (Q_L), for which equation 5.6 was employed.

$$Q_L = \frac{f_r}{BW} \tag{5.6}$$

Then the unloaded quality factor (Q_U) was computed using equation 5.7.

$$Q_U = \frac{Q_L}{1 - 10^{S_{21(f_r)}/20}} \tag{5.7}$$

, where f_r is the measured resonance frequency, BW is the $-3\,\mathrm{dB}$ bandwidth, and $S_{21(f_r)}$ is the measured S_{21} parameter at the resonance frequency in dB.

The resonant frequency obtained from the calibration measurement was used in the equation 5.8 to estimate the effective dimensions of the analytical cavity.

$$f_{r(nmp)}^{TE} = \frac{1}{2\pi\sqrt{\mu_0\varepsilon_0}}\sqrt{\left(\frac{P'}{a}\right)^2 + \left(\frac{p\pi}{H_h}\right)^2} \tag{5.8}$$

Next, an effective conductivity (σ_{eff}) of the cavity metal walls is inferred from the quality factor. This effective conductivity includes the effect of all loss sources, including the influence of coupling elements, gap discontinuities, ohmic loss, and roughness. Equations 5.9 and

5.10 were employed to calculate the effective conductivity (σ_{eff}) and sheet resistance (R_s) of the cavity walls, respectively.

$$\sigma = \frac{2\pi f \mu_0}{2R_s^2} \tag{5.9}$$

$$R_s = \frac{(ka)^3 2H_h}{4\left(P'_{11}\right)^2 Q_U} \frac{1 - \left(\frac{1}{\left(P'_{11}\right)^2}\right)^2}{aH_h\left[1 + \left(\frac{a\pi}{2H_h\left(P'_{11}\right)^2}\right)\right] + \left(\frac{\pi a^2}{2H_h P'_{11}}\right)^2 \left(1 - \frac{1}{\left(P'_{11}\right)^2}\right)} \tag{5.10}$$

After the calibration process, the glass samples are placed in the middle of the cavity, and the measured response is used to determine its electromagnetic properties. To accomplish this, the filled resonator was modelled as a cylindrical cavity consisting of three regions: two regions filled with air and a central region filled with the sample material. It is important to note that this model is an approximation as it does not consider the effect of the gap between the two parts of the split cylinder. It has been demonstrated that this assumption is valid for optically thin samples whose thickness satisfies the following condition [149]:

$$\frac{2\pi}{\lambda} \cdot h\sqrt{\varepsilon'_r} << 1 \tag{5.11}$$

Assuming this simplified model, the permittivity and loss tangent of the glasses can be obtained by employing the Kent method described in [160, 161].

Modal method In this case, the full-wave analysis described in [162, 163] was employed to obtain the permittivity of the LC cells through the measured response of the split-cylinder resonator. In this method, the split resonator is segmented into simpler and smaller networks characterised by their generalised admittance matrix computed using the mode matching method. The structure of the split-resonator cavity was divided into eight sub-circuits, as shown in Figure 5.11. This method can characterise the permittivity of non-homogeneous sample materials like liquid crystal cells. However, it requires knowing the dimensions of the LC cells and the permittivity of the glass.

The method considers any possible mode (TE_{nm} and TM_{nm}) inside the networks. The electric and magnetic fields at the ports of each circuit are represented by a series expansion using base functions:

$$\vec{E}_{port} = \sum_n e_n \cdot \vec{E_n} \quad ; \quad \vec{H}_{port} = \sum_n h_n \cdot \vec{H}_n \tag{5.12}$$

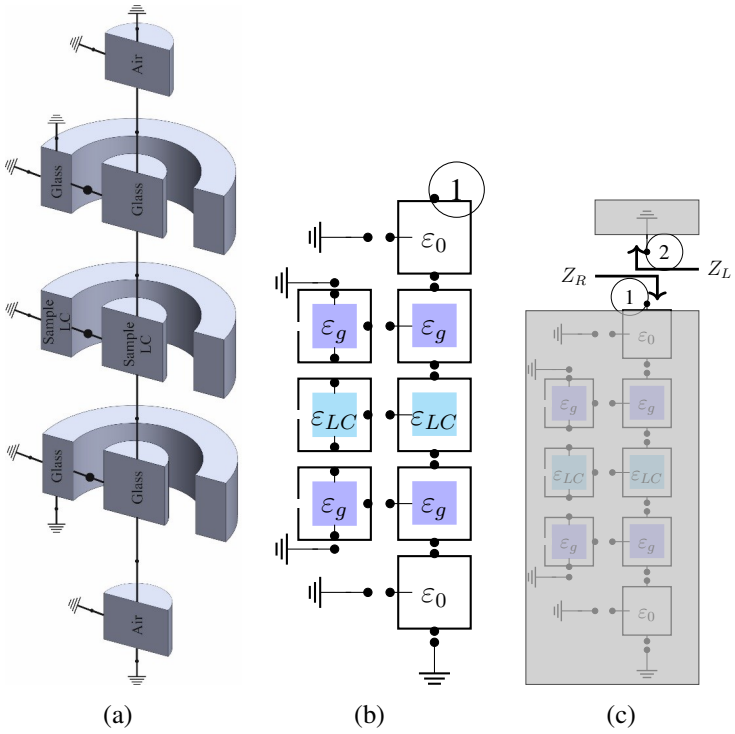

Figure 5.11: Simplified model of the split-cylinder-cavity resonator with a liquid crystal cell: (a) longitudinal cross-section view of the 3D segmented representation, (b) schematic representation of the segmented structure, and (c) schematic representation forcing the resonance condition.

, were $\vec{E}port$ and $\vec{H}port$ are the electric and magnetic fields at the ports of each circuit, e_n and h_n are the amplitudes of the base function, and $\vec{E}n$ and $\vec{H}n$ are the base functions for the electric and magnetic fields.

Then, the relationship between the electric and magnetic fields in the network is established using the generalised admittance matrix, as demonstrated below.

$$h = \begin{pmatrix} h_1 \\ h_2 \\ \dots \\ h_N \end{pmatrix} = \begin{pmatrix} \mathbf{Y_{11}} & \mathbf{Y_{12}} & \dots & \mathbf{Y_{1N}} \\ \mathbf{Y_{21}} & \mathbf{Y_{22}} & \dots & \mathbf{Y_{2N}} \\ \dots & \dots & \dots & \dots \\ \mathbf{Y_{N1}} & \mathbf{Y_{N2}} & \dots & \mathbf{Y_{NN}} \end{pmatrix} \begin{pmatrix} e_1 \\ e_2 \\ \dots \\ e_N \end{pmatrix} = Y \cdot e \tag{5.13}$$

, where N represents the number of ports of the network, h_n and e_n are vectors with coefficients of the series expansion defined in equation 5.12, and each Y_{ij} is a matrix.

After computing the generalised admittance matrix of each network, they are connected together, forming the matrix of the entire circuit. Finally, the input and output ports of the

circuit are short-circuited, and the resonance condition is imposed as follows:

$$\left|\det\left(\overline{\overline{Z}}_r(dim,\varepsilon,\mu,f_r)+\overline{\overline{Z}}_l(dim,\varepsilon,\mu,f_r)\right)\right|=0 \tag{5.14}$$

, where $\overline{\overline{Z}}_r$ and $\overline{\overline{Z}}_l$ are the generalised impedance matrices of the entire network, dim represents the dimensions of the resonator and the LC cell, ε and μ are the permittivity and permeability of the liquid crystal, and f_r is the resonance frequency of the cavity when the sample is placed in the resonator.

The generalised admittance matrix depends on the dimensions and electromagnetic properties of the material sample and the split-cylinder cavity. Given that all these parameters are already known, except for the liquid crystal's permittivity, we can determine the complex permittivity by meeting the resonance condition [162].

Numerical method Numerical simulations of the empty and filled resonators were conducted using the CST full-wave simulator. These simulations were used to validate the results and assess the accuracy of the modal method. The numerical analysis starts by calibrating a numerical model of the split-cylinder resonator. As with all other analysis methods, calibration consists in optimising the dimensions and properties of the resonator to match the simulated response to the measured response of the empty resonator. In this case, the optimised parameters were the diameter and length of the cavity, the penetration of the feeding loop, and the effective conductivity of the resonator. After calibration, the model was simulated, including the liquid crystal cells, and the permittivity and loss tangent of the liquid crystal material were optimised to fit the measured response of the filled resonator. The optimisation process was considered complete when the error in the resonant frequency was less than $1\,\mathrm{MHz}$ and the error in the quality factor was less than 5.

5.2.2.4 Post-processing

The proposed approach allows to obtain the values of the two extreme permittivities of a liquid crystal mixture without the need to apply any polarisation field, whether electric or magnetic. By positioning the liquid crystal cell at the centre of the cavity in two different orientations, one parallel and the other perpendicular to the electric field in the centre of the cavity, the permittivity values ε_1, and ε_2 can be obtained. However, as the electric field of the TE_{111} mode is not straight and parallel along the entire section of the cylinder resonator, the extrapolated permittivity (ε_1, and ε_2) do not directly correspond to the parallel ($\varepsilon_\parallel$) and perpendicular ($\varepsilon_\perp$) permittivity of the sample. To accurately determine these values, it is necessary to consider the actual field distribution of the TE_{111} mode, as expressed in the

following equation.

$$\begin{aligned} \varepsilon_{rpos1} \iint |\overrightarrow{E}| dS &= \varepsilon_{r\perp} \iint E_{\perp} dS + \varepsilon_{r\parallel} \iint E_{\parallel} dS \\ \varepsilon_{rpos2} \iint |\overrightarrow{E}| dS &= \varepsilon_{r\parallel} \iint E_{\perp} dS + \varepsilon_{r\perp} \iint E_{\parallel} dS \end{aligned} \tag{5.15}$$

, where ε_{rpos1} and ε_{rpos2} are the complex permittivity values obtained with the analyses methods when the LC cells are oriented at position 1 and 2. $|\overrightarrow{E}|$ is the module of the electric field considering the real polarisation of the TE_{111} mode. $E_{\parallel}$ is the component of the electric field in the parallel direction. $E_{\perp}$ is the component of the electric field in the normal direction.

With this equation, the complex permittivity of the liquid crystal samples at their parallel and perpendicular polarisation can be extrapolated from the values obtained through the modal and numerical analyses. This correction factor helps to account for the assumption of an isotropic material and provides more accurate estimations of the liquid crystal permittivity values.

5.2.2.5 Liquid crystal samples

The typical structure of a liquid crystal cell is depicted in Figure 5.3. It consists of two parallel plates on which an aligning layer is deposited. Spacers separate these plates to create an empty cavity that can be filled with the liquid crystal sample. The anchoring layer aligns the molecules of the liquid crystal in a preferred direction, and the top and bottom plates are coated with a conductor or semiconductor material to apply a low-frequency biasing voltage. This combination of anchoring layer and biasing voltage allows the orientation of the liquid crystal molecules at different angles between the parallel and perpendicular polarisation states.

In this particular case, we do not need the cell's top and bottom plates to be electrically conductive, as the molecules rotation will be accomplished by physically rotating the cell. The materials used for the construction of our cells are $0.410\,\mathrm{mm}$ thickness glasses, Mylar spacers with a thickness of $0.100\,\mathrm{mm}$, and Norland UV Sealant 91 adhesive. The anchoring layer is made of polyimide, and the empty cavity between both plates is filled with the liquid crystal sample.

The manufacturing process of the liquid crystal cells was as follows:

- **Anchoring layer:** a thin layer of polyimide with a thickness of approximately $100\,\mathrm{nm}$, was spin-coated on one surface of each glass. The thickness of this layer was measured using a contact profilometer by performing a thin dent in the coating.

The coating process was as follows: the glass was covered with polyimide and centrifuged at $16\,\mathrm{rpm}$ for $10\,\mathrm{s}$ and then at $66\,\mathrm{rpm}$ for $60\,\mathrm{s}$. After the deposition, the polyimide was solidified under $90\,^{\circ}\mathrm{C}$ during the time needed for polymerisation.

Finally, the polyimide coating was rubbed with natural velvet. This process creates a series of parallel grooves on their surface that are used to align the molecules of the liquid crystal.

- **Cell assembly:** four mylar spacers were adhered at the corners of one of the glasses. Then another glass was glued on the top of the other one. Both glasses were oriented so that their alignment layers were parallel, implementing a very effective anchoring layer. Once the two glasses were correctly positioned, the adhesive was solidified using an ultraviolet light, consolidating the structure.

- **Cell filling:** the empty cavities of the cells were filled with samples of different liquid crystal mixtures. After a visual inspection for bubbles, the cells were sealed with more Norland adhesive to prevent leakage.

- **Cell inspection:** Four liquid crystal cells were manufactured. The thickness of the glasses was measured at eight different positions with a mechanical micrometer screw before assembling the cells. The average thickness of the glasses is listed in Table 5.1.

Table 5.1: Thickness of the glass plates (h_{gi}) that forms the different cells.

Cell	Bottom glass [µm]	Top glass [µm]
Cell 1	410	410
Cell 2	404	410
Cell 3	410	410
Cell 4	409	409

The empty LC cell performs a Fabry-Pérot resonator whose resonant response is proportional to the thickness of the cavity. This allows us to accurately characterise the thickness of the LC cavity using a spectrophotometer Cary 5000 UV-Vis-NIR from Agilent. The interferometric results were checked by measuring the thick of each glass and the thickness of the liquid crystal cell with a micrometer screw. Table 5.2 depicts the thickness of the LC cavity for the four liquid crystal cells used in this thesis.

After filling and sealing the cells, the correct operation of the anchoring layer was verified using two linear polarisers. When two orthogonally oriented polarisers (crossed polarisers) are placed over a light source, the light transmission should be blocked. However, if an oriented volume of LC is introduced between the two polarisers with

Table 5.2: Thickness of the liquid crystal cavity (h_{LC}) of the different cells used in this thesis.

Cell	Optic measurement [µm]	Mechanical measurement [µm]
Cell 1	156	155 ± 9
Cell 2	151	150 ± 8
Cell 3	153	151 ± 3
Cell 4	146	144 ± 3

the longer axis of its molecules rotated $45°$ with respect to the light polarisers, the light with linear polarisation that passes through the first polariser can be split into the major and minor axes of the LC molecules. These two polarisations experience different permittivity, causing a rotation of the polarization from linear to elliptical. This rotation allows part of the light to pass through the second linear polariser, confirming that the liquid crystal molecules are aligned in the desired direction. Figure 5.12 shows an example of this phenomenon.

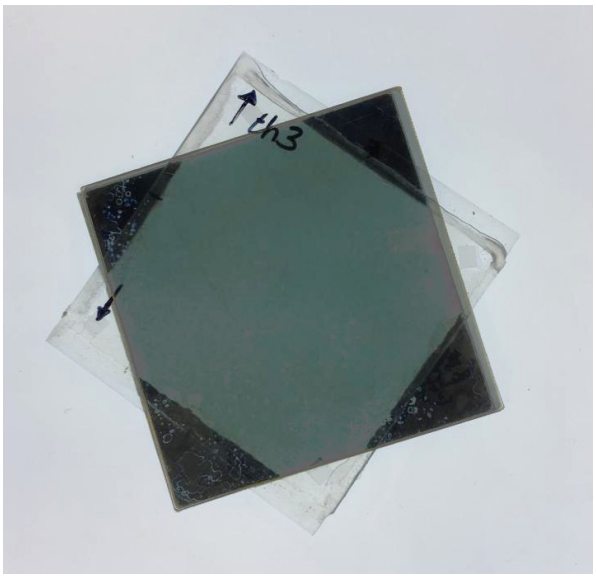

Figure 5.12: LC cell placed between two crossed linear polarisers. Light transmission confirms the correct polarisation of the liquid crystal.

The anchoring layer and liquid crystal cells were manufactured and assembled at the "Departamento de Física de la Materia Condensada" of the "Universidad de Zaragoza".

5.2.2.6 Calibration

The initial stage of the characterisation process involves calibrating the empty resonators by measuring their responses without any sample material. This calibration step is essential to ensure the accurate adjustment of the analysis models to the specific measurement conditions. The calibration process entails optimising parameters such as the effective radius, loop coupling penetration, and ohmic loss in the resonator models. It is important to note that if any modifications are made to the feeding network of the resonators, a recalibration is needed to maintain accuracy and reliability in the measurements.

Table 5.3 summarises the calibrated parameters of the split-cylinder-cavity resonators for the measurements performed at $5\,\mathrm{GHz}$ and $9.5\,\mathrm{GHz}$, where a_{eff} is the effective radius of the resonator, σ_{eff} the effective conductivity of the brass, and I_{loop} the insertion of the feeding loop.

Table 5.3: Calibration parameters of the $5\,\mathrm{GHz}$ and $9.5\,\mathrm{GHz}$ resonators for various analysis methods.

Frequency	Kent		Modal		Numerical	
$5\,\mathrm{GHz}$	a_{eff}	$20.018\,\mathrm{mm}$	a_{eff}	$20.026\,\mathrm{mm}$	a_{eff}	$20.015\,\mathrm{mm}$
	σ_{eff}	$8.573 \cdot 10^6\ \mathrm{S/m}$	σ_{eff}	$8.592 \cdot 10^6\ \mathrm{S/m}$	σ_{eff}	$8.553 \cdot 10^6\ \mathrm{S/m}$
					I_{loop}	$0.037\,\mathrm{mm}$
$9.5\,\mathrm{GHz}$	a_{eff}	$15.1014\,\mathrm{mm}$	a_{eff}	$15.057\,\mathrm{mm}$	a_{eff}	$15.046\,\mathrm{mm}$
	σ_{eff}	$7.744 \cdot 10^6\ \mathrm{S/m}$	σ_{eff}	$6.775 \cdot 10^6\ \mathrm{S/m}$	σ_{eff}	$7 \cdot 10^6\ \mathrm{S/m}$
					I_{loop}	$0.300\,\mathrm{mm}$

For the $5\,\mathrm{GHz}$ and $9.5\,\mathrm{GHz}$ resonators, all measurements were conducted using the same feeding configuration. However, five distinct feeding configurations were utilised for the $11\,\mathrm{GHz}$ measurements, necessitating five separate calibration procedures. Table 5.4 provides a summary of the calibrated parameters for the split-cylinder-cavity resonator corresponding to the different configurations employed at $11\,\mathrm{GHz}$.

5.2.2.7 Glass characterisation

We used the Kent methods described in [160, 161] to characterise the dielectric permittivity of the glass material used in the liquid crystal cells. Since glass is a crystalline solid that can exhibit dielectric anisotropy, we decided to determine its permittivity at two orthogonal orientations. Additionally, we decided to characterise two glasses with thicknesses of $0.394\,\mathrm{mm}$ and $0.403\,\mathrm{mm}$ to verify the homogeneity of the results.

The measurement procedure consisted in introducing the glass in the resonator following a preferred direction and measuring the S parameters. Then, the glass was rotated by $90°$,

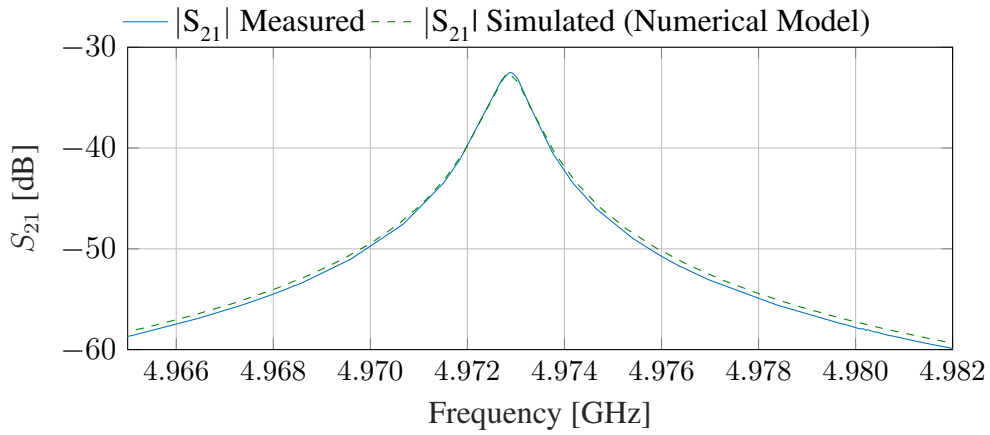

(a)

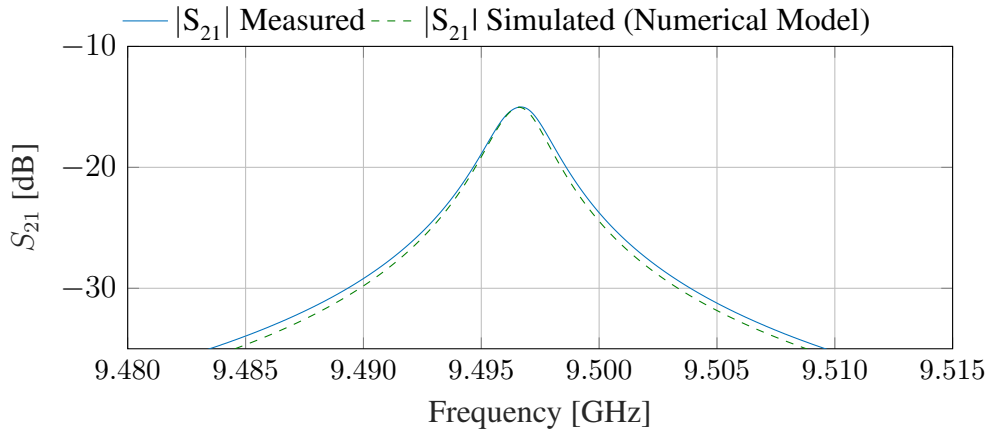

(b)

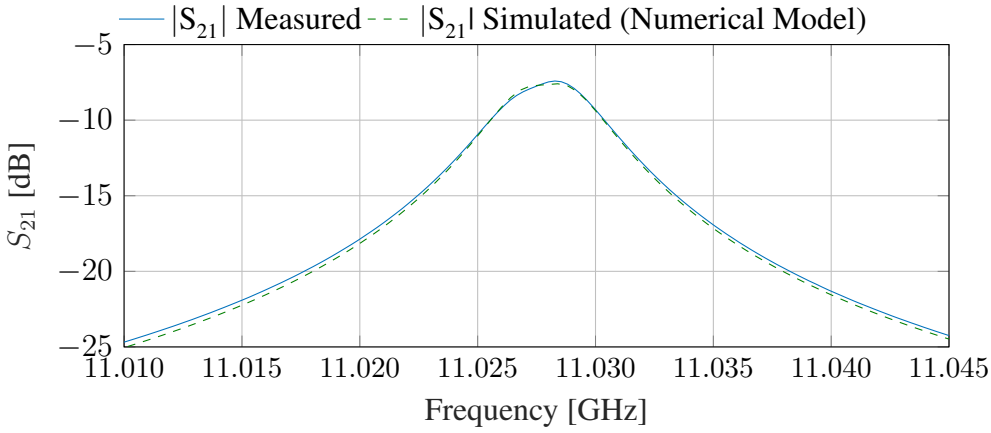

(c)

Figure 5.13: Comparison between the measured response of the empty resonators and the adjusted response of the numerical method analysis for the: (a) 5 GHz resonator, (b) 9.5 GHz resonator, and (c) 11 GHz resonator.

Table 5.4: Calibration parameters of the 11 GHz resonator for various analysis methods and measurement runs.

Calibration	Kent	Modal	Numerical
Glass measurement 1	a_{eff} 10.002 mm σ_{eff} $8.431 \cdot 10^6$ S/m	a_{eff} 10.003 mm σ_{eff} $8.367 \cdot 10^6$ S/m	a_{eff} 9.999 mm σ_{eff} $10 \cdot 10^6$ S/m I_{loop} 0.3 mm
Cell measurement 2	Not applicable	a_{eff} 10.118 mm σ_{eff} $5.739 \cdot 10^6$ S/m	a_{eff} 10.013 mm σ_{eff} $9.000 \cdot 10^6$ S/m I_{loop} 0.309 mm
Cell measurement 3	Not applicable	a_{eff} 10.012 mm σ_{eff} $7.120 \cdot 10^6$ S/m	a_{eff} 9.997 mm σ_{eff} $10.000 \cdot 10^6$ S/m I_{loop} 0.300 mm
Cell measurement 4	Not applicable	a_{eff} 10.003 mm σ_{eff} $8.367 \cdot 10^6$ S/m	a_{eff} 9.998 mm σ_{eff} $10.000 \cdot 10^6$ S/m I_{loop} 0.290 mm
Cell measurement 5	Not applicable	a_{eff} 10.012 mm σ_{eff} $7.120 \cdot 10^6$ S/m	a_{eff} 9.997 mm σ_{eff} $10.000 \cdot 10^6$ S/m I_{loop} 0.300 mm

and the S-parameters of the system were measured again. This process was repeated for both glasses at the three frequencies of interest. Figures 5.14 (a), (b), and (c) illustrate the measured response of the split-cylinder resonators when loaded with the thinner glass. The results of the thick glass were similar.

Once the measurements had been performed, the resonance frequency and quality factor were calculated and analysed to obtain the associated dielectric permittivity. Table 5.5 shows the average permittivity for both glasses obtained with the different analysis methods.

Table 5.5: Average permittivity and loss tangent of the two glasses considered for the study.

Glass	5 GHz		9.5 GHz		11 GHz	
	ε_r	$\tan\delta$	ε_r	$\tan\delta$	ε_r	$\tan\delta$
Glass 1	7.287	0.0144	7.163	0.0142	7.148	0.0166
Glass 2	7.254	0.0144	7.090	0.0149	7.120	0.0164

It can be concluded that the employed glasses are isotropic dielectrics and exhibit a very homogeneous permittivity between samples. These permittivity values of the glass will be used to compute the dielectric permittivity of the liquid crystal cells.

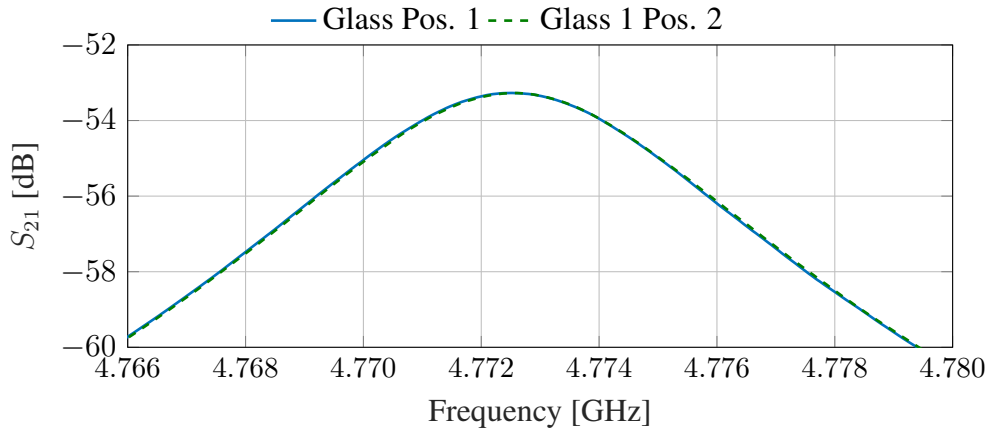

(a)

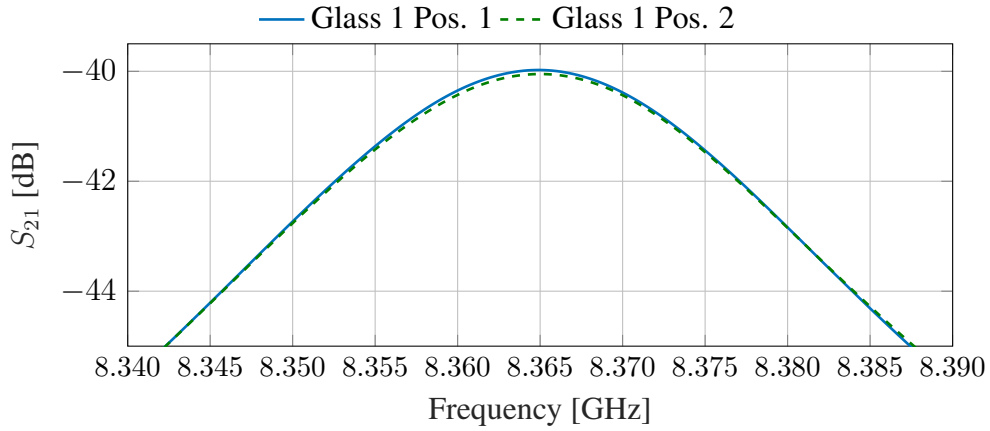

(b)

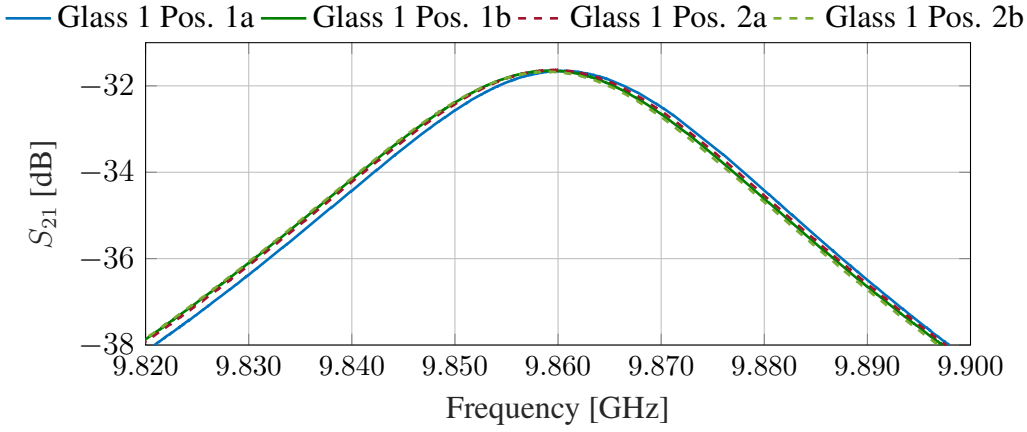

(c)

Figure 5.14: Comparison between the measured response of the resonators filled with a homogeneous glass and the adjusted response of the numerical method analysis for the: (a) 5 GHz resonator, (b) 9.5 GHz resonator, and (c) 11 GHz resonator.

5.2.2.8 Liquid crystal characterisation

It was decided to study four commercial mixtures of LC: the QYPDLC-036, QYPDLC-142, and QYPDLC-193 mixtures from Qingdao QY Liquid Crystal Co., and the GT3-23002 mixture from Merck KGaA. Table 5.6 summarises the most important properties of these liquid crystals.

Table 5.6: Most important electromagnetic properties of the considered LC samples.

Cell	Liquid Crystal	λ_{meas} (nm)	$n_\perp$	$\varepsilon_\perp$	$n_\parallel$	$\varepsilon_\parallel$
Cell 1	QYPDLC-036	589	1.5210	2.3134	1.7710	3.1364
Cell 2	QYPDLC-142	589	1.5235	2.3211	1.7745	3.1488
Cell 3	QYPDLC-193	589	1.5250	2.3256	1.7770	3.1577
Cell 4	GT3-23002	589	1.5094	2.2783	1.7986	3.2350

The measurement procedure consists in introducing the liquid crystal cell in the middle of the split-cylinder-cavity resonator with their molecules orientated parallel to the electric field and measuring the S parameters of the filled resonator. Then, the cell is rotated $90°$ to measure the S parameters of the resonator filled with the molecules of the liquid crystal perpendicularly orientated with the electric field. This measuring process was repeated three times per sample and position in order to obtain several realisations and reduce the effect of measurement errors. Then, these measurements, along with the measurement of the empty resonator, were analysed using the modal and numerical method to obtain the associated permittivity and loss tangent of the liquid crystal.

Several factors can introduce errors in the calculation of permittivity. These include uncertainties in the measurement of the dimensions of the split-cylinder cavity (such as radius and length), changes in the properties of the resonator (like conductivity of the brass and penetration of the feeding loop), errors in the measurement of centre frequency and quality factor, and discrepancies in the dimensions of the LC cell (such as the thickness of the two glasses, h_{g1} and h_{g2}, and the thickness of the liquid crystal cavity, h_{LC}). While the calibration process can compensate for the cavities' dimensions and their conductivity and feeding network errors, measurement uncertainties in other parameters can still impact the permittivity calculation. The uncertainties (σ_i) in these measurements result in an error contribution to the value of the complex permittivity ($\partial\varepsilon/\partial i$). Supposing the variables are uncorrelated, we can propagate the uncertainties to obtain the total uncertainty of the complex dielectric permittivity using the equation 5.16. The uncertainty of each variable was estimated based on the dispersion observed in their multiple measurements and the typical error of the measurement systems, and the error contribution of each variable was estimated using the numerical

method.

$$\sigma_\varepsilon = \sqrt{\left|\frac{\partial\varepsilon}{\partial h_{g1}}\right|^2 \sigma_{h_{g1}}^2 + \left|\frac{\partial\varepsilon}{\partial h_{g2}}\right|^2 \sigma_{h_{g2}}^2 + \left|\frac{\partial\varepsilon}{\partial h_{LC}}\right|^2 \sigma_{h_{LC}}^2 + \left|\frac{\partial\varepsilon}{\partial f}\right|^2 \sigma_f^2 + \left|\frac{\partial\varepsilon}{\partial Q}\right|^2 \sigma_Q^2} \tag{5.16}$$

Figures 5.15 (a), (b), and (c) depict the measurements and adapted responses of cell 4, which was filled with the GT3-23002 mixture from Merck. As observed in this figure, the measurements are very consistent for the different measurement realisations of the same cell position. Moreover, the resonance frequency of position 1 is lower than that observed for position 2, which indicates that the parallel permittivity is higher than that of the perpendicular one. This aligns with the typical behaviour of liquid crystals [150]. Similar results were obtained in the other split-cylinder cavities.

Tables 5.7 and 5.8 present the computed permittivity values of the various LC mixtures for the $5\,\mathrm{GHz}$ resonator, along with their uncertainties. The assumption of dielectric isotropy has already been corrected using equation 5.15 so that the permittivity values presented in the tables represent the parallel and perpendicular permittivity. The results obtained using both analysis methods are consistent, and the computed permittivity and loss tangent values agree with similar findings reported in the literature [150].

Table 5.7: Calculated permittivity of different liquid crystals at 5 GHz using the modal method

LC	$\varepsilon_{r\parallel}$	$tan\delta_{\parallel} \times 10^3$	$\varepsilon_{r\perp}$	$tan\delta_{\perp} \times 10^3$
Q036	3.08±0.19	17.06±2.08	2.28±0.15	75.45±7.89
Q142	2.72±0.17	7.95±1.09	2.27±0.16	58.51±7.20
Q193	3.03±0.19	7.14±0.97	2.22±0.15	91.90±7.55
GT3	2.59±0.15	5.13±1.79	1.94±0.14	39.33±10.90

Table 5.9 summarises the computed permittivity of the LC mixtures for the $9.5\,\mathrm{GHz}$ resonator. Only the modal method could be applied in this case, as the numerical method did not achieve a valid solution. The data obtained at this frequency are not physically plausible as the perpendicular permittivity values are higher than the parallel ones, and the loss-tangent values are inconsistent, with some loss-tangent values being negative, which is absolutely impossible. These results are clearly invalid and are likely due to an error in the measurement setup or in the mechanism used to feed the resonator.

Tables 5.10 and 5.11 display the calculated permittivities of the different LC mixtures for the $11\,\mathrm{GHz}$ resonator. As for the $5\,\mathrm{GHz}$ resonator, the permittivity values have already been corrected using equation 5.15 to obtain the parallel and perpendicular permittivity. The

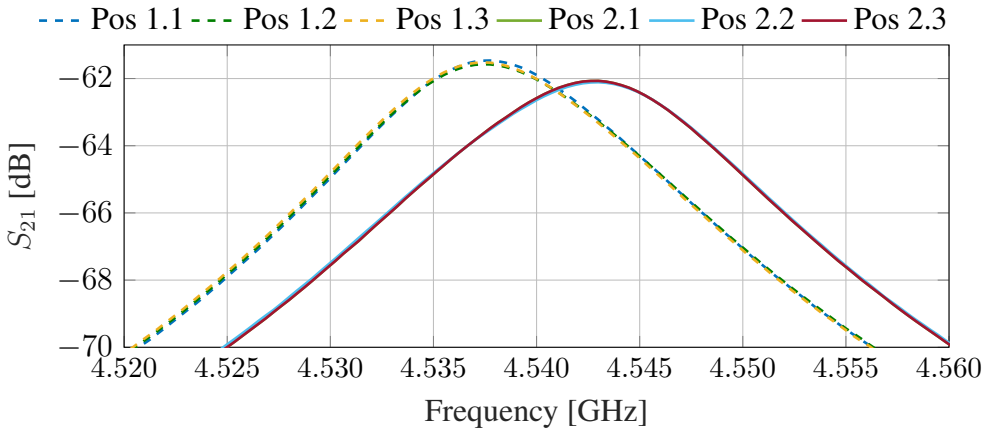

(a)

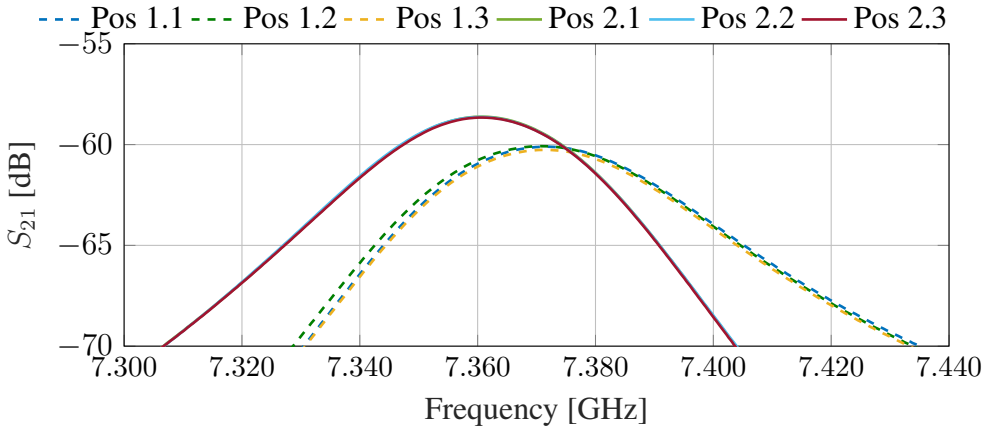

(b)

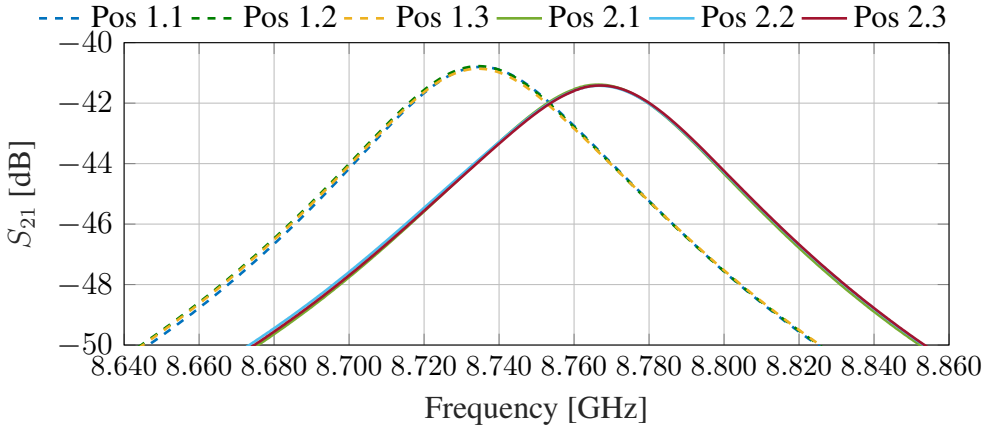

(c)

Figure 5.15: Response of resonators loaded with Cell 4 (GT3-23002) at different positions and for different frequencies: (a) 5 GHz resonator, (a) 9.5 GHz resonator, and (c) 11 GHz resonator.

Table 5.8: Calculated permittivity of different liquid crystals at 5 GHz using using numerical method.

LC	$\varepsilon_{r\|\|}$	$tan\delta_{\|\|} \times 10^3$	$\varepsilon_{r\perp}$	$tan\delta_{\perp} \times 10^3$
Q036	3.11±0.22	17.01±2.67	2.29±0.19	75.61±9.45
Q142	2.74±0.15	8.73±2.03	2.26±0.13	65.97±6.70
Q193	3.07±0.10	6.64±0.70	2.22±0.13	94.82±14.51
GT3	2.63±0.16	4.81±2.27	1.97±0.17	39.14±11.81

Table 5.9: Calculated permittivity of different liquid crystals at 9.5 GHz using the modal method.

	Position 1		Position 2	
Liquid Crystal	ε_r	$tan\delta$	ε_r	$tan\delta$
QYPDLC-036	2.8725	0.0062	3.1203	-0.0123
QYPDLC-142	2.6170	-0.0098	3.0104	-0.0273
QYPDLC-193	3.5268	0.0055	3.7201	-0.0031
GT3-23002	2.592	-0.0076	2.8579	-0.0297

results obtained using both analysis methods are consistent and fit similar research reported in the literature [150].

Table 5.10: Calculated permittivity of different liquid crystals at 11 GHz using the modal method.

LC	$\varepsilon_{r\|\|}$	$tan\delta_{\|\|} \times 10^3$	$\varepsilon_{r\perp}$	$tan\delta_{\perp} \times 10^3$
QYPDLC-036	3.22±0.19	3.95±0.67	2.24±0.15	57.51±6.80
QYPDLC-142	3.05±0.18	5.80±1.06	2.36±0.16	40.88±4.92
QYPDLC-193	3.26±0.20	1.97±0.11	2.40±0.17	63.31±4.40
GT3-23002	3.25±0.21	2.50±0.83	2.35±0.17	22.05±3.81

Table 5.11: Calculated permittivity of different liquid crystals at 11 GHz using numerical method.

LC	$\varepsilon_{r\|\|}$	$tan\delta_{\|\|} \times 10^3$	$\varepsilon_{r\perp}$	$tan\delta_{\perp} \times 10^3$
QYPDLC-036	3.22±0.20	3.47±0.80	2.23±0.19	71.38±18.57
QYPDLC-142	3.09±0.21	6.63±1.76	2.33±0.15	43.05±3.77
QYPDLC-193	3.26±0.16	3.58±0.54	2.34±0.17	60.43±4.75
GT3-23002	3.32±0.20	3.70±1.00	2.32±0.0.16	19.92±5.20

In conclusion, the study successfully measured the permittivity values of different liquid crystal mixtures using split-cylinder resonators at two frequencies, $5\,\mathrm{GHz}$ and $10\,\mathrm{GHz}$. The results showed that QYPDLC-036 and QYPDLC-193 had the highest dielectric anisotropy

but also the highest loss tangent values, while the GT3 mixture presented a good balance between dielectric anisotropy and low loss tangent. Considering the high loss-tangent values of the other mixtures, the GT3 liquid crystal is the most appropriate candidate for microwave applications.

5.2.3 Substrate-Integrated Resonator

Nematic liquid crystals have a significant limitation for microwave applications: the lack of proper characterisation of commercial mixtures at this frequency band. While the split-cylinder-cavity resonator method discussed earlier accurately determines the dielectric properties of four liquid crystals, it does not provide information on important properties such as the splay elastic constant K_{11} and the rotational viscosity γ_{11}. As was introduced in Section 5.1, these parameters are closely related to the threshold voltage and reconfiguration speed of the liquid crystals, parameters that significantly impact the performance of tunable devices. This section introduces the design of a tunable resonator implemented on a reliable substrate-integrated resonator that can be used to compute the dielectric permittivity, loss tangent, K_{11}, and γ_{11} of a liquid crystal sample.

5.2.3.1 LC parameters extraction

The characterisation method is primarily based on the operational mechanism of the LC cell depicted in Figure 5.16 and explained in Section 5.1. In a liquid crystal cell, the orientation and rotation of the liquid crystal molecules is achieved by combining the effects of an anchoring layer and a low-frequency bias voltage (typically operating at $1\,\mathrm{kHz}$).

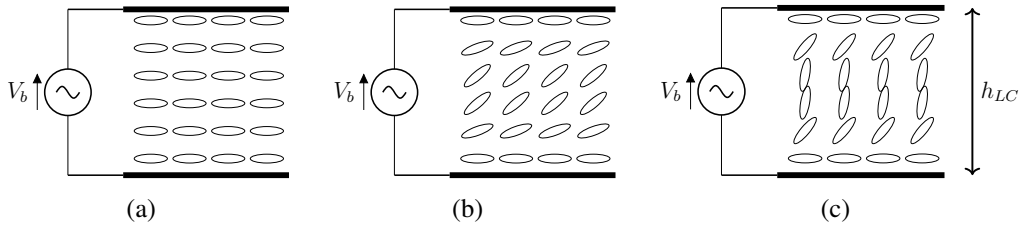

Figure 5.16: Alignment and polarisation of an LC cell under different bias voltages (V_b): (a) $V_b < V_{th}$, (b) $V_b > V_{th}$, and (c) $V_b >> V_{th}$.

The behaviour of the liquid crystal molecules in this structure can be effectively modelled using the analytical solution to the Fréedericksz transition, originally developed in [164]. This solution accurately describes the electrodynamics of liquid crystals when a strong electric

or magnetic field is applied to a perfectly aligned volume of liquid crystal. Below a certain threshold field intensity, the forces of the anchoring layer predominate over the electric forces, and the orientation of the liquid crystal molecules remains undistorted. However, once the field intensity surpasses this threshold value, the molecules begin to rotate. The critical field intensity for this transition can be determined using the following equation:

$$E_{th} = \frac{\pi}{h_{LC}} \sqrt{\frac{K_{11}}{\varepsilon_0 \Delta\varepsilon^{LF}}} \tag{5.17}$$

where K_{11} represents the splay deformation constant, h_{LC} denotes the height of the liquid crystal cavity, ε_0 stands for the vacuum permittivity, and $\Delta\varepsilon^{LF}$ represents the dielectric anisotropy of the liquid crystal at the low-frequency biasing signal.

If the dimensions of the liquid crystal cell and the LC anisotropy are known, the K_{11} constant can be determined by characterising the threshold electric field.

The Fréedericksz transition solution also provides an approximation for the response time of the transition between parallel and perpendicular polarisation states of the LC material. The switch-on response time (τ_{on}) required to transition from the steady state ($V_b = 0$) to the perpendicular state ($V_b = V_{max}$), and the switch-off response time (τ_{off}) needed to transition from the parallel state ($V_b = V_{max}$) to the steady state ($V_b = 0$) are defined by the following expressions [148, 150, 164]:

$$\tau_{on} = \frac{\gamma_{11} h_{LC}^2}{K_{11}\pi^2 (\frac{V_{max}^2}{V_{th}^2} - 1)} \tag{5.18}$$

$$\tau_{off} = \frac{\gamma_{11} h_{LC}^2}{K_{11}\pi^2} \tag{5.19}$$

where γ_{11} represents the rotational viscosity of the liquid crystal, V_{th} is the threshold voltage applied between two plates of the cell ($V_{th} = E_{th} \cdot h_{LC}$), and V_{max} is the biasing voltage applied to achieve the switch-on transition. It is important to note that these equations are valid under the assumption that backflow and inertial effects are negligible [165].

The previous equations can be used to approximate the value of the rotational viscosity γ_{11} after measuring the switch-off or switch-on times of a commutable device. However, equation 5.18 is only valid when the applied voltage V_{max} is not much higher than the threshold voltage V_{th} [148]. As this condition is difficult to determine in liquid crystal mixtures with unknown characteristics, it is preferable to use the relaxation time expression given by equation 5.19 to compute the rotational viscosity γ_{11}.

In conclusion, the rotational viscosity γ_{11} and splay deformation constant K_{11} of an unknown liquid crystal can be estimated by measuring the threshold voltage and switch-on time

of a tunable device. Provided that the topology of the device resembles an LC cell, including an effective anchoring layer and two parallel conductors that facilitate the application of a polarisation electric field. The following section provides a comprehensive description of a newly developed substrate-integrated cavity specifically designed to fulfil these requirements.

5.2.3.2 Substrate-integrated-cavity resonator

The proposed resonator layout, as shown in Figure 5.17, consists of a rectangular cavity resonator integrated within a stack of 5 PCBs. The top and bottom covers of the cavity resonator are implemented in layers 1 and 5, while layers 2, 3, and 4 incorporate the resonator, which includes two LC cavities, the feeding mechanism, the patch polarisers, and the biasing network. This structure enables the orientation and rotation of liquid crystal molecules by combining an anchoring layer and an electric field excited between the LC polarisers and the resonator's cavities, implementing a continuous reconfigurable resonator.

The resonator design consists of three stacked rectangular cavities: two empty cavities implemented in layers 2 and 4 and a thin rectangular substrate-integrated waveguide cavity implemented in layer 3. The empty ESIW cavities implemented in layers 2 and 4 house the liquid crystal, while the SIW cavity implemented in layer 3 incorporates two inductive feeding apertures and the LC reconfiguration system. This configuration synthesises a non-homogeneously filled cavity (as depicted in the cross-section depicted in Figure 5.18), where the top and bottom regions are filled with liquid crystal, and the middle region is composed of RO4003C substrate. This arrangement difficulties the electromagnetic analysis but enables the convenient polarisation of the liquid crystal using two polarisation patches milled into the top and bottom cladding of the third layer, as shown in Figure 5.17. These patches are electrically isolated from the rest of the structure and connected to the biasing system through a specially designed biasing network. The biasing network consists of a high-impedance strip line and an open-ended $\lambda/4$-stub line, as illustrated in Figure 5.17 (c) and (d). This configuration serves as a stop-band filter, effectively blocking the transmission of the RF signal through the biasing system.

The proposed resonator behaves as an inhomogeneously filled rectangular cavity resonator, allowing the determination of the dielectric properties of a liquid crystal sample ($\varepsilon_{r(\perp,\parallel)}$ and $\tan\delta_{r(\perp,\parallel)}$) through its resonant parameters. Additionally, by introducing anchoring layers in layers 1, 3, and 5, the liquid crystal cavities resemble the structure of two liquid crystal cells, facilitating the characterisation of mechanical parameters of the liquid crystal sample, including the splay deformation constant (K_{11}) and the rotational viscosity (γ_{11}) of the sample.

The resonator was designed to operate under the TE_{101} mode at $11\,\mathrm{GHz}$ when both cavi-

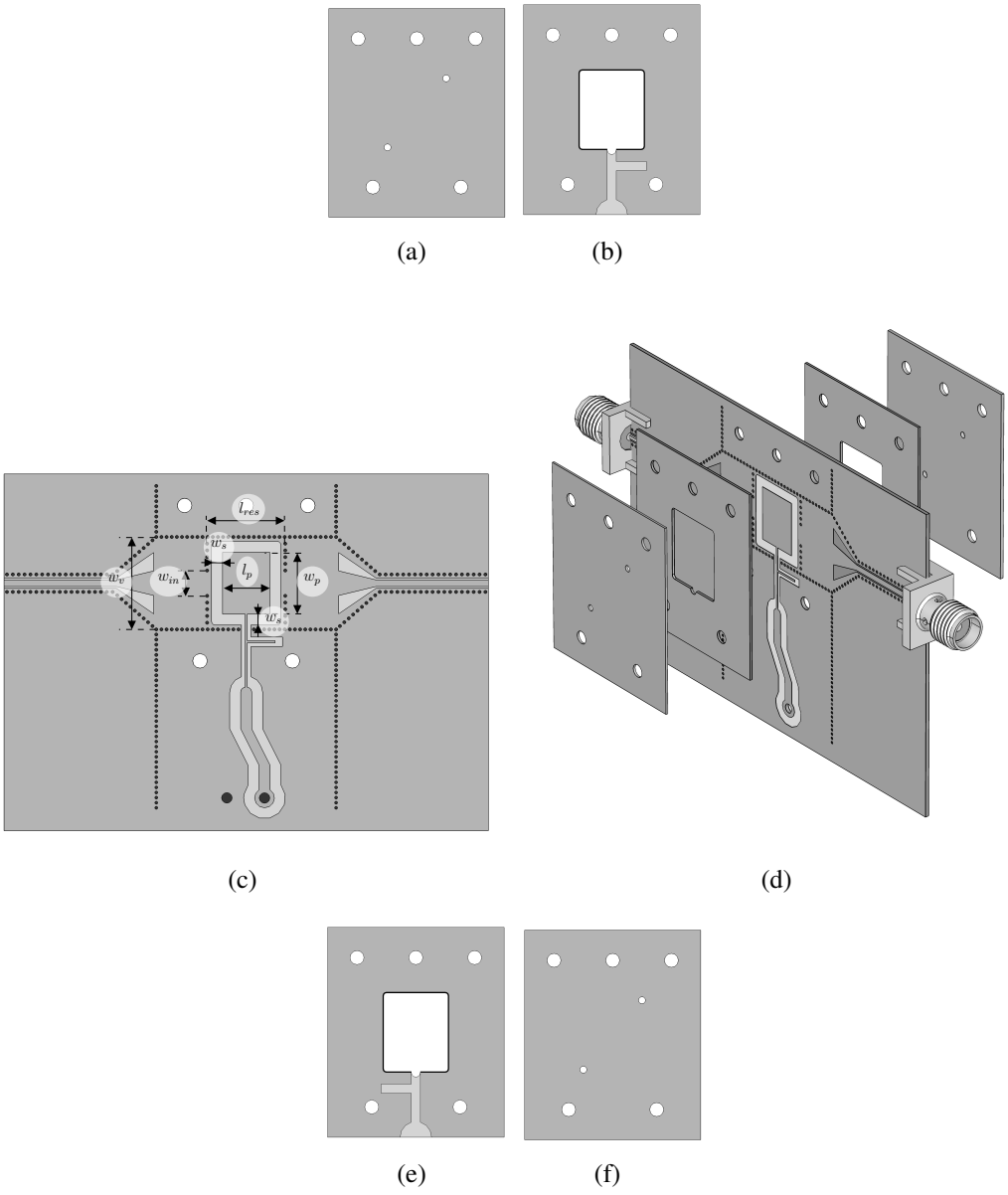

Figure 5.17: Layouts of the proposed resonator: (a) top view of layer 1, (b) top view of layer 2, (c) top view of layer 3, (d) exploded view of the resonator, (e) bottom view of layer 4, and (f) top view of layer 5. Copper is depicted in dark grey, substrate in light grey, empty areas in white, and plated through-hole holes and plated cuts are shown in black.

Figure 5.18: Cross-section of the substrate-integrated resonator. Copper is depicted in yellow, substrate in green, plated through holes in grey, and liquid crystal is represented in blue.

ties are filled with the GT3-23002 liquid crystal ($\varepsilon_{\parallel} = 3.25$ and $\varepsilon_{\perp} = 2.35$). Layers 1 and 5 were implemented on FR4 substrate, while layers 2 and 4 use RO4003C substrate with a dielectric thickness of $0.305\,\mathrm{mm}$. Layer 3 was also developed on RO4003C substrate but with a thickness of $h_{RO} = 0.508\,\mathrm{mm}$. All substrates included top and bottom copper claddings with a thickness of $17\,\mu\mathrm{m}$. The biasing network employed a Phoenix connector with a maximum operation voltage of $300\,\mathrm{Vpp}$, and end-launch SMA connectors were soldered at the input and output feeding lines of the resonator.

Table 5.12 provides the main design parameters of the structure. Figure 5.19 depicts the simulated response of the resonator under different polarisation states of the GT3-23002 liquid crystal. These simulations considered the liquid crystal permittivity and loss tangent values obtained with the split-cylinder resonator method developed in the previous section of the thesis ($\varepsilon_{\parallel} = 3.25$, $\tan\delta_{\parallel} = 0.0025$, $\varepsilon_{\perp} = 2.35$, and $\tan\delta_{\perp} = 0.022\,05$).

Table 5.12: Dimensions of the substrate-integrated resonator.

Parameter	Dimension [mm]	Parameter	Dimension [mm]
W_v	12.7	l_{res}	10.15
W_{win}	3.48	W_s	1.5
W_p	8.5	l_p	3.8
d	0.5	p	0.7

5.2.3.3 Anchoring layer

To ensure an effective anchoring layer, a homogeneous polyimide layer is required. However, the copper surface of layers 1, 5, and 3 of the proposed structure is not as smooth as glass, and the copper roughness can diminish the effectiveness of the anchoring layer, potentially causing malfunctions. Other studies have solved this problem by applying a denser polyimide deposition, resulting in a thicker coating [150, 155]. However, polyimide is very expensive and achieving a sufficiently thick layer can dramatically increase the final cost of

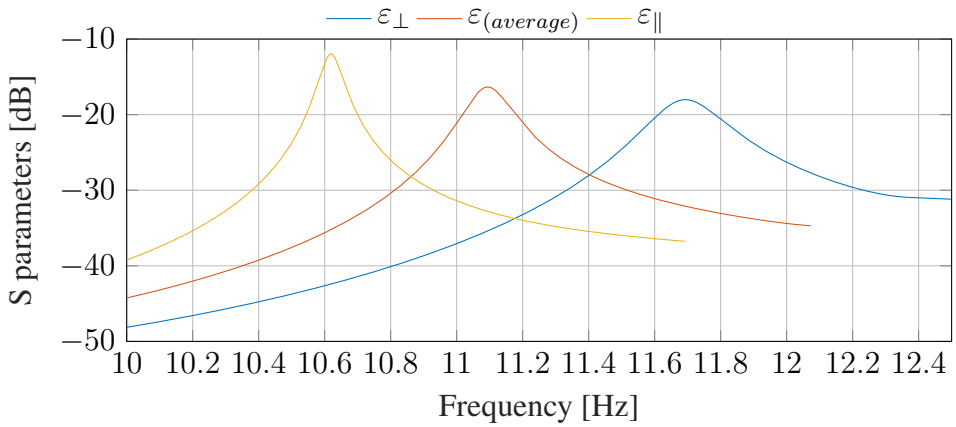

Figure 5.19: Simulated response of the substrate integrated resonator filled with GT3 liquid crystal.

the device. In this work, we proposed using a double deposition that combines a first polycarbonate coating before the polyimide deposition. In this solution, the first polycarbonate layer reduces the roughness of the material and prepares the sample for the final polyimide deposition. The deposition process of both layers is described below.

To prepare the substrates for the anchoring layer deposition, the areas that should not be covered by the layer are masked using Kapton tape. Next, a solution of polycarbonate dissolved in chloroform (methylene chloride) is prepared with a concentration of $15\,\mathrm{mg}$ of polycarbonate per $100\,\mu\mathrm{L}$ of solvent. This solution is then applied to the substrates using a coating blade, and it solidifies within a few seconds at room temperature.

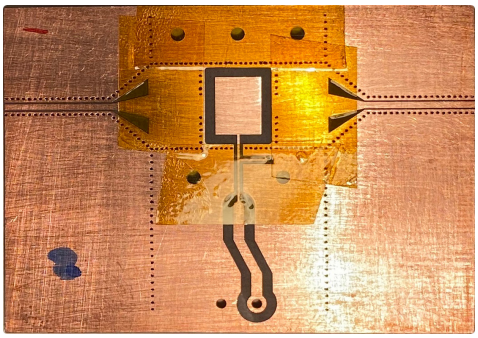

Figure 5.20: Top view of the third layer of the resonator with the Kapton mask.

After applying the polycarbonate coating, we performed several profilometric measurements to assess the thickness of the deposited layer and the reduction of surface roughness. Roughness measurements were taken perpendicular to the propagation direction of the microwave field, and the thickness of the deposition was determined by measuring the surface

profile of a small dent performed in the polycarbonate layer using the profilometer. Figure 5.21 provides the roughness profiles of two substrates: one without the polycarbonate deposition and another with the deposition.

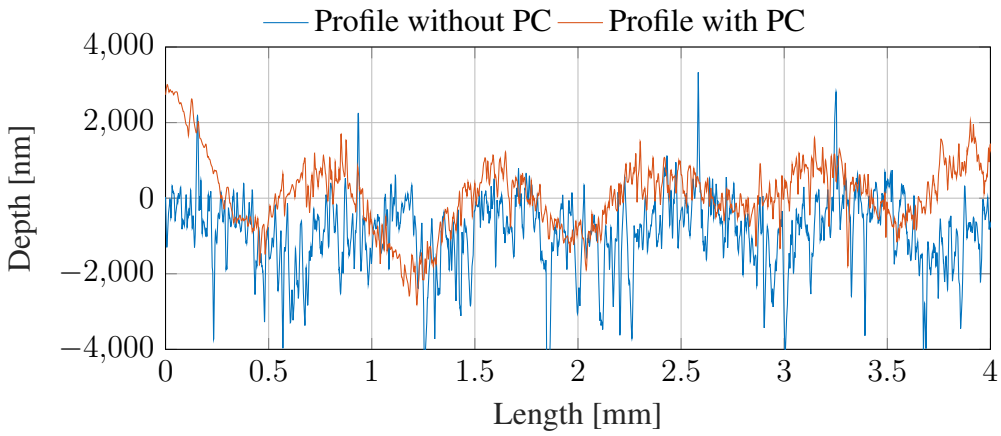

Figure 5.21: Surface roughness profiles before and after the deposition of polycarbonate.

It is important to distinguish between waviness and roughness in the measurements shown in Figure 5.21. Waviness represents gradual depth variations that, in this particular case, are caused by sanding the copper surface with 400-grit sandpaper. These low-frequency variations are difficult to be eliminated, but they do not compromise the effectiveness of the anchoring layer. In contrast, the roughness, characterised by rapid depth fluctuations, does impact the performance of the anchoring layer. The measured copper surface roughness is approximately $417\,\mathrm{nm}$, which is reduced by around $26\,\%$ through the polycarbonate deposition. This decrease ensures a smoother substrate for anchoring layer application, thereby facilitating an effective anchoring.

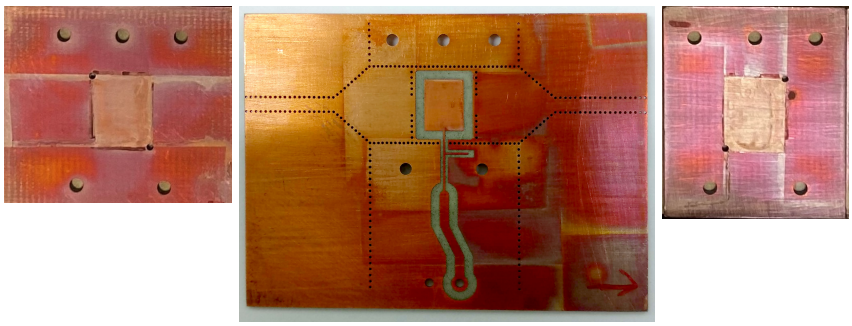

Figure 5.22: From left to right: layers 1, 3, and 5 of the resonator after the application of the double deposition and removal of the Kapton mask.

Once the copper surface had been smoothed, the polyimide was deposited onto the poly-

carbonate deposition by spin coating, using the same profile used for the liquid crystal cells of the split cylinder. Subsequently, the surface of the polyimide layer underwent a series of microgrooves through a rubbing process with a velvet cloth. Finally, the Kapton mask was meticulously removed by delicately cutting the polymeric coating; see Figure 5.22. Notably, the temperature treatment during polyimide solidification contributed to strengthening the adherence of the polycarbonate deposition to the substrate and facilitated the unmasking procedure.

In order to evaluate the efficacy of the double polymeric anchoring layer, it was applied to a glass cell that was subsequently filled with a small volume of GT3 liquid crystal. Light transmission measurements were conducted by positioning the cell between crossed light polarisers. As illustrated in Figure 5.23 (a), blocked light indicates the parallel alignment of the liquid crystal molecules with one of the polarisers. On the other hand, Figure 5.23 (b) displays transmitted light, which occurs when the angle between the liquid crystal molecules and the polarisers is approximately $45°$. Notably, Figure 5.23 (b) also reveals the visible grooves of the anchoring layer.

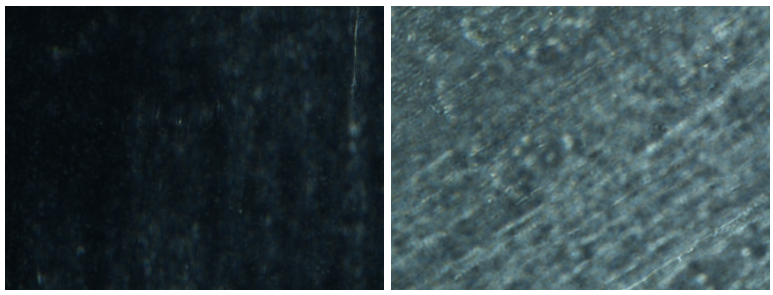

(a) (b)

Figure 5.23: Visual inspection of the liquid crystal polarisation: (a) LC cell aligned with crossed polarisers, (b) LC cell rotated $45°$ with respect to the crossed polarisers. Light transmission in (b) confirms the correct polarisation of the liquid crystal.

5.2.3.4 Assembling and filling

After applying the anchoring layer, the five layers of the substrate-integrated resonator were assembled and fastened. The five layers of the prototype were soldered using low-temperature, no-water-washable solder paste SMDLTLFP10T5 from Chipquik. Subsequently, the frequency response of the empty resonator was measured to verify the proper functioning of the device and detect any potential manufacturing anomalies. This measurement also served to calibrate the analysis model of the resonator, where the width and length of the cavity model were optimised to fit the measured response. Finally, the cavities in layers 2

and 4 were filled with GT3-23002 liquid crystal using a syringe, and the device was sealed using Norland adhesive.

5.2.3.5 Measurement setup

The measurement setup is shown in Figure 5.24. The biasing system consists of a signal generator and a low-frequency amplifier connected to the Phoenix connector of the biasing network. The biasing signal is a sinusoidal wave with a frequency of $1\,\mathrm{kHz}$, which amplitude can vary from $0\,V_{pp}$ to $300\,V_{pp}$. The resonator's frequency response was measured for different bias voltage levels using a calibrated VNA that included additional DC blocks for protection.

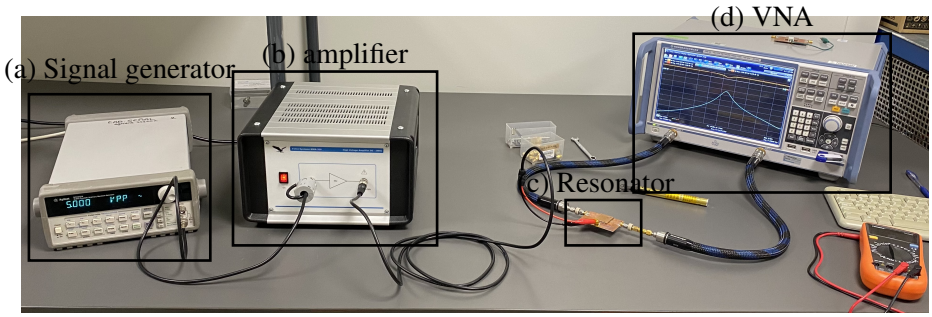

Figure 5.24: Measurement setup: (a) signal generator, (b) low-frequency amplifier, (c) device under test and (d) Vectorial Network Analyser (VNA).

5.2.3.6 Results and discussion

The characterisation procedure consisted in measuring the S parameters of the device under different biasing voltages. The biasing voltage was gradually increased, and when a noticeable change in the resonance frequency of the resonator was detected, the applied voltage was considered as the threshold voltage (V_{th}). This result was used in equation 5.17 to calculate the K_{11} constant. Afterwards, the bias amplitude was gradually increased until reaching the maximum voltage threshold of the Phoenix connectors ($300\,V_{pp}$). Finally, the bias voltage was disconnected, and the switch-off time was measured to determine the liquid crystal's γ_{11} factor using equation 5.19. Table 5.13 compares the results obtained with this method with the manufacturer's data.

Table 5.13: Threshold voltage and response times with their related parameters.

Parameter	Measured	Data sheet
V_{th}	2.48 V_{rms}	2.99 V
τ_{on}	2.20 s	1.19 s
τ_{off}	426.68 s	258.50 s
$\Delta\varepsilon_{r,1kHz}$	-	2.6
K_{11}	14.35 pN	20.90 pN
γ_{11}	393.1 mPa·s	347.0 mPa·s

The computed values demonstrate a reasonable fit with the manufacturing data. The observed discrepancies can be attributed to uncertainties in measuring the liquid crystal cavity height, imperfections in the alignment layer that are not accounted for in the Fréedericksz solution (which affects the K_{11} calculation), and the omission of backflow and inertial effects in the τ_{off} transition within the Fréedericksz solution.

The resonator can also be used to extract the permittivity of the liquid crystal at different polarisation states. In order to do so, the S parameters of the resonator under different biasing voltages were obtained. These polarisation states encompassed the extreme states of the liquid crystal ($\varepsilon_{(r,V_b=0)} \approx \varepsilon_{(r,\perp)}$ and $\varepsilon_{(r,V_b=V_{max})} \approx \varepsilon_{(r,\parallel)}$), as well as several intermediate polarised states ($0 < V_b < V_{max}$).

As a resonator-based method, the complex permittivity of the liquid crystal sample was determined by analysing the resonance frequency and quality factor of the resonator. Since the proposed resonator is non-homogeneous, an equivalent theoretical solution is not available. Instead, a realistic numerical model of the devices was modelled and simulated in the CST simulation software. The dielectric properties of the liquid crystal were obtained by adjusting the simulated responses to the measured responses. To improve the accuracy of the method, the numerical model was firstly calibrated by fine-tuning the length and width of the cavity, as well as the width of the coupling apertures, to align the simulated and measured responses of the empty resonator (without liquid crystal).

The measured and adapted responses of the empty prototype are shown in Figure 5.25. While there is some deviation between the simulation and measurement outside the resonance frequency range, the resonance frequency and quality factor remain consistent between the two models. This slight discrepancy can be attributed to two factors: the omission of SMA connectors in the numerical model and the potential manufacturing tolerances in the transitions and resonator feeding networks.

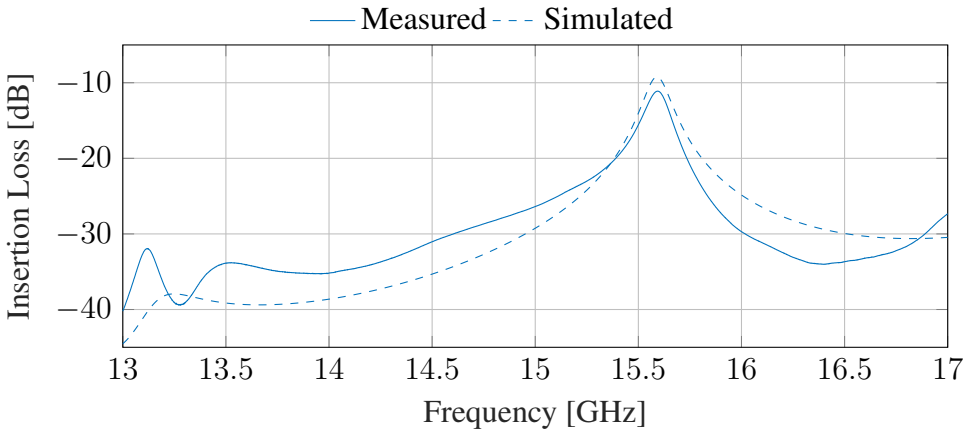

Figure 5.25: Comparison of the measured empty resonator with the adapted response from the numerical simulation.

After calibrating the simulation model, the response of the model filled with liquid crystal was optimised to match the measured responses under different bias voltages, obtaining the complex dielectric permittivity of the GT3-23002 liquid crystal at different polarisation states.

The optimisation process began by computing the dielectric properties at the extreme positions ($\varepsilon_{r,V_b=0}$ and $\varepsilon_{r,V_b=V_{max}}$). The optimisation process started with the permittivity and loss tangent values obtained from a theoretical model based on a TE_{101} mode rectangular resonator. The resonance frequency and quality factor of this theoretical model can be computed by equations 5.20 and 5.21, respectively. Since these equations relate the resonant frequency and quality factor of the resonator with the relative permittivity and loss tangent of the material, the value of these parameters can be directly derived from measurements.

$$f_r^{TE_{101}} = \frac{1}{2\pi\sqrt{\mu \cdot \varepsilon_{eff}}}\sqrt{\left(\frac{\pi}{W_v}\right)^2 + \left(\frac{\pi}{l_{res}}\right)^2} \tag{5.20}$$

$$Q_u = \frac{1}{tan\delta : eff} \tag{5.21}$$

As the actual resonator is not homogeneously filled, the permittivity value obtained with equation 5.20 represents the effective permittivity (ε_{eff}) of an equivalent material that homogeneously fills the resonator. Assuming that the electric field inside the resonator is evenly distributed in height, the permittivity of the liquid crystal can be approximated using the following equation:

$$\varepsilon_{r,eff} = (2 \cdot h_{LC} \cdot \varepsilon_r^{LC} + h_{RO} \cdot \varepsilon_r^{RO})/(2 \cdot h_{LC} + h_{RO}) \tag{5.22}$$

, where $\varepsilon_{r,eff}$ is the effective permittivity of the equivalent homogeneous material of the theoretical model, h_{LC} is the thickness of one of the liquid crystal cavities, h_{RO} is the thickness of the substrate in the centre layer of the resonator, and ε_r^{RO} is the relative dielectric constant of the RO4003C substrate.

Similarly, the loss tangent can be approximated using equation 5.23.

$$tan\delta_{eff} = (2 \cdot h_{LC} \cdot tan\delta^{LC} + h_{RO} \cdot tan\delta^{RO})/(2 \cdot h_{LC} + h_{RO}) \tag{5.23}$$

, where $tan\delta_{eff}$ is the effective loss tangent of the equivalent homogeneous material of the theoretical model, h_{LC} is the thickness of one of the liquid crystal cavities, h_{RO} is the thickness of the substrate in the centre layer of the resonator, and $tan\delta^{RO}$ is the loss tangent of the RO4003C substrate.

It should be noted that the theoretical model did not account for the ohmic loss in the resonator and the radiation loss of the SIW cavities and assumes that the electric field is homogeneously distributed in height. However, the results obtained with this model were used as starting points for the optimisation process, not impacting the final accuracy of the method.

Figure 5.26 shows the frequency response of the resonator at steady ($V_b = 0$) and parallel (V_b=V_{max}) polarisation states versus the adapted simulations. The simulated response of the resonator for a parallel and perpendicular polarisation permittivity obtained with the previous split-cylinder-cavity method listed in Table 5.10 have been included for validation purposes.

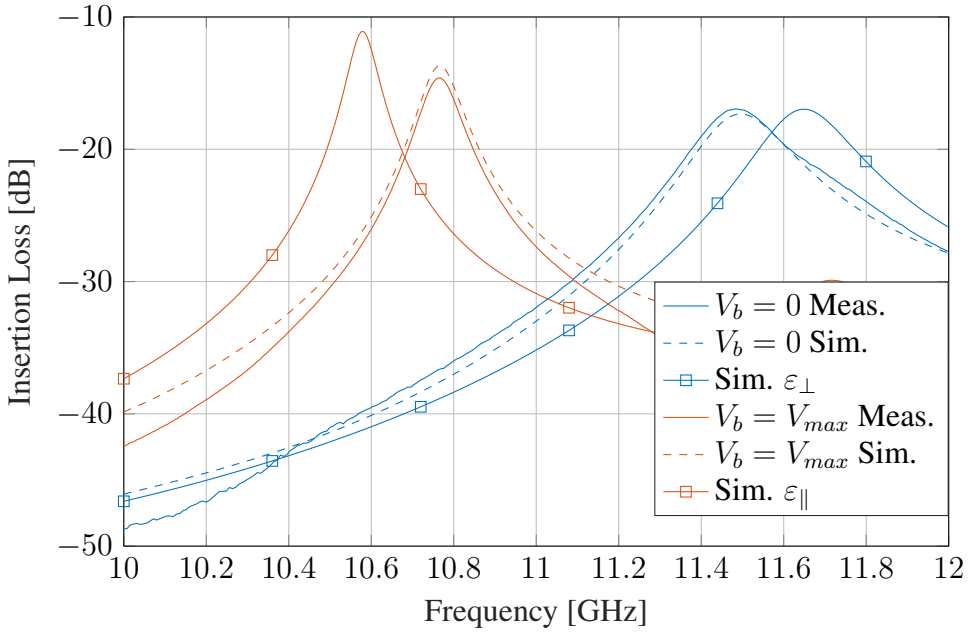

Figure 5.26: Frequency response of the resonator at its two extreme polarisations ($V_b = 0$ and $V_b = V_{max}$) versus the simulation with $\varepsilon_\perp$ and $\varepsilon_\parallel$ obtained from the split cylinder analysis.

As observed in Figure 5.26, the frequency responses of the simulated structure closely match the measurements, and both are in good agreement with the validation results. However, there are slight differences between the measured and validation responses, being the resonance frequency of the unbiased state above the simulated result for the perpendicular polarisation and the simulated frequency of the biased state below the simulated results for the parallel polarisation.

Regarding the differences between the unbiased results and the simulations for the perpendicular polarisation state ($\varepsilon_{r,\perp}$, $V_b = 0$), the observed differences are likely attributed to the non-perfect orientation of the liquid crystal molecules in the resonator. Under no biasing signal, the liquid crystal molecules are aligned with the anchoring layer following the direction of the microgrooves. Since the height of the liquid crystal volume is approximately $400\,\mu\text{m}$, and the roughness of the copper surface was not completely corrected, it is possible that the alignment of the LC molecules was not fully achieved.

On the other hand, the discrepancies related to $\varepsilon_{r,\parallel}$ ($V_b = V_{max}$) can be attributed to the simplification of the molecule orientation in the numerical model. In the simulations, the liquid crystal director was assumed to be parallel to the microwave electric field in the patch area and perpendicular to the electric field in the surrounding areas. However, this assumption is not entirely accurate due to the fringing effect experienced by the electric polarisation field

at the border of the patches. For future work, it is recommended to consider the actual director distribution to further improve the method's accuracy.

Despite these limitations, the proposed resonator demonstrates a reconfigurability range of $6.73\,\%$, resulting in a frequency variation between $f_{(V_b=0)} = 11.51\,\text{GHz}$ and $f_{(V_b=V_{max})} = 10.76\,\text{GHz}$, and showing an unloaded quality factor that ranges from 55.60 to 139.58.

The permittivity characterisation begins by determining the dielectric properties of the parallel and perpendicular polarisation states ($\varepsilon_{(V_b=0)}$, $\varepsilon_{(V_b=V_{max})}$, $\tan\delta_{(V_b=0)}$, and $\tan\delta_{(V_b=V_{max})}$). These values are then used to approximate the permittivity and loss tangent at intermediate polarisation states ($V_{pp} < V_b < V_{max}$) using the frequency dependence shown in equation 5.20. Given that the resonance frequency (f_r) of a rectangular resonant cavity is inversely proportional to the square root of the permittivity ($\sqrt{\epsilon_r}$), and that the quality factor (Q) is proportional to the loss factor ($\tan\delta$), it is possible to infer curves for the resonance frequency versus permittivity and quality factor versus loss tangent, obtaining the results depicted in Figure 5.27.

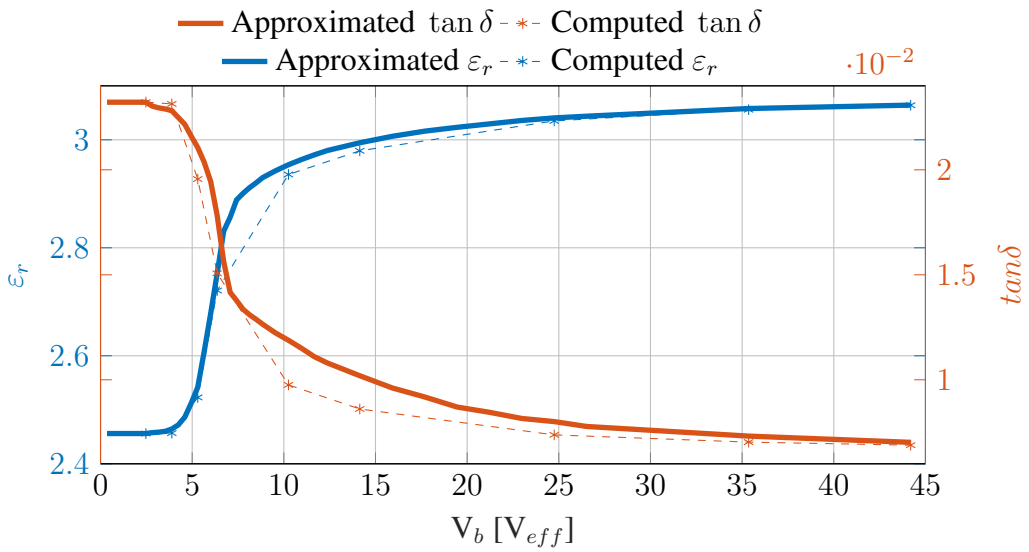

Figure 5.27: Permittivity and loss tangent of the GT3-23002 liquid crystal at different bias voltages.

The extracted values of ε_r (relative permittivity) and $\tan\delta$ (loss tangent) obtained using the resonator-based method are consistent with the values obtained with the split-cylinder method. Furthermore, the variation of permittivity and loss tangent with bias voltage aligns with the expected behaviour, as reported in previous studies [150]. These results validate the accuracy and effectiveness of the resonator-based method for characterising the dielectric properties of the liquid crystal sample.

This study presented a comprehensive characterisation method for determining the dielectric properties of a liquid crystal material under different polarisation states. By employing a substrate-integrated resonator and numerical simulations, the effective permittivity and loss tangent of the liquid crystal at extreme polarisation points were accurately determined. The method was further extended to calculate the dielectric properties at intermediate polarisation states. The results demonstrated a close agreement between the measured and simulated responses, validating the accuracy of the approach. Despite certain limitations, such as imperfect molecular alignment and simplifications in the numerical model, the proposed resonator exhibited a significant reconfigurability range. Overall, this characterisation method provides valuable insights for understanding the behaviour of liquid crystal materials that can be useful for the design and optimisation of reconfigurable microwave devices.

5.3 Tunable Phase Shifter

Phase shifters are essential components in radar systems, electromagnetic sensors, phased array antennas and beamforming. These elements enable the control of the phase of the RF signal, allowing for beam steering and beamforming of phased arrays and signal cancellation in notch filters and interferometers. Several technologies are available for implementing phase shifters, each with its own advantages and characteristics.

One widely used technology for phase shifters is based on semiconductor switches, such as PIN diodes or field-effect transistors. These devices offer fast switching times and wide bandwidth. They allow discrete phase shifts in fixed increments, providing a precise control over the phase shifts. However, digital phase shifters have a limited number of selectable phase states, resulting in a discrete phase response instead of a continuous range of phase shifts (digital phase shifter). Additionally, phase shifters based on these elements normally require complex topologies involving loaded lines or commutable matrices.

Another technology used in phase shifters is the analog phase shifters based on varactor diodes. These devices provide a continuous range of phase shifts by varying the control voltage, offering a high phase resolution and low harmonic distortion. However, they have higher insertion loss than the previously mentioned technologies and can be more susceptible to variations in the temperature and control voltage.

Micro-Electro-Mechanical Systems phase shifters are another technology gaining popularity. These phase shifters utilise micro-scale mechanical structures to achieve both analog and digital phase control. Micro-Electro-Mechanical Systems offer fast switching times, low power consumption, and good linearity. However, they may have a limited phase range and can be sensitive to mechanical vibrations or shock. Moreover, this technology offers a finite

number of actuation cycles, reducing the lifespan of the system.

Functional materials have emerged as a promising technology for phase shifters. These materials exhibit unique properties that allow the control of their electromagnetic properties through an external stimuli. Ferroelectric materials have been traditionally used for implementing tunable devices at microwave frequencies, including phase shifters. They provide fast response times, low power consumption, and a broad range of phase shifts. These materials can work at high frequencies and offer wide bandwidth. However, they are very susceptible to temperature variations, have limited power handling capabilities, and their integration in planar circuits is complex.

On the other hand, liquid crystal phase shifters offer continuous and wide-range phase shifts with relatively low insertion loss and power consumption. They can be easily integrated into planar transmission lines, which makes them suitable for compact designs. Moreover, they offer wide bandwidth and work at high frequencies, which makes them particularly suitable for the new scenario of the space sector.

This section emphasises the design and measurement of a line-based phase shifter using liquid crystal. These phase shifters are attractive due to their straightforward design, involving a transmission line section filled with the functional material. Liquid crystal enables a continuous tuning of the phase shift and does not need a complex design based on loaded lines or switching matrices like other technologies. Moreover, several studies have demonstrated the reliability of liquid crystal under space ambient conditions, with no significant issues reported [166–168]. The following section provides a comprehensive explanation of the phase shifter's topology, the design process, and the measurement results.

5.3.1 Phase Shifter Structure

The proposed phase shifter is a section of an Empty Substrate Integrated Coaxial Line (ESICL) line filled with liquid crystal. In this configuration, the phase shift of the transmission line can be controlled by changing the permittivity of the liquid crystal, enabling continuous tunability. The ESICL line was selected because it has very low losses, a broadband single-mode operation bandwidth, and easy integration to planar subsystems. Moreover, as the ESICL line propagates a TEM mode, their two conductors can be used to excite the polarisation voltage needed to configure the LC. This eliminates the need for complex polariser structures, enormously simplifying the design.

A cross-section of the phase shifter is shown in Figure 5.28. It illustrates the typical stack-up of 5 PCBs required to create an ESICL line.

The phase shifter was designed to have a characteristic impedance of $50\,\Omega$, a square geometry, and a small and uniform spacing between conductors. The $50\,\Omega$ impedance facilitates

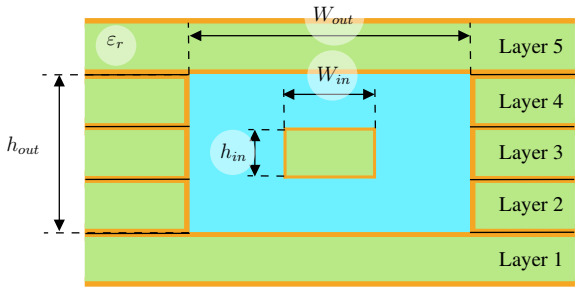

Figure 5.28: Cross-section of the ESICL phase shifter, illustrating the different components. The copper layers are represented in orange, the substrate in green, and the liquid crystal in blue.

the integration into communication systems, while the square geometry enhances the single-mode bandwidth, as was studied in Section 4.4.1. Finally, as the inner and outer conductor of the line serve as LC polarisers, the uniformity and small separation between conductors ensure a consistent polarisation of the liquid crystal for low biasing voltages.

Another important factor when designing the line is the selection of the substrate. The permittivity variation of the liquid crystal can impact the performance of the ESICL transition. In order to mitigate this effect, a substrate with a relatively high dielectric permittivity was chosen. Among the available options, it was decided to use the RO4360G2 substrate with a permittivity of $\varepsilon_r = 6.15$. This substrate offers the advantage of having a permittivity that doubles that of the liquid crystal. Additionally, it is easier to process than Teflon-based substrates, which can be challenging to mill and metallise despite having a higher dielectric permittivity.

The chosen stack-up consisted of a $0.305\,\mathrm{mm}$ thick RO4360G2 substrate for layer 3, $0.508\,\mathrm{mm}$ thick RO4360G2 substrates for layers 2 and 4, and a $1.5\,\mathrm{mm}$ thick FR4 substrate for the top and bottom covers (layers 1 and 5). Each layer includes a top and bottom copper cladding of $17.5\,\mu\mathrm{m}$ thickness. Moreover, layers 2, 3, and 4 underwent an additional metallisation during manufacturing, adding an $30\,\mu\mathrm{m}$ of copper, and a solder paste layer of approximately $50\,\mu\mathrm{m}$ thickness was applied between the different layers of the structure. With the defined impedance and substrate stack-up, the final dimensions of the ESICL line are: $W_{in} = 0.430\,\mathrm{mm}$, $W_{out} = 1.838\,\mathrm{mm}$, $h_{in} = 0.400\,\mathrm{mm}$, $h_{out} = 1.809\,\mathrm{mm}$. These dimensions were calculated using equation 4.5, considering an average permittivity of $\varepsilon_{eff} \approx 2.9$ for the liquid crystal.

5.3.2 Transition

Due to the reduced cross-section of the inner conductor of the designed ESICL line, the transition developed in Section 4.4.1 was chosen. This new transition replaced the lateral cuts of the previous design [87] with a row of plated bias, enhancing the mechanical reliability of the structure. The layout of the transition can be seen in Figure 5.29, it consists of a coplanar feeding line, a quarter wavelength stripline, a suspended stripline section, and the feeding iris mentioned earlier. Additionally, a tapered transition was incorporated into the suspended stripline to improve the matching between the high permittivity substrate and the LC-filled ESICL.

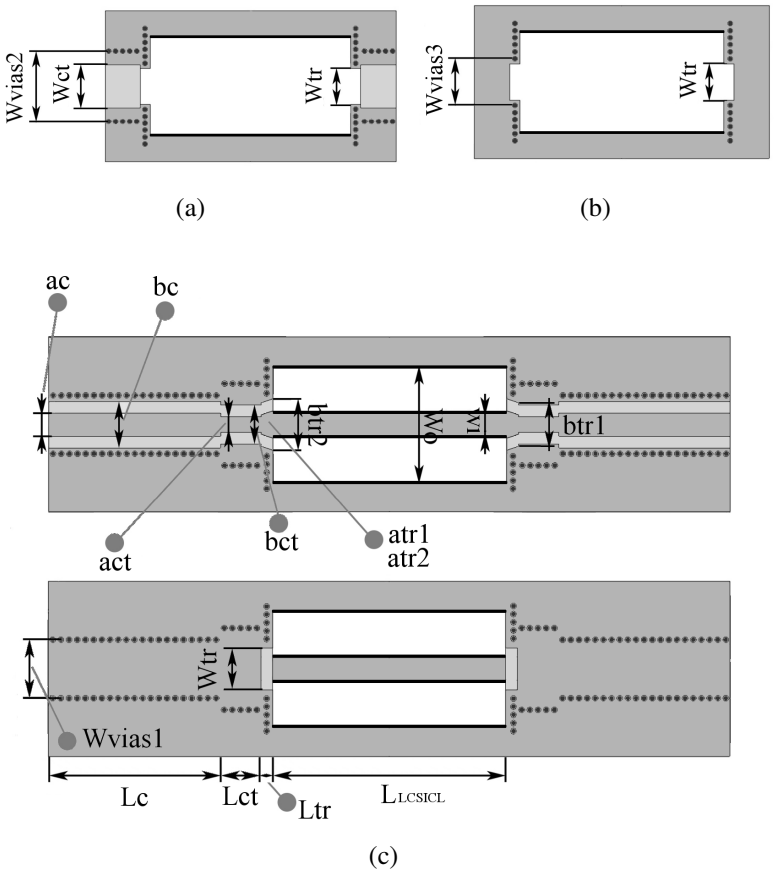

Figure 5.29: Layout of the ESICL phase shifter: (a) bottom view of layer 4, (b) top and bottom view of layer 2, and (c) from top to bottom, the top and bottom view of the third layer. Copper is depicted in dark grey, substrate in light grey, empty areas in white, and plated through-hole holes and plated cuts are shown in black.

The design procedure followed a similar approach to that described in [87] and explained in Section 4.4.1. Initially, the dimensions of the coplanar waveguide and stripline were chosen

to achieve a $50\,\Omega$ impedance. The coplanar waveguide was chosen to have a length of $15\,\mathrm{mm}$ to facilitate the end-launch connectors assembly, and the initial length of the stripline was $\lambda/4$. The widths of the tapered suspended stripline were adjusted to match the width of the stripline and the inner conductor of the ESICL. For simplicity, the length of the tapered suspended stripline was initially set to $1\,\mathrm{mm}$. Finally, the width and length of the stripline, and both widths of the tapered suspended striplines were optimised to achieve a minimum insertion loss of $-15\,\mathrm{dB}$ from $0\,\mathrm{Hz}$ to $20\,\mathrm{GHz}$. The final dimensions of the phase shifter and transition are provided in Table 5.14.

Table 5.14: Dimensions for the coplanar to liquid crystal ESICL transition

Parameter	Dimensions [mm]	Parameter	Dimensions [mm]
a_c	0.40	W_o	1.838
b_c	1.30	W_{vias1}	2.300
act	0.25	W_{vias2}	3.200
b_{ct}	1.30	W_{vias3}	2.300
a_{tr1}	0.36	W_{ct}	2.300
a_{tr2}	0.44	L_c	14.700
b_{tr1}	0.95	L_{ct}	3.500
b_{tr2}	1.10	L_{tr}	1.000
W_{tr}	1.30	L_{LCSICL}	20.000
W_i	0.43	d_{vias}	0.500

Figure 5.30 illustrates the frequency response of the optimised transition for an intermediate polarisation state of the liquid crystal, characterised by an average permittivity of $\varepsilon_r = (\varepsilon_\parallel + \varepsilon_\perp)/2 = 2.8$. It can be observed that the return loss remains above the $15\,\mathrm{dB}$ specification across the design bandwidth, having a maximum insertion loss of $1.92\,\mathrm{dB}$ at $20\,\mathrm{GHz}$.

Thanks to the liquid crystal, the phase shift of the line can be directly controlled through a biasing voltage (V_b) at $1\,\mathrm{kHz}$ applied between the inner and outer conductor of the ESICL. The following expression can determine the maximum achievable phase shift:

$$\Delta\theta = \theta_2 - \theta_1 = \frac{2\pi f L_{LCSICL}}{c_0}\left(\sqrt{\varepsilon_2} - \sqrt{\varepsilon_1}\right) \tag{5.24}$$

where: $\Delta\theta$ is the relative phase shift between the two extreme polarisation states of the liquid crystal, f stands for the frequency, L_{LCSICL} is the length of the liquid crystal filled ESICL, c_0 is the speed of light in vacuum, ε_1 is the relative permittivity of the liquid crystal at steady state ($V_b = 0$), and ε_2 is the relative permittivity of the liquid crystal under a high

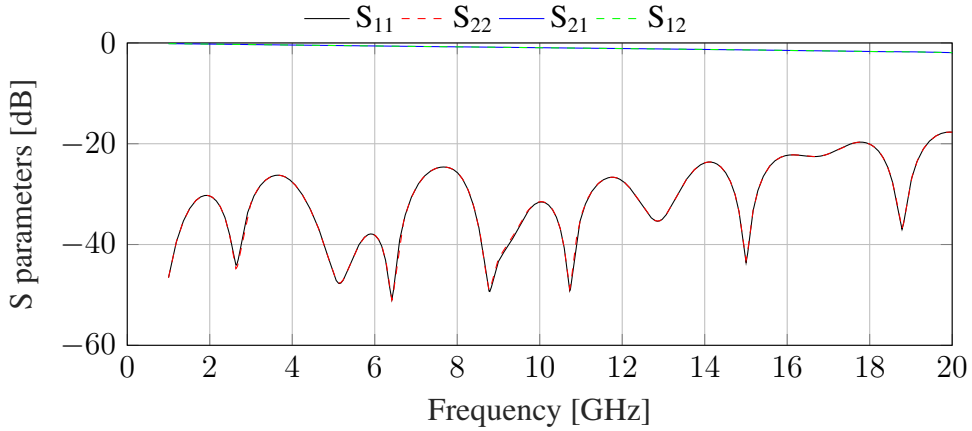

Figure 5.30: Simulated frequency response of the ESICL phase shifter at an average polarisation state, i.e. $\varepsilon_r = (\varepsilon_{\parallel} + \varepsilon_{\perp})/2 = 2.8$ and $\tan\delta = (\tan\delta_{\parallel} + \tan\delta_{\perp})/2 = 0.01121$.

polarisation voltage ($V_b = V_{max}$).

Due to the geometry of the line, the effective anchor layer in this design was infeasible. In the absence of a proper anchoring layer, the liquid crystal molecules arranged in small domains, macroscopically behaving as a dielectric medium with an average relative permittivity of $\varepsilon_1 = (\varepsilon_{\parallel} + \varepsilon_{\perp})/2$ [148]. As the biasing voltage is gradually increased, the molecules start rotating to orientate their major axis parallel to the polarisation field. Eventually, at a sufficiently high voltage, all the molecules align with the low-frequency field of the biasing signal, resulting in a parallel orientation characterised by the following relative permittivity: $\varepsilon_2 = \varepsilon_{\parallel}$. Thus, the total reconfiguration range goes from $\varepsilon_1 = (\varepsilon_{\parallel} + \varepsilon_{\perp})/2$ to $\varepsilon_2 = \varepsilon_{\parallel}$, reducing the reconfigurability of the phase shifter by a $50\,\%$. Moreover, since the anchoring forces of the liquid crystal without an anchoring layer are very small, the relaxation time (τ_{off}) increases extraordinarily. Despite all this, the proposed configuration also reduces the threshold voltage required for the phase shift [148]. Figure 5.32 illustrates the expected maximum phase shift when the ESICL line is filled with the GT3-23002 mixture from Merck KGaA ($\varepsilon_{\parallel} = 3.25$, $\tan\delta_{\parallel} = 0.0025$, $\varepsilon_{\perp} = 2.35$, and $\tan\delta_{\perp} = 0.02205$).

A typical figure of merit (FoM) for phase shifters can be defined as follows for comparison purpose.

$$\mathrm{FoM}_{(f)} = \frac{\Delta\theta_{(f)}}{IL_{(f)}} \tag{5.25}$$

With the simulated results, the phase shifter is expected to have an FoM of $14\,\mathrm{deg/dB}$ for an ideal reconfiguration range and $7\,\mathrm{deg/dB}$ for the expected range.

5.3.3 Results and Discussion

A prototype of the ESICL phase shifter with a length of $L_{LCSICL} = 20.00\,\mathrm{mm}$ was manufactured and tested. The manufacturing process was the same as that of a conventional ESICL line. First, the coaxial cavities were cut, and the plated-through holes were drilled. Afterwards, the PCBs were plated, and the transition layout milled. The different layers of the prototype were then soldered together using a non-water washable solder paste from Chipquik, conforming a layer of soldering material with a thickness of $50\,\mu\mathrm{m}$. Finally, the layers of the line were sealed using Norland adhesive, and the cavities of the coaxial line were filled with the GT3-23002 liquid crystal through two filling holes located at the corners of the ESICL.

Figure 5.31 presents the measured response of the prototype under steady-state conditions, i.e., $V_b = 0$ and $\varepsilon_r = (\varepsilon_{\parallel} + \varepsilon_{\perp})/2$. Notably, the measured return loss deviates significantly from the simulated values, adversely affecting the insertion loss and impacting the figure of merit. This disparity can be attributed to manufacturing variations, increased by the reduced cross-section of the inner conductor of the line. Furthermore, the presence of Norland adhesive on the coplanar line can introduce unexpected reflections, further increasing the return loss. The prototype achieves a minimum insertion loss of $0.11\,\mathrm{dB}$ and a maximum value of $4\,\mathrm{dB}$. The return loss remains above $5\,\mathrm{dB}$ across the frequency range from $0\,\mathrm{Hz}$ to $17.5\,\mathrm{GHz}$.

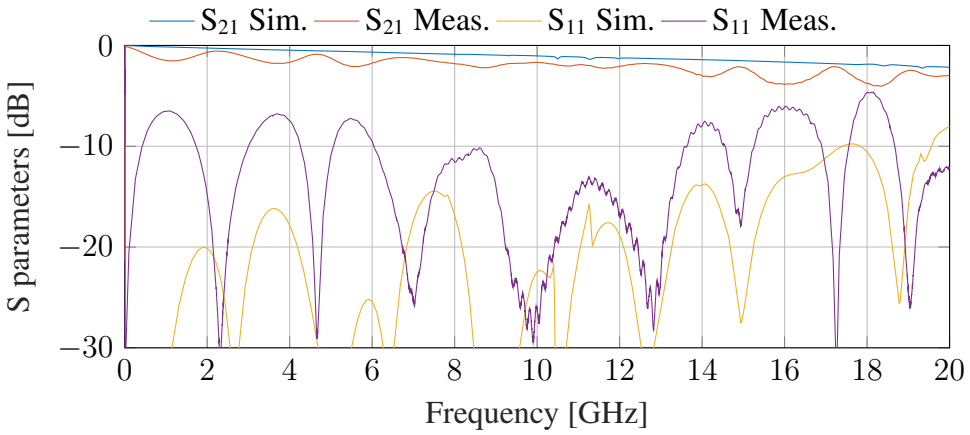

Figure 5.31: Simulated and measured frequency response of the ESICL phase shifter at the steady polarisation state, i.e., $V_b = 0$.

The phase of the devices under different biasing voltages ($0 < V_b < V_{max}$) was measured using a VNA. Two DC blocks and a bias tee were used to protect the biasing system and the VNA. Since the bias signal follows the same path as the RF signal in this device, the DC

blocks and bias tees must withstand very high voltages. This forced us to use capacitors with a higher capacitance than those used in the integrated resonator developed in Section 5.2.3. The use of these DC blocks results in increased insertion losses that make it impossible to calibrate the measurement test bench. As a result, obtaining reliable S-parameter modulus measurements was not possible. Nevertheless, the measurements of phase shift were reliable, they can be found in Figure 5.32. This figure depicts the phase shift of the line between the steady state ($V_b = 0$) and the polarised state ($V_b = 200\,V_{pp}$) of the liquid crystal. It is important to note that the DC blocks and bias tee, designed to block high voltages, affected the accuracy of the measurements. Therefore, the observed ripple in the measurement results shown in Figure 5.32 can be attributed to the influence of these components.

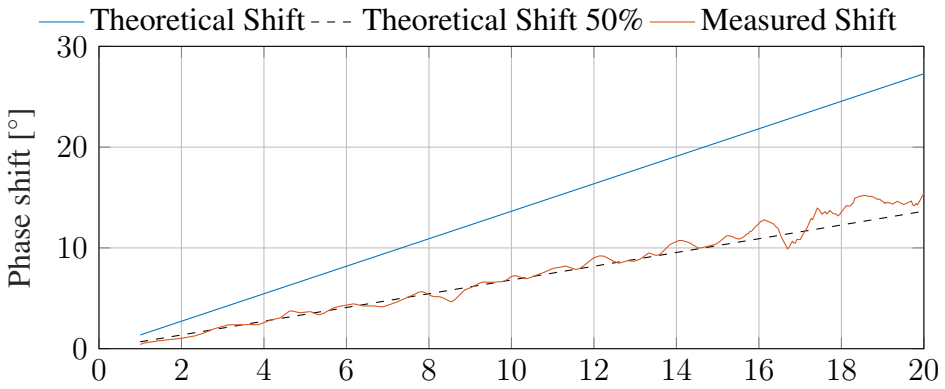

Figure 5.32: Simulated and measured phase shift between the two extreme polarisation states of the ESICL phase shifter, assuming a perfectly parallel orientation of the LC, $\varepsilon_{\parallel}$, for $V_b = V_{max}$ and an average polarisation, $(\varepsilon_{\parallel} + \varepsilon_{\perp})/2$, for $V_b = 0$.

The prototype achieves the expected efficiency of $50\,\%$ in phase shift due to the absence of an anchoring layer, resulting in a maximum phase shift of $15.4°$ at $20\,\mathrm{GHz}$. The insertion loss remains below $3\,\mathrm{dB}$ across the entire operational bandwidth, yielding a maximum figure of merit of $8\,°/\mathrm{dB}$. Although this figure of merit is too low for practical applications, it is important to highlight that the cause of the high reflections has yet to be determined, offering potential avenues for improvement in future works of similar nature.

The phase shift can be enhanced by implementing a polarisation mechanism based on magnetic fields. Toroidal magnets or coils can be used to force an anchoring layer in opposition to the electric biasing, achieving the maximum reconfigurability range of the liquid crystal. This approach can significantly increase the figure of merit, making the phase shifter suitable for being used in real communication systems. However, magnetic alignment may not be desirable in certain applications due to the weight and bulkiness of magnets, as well as the relatively high power consumption of coils.

In conclusion, the development of the liquid crystal-filled ESICL as a phase shifter has shown both potential and challenges. The prototype implementation has established the feasibility of utilising the ESICL for reconfigurable microwave devices, albeit with deviations between the measured and simulated results. The limitations in achieving a complete polarisation of the liquid crystal and the impact of manufacturing deviations on performance were identified. Despite these challenges, the proposed phase shifter exhibits low losses and suggests the potential of employing magnetic field alignment to improve performance. Further research and analysis efforts are required to address these limitations and unlock the full potential of liquid-crystal-filled ESICL technology in practical communication systems.

Chapter 6

Conclusions and Future Work

The landscape of satellite communications is facing a changing scenario with a saturated spectrum and new competitors driving the development of new communications systems. Much has changed over the past decades in the space industry. The demand for bandwidth and ubiquitous connectivity has skyrocketed, showing no signs of slowing down. Private companies have identified this market opportunity and have proposed new business models based on high-throughput satellites and big constellations. Consequently, the satellite technology must advance to meet the evolving requirements of an industry that is experiencing its first significant transformation in decades.

In this evolving context, RF and microwave systems play a pivotal role. They are expected to provide not only improvements in terms of spectral efficiency and adaptability but also a high degree of integration and a significant reduction of cost and weight. This thesis arises from this growing need for cost-effective, lightweight microwave devices with improved performance and seamless interconnection.

This work starts with an extensive literature review, encompassing the current state of the space industry, the most employed microwave filter topologies, and the unique space conditions discussed in Chapters 1 and 2. The findings indicate that there are excellent options for developing communication filters with optimal performance and cost-effectiveness: the Substrate Integrated Circuit (SIC) technology and the combination of Additive Manufacturing (AM) and Surface-Mount Technology (SMT).

The SIC topologies allow seamless integration with planar circuits, delivering commendable performance while minimising weight and offering moderate production costs. On the other hand, Additive Manufacturing (AM) filters using Surface-Mount Technology (SMT) enable effortless connection with planar systems, resulting in an excellent performance, a significant reduction of weight, and a reduction of cost for small to medium production sizes. In summary, the SIC technology proves to be more suitable for constellations involving a

high number of satellites, while Additive Manufacturing (AM) filters are better suited for small constellations and high-throughput GEO satellites.

The first objective of this thesis was to develop and characterise a novel manufacturing technique using Additive Manufacturing (AM) and to apply it to the development of high-performance filters with easy integration with planar systems. This objective has been successfully achieved, as outlined in Chapter 3. Section 3.1 provides an extensive literature review on additive manufacturing and its application to microwave and RF devices. This investigation concluded that a combination of Stereolithography Apparatus (SLA) printing technology and electroless metallisation is the ideal choice for developing microwave devices.

The SLA printing technology enables the utilisation of lightweight materials with medium to high mechanical resistance while ensuring the good dimensional accuracy and surface finish required at microwave frequencies. Moreover, it was determined that composite materials with a high concentration of solid particles exhibit superior printing precision, as these materials exhibit minimal shrinkage deformation and have a higher Heat Deflection Temperature (HDT) compared to their $100\,\%$ plastic counterparts.

The proposed manufacturing process is thoroughly explained in Section 3.2. A classical H-plane bandpass filter was designed, manufactured, and extensively tested to validate the suitability of the proposed manufacturing methods. The results, presented in detail in Section 3.4, demonstrate excellent performance, further supporting the efficacy of the developed manufacturing techniques.

After proving the suitability of the proposed manufacturing method, Section 3.3 delves into the investigation and design of Surface-Mount Technology (SMT) transitions for rectangular and circular cavity filters. The proposed SMT assembly facilitates the seamless integration of waveguide devices with planar subsystems, predominantly microstrip, although it can be readily adapted to cope with coplanar and stripline circuits. Three SMT filters were designed and manufactured To demonstrate the practicality of the proposed approach, yielding highly promising results as discussed in Section 3.4.

During the testing phase, it was noted that flat devices exhibited significant deformations. Consequently, a sensitivity analysis and an in-depth examination of manufacturing issues were conducted, with the findings summarised in Section 3.5. This study revealed that thin geometries were more prone to manufacturing deviations due to the shrinkage contraction of the printing material. Moreover, it was observed that rectangular resonators were more susceptible to assembling gaps compared to their circular counterparts.

Furthermore, the study concluded that the proposed combination of AM and SMT is ideally suited for relatively low frequencies, specifically C-band and below. However, for the

X band and higher frequencies, the successful application of this approach necessitates the incorporation of tunable elements to deal with the observed manufacturing tolerance.

Finally, the SMT filter prototypes underwent a series of space qualification tests, as detailed in Section 3.6. Despite being constructed of plastic, the prototypes successfully passed rigorous thermal cycling and vibration tests, demonstrating the viability of additive manufacturing technology for space missions without apparent problems.

Furthermore, the tested multipactor threshold confirmed that the SMT filters could be effectively utilised in the output RF chain of LEO and MEO satellites, and the classical waveguide filters developed using additive manufacturing exhibited a comparable power threshold to their metal counterparts, reinforcing their suitability for high-power applications.

The second objective of this research was to analyse and evaluate the performance of various Substrate Integrated Circuit (SIC) filter topologies. Four different filter topologies (SIW, ESIW, ADLS, and ESICL) were developed and described in detail in Section 3.4. Subsequently, the effect of manufacturing deviations was thoroughly analysed in Section 3.5. The results were satisfactory, and the observed deviations can be attributed to manufacturing deviations.

The study revealed that the empty structures demonstrated lower sensitivity to manufacturing tolerances, and particularly the ESICL topology exhibited extremely low sensitivity to assembling gaps. The developed prototypes underwent thermal cycling and vibration testing to validate their suitability for space applications, as outlined in Section 4.3. The results demonstrated the viability of SIC filters in withstanding the extreme conditions associated with space and launch scenarios. Notably, the performance of SIC filters remained consistent under temperature gradients and mechanical vibrations, obtaining comparable results to the additively manufactured prototypes developed in Chapter 3. A multipactor analysis was performed on the empty topologies (ESIW, ADLS, and ESICL), indicating that Substrate Integrated Circuit (SIC) filters can withstand the high power requirements associated with LEO applications. Additionally, based on the promising results observed with the ESICL topology, several power divider topologies were developed as a proof of concept using this technology. The outcomes of these prototypes are included in Section 4.4, demonstrating that ESICL is an excellent candidate for implementing wideband, low-frequency applications.

Finally, the final objective of this thesis focused on exploring the reconfiguration capabilities of Liquid Crystal (LC) and its application in the development of reconfigurable SIC devices. Given that the electromagnetic properties of liquid crystal mixtures are not well-characterised at microwave frequencies, two characterisation methods were developed and employed during this thesis.

Firstly, in Section 5.2.2, the split-cylinder-cavity-resonator method was used to deter-

mine the dielectric permittivity and loss tangent of four commercially available liquid crystal mixtures. The samples were introduced into LC cells with mechanical anchoring layers to achieve the two extreme polarisation states of the LC. Thus, the two extreme polarisation states could be easily obtained by rotating the sample within the split resonator. Two different analysis methods were employed to obtain the two extreme values of permittivity and loss tangent for the four samples at 5 and $11\,\mathrm{GHz}$. Based on the results, it was concluded that the GT3-23002 liquid crystal from Merck KGaA exhibited the most favourable characteristics for tunable applications at microwave frequencies.

Secondly, in Section 5.2.3, a SIC resonator was employed to approximate the dielectric permittivity and loss tangent of the GT3 liquid crystal under various polarisation states. The resonator utilised a combination of an anchoring layer and a biasing voltage to enable a continuous range of polarisation states. The biasing signal was applied to two polarisation patches implemented within the resonator layout. The resonator patches were also designed to serve as DC blocks, safeguarding the measurement system from the high-voltage biasing signal. A distributed bias tee was incorporated into the resonator to prevent the RF signal from propagating into the biasing network. Leveraging the characteristics of this resonator, it was possible to estimate the splay deformation constant and rotational viscosity of the GT3 liquid crystal.

As the final aspect of this thesis, a tunable phase shifter based on a liquid crystal-filled ESICL was developed in Section 5.3. The two-conductor structure of the ESICL allowed for applying the electric biasing fields needed to polarise the liquid crystal molecules. However, the square geometry of the line restricted the use of mechanical anchoring layers, reducing the expected phase shift by half. Unfortunately, the prototype exhibited higher return losses than anticipated, significantly impacting insertion losses and diminishing the device's figure of merit. Nonetheless, the results obtained in this research validate the potential of ESICL technology and LC as a viable option for implementing reconfigurable devices.

In conclusion, all the main goals of the thesis have been successfully accomplished. As a result, numerous publications in reputed journals and conferences dedicated to microwave engineering have been produced, as summarised in Appendix A. Furthermore, the additive manufacturing method and SMT assembly of microwave devices developed in this thesis granted a patent in 2018. This recognition highlights the novelty and potential impact of the proposed techniques in the field of microwave engineering.

This thesis has started several new research lines that need to be further explored in the future. The most important ones are summarised below:

- **Evolution of the metallisation technique for additively manufactured devices.** As stated in Chapter 3, the developed metallisation process allows plating the entire sur-

face of additively manufactured devices. In this context, it would be interesting to explore the use of high-performance metals such as gold, silver or nickel. It would also be interesting to adapt the autocatalytic deposition method to enable a selectable metallisation. This can be done by selectively applying the surface treatment using a laser or plasma etching, allowing the sensitisation of specific surface areas. This selectable metallisation can also be done by employing a polymeric mask that prevents the deposition of copper in certain zones. This would enable the development of planar circuits in arbitrary geometries, directly integrating the RF systems into their packaging.

- **Improvement of the SMT devices developed in this thesis to make them less sensitive to manufacturing and assembling tolerances.** The performances of the SMT devices developed in this work were affected by manufacturing tolerances, and especially by the assembling gaps. These effects need to be more deeply studied in order to compensate them in the design stage. In this context, a set of SMT resonators could be developed to clearly quantify the effect of the assembling gap in the performance of resonant devices. Once the undesired effects of the gap have been identified, the design dimensions of the resonators and coupling elements of a filter can be tuned to compensate for them. Another option is to study the use of tuning elements, such as tuning screws, in resonators and coupling elements. Introducing these elements should be simple and could compensate for the effect of gaps and manufacturing tolerances. Finally, the use of groove gap waveguides should be studied, as these structures are not sensitive to gaps between their two parts, and they can benefit from the design slot transition to achieve a SMT assembly.

- **Complete the multipactor analysis on SIC filters.** The preliminary analysis proved that SIC filters can withstand signals with more than $250\,\mathrm{W}$ of power. As the analysis was very conservative, it is expected that real prototypes support even higher power, which makes the use of coaxial connectors impractical. Thus, it is necessary to develop transitions between the proposed structures (ESIW, ADLS, and ESICL) and a rectangular waveguide. For ESIW and ADLS filters, the transition can consist of a Chebyshev impedance transformer as the one employed in the multipactor test prototype of the rectangular SMT filter developed in Section 3.6.3. Regarding the ESICL filter, the transition can reassemble the classical E-plane transitions between coaxial cables and rectangular waveguides, where the inner conductor of the coaxial cable penetrates in the centre of the waveguide. Finally, the structure of filters should be redesigned to fit the outgassing and electron seeding properties of the multipactor test. After this redesign, more accurate analyses of the multifactor effect should be performed to narrow

down the test case.

- **Study of new SIC topologies for liquid crystal devices.** The ESICL technology has demonstrated to be of interest for the development of tunable devices using liquid crystal. The line provides a two-conductor structure that can be used to rotate the liquid crystal molecules using a low-frequency biasing signal. However, the square geometry of this line makes it difficult to build an effective anchoring layer, reducing the reconfigurability range of the liquid crystal by half. Although this problem can be solved using a static magnetic field to orientate the molecules of the liquid crystal, the generation of such fields needs big and heavy magnets or power-consuming coils, which makes its use difficult in the industry. It is necessary to explore new SIC topologies with two conductors that allow the integration of an anchoring layer. For instance, a preliminary study has been performed to implement a tunable phase shifter and bandpass filter in a microstrip-ridge gap waveguide.

Appendix A

List of publications

A.1 International Journal Publications

A.1.1 Q1 Publications

- **V. Nova**, C. Bachiller, J. Pascual-Folch, A. Ferrer, L. N. Ponce-Gonzalez, M. L. Marín, V. E. Boria, “3-D Printed Waveguide Filters: Manufacturing Process and Surface Mounted Assembly." *IEEE Transactions on Microwave Theory and Techniques*, 2023, doi: 10.1109/TMTT.2023.3276205.

- C. Bachiller, **V. Nova**, A. Ferrer, M. L. MarínL. N. Ponce-Gonzalez, “Additive manufacturing and metallization of high-frequency communication devices." *Progress in Additive Manufacturing*, vol. 8, no. 1, pp. 3-8, January 2023, doi: 10.1007/s40964-022-00386-4.

- C. Bachiller, **V. Nova**, A. Ferrer, V. E. Boria, “Space Qualification of Metalized Additive Manufactured Filters." *IEEE Access*, vol. 10, pp. 96952-96966, 2022, doi: 10.1109/ACCESS.2022.3205408.

- J. M. Merello, C. Bachiller, **V. Nova**, H. Esteban, Á. Belenguer, “Study of Vibration Effects on Communication Filters in Substrate Integrated Technologies." *IEEE Access*, vol. 10, pp. 50418-50426, 2022, doi: 10.1109/ACCESS.2022.3173264.

- **V. Nova**, C. Bachiller, J. A. Martínez, H. Esteban, J. M. Merello, Á. Belenguer, O. Monerris, V. E. Boria, “Thermal Stability Analysis of Filters in Substrate Integrated Technologies Under Atmospheric Pressure and Vacuum Conditions." *IEEE Access*, vol. 8, pp. 118072-118082, 2020, doi: 10.1109/ACCESS.2020.3004875.

- J. R. Sánchez, **V. Nova**, C. Bachiller, B. Villacampa, A. de la Rua, R. Kronberger, F. Peñaranda, V. E. Boria, "Characterization of nematic liquid crystal at microwave frequencies using split-cylinder resonator method." *IEEE Transactions on Microwave Theory and Techniques*, vol. 67, no. 7, pp. 2812-2820, July 2019, doi: 10.1109/TMTT.2019.2916790.

- J. R. Sánchez, C. Bachiller, **V. Nova**, V. E. Boria, "Controlled out-of-band rejection of filters based on SIW with alternating dielectric line sections." *IEEE Microwave and Wireless Components Letters*, vol. 29, no. 4, pp. 258-260, April 2019, doi: 10.1109/LMWC.2019.2902034.

- F. Quilles, Á. Belenguer, J. A. Martínez, **V. Nova**, H. Esteban, V. E. Boria, "Compact Microstrip to Empty Substrate-Integrated Coaxial Line Transition." *IEEE Microwave and Wireless Components Letters*, vol. 28, no. 12, pp. 1080-1082, December 2018, doi: 10.1109/LMWC.2018.2874280.

- J. M. Merello, **V. Nova**, C. Bachiller, J. R. Sánchez, Á. Belenguer, V. E. Boria, "Miniaturization of power divider and 90° hybrid directional coupler for C-Band applications using empty substrate integrated coaxial lines." *IEEE Transactions on Microwave Theory and Techniques*, vol. 66, no. 6, pp. 3055-3062, June 2018, doi: 10.1109/TMTT.2018.2828089.

- J. R. Sánchez, C. Bachiller, M. Juliá, **V. Nova**, H. Esteban, V. E. Boria, "Microwave filter based on substrate integrated waveguide with alternating dielectric line sections." *IEEE Microwave and Wireless Components Letters*, vol. 28, no. 11, pp. 990-992, November 2018, doi: 10.1109/LMWC.2018.2871644.

A.1.2 Q2 Publications

- **V. Nova**, C. Bachiller, B. Villacampa, R. Kronberger, V. E. Boria, "Characterization of Nematic Liquid Crystals at Microwave Frequencies." *Crystals*, vol. 10, no. 12, pp. 1106, December 2020, doi: 10.3390/cryst10121106.

- J. R. Sánchez, C. Bachiller, **V. Nova**, V. E. Boria, "Reconfigurable resonator in decoupled empty SIW technology using liquid crystal material." *Electronics Letters*, vol. 55, no. 16, pp. 907-910, August 2019, doi: 10.1049/el.2019.1088.

- J. R. Sánchez, C. Bachiller, **V. Nova**, V. E. Boria, "Stay tuned: A novel continuously-tunable reconfigurable microwave resonator based on Liquid Crystal materials." *Electronics Letters*, vol. 55, no. 16, pp. 871-871, August 2019, doi: 10.1049/el.2019.2445.

- J. R. Sánchez, C. Bachiller, H. Esteban, Á. Belenguer, **V. Nova**, V. E. Boria, "New decoupled empty substrate integrated waveguide realisation." *Electronics Letters*, vol. 53, no. 17, pp. 1203-1205, August 2017, doi: 10.1049/el.2017.1240.

A.2 National Journal Publications

- C. Bachiller, J. R. Sánchez, **V. Nova**, J. M. Merello, V. E. Boria, "Development of substrate integrated passive microwave circuits" *WAVES magazine, iTEAM-UPV*, no. 10, pp. 35-45, 2018.

A.3 Conference Publications

A.3.1 International Conference Publications

- C. Bachiller, **V. Nova**, A. Ferrer, M. L. Marín, L. N. Ponze-Gonzalez, "Additive manufacturing and metallization of high frequency communication devices" in *Fraunhofer Direct Digital Manufacturing Conference (DDMC 2023)*, March 2023, pp. 1-4.

- J. M. Merello, **V. Nova**, C. Bachiller, V. E. Boria, 'Compact C-band Wilkinson Power Divider in Empty Substrate Integrated Coaxial Line" in *51th European Microwave Conference (EuMC 2021)*, April 2022, pp. 1-4.

A.3.2 National Conference Publications

- **V. Nova**, C. Bachiller, J. R. Sánchez,M. L. Marín, V. E. Boria, "Implementation of a 3D Printed Microwave Waveguide using Plated PLA" in *XXXIV Simposium Nacional de la Unión Científica Internacional de Radio (URSI 2019)*, September 2019, pp. 1-4.

- **V. Nova**, C. Bachiller, J. R. Sánchez, V. E. Boria, "A novel reconfigurable phase shifter based on substrate integrated coaxial line using liquid crystal" in *XXXIII Simposium Nacional de la Unión Científica Internacional de Radio (URSI 2018)*, September 2018, pp. 1-4.

A.4 Patents

- C. Bachiller, J. R. Sánchez, **V. Nova**, M. L. Marín, J. M. Merello, V. E. Boria. “Método de fabricación de dispositivos de microondas basado en guía de onda vacía integrada en sustrato." Patent Number: P201830647, Priority date: 2018-06-28, Publication date: 2019-03-26, Original Assignee: Universitat Politècnica de València.

Acronyms

ABS Acrylonitrile Butadiene Styrene.

ADLS Alternating Dielectric Line Sections.

AFSIW Air-Filled Substrate Integrated Waveguide.

AM Additive Manufacturing.

ASD Amplitude Spectral Density.

BJ Binder Jetting.

BW Bandwidth.

CNC Computer Numerical Control.

CST CST Studio Suite.

CTE Coefficient of Thermal Expansion.

CW Continuous Wave.

DLP Direct Light Processing.

DUT Device Under Test.

ECSS European Cooperation for Space Standardization.

EM Electromagnetic.

EMC Electromagnetic Compatibility.

ESA European Space Agency.

ESICL Empty Substrate Integrated Coaxial Line.

ESIW Empty Substrate Integrated Waveguide.

FDM Fused Deposition Modelling.

FESEM Field-Emission Scanning Electron Microscope.

GDM General Detection Method.

GEO Geostationary Earth Orbit.

GGW Groove Gap Waveguide.

HDT Heat Deflection Temperature.

IEEE Institute of Electrical and Electronics Engineers.

IL Insertion Loss.

IoT Internet of Things.

LC Liquid Crystal.

LDM Local Detection Method.

LEO Low Earth Orbit.

MC Monte Carlo.

MEO Medium Earth Orbit.

MJ Material Jetting.

MMIC Monolithic Microwave Integrated Circuits.

MSL Microstrip Line.

MSLA Masked Stereolithography Apparatus.

MW Minimum Workmanship.

NASA National Aeronautics and Space Administration.

PBF Powder Bed Dusion.

PCB Printed Circuit Board.

PJ PolyJet.

PLA Polylactic Acid.

PTH Plated Through Hole.

PVD Physical Vapor Deposition.

Q-factor Quality factor.

RESIW Ridge Empty Substrate Integrated Waveguide.

RF Radio Frequency.

RL Return Loss.

RMS Root Mean Square.

SEE Secondary Electron Emission.

SEY Secondary Emission Yield.

SFR Spurious Free Range.

SIC Substrate Integrated Circuit.

SIW Substrate Integrated Waveguide.

SLA Stereolithography Apparatus.

SLM Selective Laser Melting.

SLS Selective Laser Sintering.

SMT Surface-Mount Technology.

TASE Time-Average Stored Energy.

TE Transverse Electric.

TEM Transverse ElectroMagnetic.

TGA Thermogravimetric Analysis.

TRL Thru Reflect Line.

TZ Transmission Zero.

UV Ultraviolet.

VNA Vector Network Analyzer.

VSC Valencian Space Consortium.

Bibliography

[1] G. Sebestyen, S. Fujikawa, N. Galassi, and A. Chuchra, *Low earth orbit satellite design*, 1st ed., ser. Space Technology Library. Cham, Switzerland: Springer International Publishing, Feb. 2018.

[2] C. Daehnick, I. Klinghoffer, B. Maritz, and B. Wiseman, "Large LEO satellite constellations: will it be different this time?" McKinsey & Company, Tech. Rep., May 2020.

[3] D. Deslandes and K. Wu, "Integrated microstrip and rectangular waveguide in planar form," *IEEE Microwave and Wireless Components Letters*, vol. 11, no. 2, pp. 68–70, 2001.

[4] X.-P. Chen and K. Wu, "Substrate integrated waveguide filter: basic design rules and fundamental structure features," *IEEE Microwave Magazine*, vol. 15, no. 5, pp. 108–116, 2014.

[5] K. Wu, "Substrate integrated circuits (SICs) for low-cost high-density integration of millimeter-wave wireless systems," in *2008 IEEE Radio and Wireless Symposium*, 2008, pp. 683–686.

[6] R. Sorrentino and O. A. Peverini, "Additive manufacturing: a key enabling technology for next-generation microwave and millimeter-wave systems [point of view]," *Proceedings of the IEEE*, vol. 104, no. 7, pp. 1362–1366, 2016.

[7] C. Tomassoni, O. A. Peverini, G. Venanzoni, G. Addamo, F. Paonessa, and G. Virone, "3D printing of microwave and millimeter-wave filters: additive manufacturing technologies applied in the development of high-performance filters with novel topologies," *IEEE Microwave Magazine*, vol. 21, no. 6, pp. 24–45, 2020.

[8] D. S. González and A. G. Álvarez, "Additive manufacturing feasibility study & technology demonstration," European Defence Agency, Zaragoza, Spain, Tech. Rep. EDA AM State of the Art & Strategic Report, jun 2018.

[9] K. M. Peterson, "Satellite communications," in *Encyclopedia of Physical Science and Technology*, R. A. Meyers, Ed. California: Elsevier, 2001, pp. 413–438.

[10] UNOOSA, "United Nations office for outer space affairs." [Online]. Available: http://www.unoosa.org/

[11] E. S. A. (ESA). Types of orbits. [Online]. Available: www.esa.int/Enabling_Support/Space_Transportation/Types_of_orbits

[12] H. Leblond, J. Villemazet, J. Cazaux, D. Pacaud, J. Herren, L. Rigaudeau, L. Lapierre, D. Baillargeat, P. Blondy, S. Bila, S. Verdeyme, C. Delage, C. Quendo, J. Favennec, B. Potelon, E. Rius, F. Seyfert, and S. Pacchini, "When new needs for satellite payloads meet with new filters architecture and technologies," in *2009 European Microwave Integrated Circuits Conference (EuMIC)*, 2009, pp. 359–362.

[13] Q. Ren, A. U. Zaman, J. Yang, V. Vassilev, and C. Bencivenni, "Novel integration techniques for gap waveguides and MMICs suitable for multilayer waveguide applications," *IEEE Transactions on Microwave Theory and Techniques*, vol. 70, no. 9, pp. 4120–4128, 2022.

[14] W. Menzel and H. Callsen, "Integrated fin-line components for radar and radiometer applications," in *Military Microwaves '82*, Jan. 1983, pp. 449–454.

[15] T. Martin, A. Ghiotto, and F. Lotz, "Compact G-CPW fed air-filled SIW (AFSIW) filters for systems on substrate," in *2021 IEEE MTT-S International Microwave Filter Workshop (IMFW)*, 2021, pp. 59–61.

[16] Z. Ruan, D. Shen, H. Yuan, and X. Zhang, "A self-packaged ultra-wide band bandpass filter using integrated substrate gap waveguide," in *2019 IEEE MTT-S International Wireless Symposium (IWS)*, 2019, pp. 1–3.

[17] N. Delmonte, M. Bozzi, L. Perregrini, and C. Tomassoni, "Cavity resonator filters in shielded quarter-mode substrate integrated waveguide technology," in *2018 IEEE MTT-S International Microwave Workshop Series on Advanced Materials and Processes for RF and THz Applications (IMWS-AMP)*, 2018, pp. 1–3.

[18] A. Belenguer, H. Esteban, and V. E. Boria, "Novel empty substrate integrated waveguide for high-performance microwave integrated circuits," *IEEE Transactions on Microwave Theory and Techniques*, vol. 62, no. 4, pp. 832–839, 2014.

[19] A. L. Borja, A. Belenguer, H. Esteban, and V. E. Boria, "Design and performance of a high-Q narrow bandwidth bandpass filter in empty substrate integrated coaxial line at Ku-band," *IEEE Microwave and Wireless Components Letters*, vol. 27, no. 11, pp. 977–979, 2017.

[20] S. Datta, S. Mukherjee, and A. Biswas, "Design of broadband power divider based on substrate-integrated waveguide technology," in *2013 IEEE Applied Electromagnetics Conference (AEMC)*, 2013, pp. 1–2.

[21] H. Chen, X. Wang, W. Che, Y. Zhou, and T. Liu, "Novel gysel power dividers based on half-mode substrate integrated waveguide (HMSIW)," in *2018 IEEE MTT-S International Wireless Symposium (IWS)*, 2018, pp. 1–3.

[22] K. Song, F. Xia, Y. Zhou, S. Guo, and Y. Fan, "Microstrip/slotline-coupling substrate integrated waveguide power divider with high output isolation," *IEEE Microwave and Wireless Components Letters*, vol. 29, no. 2, pp. 95–97, 2019.

[23] H. Wang, D.-G. Fang, B. Zhang, and W.-Q. Che, "Dielectric loaded substrate integrated waveguide (SIW) H-plane horn antennas," *IEEE Transactions on Antennas and Propagation*, vol. 58, no. 3, pp. 640–647, 2010.

[24] J. Liu, D. R. Jackson, and Y. Long, "Substrate integrated waveguide (SIW) leaky-wave antenna with transverse slots," *IEEE Transactions on Antennas and Propagation*, vol. 60, no. 1, pp. 20–29, 2012.

[25] Y.-X. Sun, D. Wu, X. S. Fang, and N. Yang, "Compact quarter-mode substrate-integrated waveguide dual-frequency millimeter-wave antenna array for 5G applications," *IEEE Antennas and Wireless Propagation Letters*, vol. 19, no. 8, pp. 1405–1409, 2020.

[26] M. Alibakhshikenari, E. M. Ali, M. Soruri, M. Dalarsson, M. Naser-Moghadasi, B. S. Virdee, C. Stefanovic, A. Pietrenko-Dabrowska, S. Koziel, S. Szczepanski, and E. Limiti, "A comprehensive survey on antennas on-chip based on metamaterial, metasurface, and substrate integrated waveguide principles for millimeter-waves and terahertz integrated circuits and systems," *IEEE Access*, vol. 10, pp. 3668–3692, 2022.

[27] L. Silvestri, E. Massoni, C. Tomassoni, A. Coves, M. Bozzi, and L. Perregrini, "Substrate integrated waveguide filters based on a dielectric layer with periodic perforations," *IEEE Transactions on Microwave Theory and Techniques*, vol. 65, no. 8, pp. 2687–2697, 2017.

[28] J. R. Sánchez, C. Bachiller, M. Juliá, V. Nova, H. Esteban, and V. E. Boria, "Microwave filter based on substrate integrated waveguide with alternating dielectric line sections," *IEEE Microwave and Wireless Components Letters*, vol. 28, no. 11, pp. 990–992, 2018.

[29] J. D. Martínez, M. Taroncher, and V. E. Boria, "Capacitively loaded resonator for compact substrate integrated waveguide filters," in *The 40th European Microwave Conference*, 2010, pp. 192–195.

[30] J. D. Martinez, S. Sirci, M. Taroncher, and V. E. Boria, "Compact CPW-fed combline filter in substrate integrated waveguide technology," *IEEE Microwave and Wireless Components Letters*, vol. 22, no. 1, pp. 7–9, 2012.

[31] J. Sorocki and I. Piekarz, "Low-cost microwave components' fabrication in hybrid technology of laminates and additive manufacturing on an example of miniaturized suspended directional coupler," *IEEE Access*, vol. 8, pp. 128 766–128 775, 2020.

[32] A. Tamayo-Dominguez, P. Sanchez-Olivares, A. Camacho-Hernandez, and J.-M. Fernandez-Gonzalez, "Guidelines for accurate in-house electroplating and 3-D-printing processes applied to mm-wave devices," *IEEE Microwave and Wireless Components Letters*, vol. 32, no. 11, pp. 1267–1270, 2022.

[33] A. Tamayo-Dominguez, J.-M. Fernandez-Gonzalez, and M. Sierra-Perez, "Metal-coated 3D-printed waveguide devices for mm-wave applications [application notes]," *IEEE Microwave Magazine*, vol. 20, no. 9, pp. 18–31, 2019.

[34] C. Guo, X. Shang, M. J. Lancaster, and J. Xu, "A 3-D printed lightweight X-band waveguide filter based on spherical resonators," *S Microwave and Wireless Components Letters*, vol. 25, no. 7, pp. 442–444, 2015.

[35] C. Guo, X. Shang, J. Li, F. Zhang, M. J. Lancaster, and J. Xu, "A lightweight 3-D printed X-band bandpass filter based on spherical dual-mode resonators," *IEEE Microwave and Wireless Components Letters*, vol. 26, no. 8, pp. 568–570, 2016.

[36] J. R. Montejo-Garai, I. O. Saracho-Pantoja, C. A. Leal-Sevillano, J. A. Ruiz-Cruz, and J. M. Rebollar, "Design of microwave waveguide devices for space and ground application implemented by additive manufacturing," in *2015 International Conference on Electromagnetics in Advanced Applications (ICEAA)*, 2015, pp. 325–328.

[37] A. Perigaud, O. Tantot, N. Delhote, S. Bila, S. Verdeyme, and D. Baillargeat, "Continuously tunable filter made by additive manufacturing using a 3D spiral ribbon," in

2017 IEEE MTT-S International Microwave Workshop Series on Advanced Materials and Processes for RF and THz Applications (IMWS-AMP), 2017, pp. 1–3.

[38] H. García-Martínez, G. Torregrosa-Penalva, E. Ávila-Navarro, N. Delmonte, L. Silvestri, and M. Bozzi, "3D-printed electromagnetic band-gap band-pass filter based on empty single-ridge waveguide," *IEEE Access*, vol. 10, pp. 53 954–53 962, 2022.

[39] R. Dahle, P. Laforge, and J. Kuhling, "3-D printed customizable inserts for waveguide filter design at X-band," *IEEE Microwave and Wireless Components Letters*, vol. 27, no. 12, pp. 1080–1082, 2017.

[40] A. Vallecchi, D. Cadman, W. G. Whittow, J. Vardaxoglou, E. Shamonina, and C. J. Stevens, "3-D printed bandpass filters with coupled vertically extruded split ring resonators," *IEEE Transactions on Microwave Theory and Techniques*, vol. 67, no. 11, pp. 4341–4352, 2019.

[41] D. Miek, S. Simmich, F. Kamrath, and M. Höft, "Additive manufacturing of E-plane cut dual-mode X-band waveguide filters with mixed topologies," *IEEE Transactions on Microwave Theory and Techniques*, vol. 68, no. 6, pp. 2097–2107, 2020.

[42] P. Booth, J. Gilmore, E. V. Lluch, and M. Harvey, "Enhancements to satellite feed chain performance, testing and lead-times using additive manufacturing," in *2016 10th European Conference on Antennas and Propagation (EuCAP)*, 2016, pp. 1–5.

[43] O. A. Peverini, M. Lumia, G. Addamo, F. Paonessa, G. Virone, R. Tascone, F. Calignano, G. Cattano, and D. Manfredi, "Integration of an H-plane bend, a twist, and a filter in Ku/K-band through additive manufacturing," *IEEE Transactions on Microwave Theory and Techniques*, vol. 66, no. 5, pp. 2210–2219, 2018.

[44] O. A. Peverini, G. Addamo, M. Lumia, G. Virone, F. Calignano, M. Lorusso, and D. Manfredi, "Additive manufacturing of Ku/K-band waveguide filters: a comparative analysis among selective-laser melting and stereo-lithography," *IET Microwaves, Antennas & Propagation*, vol. 11, no. 14, pp. 1936–1942, 2017. [Online]. Available: https://ietresearch.onlinelibrary.wiley.com/doi/abs/10.1049/iet-map.2017.0151

[45] X. Wen, C. Guo, X. Shang, Y. Yu, M. Shu, Q. Yang, S. Li, M. M. Attallah, H. Liu, and A. Zhang, "SLM printed waveguide dual-mode filters with reduced sensitivity to fabrication imperfections," *IEEE Microwave and Wireless Components Letters*, vol. 31, no. 11, pp. 1195–1198, 2021.

[46] L. Qian, Y. Wang, S. Li, A. E.-M. A. Mohamed, M. M. Attallah, T. Skaik, P. Booth, L. Pambaguian, C. M. España, and P. Martín-Iglesias, "A narrowband 3-D printed invar spherical dual-mode filter with high thermal stability for OMUXs," *IEEE Transactions on Microwave Theory and Techniques*, vol. 70, no. 4, pp. 2165–2173, 2022.

[47] S. Sirci, E. Menargues, and S. Berry, "Triangular combline filters conceived for additive manufacturing," in *2021 IEEE MTT-S International Microwave Filter Workshop (IMFW)*, 2021, pp. 151–154.

[48] E. A. Rojas-Nastrucci, J. T. Nussbaum, N. B. Crane, and T. M. Weller, "Ka-band characterization of binder jetting for 3-D printing of metallic rectangular waveguide circuits and antennas," *IEEE Transactions on Microwave Theory and Techniques*, vol. 65, no. 9, pp. 3099–3108, 2017.

[49] "Swissto12 - 3D printing solutions." [Online]. Available: https://swissto12.com/

[50] S. Sirci, J. D. Martínez, and V. E. Boria, "Low-loss 3-bit tunable SIW filter with PIN diodes and integrated bias network," in *2013 European Microwave Conference*, 2013, pp. 1211–1214.

[51] S. Sirci, J. D. Martínez, M. Taroncher, and V. E. Boria, "Varactor-loaded continuously tunable siw resonator for reconfigurable filter design," in *2011 41st European Microwave Conference*, 2011, pp. 436–439.

[52] B. Pal, M. K. Mandal, and S. Dwari, "Varactor tuned dual-band bandpass filter with independently tunable band positions," *IEEE Microwave and Wireless Components Letters*, vol. 29, no. 4, pp. 255–257, 2019.

[53] R. H. Kenney, C. J. Walker, H. H. Sigmarsson, and J. W. McDaniel, "A varactor-based tunable combline bandpass filter using suspended integrated stripline (SISL)," *IEEE Journal on Miniaturization for Air and Space Systems*, vol. 2, no. 3, pp. 112–116, 2021.

[54] R. Hou, J. Chen, Y.-T. Zhao, T. Su, L. Li, and K.-D. Xu, "Varactor–graphene-based bandpass filter with independently tunable characteristics of frequency and amplitude," *IEEE Transactions on Components, Packaging and Manufacturing Technology*, vol. 12, no. 8, pp. 1375–1385, 2022.

[55] F. Huang, S. Fouladi, and R. R. Mansour, "High-Q tunable dielectric resonator filters using MEMS technology," *IEEE Transactions on Microwave Theory and Techniques*, vol. 59, no. 12, pp. 3401–3409, 2011.

[56] C.-C. Cheng and G. M. Rebeiz, "High-Q 4–6 GHz suspended stripline RF MEMS tunable filter with bandwidth control," *IEEE Transactions on Microwave Theory and Techniques*, vol. 59, no. 10, pp. 2469–2476, 2011.

[57] G. Chaabane, A. Pothier, M. Chatras, C. Guines, V. Madrangeas, and P. Blondy, "A 2-pole RF-MEMS tunable bandpass filter for high-power applications," in *2014 44th European Microwave Conference*, 2014, pp. 343–346.

[58] T. R. Jones and M. Daneshmand, "Miniaturized folded ridged quarter-mode substrate integrated waveguide RF MEMS tunable bandpass filter," *IEEE Access*, vol. 8, pp. 115 837–115 847, 2020.

[59] F. Gentili, F. Cacciamani, V. Nocella, R. Sorrentino, and L. Pelliccia, "RF MEMS hairpin filter with three reconfigurable bandwidth states," in *2013 European Microwave Conference*, 2013, pp. 802–805.

[60] Q. D. Huang and Y. J. Cheng, "Ferrite-loaded substrate integrated waveguide frequency-agile bandpass filter," in *2015 IEEE MTT-S International Microwave Workshop Series on Advanced Materials and Processes for RF and THz Applications (IMWS-AMP)*, 2015, pp. 1–3.

[61] E. Polat, F. Kamrath, S. Matic, H. Tesmer, A. Jiménez-Sáez, D. Wang, H. Maune, M. Höft, and R. Jakoby, "Novel hybrid electric/magnetic bias concept for tunable liquid crystal based filter," *IEEE Journal of Microwaves*, vol. 2, no. 3, pp. 490–495, 2022.

[62] M. Yazdanpanahi and D. Mirshekar-Syahkal, "Millimeter-wave liquid-crystal-based tunable bandpass filter," in *2012 IEEE Radio and Wireless Symposium*, 2012, pp. 139–142.

[63] D. Jiang, X. Li, Z. Fu, G. Wang, Z. Zheng, T. Zhang, and W.-Q. Wang, "Millimeter-wave broadband tunable band-pass filter based on liquid crystal materials," *IEEE Access*, vol. 8, pp. 1339–1346, 2020.

[64] D. Pozar, *Microwave Engineering*. Hoboken, NJ: Wiley, 2012.

[65] J.-S. Hong, *Microstrip filters for RF/microwave applications [electronic resource]*, 2nd ed. Hoboken, N.J: Wiley, 2011.

[66] P. González, C. Alcaide, R. Cervera, M. Rodríguez, O. Monerris, J. Petit, A. Rodríguez, A. Vidal, J. Vague, J. V. Morro, P. Soto, and V. E. Boria, "Multipactor threshold estimation techniques based on circuit models, electromagnetic fields, and particle simulators," *IEEE Journal of Microwaves*, vol. 2, no. 1, pp. 57–77, 2022.

[67] A. Tasic, W. A. Serdijn, and G. Setti, *Circuits and Systems for Future Generations of Wireless Communications [Online]*, 1st ed., A. Tasic, W. A. Serdijn, and G. Setti, Eds. Dordrecht: Springer Netherlands, 2009.

[68] R. J. Cameron, "Advanced filter synthesis," *IEEE Microwave Magazine*, vol. 12, no. 6, pp. 42–61, 2011.

[69] R. J. Cameron, C. M. Kudsia, and R. R. Mansour, *Microwave Filters For Communication Systems : Fundamentals, Design and Applications*. Hoboken, NJ, USA: Wiley, 2018.

[70] S. B. Cohn, "Direct-coupled-resonator filters," *Proceedings of the IRE*, vol. 45, no. 2, pp. 187–196, 1957.

[71] H. Hwang and S.-W. Yun, "The design of bandpass filters considering frequency dependence of inverters," *Microwave Journal*, vol. 45, no. 09, pp. 154–163, 2002.

[72] P. Soto, E. Tarín, V. E. Boria, C. Vicente, J. Gil, and B. Gimeno, "Accurate synthesis and design of wideband and inhomogeneous inductive waveguide filters," *IEEE Transactions on Microwave Theory and Techniques*, vol. 58, no. 8, pp. 2220–2230, 2010.

[73] J. Uher, J. Bornemann, and U. Rosenberg, *Waveguide components for antenna feed systems: Theory and CAD*. Boston: Artech House, 1993.

[74] M. del Carmen Bachiller Martín, "Métodos híbridos para el análisis y diseño eficiente de filtros avanzados para sistemas de comunicaciones espaciales," Ph.D. dissertation, Universitat Politècnica de València, 2010. [Online]. Available: https://doi.org/10.4995/thesis/10251/8657

[75] P.-S. Kildal, "Waveguides and transmission lines in gaps between parallel conducting surfaces," US Patent US20 110 181 373A1, 2009.

[76] E. Rajo-Iglesias, M. Ferrando-Rocher, and A. U. Zaman, "Gap waveguide technology for millimeter-wave antenna systems," *IEEE Communications Magazine*, vol. 56, no. 7, pp. 14–20, 2018.

[77] J. L. Vazquez-Roy, E. Rajo-Iglesias, G. Ulisse, and V. Krozer, "Design and realization of a band pass filter at D-band using gap waveguide technology," *Journal of Infrared, Millimeter, and Terahertz Waves*, vol. 41, no. 12, pp. 1469–1477, Aug. 2020. [Online]. Available: https://doi.org/10.1007/s10762-020-00729-8

[78] M. B. Vicente, "Design of microwave filters and multiplexers in waveguide technology using distributed models," Ph.D. dissertation, Universitat Politècnica de València, 2014. [Online]. Available: https://doi.org/10.4995/thesis/10251/48492

[79] K. Wu, M. Bozzi, and N. J. G. Fonseca, "Substrate integrated transmission lines: review and applications," *IEEE Journal of Microwaves*, vol. 1, no. 1, pp. 345–363, 2021.

[80] B. Potelon, J.-c. Bohorquez, J.-f. Favennec, C. Quendo, E. Rius, and C. Person, "Design of Ku-band filter based on substrate-integrated circular cavities (SICCs)," in *2006 IEEE MTT-S International Microwave Symposium Digest*, 2006, pp. 1237–1240.

[81] T. Zhou, T. Liu, S. Wu, J. Xie, Y. Ye, and G. Xu, "Isosceles triangular cavity based dual-band SIW filters for 5G millimeter-wave systems," in *2021 International Conference on Microwave and Millimeter Wave Technology (ICMMT)*, 2021, pp. 1–3.

[82] A. Pourghorban Saghati, A. Pourghorban Saghati, and K. Entesari, "Ultra-miniature SIW cavity resonators and filters," *IEEE Transactions on Microwave Theory and Techniques*, vol. 63, no. 12, pp. 4329–4340, 2015.

[83] S. Moscato, C. Tomassoni, M. Bozzi, and L. Perregrini, "Quarter-mode cavity filters in substrate integrated waveguide technology," *IEEE Transactions on Microwave Theory and Techniques*, vol. 64, no. 8, pp. 2538–2547, 2016.

[84] W. Hong, B. Liu, Y. Wang, Q. Lai, H. Tang, X. X. Yin, Y. D. Dong, Y. Zhang, and K. Wu, "Half mode substrate integrated waveguide: a new guided wave structure for microwave and millimeter wave application," in *2006 Joint 31st International Conference on Infrared Millimeter Waves and 14th International Conference on Teraherz Electronics*, 2006, pp. 219–219.

[85] M. Bozzi, S. Winkler, and K. Wu, "Broadband and compact ridge substrate-integrated waveguides," *IET Microwaves, Antennas and Propagation*, vol. 4, no. 11, p. 1965, 2010. [Online]. Available: https://doi.org/10.1049/iet-map.2009.0529

[86] S. Sirci, M. A. Sánchez-Soriano, J. D. Martínez, and V. E. Boria, "Electronically reconfigurable doublet in dual-mode coaxial SIW," in *2019 IEEE MTT-S International Microwave Symposium (IMS)*, 2019, pp. 17–20.

[87] A. Belenguer, A. L. Borja, H. Esteban, and V. E. Boria, "High-performance coplanar waveguide to empty substrate integrated coaxial line transition," *IEEE Transactions on Microwave Theory and Techniques*, vol. 63, no. 12, pp. 4027–4034, 2015.

[88] D. Herraiz, H. Esteban, J. A. Martínez, A. Belenguer, and V. Boria, "Microstrip to ridge empty substrate-integrated waveguide transition for broadband microwave applications," *IEEE Microwave and Wireless Components Letters*, vol. 30, no. 3, pp. 257–260, 2020.

[89] E. C. for Space Standardization (ECSS), "Space engineering testing," European Cooperation for Space Standardization (ECSS), Noordwijk, The Netherlands, Tech. Rep. ECSS-E-ST-10-03C Rev.1, May 2022.

[90] D. G. Gilmore, *Spacecraft Thermal Control Handbook*, 2nd ed. El Segundo, CA: Aerospace Press, Aug. 2002.

[91] G. Sebestyen, S. Fujikawa, N. Galassi, and A. Chuchra, *Low earth orbit satellite design*, 1st ed., ser. Space Technology Library. Basel, Switzerland: Springer International Publishing, Feb. 2018.

[92] T. Djerafi, K. Wu, and D. Deslandes, "A temperature-compensation technique for substrate integrated waveguide cavities and filters," *IEEE Transactions on Microwave Theory and Techniques*, vol. 60, no. 8, pp. 2448–2455, Aug 2012.

[93] T. Martin, A. Ghiotto, T. Vuong, and F. Lotz, "Self-temperature-compensated air-filled substrate-integrated waveguide cavities and filters," *IEEE Transactions on Microwave Theory and Techniques*, vol. 66, no. 8, pp. 3611–3621, Aug 2018.

[94] E. secretariat, "European cooperation for space standardization." [Online]. Available: https://ecss.nl

[95] V. Nova, C. B. Martin, J. A. Martínez, H. E. González, J. M. Merello, A. B. Martínez, O. Monerris, and V. E. Boria, "Thermal stability analysis of filters in substrate integrated technologies under atmospheric pressure and vacuum conditions," *IEEE Access*, vol. 8, pp. 118 072–118 082, 2020.

[96] Arianespace, *Ariane 5 User's Manual*, Arianespace.

[97] Arianespace, *Soyuz User's Manual*, Arianespace.

[98] N. Aeronautics and S. A. (NASA), "Payload Vibroacoustic Test Criteria," National Aeronautics and Space Administration (NASA), Washington D.C., Tech. Rep. NASA-STD-7001A, Jan. 2011.

[99] M. Yu, "Power-handling capability for RF filters," *IEEE Microwave Magazine*, vol. 8, no. 5, pp. 88–97, 2007.

[100] A. J. Hatch and H. B. Williams, "Multipacting modes of high-frequency gaseous breakdown," *Phys. Rev.*, vol. 112, pp. 681–685, Nov 1958. [Online]. Available: https://link.aps.org/doi/10.1103/PhysRev.112.681

[101] E. C. for Space Standardization (ECSS), "Space engineering multipactor design and test," European Cooperation for Space Standardization (ECSS), Noordwijk, The Netherlands, Tech. Rep. ECSS-E-ST-20-01C, Jun. 2020.

[102] I. O. for Standardization (ISO), "Additive manufacturing — General principles — Terminology," International Organization for Standardization, Standard, Dec. 2015.

[103] E. Hammerstad and O. Jensen, "Accurate models for microstrip computer-aided design," in *1980 IEEE MTT-S International Microwave symposium Digest*, 1980, pp. 407–409.

[104] G. Gold and K. Helmreich, "Surface impedance concept for modeling conductor roughness," in *2015 IEEE MTT-S International Microwave Symposium*, 2015, pp. 1–4.

[105] P. G. Huray, S. Hall, S. Pytel, F. Oluwafemi, R. Meilitz, D. Hua, and P. Ye, "Fundamentals of a 3-D "snowball" model for surface roughness power losses," *IEEE Electromagnetic Compatibility Magazine*, vol. 9, no. 2, pp. 62–65, 2020.

[106] G. Jialanella, "9 - advances in bonding plastics," in *Advances in Structural Adhesive Bonding*, ser. Woodhead Publishing in Materials, D. A. Dillard, Ed. Woodhead Publishing, 2010, pp. 237–264. [Online]. Available: https://www.sciencedirect.com/science/article/pii/B9781845694357500092

[107] A. Baptista, F. Silva, J. Porteiro, J. Míguez, G. Pinto, and L. Fernandes, "On the physical vapour deposition (PVD): Evolution of magnetron sputtering processes for industrial applications," *Procedia Manufacturing*, vol. 17, pp. 746–757, 2018, 28th International Conference on Flexible Automation and Intelligent Manufacturing (FAIM2018), June 11-14, 2018, Columbus, OH, USA Global Integration of Intelligent Manufacturing and Smart Industry for Good of Humanity. [Online]. Available: https://www.sciencedirect.com/science/article/pii/S2351978918312435

[108] M. G. Eberhardt, A. M. Hodge, and P. S. Branicio, "Atomistic modeling of physical vapor deposition on complex topology substrates," *Computational Materials Science*, vol. 203, p. 111111, 2022. [Online]. Available: https://www.sciencedirect.com/science/article/pii/S0927025621007795

[109] J. W. Dini, "Properties of coatings: comparisons of electroplated, physical vapor deposited, chemical vapor deposited, and plasma sprayed coatings," *Materials and Manufacturing Processes*, vol. 12, no. 3, pp. 437–472, 1997.

[110] Y. Song, D. Shan, and E. Han, "Corrosion behaviors of electroless plating Ni–P coatings deposited on magnesium alloys in artificial sweat solution," *Electrochimica Acta*, vol. 53, no. 4, pp. 2009–2015, 2007, POLYMER ELECTROLYTES Selection of papers from the 10th International Symposium (ISPE-10)15-19 October 2006, Foz do Iguaçú-PR, Brazil. [Online]. Available: https://www.sciencedirect.com/science/article/pii/S0013468607010870

[111] K. Moraczewski, R. Malinowski, P. Rytlewski, and M. Zenkiewicz, "Autocatalytic metallization of polylactide," *Polimery*, vol. 60, no. 07/08, pp. 492–500, Jul. 2015.

[112] D. Liu, H. Nakano, X. Qing, and T. Zwick, Eds., *Handbook of Antenna Technologies*, 1st ed., ser. Handbook of Antenna Technologies. Singapore, Singapore: Springer, Jun. 2016.

[113] T.-Y. Huang, T.-M. Shen, and R.-B. Wu, "Design and modeling of microstrip line to substrate integrated waveguide transitions," in *Passive Microwave Components and Antennas*, V. Zhurbenko, Ed. Rijeka: IntechOpen, 2010, ch. 11. [Online]. Available: https://doi.org/10.5772/9418

[114] X. Huang and K.-L. Wu, "A broadband U-slot coupled microstrip-to-waveguide transition," *IEEE Transactions on Microwave Theory and Techniques*, vol. 60, no. 5, pp. 1210–1217, 2012.

[115] H. Esteban, A. Belenguer, J. R. Sánchez, C. Bachiller, and V. E. Boria, "Improved low reflection transition from microstrip line to empty substrate-integrated waveguide," *IEEE Microwave and Wireless Components Letters*, vol. 27, no. 8, pp. 685–687, 2017.

[116] "High resolution SLA and SLS 3D printers for professionals." [Online]. Available: https://formlabs.com/

[117] Z. Ren, W. Zhou, Y. Qing, S. Duan, H. Pan, and Y. Zhou, "Improved mechanical and microwave absorption properties of SiCf/SiC composites with SiO2 filler," *Ceramics International*, vol. 47, no. 10, Part A, pp. 14 455–14 463, 2021. [Online]. Available: https://www.sciencedirect.com/science/article/pii/S0272884221003710

[118] Q. Zhang, S. Weng, C. M. Hamel, S. M. Montgomery, J. Wu, X. Kuang, K. Zhou, and H. J. Qi, "Design for the reduction of volume shrinkage-induced distortion

in digital light processing 3D printing," *Extreme Mechanics Letters*, vol. 48, p. 101403, 2021. [Online]. Available: https://www.sciencedirect.com/science/article/pii/S235243162100136X

[119] J. D. Martínez, S. Sirci, and V. E. Boria, "Compact SIW filter with asymmetric frequency response for C-band wireless applications," in *2013 IEEE International Wireless Symposium (IWS)*, 2013, pp. 1–4.

[120] C. Máximo-Gutiérrez, J. Hinojosa, and A. Álvarez melcon, "Narrowband and wideband bandpass filters based on empty substrate integrated waveguide loaded with dielectric elements," *IEEE Access*, vol. 9, pp. 32 094–32 105, 2021.

[121] F. Zhu, Y. Wu, P. Chu, G. Q. Luo, and K. Wu, "Single-layer substrate-integrated waveguide inline filters with flexible transmission zeros," *IEEE Microwave and Wireless Components Letters*, vol. 32, no. 6, pp. 495–498, 2022.

[122] F. Cheng, X. Q. Lin, M. Lancaster, K. Song, and Y. Fan, "A dual-mode substrate integrated waveguide filter with controllable transmission zeros," *IEEE Microwave and Wireless Components Letters*, vol. 25, no. 9, pp. 576–578, 2015.

[123] A. Basti, S. Bila, S. Verdeyme, A. Perigaud, L. Estagerie, and H. Leblond, "Design of a compact hybrid filter using microstrip resonators and surface mounted cavities," in *2014 IEEE MTT-S International Microwave Symposium (IMS2014)*, 2014, pp. 1–4.

[124] P. Chu, J. Feng, L. Guo, L. Zhang, L. Liu, and K. Wu, "Multilayer substrate integrated waveguide filter with multimode suppression and wide stopband," *IEEE Transactions on Circuits and Systems II: Express Briefs*, vol. 69, no. 11, pp. 4553–4557, 2022.

[125] Formlabs, "Form 3 Dimensional Accuracy Report," Formlabs, Tech. Rep., May 2021. [Online]. Available: https://media.formlabs.com/m/31d467c9bde28d36/original/-ENUS-Form-3-Dimensional-Accuracy-Report.pdf

[126] S. Johann, F. William, P. Aurélien, T. Olivier, D. Nicolas, S. Bila, V. Serge, P. Jean-Baptiste, and R.-P. Gramond, "Plastic and metal additive manufacturing technologies for hyperfrequency passive components up to Ka band," in *2016 46th European Microwave Conference (EuMC)*, 2016, pp. 373–376.

[127] M. Dionigi, C. Tomassoni, G. Venanzoni, and R. Sorrentino, "Simple high-performance metal-plating procedure for stereolithographically 3-D-printed waveguide components," *IEEE Microwave and Wireless Components Letters*, vol. 27, no. 11, pp. 953–955, 2017.

[128] B. F. Keats, "Bimetal Temperature Compensation for Waveguide Microwave Filters," Doctoral Dissertation, University of Waterloo, Feb. 2007.

[129] O. Monerris, E. Diaz, J. Ruiz, and V. E. Boria, "Automatic, calibrated and accurate measurement of S-parameters in climatic chamber," *IEEE Microwave and Wireless Components Letters*, vol. 25, no. 6, pp. 412–414, jun 2015.

[130] A. D. MacDonald, *Microwave Breakdown in Gases*. New York: Wiley, 1996.

[131] E. C. for Space Standardization (ECSS), "Space product assurance - Thermal vacuum outgassing test for the screening of space materials," ESA-ESTEC, Noordwijk, The Netherlands, Standard ECSS-Q-ST-70-02C, Nov. 2008.

[132] Sergio Anza Hormigo, "Multipactor in multicarrier systems, theory and prediction," Ph.D. dissertation, Universitat Politècnica de València, Jul. 2014.

[133] C. Ernst, V. Postoyalko, and N. Khan, "Relationship between group delay and stored energy in microwave filters," *IEEE Transactions on Microwave Theory and Techniques*, vol. 49, no. 1, pp. 192–196, 2001.

[134] D. Deslandes and K. Wu, "Accurate modeling, wave mechanisms, and design considerations of a substrate integrated waveguide," *IEEE Transactions on Microwave Theory and Techniques*, vol. 54, no. 6, pp. 2516–2526, 2006.

[135] F. Xu and K. Wu, "Guided-wave and leakage characteristics of substrate integrated waveguide," *IEEE Transactions on Microwave Theory and Techniques*, vol. 53, no. 1, pp. 66–73, 2005.

[136] F. Parment, A. Ghiotto, T.-P. Vuong, J.-M. Duchamp, and K. Wu, "Broadband transition from dielectric-filled to air-filled substrate integrated waveguide for low loss and high power handling millimeter-wave substrate integrated circuits," in *2014 IEEE MTT-S International Microwave Symposium (IMS2014)*, 2014, pp. 1–3.

[137] T.-S. Chen, "Determination of the capacitance, inductance, and characteristic impedance of rectangular lines," *IEEE Transactions on Microwave Theory and Techniques*, vol. 8, no. 5, pp. 510–519, 1960.

[138] D. Deslandes, "Design equations for tapered microstrip-to-substrate integrated waveguide transitions," in *2010 IEEE MTT-S International Microwave Symposium*, 2010, pp. 704–707.

[139] I. Hunter, *Theory and design of microwave filters*, ser. Electromagnetics and Radar. Stevenage, England: Institution of Engineering and Technology, Feb. 2001.

[140] H. Peng, X. Xia, J. Dong, and T. Yang, "An improved broadband transition between microstrip and empty substrate integrated waveguide," *Microwave and Optical Technology Letters*, vol. 58, no. 9, pp. 2227–2231, 2016. [Online]. Available: https://onlinelibrary.wiley.com/doi/abs/10.1002/mop.30015

[141] F. Quiles, A. Belenguer, J. A. Martínez, V. Nova, H. Esteban, and V. Boria, "Compact microstrip to empty substrate-integrated coaxial line transition," *IEEE Microwave and Wireless Components Letters*, vol. 28, no. 12, pp. 1080–1082, 2018.

[142] J. M. Merello, V. Nova, C. Bachiller, J. R. Sánchez, A. Belenguer, and V. E. Boria Esbert, "Miniaturization of power divider and 90° hybrid directional coupler for C-band applications using empty substrate-integrated coaxial lines," *IEEE Transactions on Microwave Theory and Techniques*, vol. 66, no. 6, pp. 3055–3062, 2018.

[143] R. Udiljak, "Multipactor in low pressure gas and in nonuniform RF field structures," Ph.D. dissertation, Chalmers University of Technology, 2007. [Online]. Available: https://research.chalmers.se/en/publication/26429

[144] T. Djerafi, D. Hammou, K. Wu, and S. O. Tatu, "Ring-shaped substrate integrated waveguide wilkinson power dividers/combiners," *IEEE Transactions on Components, Packaging and Manufacturing Technology*, vol. 4, no. 9, pp. 1461–1469, 2014.

[145] W. Liang and W. Hong, "Substrate Integrated Coaxial Line 3 dB coupler," *Electonics Letters*, vol. 48, no. 1, pp. 35–36, Jan 2012.

[146] B. Senyuk, "Liquid crystals: A simple view on a complex matter," Apr 2006. [Online]. Available: https://www.personal.kent.edu/~bisenyuk/liquidcrystals/index.html

[147] J. Chen, W. Cranton, and M. Fihn, Eds., *Handbook of visual display technology / handbook of visual display technology*, 2nd ed., ser. Handbook of Visual Display Technology. Cham, Switzerland: Springer International Publishing, Jul. 2016.

[148] D.-K. Yang and S.-T. Wu, *Fundamentals of liquid crystal devices*. Wiley, sept 2014. [Online]. Available: https://doi.org/10.1002/9781118751992

[149] L. F. Chen, C. K. Ong, C. P. Neo, V. V. Varadan, and V. K. Varadan, *Microwave Electronics: measurement and Materials Characterization*. Hoboken, NJ: Wiley-Blackwell, Mar. 2004.

[150] D. C. Zografopoulos, A. Ferraro, and R. Beccherelli, "Liquid-crystal high-frequency microwave technology: materials and characterization," *Advanced Materials Technologies*, vol. 4, no. 2, p. 1800447, 2019. [Online]. Available: https://onlinelibrary.wiley.com/doi/abs/10.1002/admt.201800447

[151] A. Penirschke, S. Muller, P. Scheele, C. Weil, M. Wittek, C. Hock, and R. Jakoby, "Cavity perturbation method for characterization of liquid crystals up to 35 GHz," in *34th European Microwave Conference, 2004.*, vol. 2, 2004, pp. 545–548.

[152] A. Gaebler, F. Goelden, S. Mueller, and R. Jakoby, "Triple-mode cavity perturbation method for the characterization of anisotropic media," in *2008 38th European Microwave Conference*, 2008, pp. 909–912.

[153] R. Kowerdziej, J. Krupka, E. Nowinowski-Kruszelnicki, M. Olifierczuk, and J. Parka, "Microwave complex permittivity of voltage-tunable nematic liquid crystals measured in high resistivity silicon transducers," *Applied Physics Letters*, vol. 102, no. 10, mar 2013, 102904. [Online]. Available: https://doi.org/10.1063/1.4795534

[154] Y. Utsumi, T. Kamei, and R. Naito, "Measurements of effective dielectric permittivity of microstrip-line-type liquid crystal devices using inductive coupled ring resonator," *Electronics Letters*, vol. 39, no. 11, p. 849, 2003. [Online]. Available: https://doi.org/10.1049/el:20030568

[155] M. Yazdanpanahi, S. Bulja, D. Mirshekar-Syahkal, R. James, S. E. Day, and F. A. Fernandez, "Measurement of dielectric constants of nematic liquid crystals at mm-wave frequencies using patch resonator," *IEEE Transactions on Instrumentation and Measurement*, vol. 59, no. 12, pp. 3079–3085, 2010.

[156] D. E. Schaub and D. R. Oliver, "A circular patch resonator for the measurement of microwave permittivity of nematic liquid crystal," *IEEE Transactions on Microwave Theory and Techniques*, vol. 59, no. 7, pp. 1855–1862, 2011.

[157] W. Hu, O. H. Karabey, A. E. Prasetiadi, M. Jost, and R. Jakoby, "Temperature controlled artificial coaxial line for microwave characterization of liquid crystal," in *GeMiC 2014; German Microwave Conference*, 2014, pp. 1–4.

[158] O. H. Karabey, *Electronic Beam Steering and Polarization Agile Planar Antennas in Liquid Crystal Technology*. Springer International Publishing, 2014. [Online]. Available: https://doi.org/10.1007/978-3-319-01424-1

[159] P. Deo, D. Mirshekar-Syahkal, L. Seddon, S. E. Day, and F. A. Fernández, "Microstrip device for broadband (15–65 GHz) measurement of dielectric properties of nematic liquid crystals," *IEEE Transactions on Microwave Theory and Techniques*, vol. 63, no. 4, pp. 1388–1398, 2015.

[160] G. Kent, "Nondestructive permittivity measurement of substrates," *IEEE Transactions on Instrumentation and Measurement*, vol. 45, no. 1, pp. 102–106, 1996.

[161] M. D. Janezic, "Nondestructive relative permittivity and loss tangent measurements using a split-cylinder resonator," Ph.D. dissertation, University of Colorado at Boulder, 2003.

[162] F. L. Penaranda-Foix and J. M. Catala-Civera, "Circuital analysis of cylindrical structures applied to the electromagnetic resolution of resonant cavities," in *Passive Microwave Components and Antennas*, V. Zhurbenko, Ed. Rijeka: IntechOpen, 2010, ch. 7. [Online]. Available: https://doi.org/10.5772/9400

[163] F. L. Penaranda-Foix, M. D. Janezic, J. M. Catala-Civera, and A. J. Canos, "Full-wave analysis of dielectric-loaded cylindrical waveguides and cavities using a new four-port ring network," *IEEE Transactions on Microwave Theory and Techniques*, vol. 60, no. 9, pp. 2730–2740, Sept 2012.

[164] V. Fréedericksz and A. Repiewa, "Theoretisches und experimentelles zur frage nach der natur der anisotropen flüssigkeiten," *Zeitschrift för Physik*, vol. 42, no. 7, pp. 532–546, Jul. 1927. [Online]. Available: https://doi.org/10.1007/bf01397711

[165] X. Nie, H. Xianyu, R. Lu, T. X. Wu, and S. Wu, "Pretilt angle effects on liquid crystal response time," *Journal of Display Technology*, vol. 3, no. 3, pp. 280–283, 2007.

[166] E. Oton, J. Perez-Fernandez, D. Lopez-Molina, X. Quintana, J. M. Oton, and M. A. Geday, "Reliability of liquid crystals in space photonics," *IEEE Photonics Journal*, vol. 7, no. 4, pp. 1–9, Aug. 2015. [Online]. Available: https://doi.org/10.1109/jphot.2015.2451626

[167] C. D. Woehrle, D. T. Doyle, S. A. Lane, and C. G. Christodoulou, "Space radiation environment testing of liquid crystal phase shifter devices," *IEEE Antennas and Wireless Propagation Letters*, vol. 15, pp. 1923–1926, 2016.

[168] D. Doyle, C. Woehrle, D. Wellems, and C. G. Christodoulou, "Environmental concerns with liquid-crystal-based printed reflectarrays in space," *IEEE Antennas and Wireless Propagation Letters*, vol. 15, pp. 1919–1922, 2016.